Physics of Atomic Nuclei, Vol. 67, No. 9, 2004, pp. 1611–1618. From Yadernaya Fizika, Vol. 67, No. 9, 2004, pp. 1637–1644.

Proton–Neutron Interaction near Closed Shells*

A. Covello**, **L. Coraggio**, **A. Gargano**, and **N. Itaco**

Dipartimento di Scienze Fisiche, Università di Napoli Federico II, and Istituto Nazionale di Fisica Nucleare, Complesso Universitario di Monte S. Angelo, Napoli, Italy

Received January 21, 2004

Abstract—Odd–odd nuclei around double shell closures are a direct source of information on the proton–neutron interaction between valence nucleons. We have performed shell-model calculations for doubly odd nuclei close to ^{208}Pb, ^{132}Sn, and ^{100}Sn using realistic effective interactions derived from the CD-Bonn nucleon–nucleon potential. The calculated results are compared with the available experimental data, attention being focused on particle–hole and particle–particle multiplets. While good agreement is obtained for all the nuclei considered, a detailed analysis of the matrix elements of the effective interaction shows that a stronger core-polarization contribution seems to be needed in the particle–particle case.

1. INTRODUCTION

Odd–odd nuclei around double shell closures provide the best testing ground for the matrix elements of the proton–neutron interaction between valence nucleons. In this context, of special interest are nuclei in the close vicinity to ^{208}Pb, ^{132}Sn, and ^{100}Sn, which show strong shell closures for both protons and neutrons. From the experimental point of view, the ^{208}Pb neighbors have been extensively investigated and a large amount of data is available for them. On the other hand, the ^{132}Sn and ^{100}Sn neighbors lie well away from the valley of stability, which makes it very difficult to obtain information on their spectroscopic properties. In recent years, however, substantial progress in the development of spectroscopic techniques has opened the way to the exploration of nuclear structure in the regions of shell closures off stability. This has led to new experimental data for the immediate odd–odd neighbors of both ^{132}Sn and ^{100}Sn. The information presently available for nuclei of this kind, although still rather scanty, is of great value for the understanding of the effective proton–neutron interaction in these two regions as well as for a comparison with the proton–neutron interaction in the ^{208}Pb region.

During the past several years, we have studied a number of nuclei around ^{208}Pb, ^{132}Sn, and ^{100}Sn within the framework of the shell model employing realistic effective interactions derived from modern nucleon–nucleon (NN) potentials. In most of these studies, however, we have been concerned with nuclei having few identical valence particles or holes. A summary of the results obtained through 2000 is given in [1].

More recently [2, 3], we have turned our attention to nuclei with unlike valence nucleons to try to gain information on the neutron–proton effective interaction. The main aim of this paper is to report on some selected results of our current work along these lines, which we have obtained starting from the CD-Bonn free NN potential [4]. In particular, we consider the six odd–odd nuclei ^{208}Bi, ^{210}Bi, ^{132}Sb, ^{134}Sb, ^{98}Ag, and ^{102}In and focus attention on the particle–hole and particle–particle multiplets, which offer the opportunity to test directly the matrix elements of our calculated realistic effective interaction.

To place this study in its proper perspective, it should be mentioned that the particle–hole multiplets in the ^{208}Pb region were the subject of great theoretical and experimental interest [5–8] some thirty-five years ago. In particular, the spectrum of ^{208}Bi was extensively studied through pickup and stripping reactions and several proton–neutron hole multiplets were identified [5, 6]. The pattern exhibited by the observed multiplets was well reproduced by the shell-model calculations of [7], where particle–hole matrix elements derived from the Hamada–Johnston NN potential [9] were used.

Despite these early achievements in the understanding of the effective proton–neutron interaction around closed shells, little work along the same lines has been done during the last three decades. The new data which are becoming available in the ^{132}Sn and

*This article was submitted by the authors in English.

**e-mail: covello@na.infn.it

Table 1. Proton single-particle and neutron single-hole and single-particle energies (in MeV) for the ^{208}Pb region

$\pi(n,l,j)$	ϵ	$\nu(n,l,j)^{-1}$	ϵ	$\nu(n,l,j)$	ϵ
$0h_{9/2}$	0	$2p_{1/2}$	0	$1g_{9/2}$	0
$1f_{7/2}$	0.896	$1f_{5/2}$	0.570	$0i_{11/2}$	0.779
$0i_{13/2}$	1.609	$2p_{3/2}$	0.898	$0j_{15/2}$	1.423
$1f_{5/2}$	2.826	$0i_{13/2}$	1.633	$2d_{5/2}$	1.567
$2p_{3/2}$	3.119	$1f_{7/2}$	2.340	$3s_{1/2}$	2.032
$2p_{1/2}$	3.633	$0h_{9/2}$	3.414	$1g_{7/2}$	2.491
				$2d_{3/2}$	2.538

Table 2. Proton single-particle and neutron single-hole and single-particle energies (in MeV) for the ^{132}Sn region

$\pi(n,l,j)$	ϵ	$\nu(n,l,j)^{-1}$	ϵ	$\nu(n,l,j)$	ϵ
$0g_{7/2}$	0	$1d_{3/2}$	0	$1f_{7/2}$	0
$1d_{5/2}$	0.962	$0h_{11/2}$	0.100	$2p_{3/2}$	0.854
$1d_{3/2}$	2.439	$2s_{1/2}$	0.332	$0h_{9/2}$	1.561
$0h_{11/2}$	2.793	$1d_{5/2}$	1.655	$2p_{1/2}$	1.656
$2s_{1/2}$	2.800	$0g_{7/2}$	2.434	$1f_{5/2}$	2.055
				$0i_{13/2}$	2.694

^{100}Sn regions, as well as the prospect of spectroscopic studies of unstable nuclei opened up by the development of radioactive ion beams, have motivated us to undertake the present study and perform shell-model calculations making use of a modern NN potential and improved many-body methods for deriving the effective interaction.

The outline of the paper is as follows. In Section 2, we give a brief description of our calculations. Our results are presented and compared with the experimental data in Section 3, where we also discuss the effects of the core polarization. In Section 4, we draw the conclusions of our study.

2. CALCULATIONS

In our calculations for the Bi isotopes, we assume that ^{208}Pb is a closed core and let the valence proton and neutron hole occupy the six single-particle levels $0h_{9/2}$, $1f_{7/2}$, $0i_{13/2}$, $1f_{5/2}$, $2p_{3/2}$, and $2p_{1/2}$ of the 82–126 shell, while for the valence neutron the model space includes the seven orbits $1g_{9/2}$, $0i_{11/2}$, $0j_{15/2}$, $2d_{5/2}$, $3s_{1/2}$, $1g_{7/2}$, and $2d_{3/2}$. Similarly, for the Sb isotopes, we assume that the valence proton and neutron hole occupy the five single-particle levels $0g_{7/2}$, $1d_{5/2}$, $1d_{3/2}$, $2s_{1/2}$, and $0h_{11/2}$ of the 50–82 shell, while the valence neutron outside the ^{132}Sn core occupies the orbits of the 82–126 shell. As regards ^{98}Ag and ^{102}In, we assume that the valence neutrons outside the ^{100}Sn core occupy the orbits of the 50–82 shell, while for the proton holes the model space includes the four orbits $0g_{9/2}$, $1p_{1/2}$, $1p_{3/2}$, and $0f_{5/2}$ of the 28–50 shell.

As regards the choice of the single-particle and single-hole energies, we have proceeded as follows. For the Bi isotopes, we have taken them from the experimental spectra [10] of ^{209}Bi, ^{209}Pb, and ^{207}Pb. In the same way, for the Sb isotopes, we have made use of the experimental spectra of ^{133}Sb [11], ^{133}Sn [12], and ^{131}Sn [10]. In the spectra of the two former nuclei, however, some single-particle levels are still missing. More precisely, this is the case of the proton $2s_{1/2}$ and neutron $0i_{13/2}$ levels, whose energies have been taken from [13] and [14], respectively, to which we refer for details. As regards the neutron hole energy $\epsilon_{h_{11/2}}$ in ^{131}Sn, we have adopted the value of 0.100 MeV, which has been recently suggested in [15]. This is somewhat smaller than that reported in [10]. For ^{98}Ag and ^{102}In, the single-particle and single-hole energies cannot be taken from experiment, since no spectroscopic data are yet available for ^{101}Sn and ^{99}In. Therefore, we have taken them from [16] and [17], where they have been determined by an analysis of the low-energy spectra of the Sn isotopes with $A \leq 111$ and of the $N = 50$ isotones with $A \geq 89$. For completeness, our adopted values for the single-particle and single-hole energies are reported in Tables 1–3.

As already mentioned in the Introduction, in our shell-model calculations, we have made use of a realistic effective interaction derived from the CD-Bonn free nucleon–nucleon potential [4]. This high-quality NN potential, which is based upon meson exchange, fits very accurately (χ^2/datum ≈ 1) the world NN data below 350 MeV available in the year 2000.

The shell-model effective interaction V_{eff} is defined, as usual, in the following way. In principle, one should solve a nuclear many-body Schrödinger equation of the form

$$H\Psi_i = E_i\Psi_i, \tag{1}$$

with $H = T + V_{NN}$, where T denotes the kinetic energy. This full-space many-body problem is reduced to a smaller model-space problem of the form

$$PH_{\text{eff}}P\Psi_i = P(H_0 + V_{\text{eff}})P\Psi_i = E_iP\Psi_i. \tag{2}$$

Here, $H_0 = T + U$ is the unperturbed Hamiltonian, U being an auxiliary potential introduced to define a

convenient single-particle basis, and P denotes the projection operator onto the chosen model space,

$$P = \sum_{i=1}^{d} |\psi_i\rangle\langle\psi_i|, \tag{3}$$

d being the dimension of the model space and $|\psi_i\rangle$ the eigenfunctions of H_0. The effective interaction V_{eff} operates only within the model space P. In operator form, it can be schematically written [18] as

$$V_{\text{eff}} = \hat{Q} - \hat{Q}' \int \hat{Q} + \hat{Q}' \int \hat{Q} \int \hat{Q} \tag{4}$$
$$- \hat{Q}' \int \hat{Q} \int \hat{Q} \int \hat{Q} + \ldots,$$

where $\hat{Q}$, usually referred to as the $\hat{Q}$-box, is a vertex function composed of irreducible linked diagrams, and the integral sign represents a generalized folding operation. $\hat{Q}'$ is obtained from $\hat{Q}$ by removing terms of first order in the interaction. Once the $\hat{Q}$-box is calculated, the folded-diagram series of Eq. (4) can be summed up to all orders by iteration methods, as, for instance, the Lee–Suzuki one [19, 20].

A main difficulty encountered in the derivation of V_{eff} from any modern NN potential is the existence of a strong repulsive core which prevents its direct use in nuclear structure calculations. This difficulty is usually overcome by resorting to the well-known Brueckner G-matrix method. Here, we have made use of a new approach [21] which has proved to be an advantageous alternative [21–23] to the use of the above method. The basic idea underlying this approach is to construct a low-momentum NN potential, $V_{\text{low-}k}$, that preserves the physics of the original potential V_{NN} up to a certain cutoff momentum Λ. In particular, the scattering phase shifts and deuteron binding energy calculated by V_{NN} are reproduced by $V_{\text{low-}k}$. The latter is a smooth potential that can be used directly as input for the calculation of shell-model effective interactions. A detailed description of our derivation of $V_{\text{low-}k}$ can be found in [21], where a criterion for the choice of the cutoff parameter Λ is also given. We have used here the value $\Lambda = 2.1$ fm^{-1}.

Once $V_{\text{low-}k}$ is obtained, the calculation of the matrix elements of the effective interaction is carried out within the framework of the folded-diagram method outlined above. The key feature of this approach is that there is no need for G-matrix procedures to eliminate the effects of a strongly repulsive core, since $V_{\text{low-}k}$ can be used directly in the calculation of the vertex function $\hat{Q}$-box. The calculation of $\hat{Q}$, which is in principle an infinite sum of irreducible diagrams, can only be made approximately by selecting certain classes of diagrams. In our calculations, we have included in $\hat{Q}$ all the one-body and two-body diagrams up to second order in $V_{\text{low-}k}$. For instance, for the particle–particle case, these are precisely the diagrams shown in [24]. In this connection, it should be pointed out that the proton–neutron matrix elements for ^{208}Bi, ^{132}Sb, ^{98}Ag, and ^{102}In have been explicitly derived in the particle–hole formalism. A description of the derivation of the particle–hole effective interaction is given in [2].

Table 3. Proton single-hole and neutron single-particle energies (in MeV) for the ^{100}Sn region

$\pi(n,l,j)^{-1}$	ϵ	$\nu(n,l,j)$	ϵ
$0g_{9/2}$	0	$1d_{5/2}$	0
$1p_{1/2}$	0.700	$0g_{7/2}$	0.200
$1p_{3/2}$	2.100	$2s_{1/2}$	2.200
$0f_{5/2}$	3.100	$1d_{3/2}$	2.300
		$0h_{11/2}$	2.700

To summarize, there are three main steps in our derivation of V_{eff}. We first derive the low-momentum $V_{\text{low-}k}$ from the CD-Bonn potential, then calculate the $\hat{Q}$-box including diagrams up to second order in $V_{\text{low-}k}$, and finally obtain V_{eff} by summing up the folded diagram series (4) by means of the Lee–Suzuki iteration method.

3. RESULTS AND COMPARISON WITH EXPERIMENT

In this section, the results of our calculations for the proton–neutron multiplets around ^{208}Pb, ^{132}Sn, and ^{100}Sn are presented and compared with the experimental data. In the first two mass regions, both proton–neutron hole and proton–neutron multiplets are considered by studying ^{208,210}Bi and ^{132,134}Sb. These nuclei, all having only two valence nucleons, are the most appropriate ones to study the effects of the proton–neutron interaction. As regards doubly magic ^{100}Sn, the two immediate odd–odd neighbors for which some experimental information is presently available are ^{98}Ag and ^{102}In, both with four valence nucleons. We have therefore considered these two nuclei to study the proton hole–neutron multiplets in this region. We present our results separately for each mass region in the three following subsections. All calculations have been performed using the OXBASH shell-model code [25].

3.1. ^{208}Pb Region: ^{208}Bi and ^{210}Bi

The particle–hole multiplets in ^{208}Bi were long ago found to exhibit a peculiar behavior [5, 6]; namely,

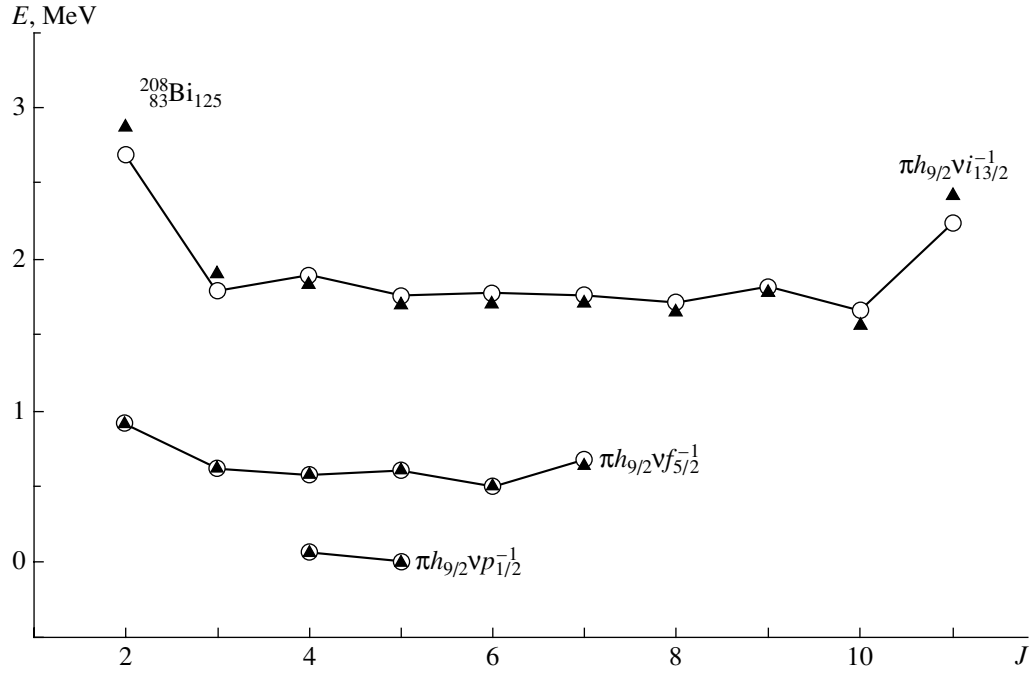

Fig. 1. Proton particle–neutron hole multiplets in ^{208}Bi. The calculated results are represented by open circles and the experimental data by solid triangles. The lines are drawn to connect the points.

the states with the minimum and maximum J have the highest excitation energy, while the state with next to highest J is the lowest one. As mentioned in the Introduction, the results of the shell-model calculations of [7] turned out to be consistent with this pattern.

In Fig. 1, our results for three multiplets are reported and compared with the experimental data [10]. Note that the energies are relative to the 5^+ ground state, which is a member of the doublet $\pi h_{9/2}\nu p^{-1}_{1/2}$. We see that the calculated energies account for the pattern of the experimental multiplets, the quantitative agreement being remarkably good with discrepancies well below 100 keV for almost all the states. It should be pointed out that our calculations give a better description of the experimental data than the early realistic calculations of [7].

Let us now come to ^{210}Bi. In Fig. 2, the calculated $\pi h_{9/2}\nu g_{9/2}$ multiplet (represented by open circles) is shown and compared with the experimental data [10]. This multiplet shows a breakdown of the Nordheim strong rule [26] in that the 1^- state is the ground state while the 0^- one lies at about 50 keV excitation energy. We see that our calculation predicts for the ground state $J^\pi = 0^-$ with the 1^- state at about 150 keV excitation energy. This is, however, the most significant discrepancy, all other experimental excitation energies being reproduced within a few tens of keV. As a whole, the pattern of this multiplet as compared to that of the particle–hole multiplets is still parabolic, but concave downward. Of course, this stems from the fact that the interaction changes from repulsive to attractive.

It should be pointed out that the behavior of all the multiplets considered above is directly related to the proton–neutron effective interaction since their members are of almost pure configuration. In this context, it is quite interesting to study the renormalization of the effective interaction, which we have taken into account through second-order diagrams in $V_{\text{low-}k}$. By way of illustration, we report in Tables 4 and 5 the diagonal matrix elements of the effective interaction for the particle–hole $\pi h_{9/2}\nu f^{-1}_{5/2}$ and particle–particle $\pi h_{9/2}\nu g_{9/2}$ configuration, respectively. In both tables, we also show the corresponding matrix elements of $V_{\text{low-}k}$ and $\langle V_{\text{ph}}\rangle$, the latter representing the contribution of the particle–hole core-polarization diagram, the so-called "bubble." Here, we do not consider the contributions coming from either other second-order diagrams or folded diagrams, both of which we have found irrelevant for the present discussion. From Table 4, we see that the matrix elements of V_{ph}, although not very large in magnitude, are quite relevant in determining the pattern of the considered particle–hole multiplet. In fact, they are repulsive for states with minimum and maximum J and attractive for $J = J_{\max} - 1$. It is worth noting that the repulsive contribution to the $J_{\max}$ state is

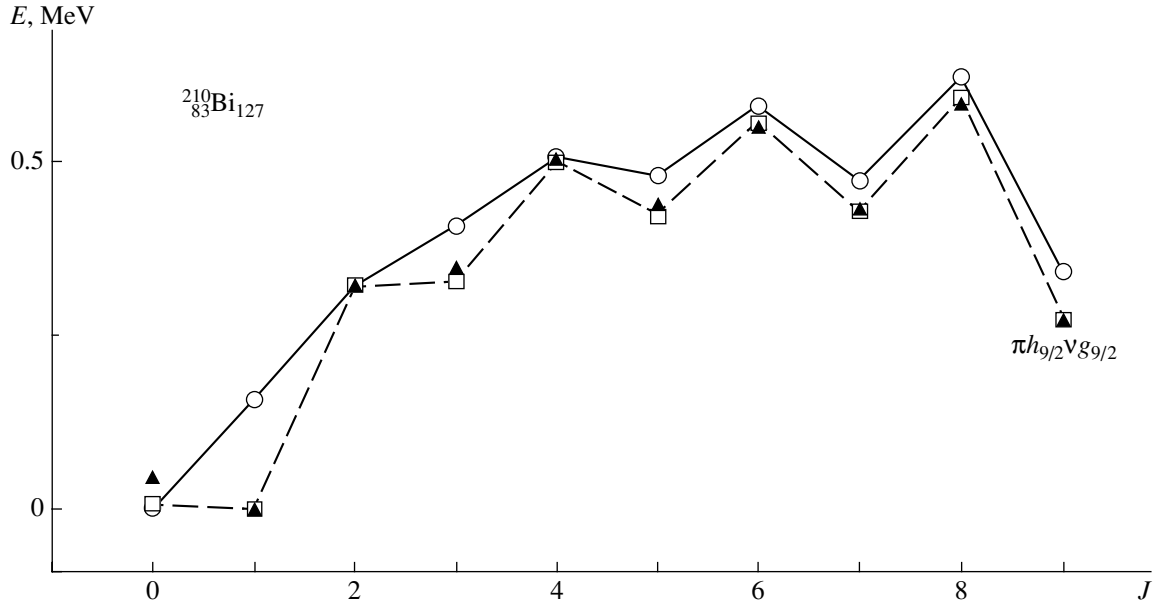

Fig. 2. Proton–neutron $\pi h_{9/2}\nu g_{9/2}$ multiplet in ^{210}Bi. The calculated results are represented by open circles and squares (see text for comments) and the experimental data by solid triangles. The lines are drawn to connect the points.

essential to place it above the state with $J = J_{\min} + 1$. For the particle–particle case, Table 5 shows that the core-polarization contribution is essentially repulsive, except for the $J^\pi = 1^-$ state. This goes in the right direction, as it reduces the spacing between the 1^- and 0^- states. However, as is evident from Fig. 2, it is not sufficient to produce the inversion of these two states.

On these grounds, we have found it interesting to modify our effective interaction for ^{210}Bi by simply increasing the diagonal matrix elements of $V_{\rm ph}$ for the $\pi h_{9/2}\nu g_{9/2}$ configuration. It turns out that all the calculated energies go in the right direction, a factor of 2.6 being sufficient to give the correct ground state. The results of this calculation (represented by open squares) are shown in Fig. 2. It can be seen that they practically overlap the experimental ones.

Table 4. Diagonal matrix elements of $V_{\rm eff}$, $V_{\text{low-}k}$, and $V_{\rm ph}$ (in MeV) for the $\pi h_{9/2}\nu f^{-1}_{5/2}$ configuration in ^{208}Bi

J	$\langle V_{\rm eff}\rangle$	$\langle V_{\text{low-}k}\rangle$	$\langle V_{\rm ph}\rangle$
2	0.479	0.512	0.102
3	0.140	0.194	−0.008
4	0.069	0.129	−0.027
5	0.071	0.091	−0.001
6	−0.020	0.044	−0.055
7	0.151	0.082	0.087

3.2. ^{132}Sn Region: ^{132}Sb and ^{134}Sb

The particle–hole and particle–particle nuclei ^{132}Sb and ^{134}Sb play in the ^{132}Sn region the role played by ^{208}Bi and ^{210}Bi in the ^{208}Pb region. In this connection, it is worth mentioning that the resemblance between the spectroscopy of these two regions has been emphasized in several recent papers [27].

Table 5. Diagonal matrix elements of $V_{\rm eff}$, $V_{\text{low-}k}$, and $V_{\rm ph}$ (in MeV) for the $\pi h_{9/2}\nu g_{9/2}$ configuration in ^{210}Bi

J	$\langle V_{\rm eff}\rangle$	$\langle V_{\text{low-}k}\rangle$	$\langle V_{\rm ph}\rangle$
0	−0.524	−0.514	0.020
1	−0.426	−0.333	−0.093
2	−0.250	−0.306	0.053
3	−0.179	−0.174	−0.002
4	−0.089	−0.153	0.065
5	−0.117	−0.138	0.025
6	−0.027	−0.084	0.061
7	−0.126	−0.157	0.034
8	0.015	−0.038	0.059
9	−0.275	−0.286	−0.003

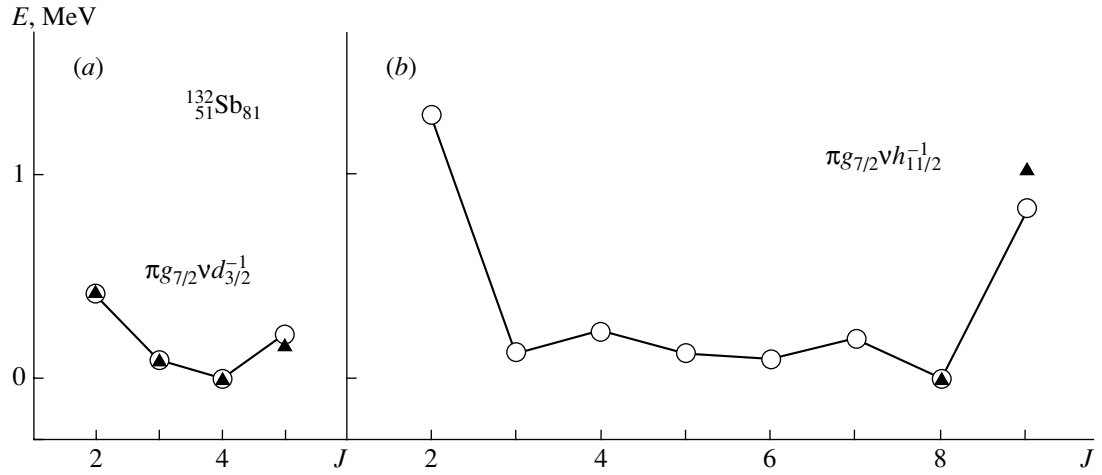

Fig. 3. As in Fig. 1, but for ^{132}Sb.

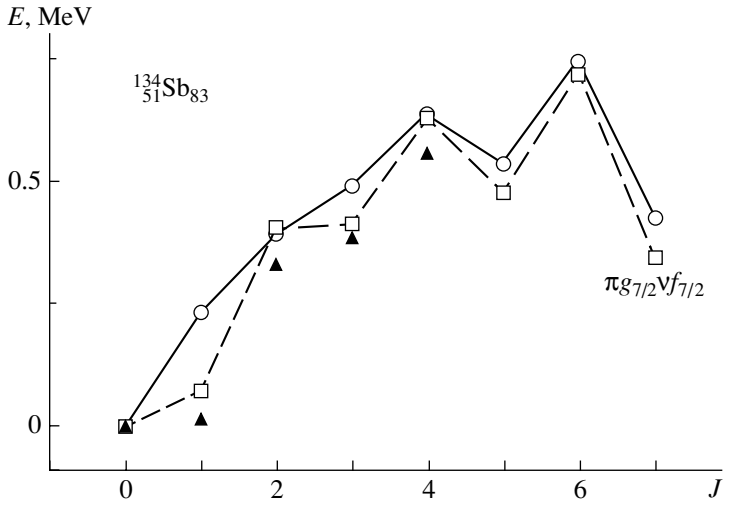

Fig. 4. As in Fig. 2, but for the $\pi g_{7/2}\nu f_{7/2}$ multiplet in ^{134}Sb.

The nucleus ^{132}Sb has been the subject of our study of [2], to which we refer for details. Some multiplets have been also reported in [28] together with some results for ^{134}Sb. For completeness, we report in Fig. 3 the $\pi g_{7/2}\nu d^{-1}_{3/2}$ and $\pi g_{7/2}\nu h^{-1}_{11/2}$ multiplets in ^{132}Sb, while Fig. 4 shows our results for the $\pi g_{7/2}\nu f_{7/2}$ multiplet in ^{134}Sb. Note that these multiplets are just the counterparts of those considered above for ^{208}Bi and ^{210}Bi (aside from the doublet $\pi g_{9/2}\nu p^{-1}_{1/2}$). Comments on the behavior of the multiplets as well as on the quality of agreement between theory and experiment can be found in [2, 28]. In the latter paper, the diagonal matrix elements of V_{eff}, $V_{\text{low-}k}$, and V_{ph} for the $\pi g_{7/2}\nu d^{-1}_{3/2}$ and $\pi g_{7/2}\nu f_{7/2}$ configurations are reported. We emphasize here that the particle–hole and particle–particle matrix elements of the effective interaction in the ^{132}Sn region show the same features as those evidenced above for the ^{208}Pb region. In particular, we have found that, also in this case, the core-polarization plays a significant role, but it is not sufficient to give the right spacing between the 0^- and 1^- states in the particle–particle multiplet of ^{134}Sb (see Fig. 4). We have then modified the effective interaction by multiplying the diagonal matrix elements of V_{ph} for the $\pi g_{7/2}\nu f_{7/2}$ configuration by the same factor used for ^{210}Bi. The corresponding results are represented by open squares in Fig. 4, where we see that they are in excellent agreement with experiment.

3.3. ^{100}Sn Region: ^{98}Ag and ^{102}In

In the ^{100}Sn region, the counterpart of ^{208}Bi and ^{132}Sb is ^{100}In, which until now has not been ac-

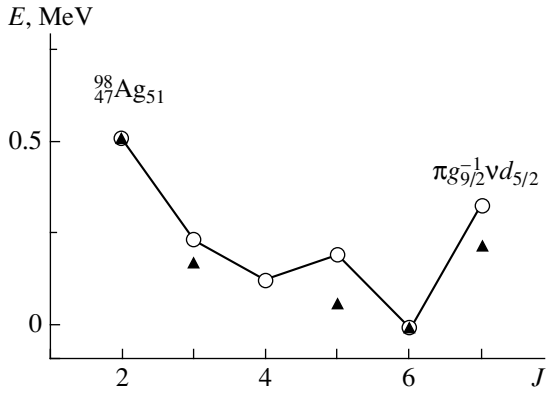

Fig. 5. Proton hole–neutron particle $\pi g_{9/2}^{-1}\nu d_{5/2}$ multiplet in ^{98}Ag. The conventions of the presentation are the same as those used in Fig. 1.

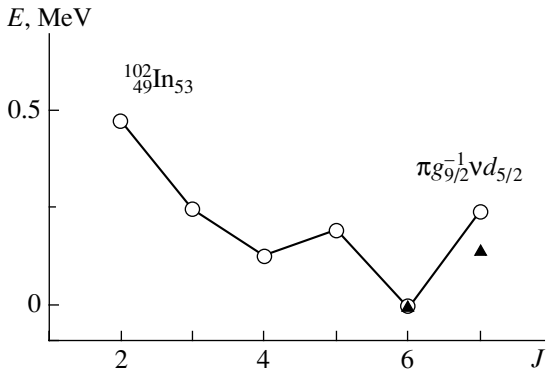

Fig. 6. As in Fig. 5, but for ^{102}In.

cessible to spectroscopic studies. We have therefore considered the two neighboring odd–odd isotopes ^{98}Ag and ^{102}In, focusing attention on the $\pi g_{9/2}^{-1}\nu d_{5/2}$ multiplet, for which some experimental information is available. The members of the calculated multiplet in both nuclei have been identified as those dominated by this configuration with the two remaining valence nucleons forming a zero-coupled pair. In Figs. 5 and 6, we report the results of our calculations for ^{98}Ag and ^{102}In, respectively, and compare them with the experimental data [10]. We see that the agreement between experiment and theory is of the same quality as that obtained in the ^{208}Pb and ^{132}Sn regions, the largest discrepancy being 130 keV for the 5^+ state in ^{98}Ag. The pattern of the calculated multiplets turns out to be similar to that of the multiplets in ^{208}Bi and ^{132}Sb. However, we find that the percentage of components other than those we have considered to characterize the multiplet is rather large. For instance, it reaches about 60% for the 7^+ state in ^{102}In.

Table 6. Diagonal matrix elements of $V_{\rm eff}$, $V_{\text{low-}k}$, and $V_{\rm ph}$ (in MeV) for the $\pi g_{9/2}^{-1}\nu d_{5/2}$ configuration in ^{100}In

J	$\langle V_{\rm eff}\rangle$	$\langle V_{\text{low-}k}\rangle$	$\langle V_{\rm ph}\rangle$
2	0.994	0.891	0.197
3	0.328	0.335	0.020
4	0.171	0.249	−0.038
5	0.196	0.175	0.021
6	−0.007	0.112	−0.102
7	0.487	0.205	0.244

A detailed discussion of the structure of the calculated states will be included in a forthcoming publication.

The diagonal matrix elements of the effective interaction for the proton hole–neutron particle $\pi g_{9/2}^{-1}\nu d_{5/2}$ configuration are reported in Table 6, where we see that their behavior is quite similar to that occurring in the heavier mass regions.

4. SUMMARY AND CONCLUSIONS

We have presented here some results of a shell-model study of odd–odd nuclei in the close vicinity to doubly magic ^{208}Pb, ^{132}Sn, and ^{100}Sn, where use has been made of realistic effective interactions derived from the CD-Bonn NN potential.

The main aim of this work has been to gain insight into the effects of the proton–neutron interaction on the pattern of the particle–hole and particle–particle multiplets. To this end, we have made a detailed comparison between the calculated results and the available experimental data as well as an analysis of the proton–neutron matrix elements of our effective interaction. It has turned out that the core polarization is essential for the effective interaction to produce a good description of all considered nuclei. In this context, we have found out that some discrepancies for the particle–particle multiplets in both ^{210}Bi and ^{134}Sb are removed when the core polarization contribution is increased by a factor of 2.6. This is likely to be traced to the coupling of the single-particle motion to the octupole excitation in ^{208}Pb and ^{132}Sn.

A relevant outcome of our calculations is that for all the particle–hole multiplets the $J_{\rm min}$ and $J_{\rm max}$ states have the highest excitation energy, while the state with next to the highest $J_{\rm max}$ is the lowest, in agreement with the predictions of the Brennan–Bernstein coupling rule [29].

In summary, we may conclude that the results of the present study show that realistic shell-model

calculations are able to describe with quantitative accuracy the effects of the proton–neutron interaction around closed shells, which gives confidence in their predictive power. This is of particular value for nuclei in the ^{132}Sn and ^{100}Sn regions, for which it is of utmost importance to gain more experimental information.

ACKNOWLEDGMENTS

This work was supported in part by the Italian Ministero dell'Istruzione, dell'Università e della Ricerca (MIUR).

REFERENCES

1. A. Covello, L. Coraggio, A. Gargano, and N. Itaco, Acta Phys. Pol. B **32**, 871 (2001), and references therein.
2. L. Coraggio, A. Covello, A. Gargano, *et al.,* Phys. Rev. C **66**, 064311 (2002).
3. A. Covello, L. Coraggio, A. Gargano, and N. Itaco, Acta Phys. Pol. B **34**, 2257 (2003).
4. R. Machleidt, Phys. Rev. C **63**, 024001 (2001).
5. J. R. Erskine, Phys. Rev. **135**, B110 (1964).
6. W. P. Alford, J. P. Schiffer, and J. J. Schwartz, Phys. Rev. Lett. **21**, 156 (1968).
7. T. T. S. Kuo, Nucl. Phys. A **122**, 325 (1968).
8. M. Moinester, J. P. Schiffer, and W. P. Alford, Phys. Rev. **179**, 984 (1969).
9. T. Hamada and I. D. Johnston, Nucl. Phys. **34**, 382 (1962).
10. Data extracted using the NNDC On-line Data Service from the ENSDF Database (file revised as of Oct. 15, 2003).
11. M. Sanchez-Vega, B. Fogelberg, H. Mach, *et al.*, Phys. Rev. C **60**, 024303 (1999).
12. P. Hoff *et al.*, Phys. Rev. Lett. **77**, 1020 (1996).
13. F. Andreozzi, L. Coraggio, A. Covello, *et al.*, Phys. Rev. C **56**, R16 (1997).
14. L. Coraggio, A. Covello, A. Gargano, and N. Itaco, Phys. Rev. C **65**, 051306(R) (2002).
15. J. Genevey, J. A. Pinston, H. Faust, *et al.*, Eur. Phys. J. A **7**, 463 (2000).
16. F. Andreozzi, L. Coraggio, A. Covello, *et al.*, Phys. Rev. C **54**, 1636 (1996).
17. L. Coraggio, A. Covello, A. Gargano, *et al.*, J. Phys. G **26**, 1697 (2000).
18. T. T. S. Kuo and E. M. Krenciglowa, Nucl. Phys. A **342**, 454 (1980).
19. S. Y. Lee and K. Suzuki, Phys. Lett. B **91B**, 173 (1980).
20. K. Suzuki and S. Y. Lee, Prog. Theor. Phys. **64**, 2091 (1980).
21. S. Bogner, T. T. S. Kuo, L. Coraggio, *et al.*, Phys. Rev. C **65**, 051301(R) (2002).
22. A. Covello, L. Coraggio, A. Gargano, *et al.*, in *Challenges of Nuclear Structure: Proceedings of the Seventh International Spring Seminar on Nuclear Physics, Maiori, Italy, 2001,* Ed. by A. Covello (World Sci., Singapore, 2002), p. 139.
23. L. Coraggio, N. Itaco, A. Covello, *et al.*, Phys. Rev. C **68**, 034320 (2003).
24. M. F. Jiang, R. Machleidt, D. B. Stout, and T. T. S. Kuo, Phys. Rev. C **46**, 910 (1992).
25. B. A. Brown, A. Etchegoyen, and W. D. M. Rae, The Computer Code OXBASH, MSU-NSCL, Report No. 524 (1986).
26. L. W. Nordheim, Phys. Rev. **78**, 294 (1950); Rev. Mod. Phys. **23**, 322 (1951).
27. B. Fornal *et al.*, Phys. Rev. C **63**, 024322 (2001), and references therein.
28. A. Gargano, L. Coraggio, A. Covello, and N. Itaco, *The Labirinth in Nuclear Structure,* Ed. by A. Bracco and C. A. Kalfas, AIP Conf. Proc. **701**, 149 (2004).
29. M. H. Brennan and A. M. Bernstein, Phys. Rev. **120**, 927 (1960).

Physics of Atomic Nuclei, Vol. 67, No. 9, 2004, pp. 1619–1626. From Yadernaya Fizika, Vol. 67, No. 9, 2004, pp. 1645–1653.

Relativistic Description of Exotic Nuclei and Nuclear Matter at Extreme Conditions*

J. Meng, S. F. Ban, J. Li, W. H. Long, H. F. Lü, S. Q. Zhang, W. Zhang, and S.-G. Zhou**

School of Physics, Peking University, Beijing, China

Received January 21, 2004

Abstract—Recent works on the relativistic description of exotic nuclei and nuclear matter at extreme conditions are reviewed. New parameter sets for the Lagrangian density in the relativistic mean field (RMF) theory, PK1, PK1r, and PKDD are proposed with the center-of-mass correction included in a microscopic way. The density-dependences of effective interactions in RMF for nuclear matter and neutron stars are discussed. They are able to provide an excellent description not only for the properties of nuclear matter and neutron stars, but also for the nuclei near or far from the beta-stability line, including halos and giant halos at the neutron drip line in nuclei and hypernuclei. As a step toward the investigation of deformed nuclei close to the drip line, the Woods–Saxon basis has been suggested to replace the widely used harmonic oscillator basis for solving the RMF equations. Based on the two-neutron separation energy, shell correction energy, and effective pairing gaps, etc., new magic numbers for superheavy nuclei are suggested.

1. INTRODUCTION

A widely used and successful approach for describing properties of nuclear matter and finite nuclei is the relativistic mean field (RMF) theory [1]. It has been used not only for describing the properties of nuclei near the valley of stability successfully [2], but also for predicting the properties of exotic nuclei with large neutron or proton excess [3, 4]. Based on the RMF theory and its generalization, some works on the relativistic description of exotic nuclei and nuclear matter at extreme conditions have been done at Peking University, including the following:

1. The ground state properties including the radius, density distribution, and one-neutron separation energy for C, N, O, and F isotopes up to the neutron drip line have been systematically studied using the self-consistent microscopic relativistic continuum Hartree–Bogolyubov (RCHB) theory. With the proton density distribution thus obtained, the charge-changing cross sections for C, N, O, F, and Na isotopes are calculated using the Glauber model. Good agreement with the data has been achieved [5, 6].

2. We study the proton magic O, Ca, Ni, Zr, Sn, and Pb isotope chains from the proton drip line to the neutron drip line with the RCHB theory. Halos and giant halos in Ca isotopes with $A > 60$ and Ne–Na–Mg drip line nuclei are investigated [7, 8].

3. Based on the systematic investigation of the data available for nuclei with $A \geq 40$, a $Z^{1/3}$ dependence for the nuclear charge radius is shown to be superior to the generally accepted $A^{1/3}$ law. A new isospin dependent $R_c/Z^{1/3}$ formula for the nuclear charge radius is proposed [9].

4. The Woods–Saxon (WS) basis is suggested to replace the widely used harmonic oscillator basis for solving the RMF equations in order to be generalized to study exotic nuclei [10, 11].

5. Structure and synthesis for superheavy elements based on RMF theory and research on nuclides beyond the drip line have been done [12, 13].

6. We also investigate the hyperon–nucleon interaction and the existence of hyperon halos and neutron halos in hypernuclei [14–16], as well as neutron stars [17–20].

7. Based on the Dirac equation, we have discussed the exact pseudospin symmetry in the particle channel and also spin symmetry in the antiparticle channel [21–24].

8. The difference of spectral statistics properties between single-j and two-j shell models has been studied in the framework of the cranking model and the particle-rotor model. The chiral doublets for nuclei in the $A \sim 100$ and $A \sim 130$ regions have been studied with the particle-rotor model [25, 26].

In this paper, we will present our new parameter sets for the Lagrangian density in RMF theory, PK1, PK1r, and PKDD, together with their description for

*This article was submitted by the authors in English.

** e-mail: mengj@pku.edu.cn

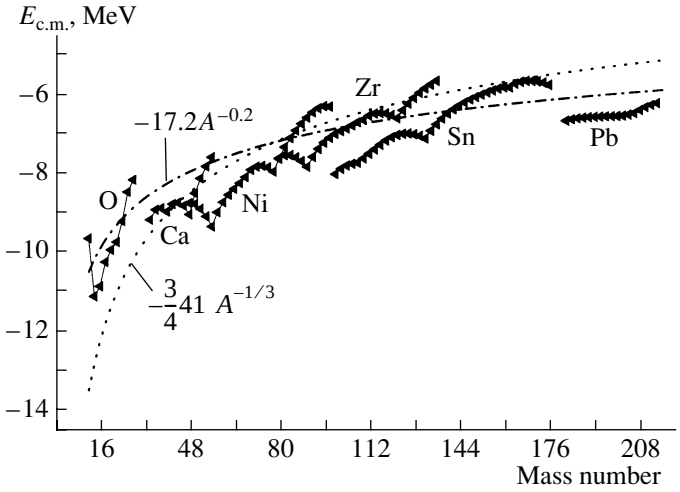

Fig. 1. The microscopic center-of-mass correction in comparison with phenomenological ones.

nuclear matter and neutron stars, halos and giant halos at the neutron drip line, the RMF theory in the Woods–Saxon basis, and new magic numbers for superheavy nuclei.

2. NEW EFFECTIVE INTERACTIONS IN RMF THEORY

In the mean field theory, the effective interactions are adjusted to reproduce various properties of nuclear matter and finite nuclei. A number of effective interactions of meson–baryon couplings based on the RMF theory have been developed, including nonlinear self-couplings for the σ meson or ω meson, such as NL1 and NL2 [27], NL3 [28], NLSH [29], and TM1 and TM2 [30]. These nonlinear interactions have problems of stability at high densities, as well as the question of their physical foundation [27]. A more natural alternative is to introduce a density dependence in the couplings [31]. Based on the results of the Dirac–Brueckner theory, Typel and Wolter proposed the density-dependent effective interaction TW-99 and expected that the model could be extrapolated to nuclear matter at extreme conditions of isospin and/or density [31]. Along this line, Nikšić *et al.* developed another effective interaction, DD-ME1 [32].

Along the β-stability line, NL1 gives excellent results for binding energies and charge radii. Far away from the stability line, the results are less satisfactory due to the large asymmetry energy $a \simeq 44$ MeV. In addition, the calculated neutron skin thickness shows systematic deviations from the data. NLSH produces an asymmetry energy $a \simeq 36$ MeV while giving a slight overbinding along the line of beta stability. It also fails to reproduce the superdeformed minima in Hg isotopes. For the nuclear matter incompressibility, NL1 predicts $K = 212$ MeV, while $K = 355$ MeV for NLSH. Both fail to reproduce the isoscalar giant monopole resonances for Pb and Zr nuclei. As an improvement, the effective interactions NL3 and TM1 provide reasonable incompressibility, $K_{\mathrm{NL3}} = 271.7$ MeV and $K_{\mathrm{TM1}} = 281.16$ MeV, and asymmetry energy ($a_{\mathrm{NL3}} = 37.4$ MeV, $a_{\mathrm{TM1}} = 36.89$ MeV), but they give a fairly small saturation density, $\rho_{\mathrm{NL3}} = 0.148$ fm^{-3} and $\rho_{\mathrm{TM1}} = 0.145$ fm^{-3}. One should note that, in all these parametrizations, the center-of-mass corrections are treated in a phenomenological way. In Fig. 1, the microscopic center-of-mass correction from the RCHB calculation [3, 4] for proton magic isotopes is shown in comparison with usual phenomenological estimates. Systematic deviations can be seen.

As the effective interaction without nonlinear ω terms leads to a strong repulsive potential for nuclear matter at high density, new effective interactions with nonlinear ω self-coupling (PK1) and also nonlinear ρ self-coupling (PK1r) have been developed. The microscopic estimates for the center-of-mass corrections have been improved by the fitting of new effective interactions. Following the density-dependent interaction TW-99 and DD-ME1, PKDD is also proposed as shown in Tables 1 and 2. In the parametrization, the masses of some spherical nuclei and the incompressibility K, the saturated density ρ_{sat}, and the symmetry energy a_{sym} of nuclear matter are included (the details can be seen in [33]).

3. NUCLEAR MATTER AND NEUTRON STARS

Using PK1, PK1r, and PKDD together with NL1 and NL2 [27], NL3 [28], NLSH [29], TM1 and TM2 [30], GL-97 [34], and the density-dependent parameter sets TW-99 [31] and DD-ME1 [32], the density

Table 1. The nonlinear effective interactions PK1, PK1r, and density-dependent effective interactions PKDD in comparison with TM1, NL3, TW-99, and DD-ME1

	PK1	PK1r	PKDD	TM1	NL3	TW-99	DD-ME1
M_n	939.5731	939.5731	939.5731	938	939	939	938.5000
M_p	938.2796	938.2796	938.2796	938	939	939	938.5000
m_σ	514.0891	514.0873	555.5112	511.198	508.1941	550	549.5255
m_ω	784.254	784.2223	783	783	782.501	783	783.0000
m_ρ	763	763	763	770	763	763	763.0000
g_σ	10.3222	10.3219	10.7385	10.0289	10.2169	10.7285	10.4434
g_ω	13.0131	13.0134	13.1476	12.6139	12.8675	13.2902	12.8939
g_ρ	4.5297	4.55	4.2998	4.6322	4.4744	3.661	3.8053
g_2	−8.1688	−8.1562	0	−7.2325	−10.4307	0	0.0000
g_3	−9.9976	−10.1984	0	0.6183	−28.8851	0	0.0000
c_3	55.636	54.4459	0	71.3075	0	0	0.0000
d_3	0	350	0	0	0	0	0

Table 2. Density-dependent parameters of PKDD for meson–nucleon coupling in comparison with TW-99 and DD-ME1

	a_σ	b_σ	c_σ	d_σ	a_ω	b_ω	c_ω	d_ω	a_ρ
PKDD	1.327423	0.435126	0.691666	0.694210	1.342170	0.371167	0.611397	0.738376	0.183305
TW-99	1.365469	0.226061	0.409704	0.901995	1.402488	0.172577	0.344293	0.983955	0.515000
DD-ME1	1.3854	0.9781	1.5342	0.4661	1.3879	0.8525	1.3566	0.4957	0.5008

dependences of various effective interaction strengths in RMF are studied and carefully compared in nuclear matter and neutron stars [35].

In Fig. 2, the dependences of the effective interaction strengths for g_σ (top), g_ω (middle), and g_ρ (bottom) in nuclear matter as a function of the nuclear density are shown. Without otherwise stating, we label the curves in the figures from top to bottom in order from left to right. The shadowed area corresponds to the empirical value of the saturation point in nuclear matter, that is, Fermi momentum $k_F = 1.35 \pm 0.05$ fm^{-1} or density $\rho = 0.166 \pm 0.018$ fm^{-3}. For the nonlinear effective interaction, the "equivalent" density dependence of the effective interaction strengths for σ, ω, and ρ is extracted from the meson field equations according to

$$g_\sigma(\rho) = g_\sigma + U'(\sigma)/\rho_s = g_\sigma + (g_2\sigma^2 + g_3\sigma^3)/\rho_s, \quad (1)$$

$$g_\omega(\rho) = g_\omega - U'(\omega)/\rho = g_\omega - (c_3\omega^3)/\rho, \quad (2)$$

$$g_\rho(\rho) = g_\rho. \quad (3)$$

For the σ meson, TW-99 and DD-ME1 are quite different from the other strengths in either magnitude or slope. In particular, the strength in TW-99 and DD-ME1 for the density interval in Fig. 2 is almost two times larger than that of GL-97. Quite different results can also be seen at the empirical nuclear matter densities. For the ω meson, except TW-99, DD-ME1, TM1, and TM2, all the other strengths are density-independent. However, the strengths are closer to each other at the empirical saturation density than that of the σ meson, although large differences can also be seen at low density. For the ρ meson, which describes the isospin asymmetry, the strengths for TW-99 and DD-ME1 show a strong density dependence in contrast with the other parameter set; PK1, PK1r, and PKDD are just in between.

The interaction strengths as a function of the baryon density for neutron star matter are given in Fig. 3. We do not include NL2 and TM2 here as they are mainly used in light nuclei. At low density, $\rho < 0.3$ fm^{-3}, Fig. 3 is similar to Fig. 2. For the scalar meson, the interaction strengths of TW-99,

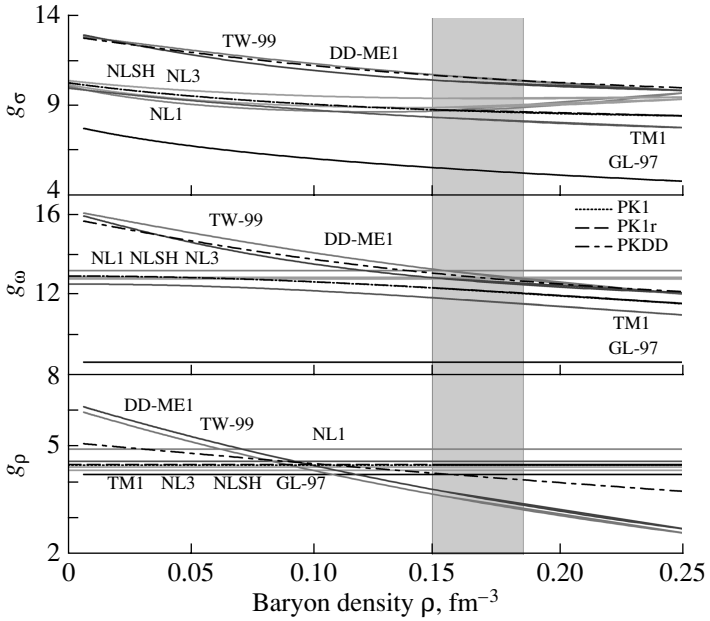

Fig. 2. Density dependence of the effective interaction strengths for g_σ (top), g_ω (middle), and g_ρ (bottom) in nuclear matter as a function of the nuclear density. The shadowed area corresponds to the empirical value of the saturation point in nuclear matter (Fermi momentum $k_{\rm F} = 1.35 \pm 0.05$ fm^{-1} or density $\rho = 0.166 \pm 0.018$ fm^{-3}).

DD-ME1, TM1, and GL-97 decrease with the baryon density in similar slopes. For NL1, NL3, and NLSH, the interaction strengths decrease with baryon density for $\rho < 0.2$ fm^{-3}, then increase afterwards. For the vector ω meson, the interaction strengths of TW-99, DD-ME1, and TM1 decrease with the baryon density. For σ and ω mesons, the strength for PKDD is in between FTW-99 and DD-ME1, while PK1 and PK1r show a similar trend as TM1. For the isospin-vector ρ meson, the interaction strengths of TW-99 and DD-ME1 decrease dramatically with baryon density and do not coincide with the others at saturated density. PKDD gives a value in between.

The binding energy per nucleon, $E_B/A = \varepsilon/\rho - m$, is also investigated for pure neutron matter, symmetric nuclear matter, and neutron stars; more details can be found in [33].

In order to study the structure of neutron stars, we must investigate the equation of state (EOS). At low density, neutron stars consist mainly of neutrons. As the density increases, high-momentum neutrons β decay into protons and electrons ($n \leftrightarrow p + e^- + \bar{\nu}_e$). When the above reaction reaches equilibrium, the chemical potentials satisfy the relation $\mu_p = \mu_n - \mu_e$ [35]. The stiffer the EOS, the larger the mass that can be sustained against collapse. There are two limits. One is that the EOS is as stiff as allowed by the causal constraint $\partial p/\partial\varepsilon \leq 1$ and the limiting mass is just over $3M_\odot$. The other corresponds to a very soft EOS by assuming that dense matter consists merely of a free Fermi gas of neutrons, protons, and leptons in equilibrium and the limiting mass is about $0.7M_\odot$. Any realistic model involving nuclear forces should be within these two limits. Here, the EOS calculated by different effective interactions is given in Fig. 4. GL-97 gives the softest EOS due to its smallest interaction strength. TW-99 and DD-ME1 give softer EOS than those of NL1, NL3, and NLSH. The EOS of TM1, which includes nonlinear self-coupling of both σ and ω mesons, is very close to those of TW-99 and GL-97. PKDD is similar as DD-ME1, while PK1 and PK1r are close to TM1 and TW-99.

For a given EOS, the Oppenheimer–Volkoff (OV) equation has a unique solution which depends on a single parameter characterizing the conditions of matter at the center. In Fig. 5, the central density (top) and radius (bottom) vs. maximum mass for neutron star for different interactions are shown. The OV limits calculated from different EOS are $2-3M_\odot$, and the corresponding radii are 10–14 km. The results calculated by DD-ME1 and TW-99, respectively, are $2.563M_\odot$, 12.552 km and $2.2325M_\odot$, 11.24 km, which are similar to those of TM1 and obviously smaller than those given by NL1, NL2, and NLSH. GL-97 gives the minimum OV limit and radii $2.0425M_\odot$ and 10.732 km. The results of PK1, PK1r, and PKDD are between TM1, TW-99, and DD-ME1 and TW-99. The introduction of nonlinear ω terms can soften the EOS.

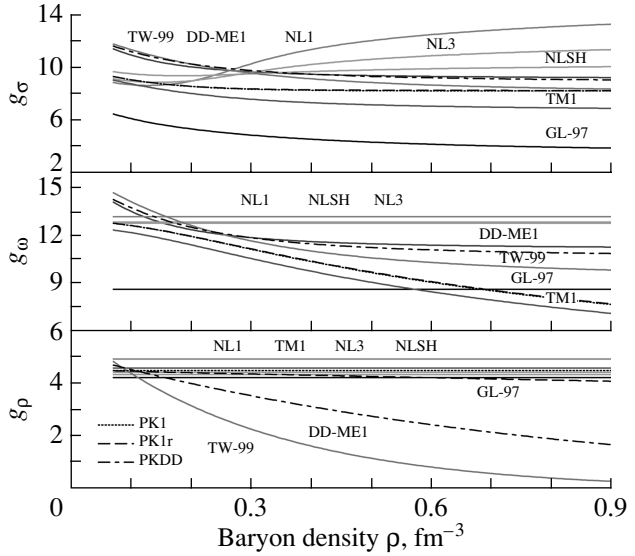

Fig. 3. Similar to Fig. 2, but for neutron star matter.

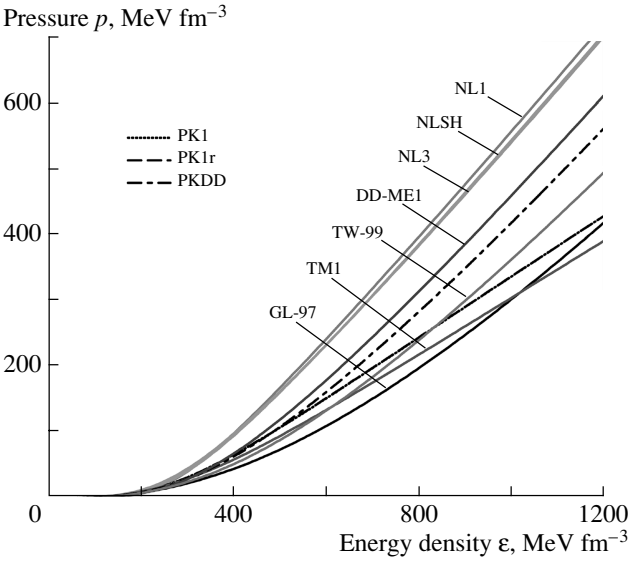

Fig. 4. EOS p vs. ε for neutron star for different effective interactions (as marked in figure).

4. HALOS AND GIANT HALOS

We calculate the even–even nuclei of Pb isotope chains with the newly obtained parameter sets. Shown in Fig. 6 are differences between the predictions of PK1, PK1r, and PKDD for Pb isotopes and the data [36]. For comparison, the results of TM1, NL3, TW-99, and DD-ME1 are also shown. All the results are calculated with RCHB theory [3]. The pairing correlations are considered self-consistently for zero-range δ force. The microscopic center-of-mass correction is used in all the calculations.

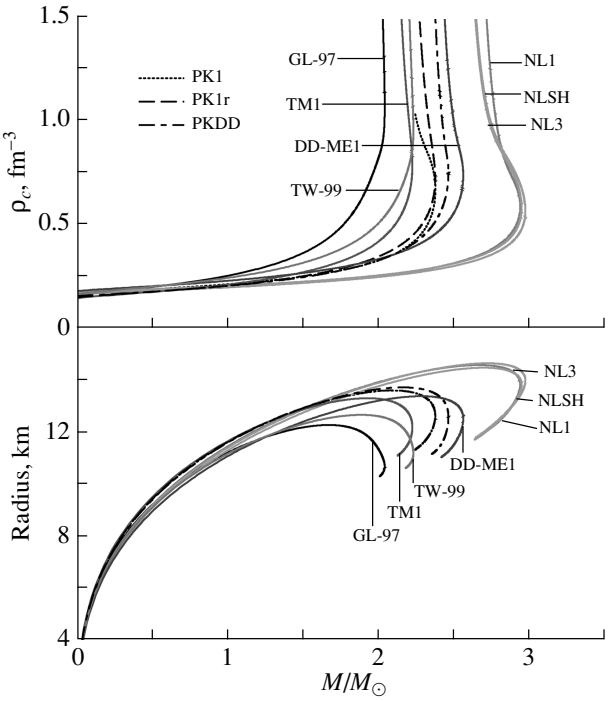

Fig. 5. The central densities (upper) and radii (lower) vs. masses for neutron star by different effective interactions (as marked in figure).

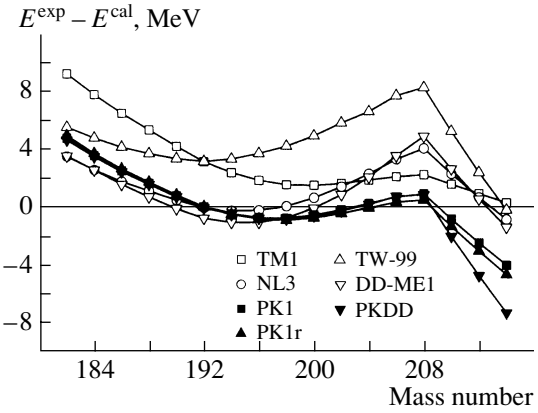

Fig. 6. The deviation of the calculated energies of Pb isotopes for RCHB with PK1, PK1r, and PKDD from the experimental values. Included also are the results with TM1, NL3, TW-99, and DD-ME1.

The newly obtained effective interactions PK1, PK1r, and PKDD provide a good descriptions of the masses for Pb isotope chains. In Fig. 6, all the effective interactions overestimate the binding energy at the beginning of the isotope chain, while from ^{190}Pb to ^{210}Pb the newly obtained interactions give better descriptions than all the others. Similar cases can also be seen for the other proton magic isotope chains.

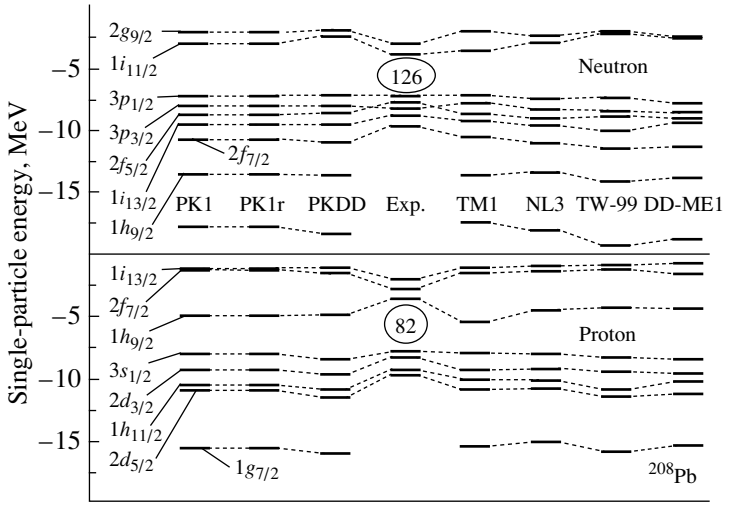

Fig. 7. The single-particle energies for ^{208}Pb, calculated with PK1, PK1r, and PKDD, in comparison with the results of TM1, NL3, TW-99, DD-ME1, and the available values.

Figure 7 shows the single-particle energies of ^{208}Pb calculated with the newly obtained parameter sets PK1, PK1r, and PKDD. The results obtained with TM1, NL3, TW-99, and DD-ME1 are also given for comparison. The experimental values are extracted from one-nucleon separation energies [36]. Good agreement with the data can be found for the single-particle energies near the shell gap. The order of levels is well described by the new effective interactions except some special case, which exists for all the effective interactions.

From the binding energies, we can extract the systematics in the two-neutron separation energies $S_{2n} = E_B(N,Z) - E_B(N-2,Z)$. In Fig. 8, the systematic behavior of two-neutron separation energies with neutron number, predicated by the new effective interactions PK1 and PKDD, is shown. As is seen from these figures, the newly obtained interactions give a good description for two-neutron separation energies. Here, all the theoretical results are from RCHB theory [3]. The interesting phenomena of the so-called giant halo predicted in Ca and Zr isotopes near the neutron drip line [3, 7, 8, 14–16] exist also for these new interactions.

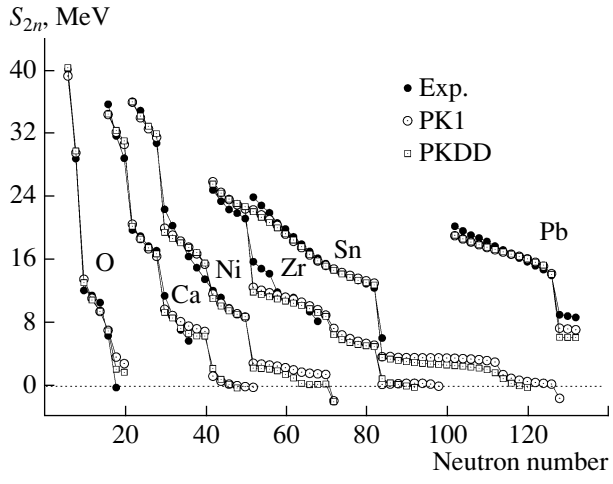

Fig. 8. The two-neutron separation energy calculated with PK1, PK1r, and PKDD for proton-magic isotopes.

5. RMF IN THE WOODS–SAXON BASIS

Although the RCHB theory has achieved success in describing the exotic nuclei near the drip line, the deformation is not included there. For deformed nuclei, working in r space becomes much more difficult and numerically very sophisticated [10]. A reconciler between the HO basis and r space may be the WS basis because (i) the WS potential represents the nuclear average field more suitably than the HO potential and (ii) in principle there is no localization restriction in the WS potential. In [11], we have solved the spherical relativistic Hartree theory in the Woods–Saxon basis (SRHWS). The Woods–Saxon basis is obtained by solving either the Schrödinger equation (SRHSWS) or the Dirac equation (SRHDWS). The formalism and numerical details for both cases can be found in [11]. The WS basis in the SRHDWS theory is much smaller than that in the SRHSWS theory. This will largely facilitate the deformed problem.

The results for ^{72}Ca from SRHWS are compared with those from solving the spherical relativistic Hartree theory in the harmonic oscillator basis, SRHHO, and those in the coordinate space, SRHR. For stable nuclei, all approaches give identical results for properties such as total binding energies and the neutron, proton, and charge rms radii as well

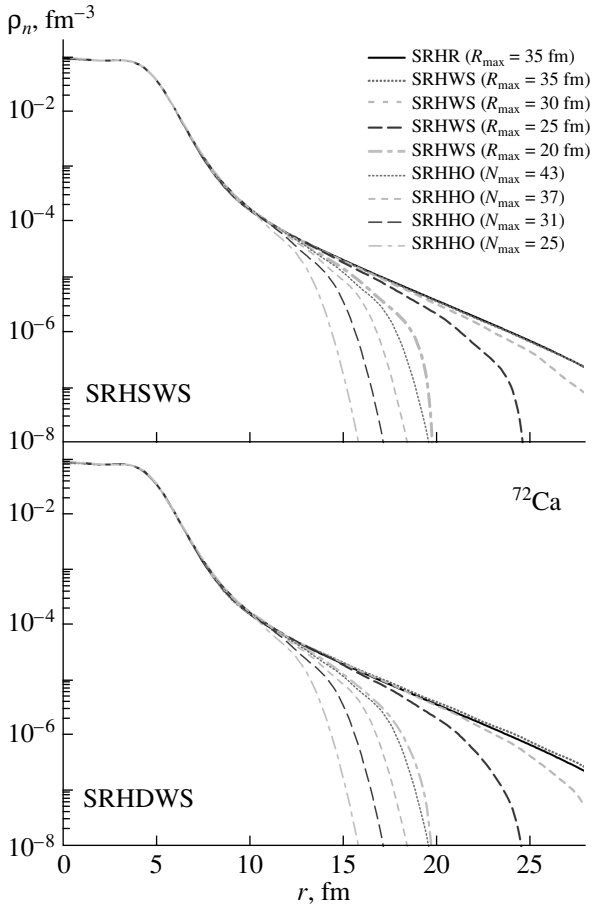

Fig. 9. Comparison of density distributions for ^{72}Ca from SRHR, SRHWS, and SRHHO. The parameter set NLSH is used for the Lagrangian. $\Delta r = 0.1$ fm for SRHR and SRHWS. $E_{cut} = 75$ MeV and $R_{max} = 20$ (thick dash-dotted curve), 25 (thick long-dashed curve), 30 (thick short-dashed curve), and 35 fm (thick dotted curve) for SRHWS. Note that the legend is both for SRHSWS (the upper panel) and for SRHDWS (the lower panel). These sets of cutoffs correspond to cutoffs in principal quantum number $N_{max} = 25$ (thin dash-dotted curve), 31 (thin long-dashed curve), 37 (thin short-dashed curve), and 43 (thin dotted curve) which are used in SRHHO calculations. The density distribution from SRHR is almost identical with that from SRHWS with the same box size. For brevity, only $\rho_n(r)$ from SRHR with $R_{max} = 35$ fm (thick solid curve) is displayed here.

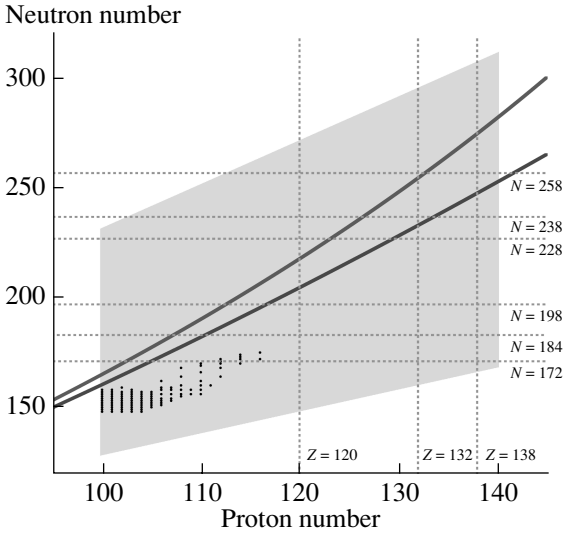

Fig. 10. Magic number for proton Z and neutron N in superheavy nuclei. The available observed and also the calculated nuclei are shown, respectively, as filled points and the shaded area.

as neutron density distributions. For neutron drip line nuclei, e.g., ^{72}Ca, which has a very small neutron Fermi energy $\lambda_n \sim 0.2$ MeV, both SRHR and SRHWS easily approach convergence by increasing the box size, while SRHHO does not. Furthermore, SRHWS can satisfactorily reproduce the neutron density distribution from SRHR, but SRHHO fails with similar cutoffs, as shown in Fig. 9.

In SRHDWS calculations, negative energy states in the Dirac sea must be included in the basis in terms of which nucleon wave functions are expanded. We studied in detail the effects and contributions of negative energy states. Without the inclusion of negative energy levels, the calculated nuclear properties depend on the initial potentials. A small component from negative energy states in the wave functions, about 10^{-4}–10^{-5}, contributes to the physical observables such as E/A and r_{rms} by 1–10% in magnitude. When the initial potentials differ more from the converged ones, the contribution from negative energy levels becomes more important. It can be concluded that the WS basis provides a compromise between the harmonic oscillator basis and the coordinate space which may be used to describe exotic nuclei both properly and efficiently [11]. The extension of the relativistic Hartree theory in the Woods–Saxon basis to deformed cases with pairing correlations included is in progress.

With this experience, we also find the relation between the spin and pseudospin symmetry in the spectrum of single nucleons and single antinucleons in a nucleus [24]. Using RMF theory to investigate single-antinucleon spectra, we find a very well developed spin symmetry in single-antineutron and single-antiproton spectra. The dominant components of the wave functions of the spin doublet are almost identical. This spin symmetry in antiparticle spectra and the pseudospin symmetry in particle spectra have the same origin [21–24]. However, it turns out that the spin symmetry in antinucleon spectra is much better developed than the pseudospin symmetry in normal nuclear single-particle spectra.

Based on the two-neutron separation energy, shell correction energy, and effective pairing gaps, etc.,

from RCHB theory with the available effective interaction, new magic numbers for superheavy nuclei $Z = 120$, 132, and 138, $N = 172$, 184, 198, 228, 238, 258 are suggested as shown in Fig. 10. The properties and the shell correction effects at equilibrium and the saddle point of these nuclides are obtained. The cross sections of cold fusion were estimated by applying the structure information obtained above. Work along this line will be published soon.

6. SUMMARY

The new effective interactions PK1, PK1r, and PKDD are proposed. They are able to provide an excellent description not only for the properties of nuclear matter and neutron stars, but also for nuclei in the nuclear chart from the proton to the neutron drip line, including halos and giant halos at the neutron drip line in nuclei and hypernuclei. As a step to describe the deformed nuclei close to the drip line, the Woods–Saxon basis has been suggested to replace the widely used harmonic oscillator basis for solving the RMF theory by solving either the Schrödinger equation or the Dirac equation. Based on the systematic calculation from RCHB theory [3], new magic numbers $Z = 120$, 132, and 138, $N = 172$, 184, 198, 228, 238, 258 for superheavy nuclei are suggested.

ACKNOWLEDGMENTS

This work is partly supported by the Major State Basic Research Development Program, contract no. G2000077407, and the National Natural Science Foundation of China, grant nos. 10025522, 10047001, 10221003, and 19935030.

REFERENCES

1. J. D. Walecka, Ann. Phys. (N.Y.) **83**, 491 (1974).
2. P. Ring, Prog. Part. Nucl. Phys. **37**, 193 (1996).
3. J. Meng, Nucl. Phys. A **635**, 3 (1998); J. Meng and P. Ring, Phys. Rev. Lett. **77**, 3963 (1996).
4. J. Meng and P. Ring, Phys. Rev. Lett. **80**, 460 (1998).
5. J. Meng, I. Tanihata, and S. Yamaji, Phys. Lett. B **419**, 1 (1998).
6. J. Meng, S.-G. Zhou, and I. Tanihata, Phys. Lett. B **532**, 209 (2002).
7. J. Meng, H. Toki, J. Y. Zeng, *et al.*, Phys. Rev. C **65**, 041302 (2002).
8. S. Q. Zhang, J. Meng, and S.-G. Zhou, Sci. China, Ser. G **33**, 289 (2003) [in Chinese].
9. S. Q. Zhang, J. Meng, S.-G. Zhou, and J. Y. Zeng, Eur. Phys. J. A **13**, 285 (2002).
10. S.-G. Zhou, J. Meng, S. Yamaji, and S. C. Yang, Chin. Phys. Lett. **17**, 717 (2000).
11. S.-G. Zhou, J. Meng, and P. Ring, Phys. Rev. C **68**, 034323 (2003).
12. J. Meng and N. Takigawa, Phys. Rev. C **61**, 064319 (2000).
13. W. H. Long, J. Meng, and S.-G. Zhou, Phys. Rev. C **65**, 047306 (2002).
14. J. Meng, H. F. Lü, S. Q. Zhang, and S.-G. Zhou, Nucl. Phys. A **722**, 366c (2003).
15. H. F. Lü, J. Meng, S. Q. Zhang, and S.-G. Zhou, Eur. Phys. J. A **19** (2004, in press).
16. H. F. Lü and J. Meng, Chin. Phys. Lett. **19**, 1775 (2002).
17. H. Y. Jia, B. X. Sun, J. Meng, and E. G. Zhao, Chin. Phys. Lett. **18**, 1517 (2001).
18. H. Y. Jia, H. F. Lü, and J. Meng, High Energy Phys. Nucl. Phys. **26**, 1050 (2002) [in Chinese].
19. B. X. Sun, H. Y. Jia, J. Meng, and E. G. Zhao, Commun. Theor. Phys. **36**, 446 (2001).
20. H. Y. Jia, J. Meng, E. G. Zhao, J. Li, and J. P. Sang, High Energy Phys. Nucl. Phys. **27**, 200 (2003) [in Chinese].
21. J. Meng, K. Sugawara-Tanabe, S. Yamaji, *et al.*, Phys. Rev. C **58**, R628 (1998).
22. J. Meng, K. Sugawara-Tanabe, S. Yamaji, and A. Arima, Phys. Rev. C **59**, 154 (1999).
23. T. S. Chen, H. F. Lü, J. Meng, and S.-G. Zhou, Chin. Phys. Lett. **20**, 358 (2003).
24. S.-G. Zhou, J. Meng, and P. Ring, nucl-th/0304067.
25. H. Madokoro, J. Meng, M. Matsuzaki, and S. Yamaji, Phys. Rev. C **62**, 061301 (2000).
26. J. Peng, J. Meng, and S. Q. Zhang, Phys. Rev. C **68**, 044324 (2003); X. R. Zhou, J. Meng, and E. G. Zhao, Commun. Theor. Phys. **37**, 323 (2002); Chin. Phys. Lett. **19**, 184 (2002); X. R. Zhou, L. Guo, J. Meng, and E. G. Zhao, Commun. Theor. Phys. **37**, 583 (2002).
27. Suk-Joon Lee *et al.*, Phys. Rev. Lett. **57**, 2916 (1986).
28. G. A. Lalazissis, J. Konig, and P. Ring, Phys. Rev. C **55**, 540 (1997).
29. M. M. Sharma, M. A. Nagarajan, and P. Ring, Phys. Lett. B **312**, 377 (1993).
30. Y. Sugahara and H. Toki, Nucl. Phys. A **579**, 557 (1994).
31. S. Typel and H. H. Wolter, Nucl. Phys. A **656**, 331 (1999).
32. T. Nikšić, D. Vretenar, P. Finelli, and P. Ring, Phys. Rev. C **66**, 024306 (2002).
33. W. H. Long, J. Meng, N. V. Giai, and S.-G. Zhou, Phys. Rev. C **69**, 034319 (2004).
34. N. K. Glendenning, *Compact Stars* (Springer, New York, 1997), p. 232.
35. S. F. Ban, J. Li, S. Q. Zhang, *et al.*, Phys. Rev. C **69**, 045805 (2004).
36. G. Audi and A. H. Wapstra, Nucl. Phys. A **595**, 409 (1995).

Physics of Atomic Nuclei, Vol. 67, No. 9, 2004, pp. 1627–1632. From Yadernaya Fizika, Vol. 67, No. 9, 2004, pp. 1654–1659.

The Neutron Drip Line in the Region of $N = 20$ and $N = 28$ Closures*

S. M. Lukyanov** **and Yu. E. Penionzhkevich**

Flerov Laboratory of Nuclear Reactions, Joint Institute for Nuclear Research, Dubna, Moscow oblast, 141980 Russia

Received January 21, 2004

Abstract—Experimental studies of neutron drip line nuclei are introduced. The neutron drip line in the oxygen–magnesium region has been explored by the projectile fragmentation of a ^{48}Ca beam. New neutron-rich isotopes, ^{34}Ne and ^{37}Na, have been observed together with some evidence for the particle instability of ^{33}Ne and ^{36}Na. Recent data on mass measurements of neutron-rich nuclei at GANIL and some characteristics of binding energies in this region are discussed. Nuclear binding energies are very sensitive to the existence of nuclear shells, and together with the measurements of instability of doubly magic nuclide ^{28}O, they provide information on changes in neutron shell closures of very neutron-rich isotopes from carbon up to calcium. The conclusion about a rearrangement in neutron shell closures is given. The spectroscopic measurements can reveal details of the underlying microscopic structures; in-beam γ-ray spectroscopy is an effective tool to check for shell closures. The results on the γ-ray energies of the first 2^+ level in even–even nuclei for the range $N = 12$–32 are discussed. The strength of $N = 20$ and $N = 28$ shells is variable in the region from carbon up to magnesium. © *2004 MAIK "Nauka/Interperiodica".*

1. INTRODUCTION

The study of the properties of neutron-rich nuclei far from stability is one of the most exciting areas of modern research in nuclear physics. The progress in our knowledge of the properties of these nuclei has enormously broadened because of the new radioactive ion beam facilities and the development of very sophisticated fragment separators. One interesting feature has been found in the region of the light neutron-rich nuclei. As was established in 1975 [1], neutron-rich nuclei with $N \sim 20$ constitute a good example of shape coexistence of spherical and deformed configurations. In the framework of the shell model, the deformed ground state for nuclei with $N = 20$ (for example, ^{32}Mg) is a consequence of the strong correlation energy of $2p$–$2h$ neutron excitations from the sd to the pf shell. It was suggested that the extra binding energy was gained by the deformation associated with the particle–hole excitation across the $N = 20$ shell gap. If a nucleus gains binding energy through deformation, the drip line extends farther than expected for a closed shell. Recent experiments at GANIL [2] and RIKEN [3] were dedicated to the study of the stability of neutron-rich nuclei with $Z > 7$ and around $N = 20$. The variation of the shell gap and deformation as a function of N and Z could be a major challenge. Modern radioactive nuclear beam facilities allow one to produce and study intense beams of very neutron-rich nuclei, previously unavailable. The aim of the experiments was to study the particle stability of these nuclei; their masses, which constitute the basic knowledge of the nucleus; and their spectroscopic characteristics.

2. PARTICLE STABILITY OF NEUTRON-RICH NUCLEI AROUND $N = 20$ AND $N = 28$

Among the recent experiments dedicated to explore the neutron drip line in the region of elements from O to Mg, one could mention those on the particle instability of the neutron-rich oxygen isotopes ^{26,28}O [4–6] and on the discovery of the particle stability of ^{31}Ne [7] and ^{31}F [2, 8]. The appearance of a so-called "island of inversion" with respect to the particle stability of isotopes has been claimed through various theoretical predictions. A particular feature in this region is the progressive development of a deformation in spite of the expected effect of spherical stability due to the magicity of the neutron number $N = 20$ [9–12]. It was argued that the deformation might lead to enhanced binding energies in some of yet undiscovered neutron-rich nuclei.

The question of the possible stability of the doubly magic nucleus ^{28}O has recently attracted much attention, even though the particle instability of ^{25,26}O beyond ^{24}O has been clearly shown by the experiments [4, 6]. The expectation for ^{28}O to be stable

*This article was submitted by the authors in English.

** e-mail: lukyanov@main1.jinr.ru

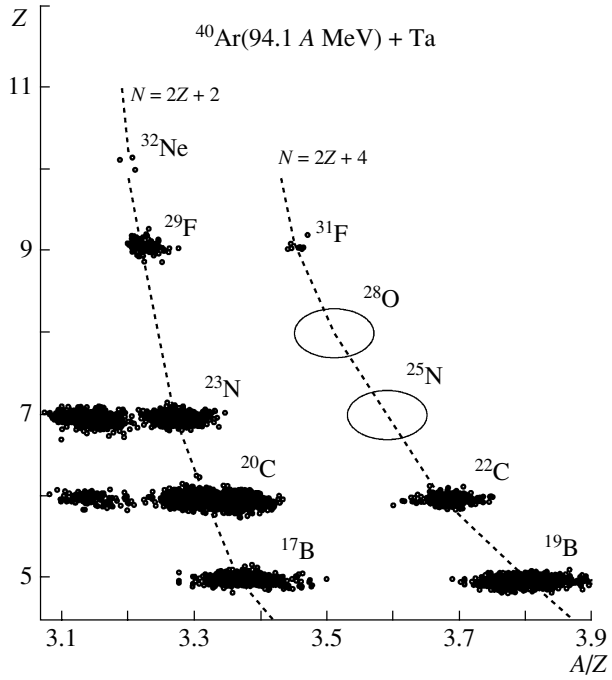

Fig. 1. Two-dimensional A/Z vs. Z plot, which was obtained in the reaction of a 94.1 A MeV ^{40}Ar beam on a 690-mg/cm^2 tantalum target during a 4-day run. The new isotope ^{31}F is clearly visible (eight events). No events associated with ^{25}N and ^{28}O or with ^{24}N, ^{25,26,27}O, and ^{30}F were obtained. In the case of the particle stability of ^{28}O or ^{25}N, the associate events are expected to appear inside the ellipses. The dashed curves are drawn to guide the eye for the isotopes with the same neutron numbers, $N = 2Z + 2$ and $N = 2Z + 4$.

stems from an enhanced stability anticipated from the double magicity or the deformation. The stability of ^{28}O has been discussed in several theoretical papers, which, however, yielded conflicting results. Recently, an attempt to search for ^{28}O has been made by using a ^{36}S beam [5]. No events of ^{28}O were observed, and the particle instability of ^{28}O was concluded from a comparison with the larger estimated yield in the case of the particle bound character of ^{28}O. Such a yield estimate was made by means of an extrapolation method using the results of heavier isotones of $N = 20$. In order to reduce possible uncertainty, use of an interpolation method, which was once applied for the first evidence for the instability of ^{26}O, should be desirable. The puzzle of the instability of the doubly magic nuclide ^{28}O becomes more intriguing regarding the next experiments to be performed. The recent discoveries of the particle stability of ^{31}Ne [7] and ^{31}F [2, 8], in contrast to most of the mass predictions, have motivated us to reexamine the location of the fluorine drip line. The production cross section of ^{31}F was then obtained to be about 0.15 ± 0.06 pb. A two-dimensional A/Z vs. Z plot is shown in Fig. 1. The new isotope ^{31}F is clearly visible (eight events). No events associated with ^{25}N and ^{28}O or with ^{24}N, ^{25,26,27}O, and ^{30}F were obtained. In the case of the particle stability of ^{28}O or ^{25}N, the associate events are expected to appear inside the ellipses. The dashed curves in Fig. 1 are drawn to guide the eye for the isotopes with the same neutron numbers $N = 2Z + 4$. The absence of events corresponding to the ^{25,26,27,28}O isotopes as well as ^{24,25}N and ^{30}F is clearly confirmed. For instance, in the case of the particle stability of ^{28}O or ^{25}N, the associate events are expected to appear inside the ellipses in Fig. 1, while no events were found in those domains. The particle stability of ^{31}F gives strong evidence on the onset of deformation in the region. One may underline that the drip line for the fluorine–magnesium elements could move far beyond the presently known boundaries.

The drip line for C, N, and O isotopes is consistent with the closure of the $2s_{1/2}$ orbital. Particle instability of the ^{26,28}O isotopes indicates that the $1d_{3/2}$ orbital energy is not low enough to bind nuclei. The additional proton makes the neutron potential deeper. For the fluorine isotopes, neutrons can fill completely the $1d_{3/2}$ orbital for ^{29}F, and the $1f_{7/2}$ orbital starts to fill in ^{31}F. Therefore, there is a great interest in studying nuclei in the region of the neutron closure $N = 28$. Experimentally, the properties of ^{44}S have been studied and it was concluded that the ground state of ^{44}S is deformed. This result suggested a significant breaking of the $N = 28$ closure for nuclei near ^{44}S. We present the results of our attempt to determine the neutron drip line for the Ne–Mg isotopes in the region of the neutron numbers $N = 20$–28. In particular, our experiment [2] was dedicated to the direct observation of the ^{31}F, ^{34}Ne, ^{37}Na, and ^{40}Mg nuclei.

The result of this experiment is shown in Fig. 2 (double dimensional matrix Z value vs. A/Z). The new isotopes ^{34}Ne (two events) and ^{37}Na (one event) are clearly visible. The discovery of ^{31}F [8] is also confirmed. No events which could be attributed to ^{33}Ne, ^{36}Na, and ^{40}Mg were observed.

Production cross section values for very neutron-rich fragments (^{31}F, ^{34}Ne, and ^{37}Na) are given in Fig. 3. The calculated estimates of the production cross sections for these fragments are given by the dashed curve. The most interesting nuclide in this region is ^{40}Mg, which is probably not bound since no counts have been observed. We estimated the upper limit for the production cross section of ^{40}Mg to be less than 0.06 pb. However, the present results do

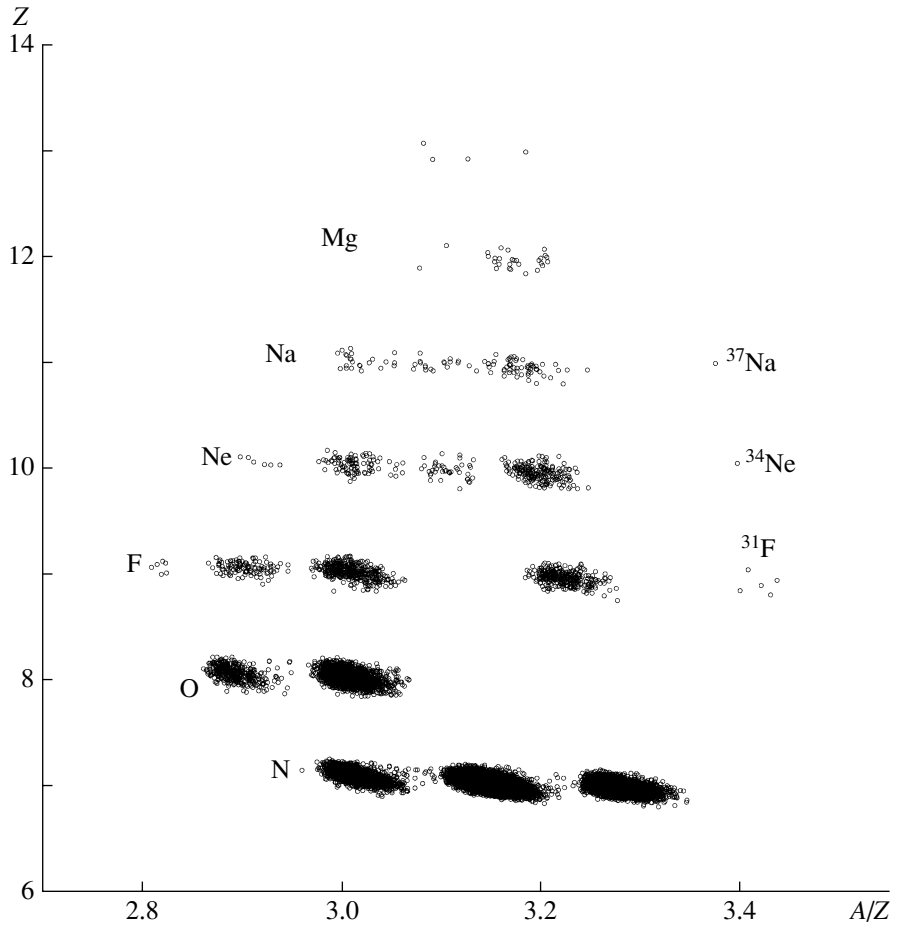

Fig. 2. Two-dimensional A/Z vs. Z plot, which was obtained in the reaction of a 58.9 A MeV ^{48}Ca beam on a 161-mg/cm^2 tantalum target during a 2.5-day run. The new isotopes ^{34}Ne (two events) and ^{37}Na are clearly visible. No events associated with ^{33}Ne, ^{36}Na, and ^{40}Mg were observed.

not allow drawing a definite conclusion on the instability of ^{40}Mg; this is also supported by the trend of the calculated yield in Fig. 3. The production cross section for ^{34}Ne and ^{37}Na was estimated to be about 0.17 and 0.06 pb, respectively. The cross section for ^{31}F is estimated to be about 0.7 pb. This value for the production of ^{31}F in the reaction 59.8 A MeV ^{48}Ca + ^{nat}Ta is about 5 times higher than that in the reaction 94.1 A MeV ^{40}Ar + Ta [8].

From the theoretical point of view, the description of the light nuclei in the sd–pf shells is still a problem. In particular, the calculation of the binding energy for the very neutron-rich isotopes of O, F, Ne, and Na is a real challenge. There are various theoretical calculations {viz., the finite-range liquid drop model (FRLD) [13], versions of the shell model (SM) [14–16], relativistic mean field theory [17], and the Hartree–Fock approach [18]} that predict different position of the neutron drip line in this region. For instance, the FRLD model gives a very strong binding energy for ^{40}Mg. In the framework of this model one- and two-neutron separation energies are even above 3.4 MeV. One may note that the FRLD model gives correct predictions for the stability of ^{31}Ne and ^{31}F, implying nuclear deformation effects for both the macroscopic and the microscopic parts. According to the shell model predictions [15], the last bound isotopes are ^{24}O, ^{27}F, ^{34}Ne, ^{37}Na, ^{38}Mg, and ^{43}Al. However, slight changes of the drip line cannot be excluded since ^{37}Na was predicted to be bound only by 250 keV, while ^{31}F, ^{40}Mg, and ^{43}Al are unbound by 145, 470, and 550 keV, respectively. According to another SM calculation [14], ^{26}O, ^{34}Ne, and ^{40}Mg are the last stable isotopes against two-neutron emission, as indicated by their maximal binding energy. Both SM and HF calculations for even-mass O, Ne, and Mg indicate a disappearance of shell magic numbers and suggest an onset of deformation and a shape coexistence in this region. The stability/instability of the present nuclei can be explained

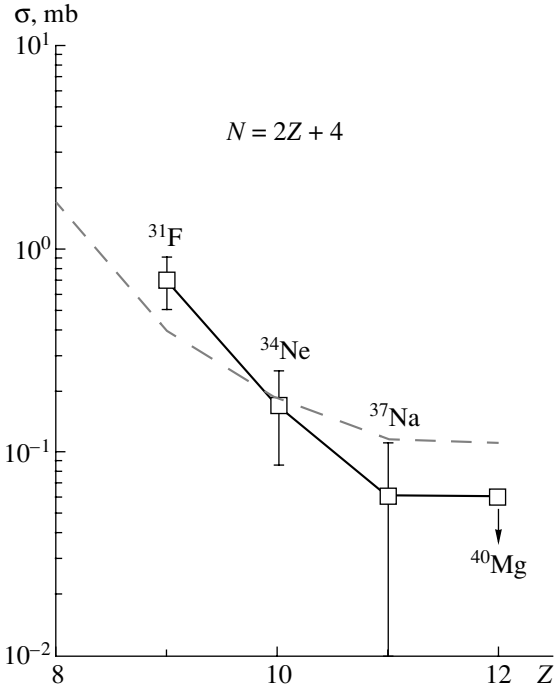

Fig. 3. Production cross sections for nuclei with the neutron number $N = 2Z + 4$. The dashed curve presents the expected yields according to the LISE code.

by taking into account various degrees of mixing in the *sd* and *fp* shells, which are related to the deformation effects. According to our results, the neutron drip line is extended beyond $N = 20$ and reaches $N = 24$ for neon and even $N = 26$ for sodium isotopes as a consequence of the mixing of the $d_{3/2}$ and $f_{7/2}$ states, while the $N = 20$ shell closure disappears. A conclusion about the vanishing of $N = 28$ and appearance of new nuclear magic number $N = 26$ is given [19].

Thus, most probably, the neutron drip line has been reached for the neon and sodium isotopes (see Fig. 4). However, it seems that, to definitely conclude whether these isotopes do mark the drip line or do not, we will need to perform further experimental efforts.

3. MASS MEASUREMENT

The question of particle stability is directly related to the masses and nuclear binding energies, which are very sensitive to the existence of shells and may provide clear signatures of shell closures. An experiment on mass measurement using a direct time-of-flight technique was undertaken [20] in order to investigate the $N = 20$ and $N = 28$ shell closures for nuclei from Ne to Ar and thus to bring some clarifications concerning the behavior of magic numbers far from stability.

The two-neutron separation energies S_{2n} derived from the measured masses are displayed in Fig. 5. Such systematics are of particular interest as the S_{2n} values correspond to a "derivative" of the mass surface. The new data are presented with error bars, while the rest, except the encircled data, are taken from Audi and Wapstra. The Ca, K, and Ar isotopes show a behavior typical of the filling of shells, with the two shell closures at $N = 20$ and $N = 28$ being evident at the corresponding sharp decrease in the S_{2n} for the next two isotopes and a moderate decrease in S_{2n} for subsequent points as the filling of the next shell starts to influence S_{2n}. The sharp drop at $N = 22$, shown by the dashed vertical line and corresponding to the shell $N = 20$, is clearly visible through all the Si–Ca region, while going to lower Z to the Al–Na region, this drop seems to move towards lower N. This was the reason why we made an attempt to clarify the situation with the two-neutron separation energies in this region. S_{2n} values must be positive and, therefore, we included the "expected" S_{2n} values of the heaviest particle-stable isotopes ^{23}N, ^{22}C, and ^{29,31}F to the graph; they are marked by circles. The "expected" S_{2n} values for ^{29,31}F point out the region where they probably have to be located due to their experimentally found particle stability (positive S_{2n} values).

These values are not crucial for determination of the shell closure at $N = 16$ [21, 22]; important is only the fact that particle-stable isotopes heavier than ^{23}N and ^{22}C do not exist. The inclusion of the S_{2n} values for ^{29}F and ^{31}F was most important, because this allowed us to observe the sharp drop of the ^{27}F value, followed by a moderate decrease in S_{2n} values for ^{29}F and ^{31}F giving a very clear evidence for the existence of the new shell closure at $N = 16$ for fluorine. A similar behavior confirming the $N = 16$ shell closure can be seen at the neon isotopes that exhibit a moderate decrease in S_{2n} values for ^{29}Ne and ^{30}Ne. We have already mentioned the sharp drop in S_{2n} values in the Al–Na region. It should be noted that the evidence for a new magic number $N = 16$ [22] follows also from Fig. 5 [22], where the S_{2n} values are plotted vs. atomic number Z. The position of various possible shells or pseudoshells are also shown in Fig. 5. As has already been pointed out, the Cl, S, and P isotopes exhibit a pronounced change of slope around $N = 26$. Moreover, this change in the Cl and S isotopes is confirmed by the sharp drop at $N = 28$.

4. γ-RAY ENERGIES OF THE FIRST 2^+ LEVEL FOR EVEN–EVEN NUCLEI

Since the spectroscopic measurements can reveal details of the underlying microscopic structures, in-beam γ-ray spectroscopy is an effective tool to check for shell closures. The information on the energy of the

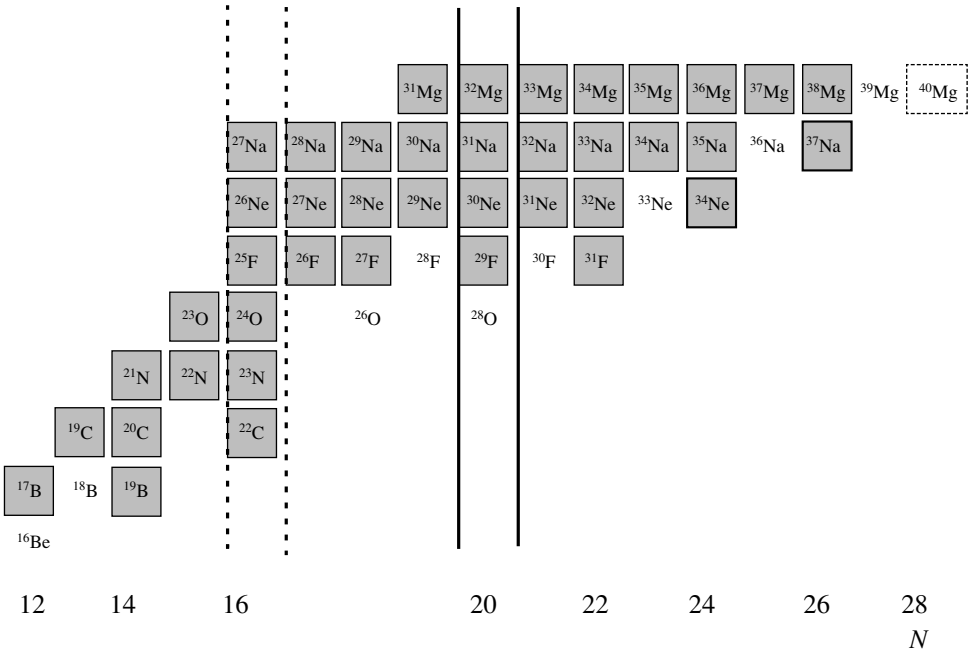

Fig. 4. The part of the nuclide chart in the region of neutron number $N = 20$ and $N = 28$.

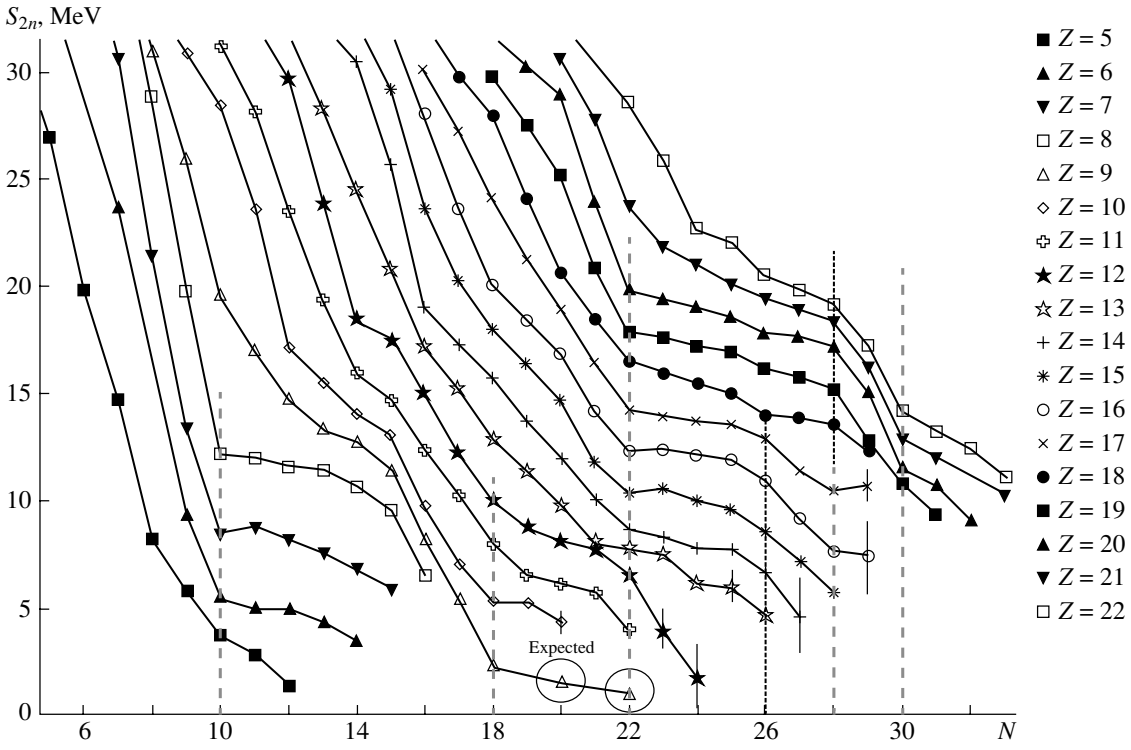

Fig. 5. Two-neutron separation energy S_{2n} vs. neutron number for O–Ca isotopes.

first excited state and on $B(E2; 0^+ \to 2^+)$ represents only the first step to understand the structure and to estimate the deformation of the nuclei. Such a measurement can probe the underlying microscopic structures, determine the shape of the nuclei under study, and give new information on gaps between neighboring orbitals. Recently, in-beam γ-ray spectroscopy measurements [23, 24] of a large number of exotic nuclei produced by fragmentation were made.

The dependence of the γ-ray energy of the first

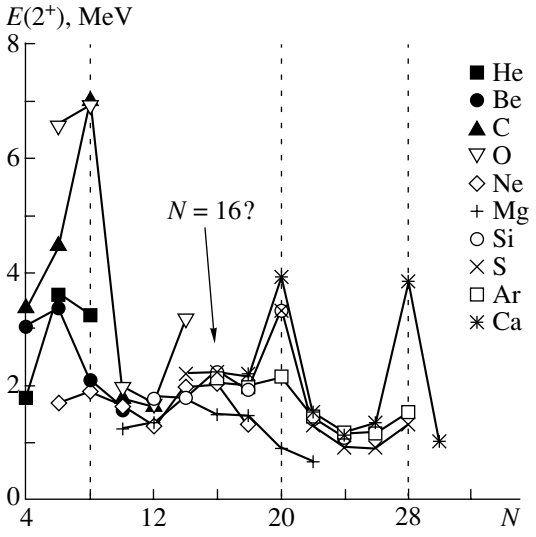

Fig. 6. The dependence of the γ-ray energy of the first 2^+ excited states vs. the neutron number N for even–even nuclei.

2^+ excited state on neutron number for even–even nuclei is presented in Fig. 6. It should be noted that oxygen isotopes exhibit the lowest $E(2^+)$ energy of 1.7 MeV for ^{20}O, i.e., near the half-occupancy of the $d_{5/2}$ subshell ($N = 12$), just as the Ne and Mg isotopes do. However, the enhancement of $E(2^+)$ energy at $N = 14$ for Ne and Mg is much smaller than that for oxygen. If the enhancement seen in oxygen also appears in carbon, it will be another confirmation of the existence of the $N = 16$ shell in the C–Ne region. Moreover, we should note that the nonexistence of a bound excited state in $N = 16$ isotones of carbon and oxygen would also indicate the existence of a shell at $N = 16$. As one can see in Fig. 6, the energy of the first 2^+ state for Ne isotopes rises from 1.25 MeV for ^{22}Ne to 2 MeV for ^{24}Ne and ^{26}Ne and then drops to 1.3 MeV for ^{28}Ne, showing a flat maximum for both neutron numbers 14 and 16 and suggesting a competition between the $1d_{5/2}$ and $2s_{1/2}$ orbits as well an elimination of the $N = 20$ shell. On the other hand, Mg isotopes show a steady decrease in the energy of the 2^+ state, confirming the weakening of the $N = 20$ shell after reaching the maximum at $N = 14$. In Fig. 6, the γ-ray energies of the first 2^+ state for even isotopes of S, Ar, and Ca are plotted. These nuclei exhibit pronounced maxima at the $N = 20$ shell; however, the strength of the $N = 16$ shell in these elements is very weak as these nuclei are no more neutron-rich but lie on the proton-rich side of the valley of stability.

Thus, one may conclude that the strength of the $N = 20$ and $N = 28$ shells is variable in the neutron-rich region from carbon up to magnesium. Some usual magic numbers disappear, while new ones ($N = 16$ or $N = 26$) could arise. Nuclei in this region have a tendency toward deformation in spite of the effect of spherical stability due to neutron number magicity.

ACKNOWLEDGMENTS

The authors would like to express their graduate to the members of the FLNR (JINR, Dubna)–GANIL–Orsay–Dubna–Rez–Bucharest and FLNR (JINR, Dubna)–RIKEN (Japan) Collaborations for the fruitful experimental efforts and discussions of the experimental results obtained in the joint experiments.

This work has been carried out with financial support from PICS (IN2P3) no. 1171, INTAS (grant no. 00-00463), and the Russian Foundation for Basic Research (project no. 96-02-17381a).

REFERENCES

1. C. Thibault *et al.*, Phys. Rev. C **12**, 644 (1975).
2. S. Lukyanov *et al.*, J. Phys. G **28**, L41 (2002).
3. M. Notani *et al.*, Phys. Lett. B **542**, 49 (2002).
4. D. Guillemaud-Mueller *et al.*, Z. Phys. A **332**, 189 (1989).
5. O. B. Tarasov *et al.*, Phys. Lett. B **409**, 64 (1997).
6. M. Fauerbach *et al.*, Phys. Rev. C **53**, 47 (1996).
7. H. Sakurai *et al.*, Phys. Rev. C **54**, R2802 (1996).
8. H. Sakurai *et al.*, Phys. Lett. B **448**, 180 (1999).
9. X. Campi *et al.*, Nucl. Phys. A **251**, 193 (1975).
10. R. Nayak and L. Satpathy, Nucl. Phys. A **304**, 64 (1978).
11. A. Poves and J. Retamosa, Nucl. Phys. A **571**, 221 (1994).
12. E. K. Warburton *et al.*, Phys. Rev. C **41**, 1147 (1990).
13. P. Möller *et al.*, At. Data Nucl. Data Tables **59**, 185 (1995).
14. G. A. Lalazissis *et al.*, Phys. Rev. C **60**, 014310 (1999).
15. E. Caurier *et al.*, Phys. Rev. C **58**, 2033 (1998).
16. Y. Utsuno *et al.*, Phys. Rev. C **64**, 011301 (2001).
17. Z. Ren *et al.*, Phys. Rev. C **52**, R20 (1995).
18. J. Terasaki *et al.*, Nucl. Phys. A **621**, 706 (1997).
19. Yu. S. Lutostansky *et al.*, Part. Nucl. Lett., No. 6 (**115**), 86 (2002).
20. F. Sarazin *et al.*, Phys. Rev. Lett. **84**, 5962 (2000).
21. A. Ozawa *et al.*, Phys. Rev. Lett. **84**, 5493 (2000).
22. Z. Dlouhy *et al.*, Nucl. Phys. A **701**, 189c (2002).
23. F. Azaiez, Phys. Scr. **88**, 118 (2000).
24. M. Belleguic *et al.*, Phys. Scr. **88**, 122 (2000).

Physics of Atomic Nuclei, Vol. 67, No. 9, 2004, pp. 1633–1639. From Yadernaya Fizika, Vol. 67, No. 9, 2004, pp. 1660–1666.

QRPA Coordinate Space Calculations of 2^+ States in $N = 20$ Isotones*

N. Van Giai[1] and M. Yamagami[2]

Received January 21, 2004

Abstract—The first 2^+ states in $N = 20$ isotones are studied within the self-consistent quasiparticle random phase approximation based on the Green's function method. The residual interaction between quasiparticles with full velocity dependence is consistently derived from the Skyrme interaction plus pairing interaction energy density functional. The $B(E2, 0_1^+ \to 2_1^+)$ transition probabilities and the excitation energies of the first 2^+ states are well described within a single framework. We discuss mainly the microscopic origin of the anomalously large $B(E2)$ value and the very low excitation energy in ^{32}Mg.

1. INTRODUCTION

Several experimental observations point to a vanishing of the shell closure at the neutron number $N = 20$ in neutron-rich nuclei. The evidence of the breaking of $N = 20$ shell closure in neutron-rich Mg and Ne isotopes is more clearly seen from the observations of $E2$ properties, the large $B(E2)$ value in ^{32}Mg [1], and the low excitation energies of the first 2^+ states in ^{32}Mg [2] and ^{30}Ne [3]. The main causes of this tendency could be attributed either to deformation effects or to pairing correlations. The experimental evidence of deformation in ^{32}Mg is not firmly established. The energy ratios of the first 4^+ and 2^+ states, $E(4^+)/E(2^+)$, are 3.0 in ^{24}Mg and 3.2 in ^{34}Mg [4], and these values are undoubtedly close to the rigid rotor limit of 3.3. On the other hand, the ratio is 2.6 in ^{32}Mg, and this value is in between the rigid rotor limit and the harmonic vibration limit 2.0 [4, 5]. Moreover, the $B(E2)$ value (in single-particle units) is 15.0 ± 2.5 in ^{32}Mg. This value is larger than that in the other stable $N = 20$ isotones but smaller than that in other deformed Mg isotones (21.0 ± 5.8 in ^{24}Mg and 19.2 ± 3.8 in ^{34}Mg).

In this paper, we emphasize how neutron pairing correlations play an essential role in the description of $E2$ properties in ^{32}Mg and ^{30}Ne. The existence of neutron pairing correlations means the breaking of the $N = 20$ shell closure. As we will see, the appearance of neutron pairing correlations is related to a special mechanism in loosely bound systems. We study the first 2^+ states in $N = 20$ isotones in the framework of the self-consistent quasiparticle random phase approximation (QRPA) with Skyrme interactions.

The QRPA equations are solved in coordinate space by using the Green's function method [6]. Spherical symmetry is assumed for simplicity. The residual interaction between the quasiparticles is self-consistently derived from the Hamiltonian density of Skyrme interaction that has an explicit velocity dependence. We will show that the $B(E2)$ values and the excitation energies of the first 2^+ states in $N = 20$ isotones from the stable nucleus ^{38}Ar to the neutron-rich nuclei ^{32}Mg and ^{30}Ne are well described within a single framework and a fixed parameter set.

The paper is organized as follows. In Section 2, we briefly describe the Hartree–Fock–Bogolyubov (HFB) plus QRPA calculations that we have done. In Section 3, we present the general results for the ground states of the $N = 20$ isotones studied here. In Section 4, we discuss the calculated and experimental $E2$ properties of these nuclei. Conclusions are summarized in Section 5.

2. FORMULATION AND INPUTS OF HFB–QRPA CALCULATIONS

We use the approach of self-consistent HFB–QRPA calculations with Skyrme interactions. The QRPA problem is solved by the response function method in coordinate space. A detailed account of the method can be found in [6]. Here, we just recall the main steps of the calculation. The QRPA Green's function $\mathbf{G}$ is solution of a Bethe–Salpeter equation:

$$\mathbf{G} = \mathbf{G}_0 + \mathbf{G}_0\mathbf{V}\mathbf{G}. \qquad (1)$$

The knowledge of $\mathbf{G}$ allows one to construct the response function of the system to a general external

*This article was submitted by the authors in English.

[1]Institut de Physique Nucléaire, CNRS-IN2P3, Université Paris-Sud, Orsay, France; e-mail: nguyen@ipno.in2p3.fr

[2]Department of Physics, Kyoto University, Kyoto, Japan.

field, and the strength distribution of the transition operator corresponding to the chosen field is just proportional to the imaginary part of the response function.

In Eq. (1), the unperturbed Green's function $\mathbf{G}_0$ is defined as

$$G_0^{\alpha\beta}(\mathbf{r}\sigma,\mathbf{r}'\sigma';\omega) = \sum_{i,j}\left[\frac{W_{i,j}^{\alpha 1}(\mathbf{r}\sigma)[W_{i,j}^{\beta 1*}(\mathbf{r}'\sigma')]_-}{\hbar\omega-(E_i+E_j)+i\eta} - \frac{W_{i,j}^{\alpha 2*}(\mathbf{r}\sigma)[W_{i,j}^{\beta 2}(\mathbf{r}'\sigma')]_-}{\hbar\omega+(E_i+E_j)+i\eta}\right], \quad (2)$$

where the functions $W(\mathbf{r}\sigma)$ are introduced as

$$W_{i,j}(\mathbf{r}\sigma) = \begin{pmatrix} U_i(\mathbf{r}\sigma)V_j(\mathbf{r}\sigma) & V_i(\mathbf{r},\sigma)U_j(\mathbf{r}\sigma) \\ U_i(\mathbf{r}\sigma)U_j(\mathbf{r}\bar{\sigma}) & V_i(\mathbf{r}\sigma)V_j(\mathbf{r}\bar{\sigma}) \\ -V_i(\mathbf{r}\sigma)V_j(\mathbf{r}\bar{\sigma}) & -U_i(\mathbf{r}\sigma)U_j(\mathbf{r}\bar{\sigma}) \end{pmatrix}. \quad (3)$$

Here, $U(\mathbf{r})$ and $V(\mathbf{r})$ are quasiparticle wave functions, and the index α ($\alpha = 1,\ 2,\ 3$) stands for particle–hole (ph), particle–particle (pp), and hole–hole (hh) channels. The notation $f(\mathbf{r}\bar{\sigma}) \equiv -2\sigma f(\mathbf{r}-\sigma)$ indicates time reversal and $[W_{i,j}]_- = W_{i,j} - W_{j,i}$.

The residual interaction $\mathbf{V}$ between quasiparticles is derived from the Hamiltonian density $\langle H\rangle$ of Skyrme interaction by the so-called Landau procedure,

$$V_{\alpha\beta}\left(\mathbf{r}\sigma\tau,\mathbf{r}'\sigma'\tau'\right) = \frac{\partial^2\langle H\rangle}{\partial\rho_\beta\left(\mathbf{r}'\sigma'\tau'\right)\partial\rho_{\bar{\alpha}}\left(\mathbf{r}\sigma\tau\right)}. \quad (4)$$

The notation $\bar{\alpha}$ means that, whenever α is $pp\,(hh)$, then $\bar{\alpha}$ is $hh\,(pp)$. The normal and abnormal densities are defined as

$$\begin{pmatrix}\rho_{ph}(\mathbf{r}\sigma)\\ \rho_{pp}(\mathbf{r}\sigma)\\ \rho_{hh}(\mathbf{r}\sigma)\end{pmatrix} = \begin{pmatrix}\rho(\mathbf{r}\sigma)\\ \kappa(\mathbf{r}\sigma)\\ \bar{\kappa}(\mathbf{r}\sigma)\end{pmatrix} = \begin{pmatrix}\langle 0|\psi^\dagger(\mathbf{r}\sigma)\psi(\mathbf{r}\sigma)|0\rangle\\ \langle 0|\psi(\mathbf{r}\bar{\sigma})\psi(\mathbf{r}\sigma)|0\rangle\\ \langle 0|\psi^\dagger(\mathbf{r}\sigma)\psi^\dagger(\mathbf{r}\bar{\sigma})|0\rangle\end{pmatrix}. \quad (5)$$

The residual interaction $\mathbf{V}$ has an explicit momentum dependence,

$$\mathbf{V}(\mathbf{r},\mathbf{r}') = \mathbf{F}[\overleftarrow{\Delta}_U + \overleftarrow{\Delta}_V, \overrightarrow{\Delta}_U + \overrightarrow{\Delta}_V, \overleftarrow{\nabla}_U \pm \overleftarrow{\nabla}_V, \overrightarrow{\nabla}_U \pm \overrightarrow{\nabla}_V]\delta(\mathbf{r}-\mathbf{r}'). \quad (6)$$

The operators with $\leftarrow$ ($\rightarrow$) act on the coordinate $\mathbf{r}$ ($\mathbf{r}'$), and the operators with the index $U(V)$ operate on the quasiparticle wave functions $U(\mathbf{r})$ ($V(\mathbf{r})$) only. In contrast with [6], where a Landau–Migdal approximation was made, these momentum dependences are explicitly treated here. Because we calculate only natural parity (non-spin-flip) excitations, we drop the spin–spin part of the residual interaction. The Coulomb and spin–orbit residual interactions are also dropped. Apart from these dropped terms, the present calculations are very close to full consistency between the mean field and the residual interaction. Consequently, one needs practically no renormalization of the residual interaction to obtain the spurious center-of-mass state at zero energy. This is to be compared with the 20% renormalization used in [6]. Note that the present calculations are the first Skyrme–QRPA calculations performed with the full velocity dependence of the residual interaction.

Another important aspect is related to the description of the low-lying states. The $B(E\lambda)$ transition probability is very sensitive to the treatment of the residual interaction. For example, the $B(E2,\ 0_1^+ \rightarrow 2_1^+)$ in ^{20}O calculated with the SkM^* parameter with (without) these momentum-dependent terms is 34.1 (20.9) e^2 fm^4. The $B(E2)$ value increases by 64%.

The experimental data is 28 ± 2 e^2 fm^4 [7], which is close to the value calculated with the momentum-dependent terms. Thus, the full residual interaction (6) is important for quantitatively describing the low-lying states and for comparison with experimental data.

We apply the above formalism to study the first 2^+ states in $N = 20$ isotones, ^{30}Ne, ^{32}Mg, ^{34}Si, ^{36}S, and ^{38}Ar. The ground states are given by Skyrme–HFB calculations. The HFB equation is diagonalized on a Skyrme–HF basis calculated in coordinate space with a box boundary condition [8–10]. Spherical symmetry is imposed on quasiparticle wave functions. The quasiparticle cutoff energy is taken to be $E_{\text{cut}} = 50$ MeV, and the angular momentum cutoff is $l_{\max} = 7\hbar$ in our HFB and QRPA calculations.

The Skyrme parameter sets SkM^* [11] and SkP [12] are used for the Hartree–Fock mean field, and the density-dependent, zero-range pairing interaction

$$V_{\text{pair}}\left(\mathbf{r},\mathbf{r}'\right) = V_{\text{pair}}\left[1-\left(\frac{\rho\left(\mathbf{r}\right)}{\rho_c}\right)^\alpha\right]\delta\left(\mathbf{r}-\mathbf{r}'\right) \quad (7)$$

is adopted for the pairing field. The parameters α and ρ_c are fixed as $\alpha = 1$ and $\rho_c = 0.16$ fm^{-3}. The strength V_0 is determined so as to reproduce the experimental neutron pairing gap in ^{30}Ne, $\Delta_{n,\text{exp}}(^{30}\text{Ne}) = 1.26$ MeV. ^{30}Ne is the lightest mass

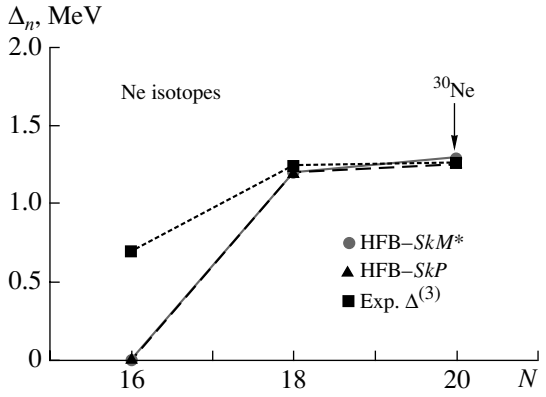

Fig. 1. HFB neutron pairing gaps in ^{26,28,30}Ne calculated with SkM^* and SkP. The pairing strengths V_0 are fixed so as to reproduce the experimental neutron gap in ^{30}Ne. The experimental pairing gaps are extracted by using the three-point mass difference formula [13].

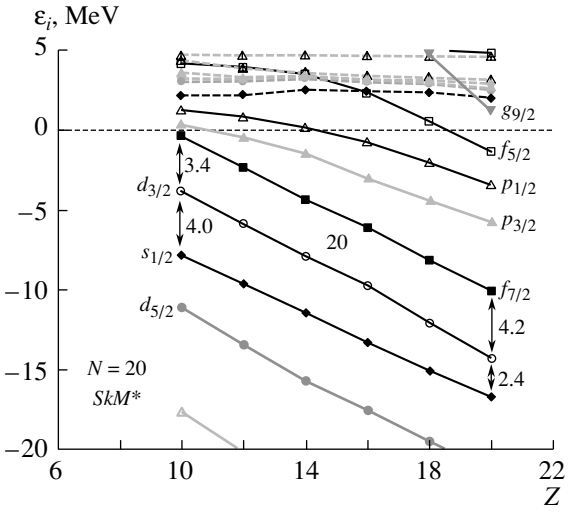

Fig. 2. Hartree–Fock neutron single-particle levels in $N = 20$ isotones calculated with SkM^*. Solid lines correspond to bound and resonance-like states; dashed lines, to positive energy discretized states.

even–even $N = 20$ nucleus. The experimental pairing gaps are extracted by using the three-point mass difference formula [13],

$$\Delta_n(N) = \Delta_n^{(3)}(N-1)$$
$$= \frac{(-1)^N}{2}[E(N-2) + E(N) - 2E(N-1)].$$

On the other hand, the average pairing gap in HFB calculations is defined as the integral of the pairing field [14],

$$\bar{\Delta}_n = \int d\mathbf{r}\tilde{\rho}_n(\mathbf{r})\Delta_n(\mathbf{r}) \Big/ \int d\mathbf{r}\tilde{\rho}_n(\mathbf{r}).$$

The pairing strength adopted for SkM^* is $V_{\text{pair}} = -418$ MeV fm^{-3}, and for SkP, $V_{\text{pair}} = -400$ MeV fm^{-3}. Figure 1 shows the experimental and the calculated pairing gaps in ^{26,28,30}Ne. With these Skyrme parameters and pairing strengths, we get a finite pairing gap in ^{30}Ne (vanishing of $N = 20$ shell gap) and zero pairing gap in ^{26}Ne (appearance of $N = 16$ shell gap) at the same time.

3. GROUND-STATE PROPERTIES

Figure 2 shows the neutron single-particle levels in $N = 20$ isotones calculated in Hartree–Fock with the SkM^* force. Results with the SkP force are qualitatively the same. The $N = 20$ shell gaps change from 4.2 MeV in ^{40}Ca to 3.4 MeV in ^{30}Ne. The $N = 16$ shell gaps change from 2.4 MeV in ^{40}Ca to 4.0 MeV in ^{30}Ne. Within Hartree–Fock, we can describe the vanishing of $N = 20$ magicity and the appearance of the $N = 16$ magic number at the same time. The change in $N = 20$ shell gaps looks moderate in comparison with the effective single-particle energies in shell model calculations [15]. However, the definitions are different. In shell model calculations, the single-particle energies are inputs of calculations and they are determined so as to reproduce the neutron separation energies and the one-particle spectra of ^{17}O and ^{41}Ca, and the change in the effective single-particle energies according to proton number is due to the change in the many-body correlations. On the other hand, the change in the single-particle energies in mean-field calculations reflects the self-consistent change in the mean-field potential.

An important feature in Fig. 2 is the behavior of low-l orbits, $2p_{3/2}$ and $2p_{1/2}$, in the fp shell. As the proton number decreases, the single-particle energies of the high-l orbit $1f_{7/2}$ change almost linearly while the changes in $2p_{3/2}$ and $2p_{1/2}$ energies become very slow around zero energy. Moreover, the spin–orbit splitting of the $2p_{3/2}$ and $2p_{1/2}$ states becomes smaller. As pointed out by Hamamoto *et al.* [16], these effects can be understood by different l dependences of the kinetic energy and the spin–orbit form factor as the single-particle energy comes close to zero. Because of these different l dependences of the single-particle energies, the level density in the fp shell becomes higher with decreasing proton number, and the three orbits $1f_{7/2}$, $2p_{3/2}$, and $2p_{1/2}$ become almost degenerate in ^{30}Ne. We can describe this behavior naturally by solving the Hartree–Fock and HFB equations in coordinate space, but it is difficult to get this property by the methods based on the harmonic oscillator basis.

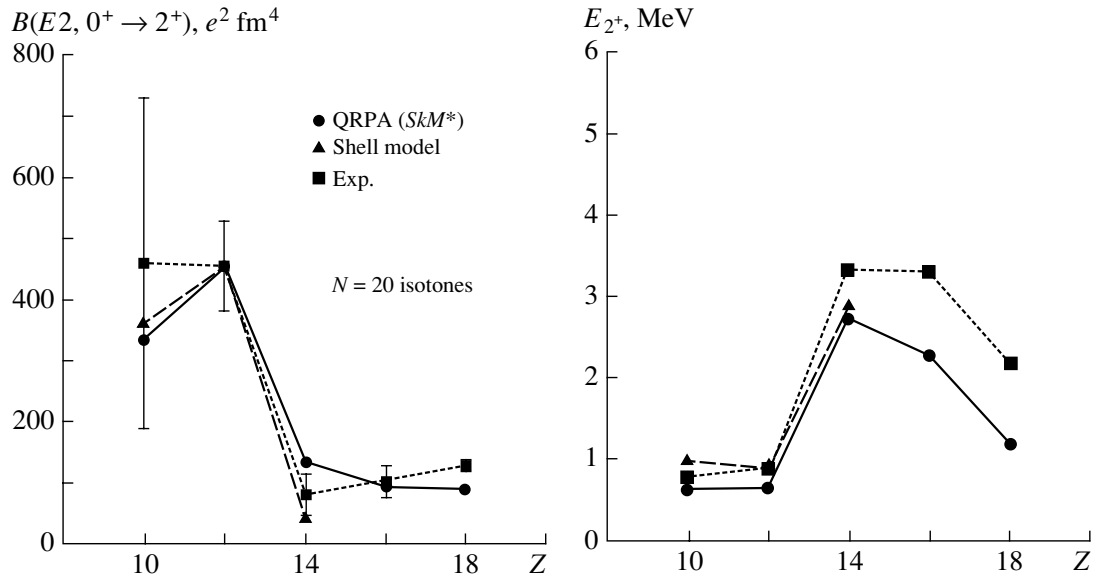

Fig. 3. The $B(E2, 0_1^+ \to 2_1^+)$ transition probabilities and excitation energies of the first 2^+ states in $N = 20$ isotones calculated in QRPA with SkM^*. For comparison are shown the predictions of MCSM [15] and the available experimental data [1–3, 19–21].

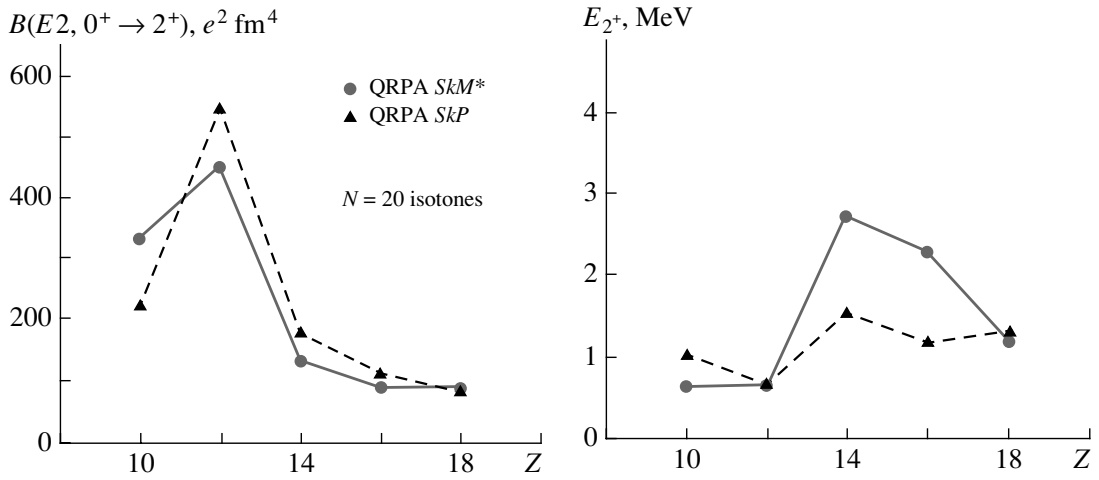

Fig. 4. The $B(E2, 0_1^+ \to 2_1^+)$ transition probabilities and excitation energies of the first 2^+ states calculated in QRPA with SkM^* and SkP interactions.

Let us examine the evolution of the HFB neutron pairing gaps in $N = 20$ isotones as a function of Z. The pairing strengths are adjusted so as to reproduce the experimental neutron pairing gap in ^{30}Ne. As the proton number increases, the neutron pairing gaps decrease monotonically and, eventually, the neutron pairing gap becomes zero (for both SkM^* and SkP) in ^{38}Ar as expected in stable $N = 20$ nuclei. The interesting point is that the $N = 20$ shell gap itself changes very moderately, but the calculated neutron pairing gap changes considerably from 1.26 MeV in ^{30}Ne to zero in ^{38}Ar. The mechanism can be understood by the increase in the level density in the fp shell when the proton number decreases, as noted above.

4. $B(E2)$ VALUES AND EXCITATION ENERGIES

We have calculated the first 2^+ states in $N = 20$ isotones in HFB–QRPA with Skyrme interactions, assuming spherical symmetry. At the mean-field level, the ground states in $N = 20$ isotones, including ^{32}Mg and ^{30}Ne, have been found to be spherical (see, e.g., [17, 18]). Our aim is to investigate

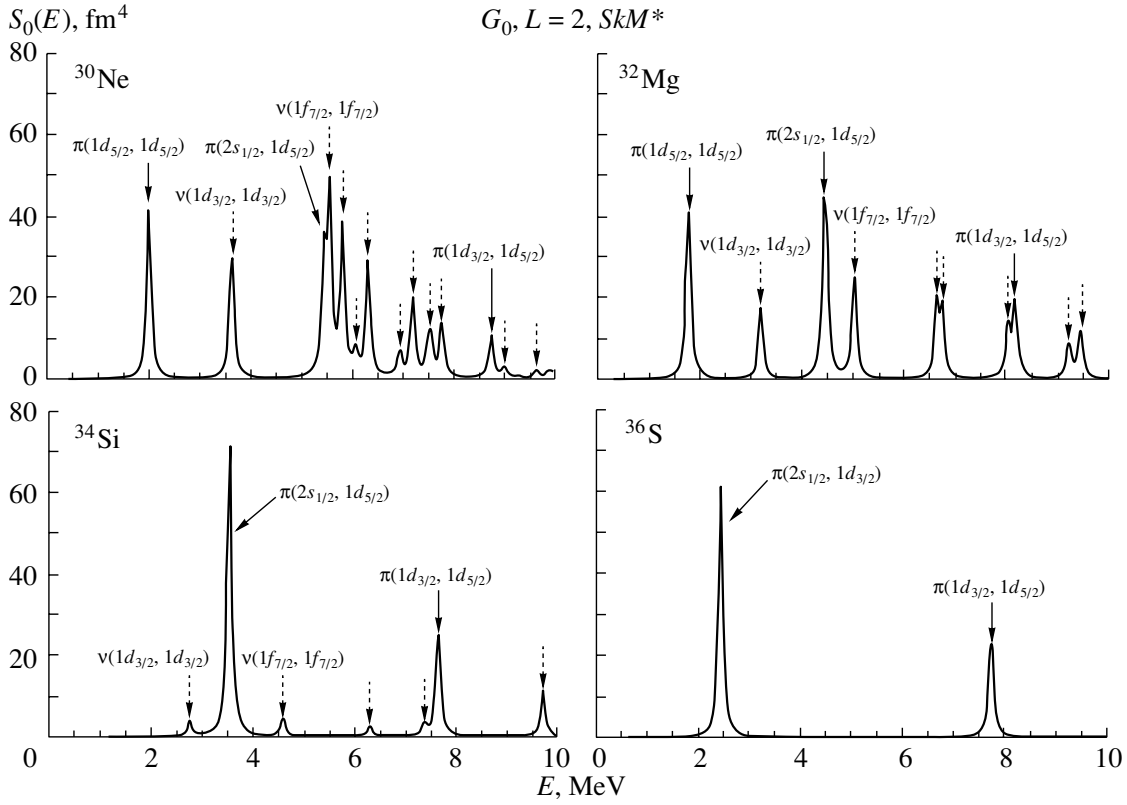

Fig. 5. The unperturbed isoscalar quadrupole strength functions in $N = 20$ isotones calculated with SkM^*. The peaks indicated by full (dotted) arrows correspond to proton (neutron) two-quasiparticle configurations.

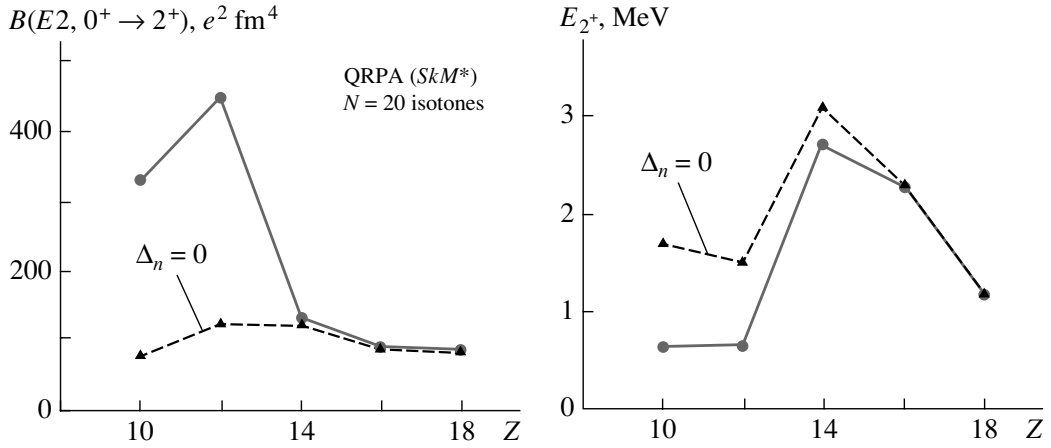

Fig. 6. The $B(E2,\ 0_1^+ \to 2_1^+)$ values and the excitation energies of the first 2^+ states in $N = 20$ isotones calculated with/without neutron pairing correlations. Proton pairing is included in both cases.

whether these 2^+ states can be described as vibrational states built on the spherical ground states.

In Fig. 3, our results of QRPA calculations with SkM^* are compared with the predictions of the Monte Carlo shell model (MCSM) [15] and the available experimental data [1–3, 19–21]. Our QRPA results are in good agreement with the experimental data and they are consistent with the MCSM prediction of the $B(E2)$ value in ^{30}Ne, which has yet to be measured experimentally. The QRPA calculations have been done with the SkM^* parameter set and the fixed pairing strength $V_0 = -418$ MeV fm^{-3}, the choice of which is explained in Section 2. The general properties of the first 2^+ states in $N = 20$

isotones, namely, very large $B(E2)$ values and very low excitation energies in ^{32}Mg and ^{30}Ne, are well reproduced within a single framework.

To check the interaction dependence, we have carried out QRPA calculations with the SkP interaction. Figure 4 shows the $B(E2)$ values and excitation energies of the first 2^+ states with SkM^* and SkP. Concerning the $B(E2)$ values, we get similar results, especially very large $B(E2)$ values in ^{32}Mg and ^{30}Ne. On the other hand, large differences are seen in the excitation energies in ^{34}Si and ^{36}S. This can be understood by the difference of about 0.5 MeV in the neutron pairing gaps calculated with SkM^* or SkP in these two nuclei. Because the neutron pairing gaps are larger with SkP than with SkM^*, the excitation energies become lower with SkP than with SkM^*.

We now explain how the neutron pairing correlations are important to make the $B(E2)$ values larger and the excitation energies lower. To see which two-quasiparticle configurations contribute to making the low-lying 2^+ states, we show the unperturbed isoscalar quadrupole strength functions in $N = 20$ isotones calculated with SkM^* in Fig. 5. The peaks indicated by full (dotted) arrows correspond to proton (neutron) two-quasiparticle configurations. All these neutron two-quasiparticle configurations appear because of the neutron pairing correlations. Many peaks of the neutron configurations are seen in ^{30}Ne, ^{32}Mg. On the other hand, the neutron configurations are negligible in ^{34}Si and they completely disappear in ^{36}S. The $B(E2)$ values are primarily made of the proton configurations in the *sd* shell, but the neutron configurations assist in making the $B(E2)$ values larger by coherence between protons and neutrons. Actually, if the neutron pairing correlations are neglected, the $B(E2)$ values become very small and the excitation energies are sizably higher in ^{32}Mg and ^{30}Ne, as shown in Fig. 6. Under these considerations, we can conclude that the very large $B(E2)$ values and the very low excitation energies in ^{32}Mg and ^{30}Ne appear thanks to the presence of the neutron pairing correlations.

We have seen in Section 3 that, around the drip line, the origin of neutron pairing correlations lies in the different behavior of the single-particle levels with different orbital angular momentum l as the levels approach the separation threshold.

Generally speaking, neutron $2p$–$2h$ configurations across $N = 20$ can originate from deformation effects or pairing effects. Both effects can a priori contribute in the nucleus ^{32}Mg. We have shown that a spherical QRPA description, i.e., putting emphasis on the pairing aspects and neglecting the possible deformation effects, can give very satisfactory results.

5. SUMMARY

We have studied the first 2^+ states in $N = 20$ isotones by the HFB–QRPA model with Skyrme interactions. The residual interaction is consistently derived from the Skyrme Hamiltonian, keeping all its explicit momentum dependence.

Because of the different behaviors of the neutron $1f_{7/2}$, $2p_{3/2}$, and $2p_{1/2}$ levels when the single-particle energies approach zero, the neutron pairing gaps have finite values. This mechanism breaks the $N = 20$ magicity in ^{32}Mg and ^{30}Ne.

Within our consistent QRPA calculation with spherical symmetry, the $B(E2,\ 0_1^+ \to 2_1^+)$ values and the excitation energies of the first 2^+ states in $N = 20$ isotones, including ^{32}Mg and ^{30}Ne, are well described. The existing experimental data are reproduced quantitatively. The $B(E2)$ value in ^{30}Ne has not been measured yet, but the QRPA value is consistent with the prediction of the MCSM. The important role of the neutron pairing correlation is emphasized. If the neutron pairing is dropped, we cannot get the correct $B(E2)$ value and excitation energy in ^{32}Mg and ^{30}Ne. In the real ^{32}Mg nucleus, both neutron pairing and deformation effects may coexist and help to make the large $B(E2)$ value, but our calculation shows that neutron pairing correlations are essential.

REFERENCES

1. T. Motobayashi, Y. Ikeda, Y. Ando, *et al.*, Phys. Lett. B **346**, 9 (1995).
2. D. Guillemaud-Mueller, C. Detraz, M. Langevin, *et al.*, Nucl. Phys. A **426**, 37 (1984).
3. Y. Yanagisawa, M. Notani, H. Sakurai, *et al.*, Phys. Lett. B **566**, 84 (2003).
4. K. Yoneda, H. Sakurai, T. Gomi, *et al.*, Phys. Lett. B **499**, 233 (2001).
5. D. Guillemaud-Mueller, Eur. Phys. J. A **13**, 63 (2002).
6. E. Khan, N. Sandulescu, M. Grasso, and Nguyen Van Giai, Phys. Rev. C **66**, 024309 (2002).
7. S. Raman, C. H. Malarkey, W. T. Milner, *et al.*, At. Data Nucl. Data Tables **36**, 1 (1987).
8. B. Gall, P. Bonche, J. Dobaczewski, *et al.*, Z. Phys. A **348**, 183 (1994).
9. J. Terasaki, P.-H. Heenen, P. Bonche, *et al.*, Nucl. Phys. A **593**, 1 (1995).
10. M. Yamagami, K. Matsuyanagi, and M. Matsuo, Nucl. Phys. A **693**, 579 (2001).
11. J. Bartel, P. Quentin, M. Brack, *et al.*, Nucl. Phys. A **386**, 79 (1982).
12. J. Dobaczewski, H. Flocard, and J. Treiner, Nucl. Phys. A **422**, 103 (1984).
13. W. Satula, J. Dobaczewski, and W. Nazarewicz, Phys. Rev. Lett. **81**, 3599 (1998).
14. M. Matsuo, Nucl. Phys. A **696**, 371 (2001).

15. Y. Utsuno, T. Otsuka, T. Mizusaki, and M. Honma, Phys. Rev. C **60**, 054315 (1999).
16. I. Hamamoto, S. V. Lukyanov, and X. Z. Zhang, Nucl. Phys. A **683**, 255 (2001).
17. J. Terasaki, H. Flocard, P.-H. Heenen, and P. Bonche, Nucl. Phys. A **621**, 706 (1997).
18. P.-G. Reinhard, D. J. Dean, W. Nazarewicz, *et al.*, Phys. Rev. C **60**, 014316 (1999).
19. B. V. Pritychenko, T. Glasmacher, P. D. Cottle, *et al.*, Phys. Lett. B **461**, 322 (1999); **467**, 309(E) (1999).
20. V. Chiste, A. Gillibert, A. Lepine-Szily, *et al.*, Phys. Lett. B **514**, 233 (2001).
21. S. Raman, C. W. Nestor, Jr., S. Kahane, and K. H. Bhatt, At. Data Nucl. Data Tables **42**, 1 (1989).

Physics of Atomic Nuclei, Vol. 67, No. 9, 2004, pp. 1640–1644. From Yadernaya Fizika, Vol. 67, No. 9, 2004, pp. 1667–1671.

Mean Field and Beyond in Nuclei Far from Stability Lines*

P. F. Bortignon[1)], F. Barranco[2)], R. A. Broglia[1),3)], G. Colò[1)], and E. Vigezzi[4)]**

Received January 21, 2004

Abstract—We calculate, for the first time, the state-dependent pairing gap of a finite nucleus (^{120}Sn) diagonalizing the bare nucleon–nucleon potential (Argonne v_{14}) in a Hartree–Fock basis. The resulting gap accounts for about half of the experimental gap. Going beyond the mean field in the particle–particle channel, the combined effect of the bare nucleon–nucleon potential and of the induced pairing interaction arising from the exchange of low-lying surface vibrations between nucleons moving in time reversal states close to the Fermi energy accounts for the experimental gap. Examples for light, halo nuclei are also reported. The more studied effects of the particle-vibration coupling in the particle–hole channel are discussed for the low-lying quadrupole vibration in ^{120}Sn and the giant dipole resonance in the unstable oxygen isotopes and ^{132}Sn. © *2004 MAIK "Nauka/Interperiodica"*.

In the study of finite many-body systems such as the atomic nucleus with its rich variety of quantal size effects, structural properties, and fluctuations, the central problem has been to identify the appropriate degrees of freedom for describing the phenomena encountered. The complementary concepts referring to the independent motion of the individual nucleons and the collective behavior of the nucleus as a whole provide, in a mean field approach, the elementary modes of excitation needed to describe the system [1]. Beyond the mean field, the unifying picture emerging from the interweaving of these degrees of freedom is well described in terms of nuclear field theory (NFT) [2–6] based on the particle-vibration coupling (for other related approaches, see, e.g., [7–10]). It has been applied to a number of schematic models and realistic situations [11–15] and its validity has been demonstrated. It thus provides a natural framework to assess the role that different degrees of freedom play in the nuclear structure. In this contribution, recent examples are presented of the effects of the particle-vibration coupling in particle–particle (*pp*) and particle–hole (*ph*) channels, following, in particular, [16].

An important subject presently under intensive study concerns the characterization of an eventual long-range component of the pairing interaction in nuclei [17–19]. In what follows, we use NFT to assess the importance that the exchange of vibrations between pairs of nucleons moving in time reversal states has in building up pairing correlations in nuclei, taking also into account self-energy and vertex corrections (cf. [20] and references therein).

In this scope, we study the quasiparticle and vibrational spectrum of odd and even isotopes of single-closed-shell nuclei, where all the richness of the single-particle and collective degrees of freedom are fully expressed, avoiding the extra complications of static deformations and associated rotations. The spectra of the $^{A}_{50}$Sn isotopes, in particular, those with mass number $A = 119$, 120, and 121, with their abundance of detailed experimental information, provide an excellent laboratory to test the importance of the residual pairing interaction and its relation to self-energy processes.

In general, one fixes the parameters of the effective interaction of nucleons in the nucleus, by requiring mean field theory, as a rule Hartree–Fock or Hartree–Fock–Bogolyubov theory if the system is superfluid, to reproduce the experimental findings: binding energies, mean-square radii, etc. This is equivalent to requiring that the solution of the Schrödinger equation describing the bound states of the electron–proton system, interacting through the Coulomb force, reproduce the energy levels of the hydrogen atom. We know that this is not possible unless the renormalization effects arising from the electron–photon coupling are properly taken into account as prescribed by QED. Similarly, the parameters of the effective nuclear interaction should reproduce the experimental findings only when the particle-vibration coupling is allowed to renormalize, screen, and dress the different

*This article was submitted by the authors in English.

[1)]Dipartimento di Fisica, Università di Milano and INFN Sezione di Milano, Italy.
[2)]Departamento de Física Aplicada III, Universidad de Sevilla, Spain.
[3)]The Niels Bohr Institute, University of Copenhagen, Denmark.
[4)]INFN Sezione di Milano, Italy.
**e-mail: pierfrancesco.bortignon@mi.infn.it

modes of elementary excitation and the interaction among them. In fact, it will be concluded that a consistent description of the low-energy nuclear spectrum requires, aside from the bare nucleon–nucleon interaction, not only the dressing of single-particle motion through the coupling to the nuclear surface, to give the right density of levels close to the Fermi energy (and thus to an effective mass $m^* \approx m$ [21]), but also the renormalization of collective vibrational modes through vertex and self-energy processes, processes which are also found to play an essential role in the pairing channel, leading to a long-range, state-dependent component of the pairing interaction.

The formalism we shall use is based on the Dyson equation [18]. It can describe on equal footing the dressed one-particle state $\tilde{a}$ of an odd nucleon renormalized by the (collective) response of all the other nucleons (Figs. 1*a*–1*d* of [16]), the renormalization of the energy $\hbar\omega_\nu$ (Figs. 2*a* and 2*b* in [16]) and of the transition probability $B(E\lambda)$ (Figs. 2*c*–2*f* in [16]) of the collective vibrations of the even system where the number of nucleons remains constant (correlated particle–hole excitations), and the induced interaction due to the exchange of collective vibrations between pairs of nucleons [17] moving in time-reversal states close to the Fermi energy (Figs. 1*e*–1*g* of [16]). We include both self-energy and vertex correction processes, thus satisfying Ward identities (cf., e.g., [20]). Within this framework, the self-consistency existing between the dynamical deformations of the density and of the potential sustained by "screened" particle-vibration coupling vertices leads to renormalization effects that make finite (stabilize) the collectivity and the self-interaction of the elementary modes of nuclear excitation, in particular, of the low-lying surface vibrational modes, providing an accurate description of many seemingly unrelated experimental findings, in terms of very few (theoretically calculable) parameters, namely, the k-mass m_k [21] and the particle vibration coupling vertex $h(ab\nu)$, associated to the process in which a quasiparticle changes its state of motion from the unperturbed quasiparticle state a to b by absorbing or emitting a vibration ν [1].

The Dyson equation describing the renormalization of a quasiparticle a, due to this variety of couplings is

$$\left[\begin{pmatrix} E_a & 0 \\ 0 & -E_a \end{pmatrix} + \begin{pmatrix} \Sigma_{11}(\tilde{E}_a) & \Sigma_{21}(\tilde{E}_a) \\ \Sigma_{21}(\tilde{E}_a) & \Sigma_{22}(\tilde{E}_a) \end{pmatrix}\right] \begin{pmatrix} \tilde{x}_a \\ \tilde{y}_a \end{pmatrix} = \tilde{E}_a \begin{pmatrix} \tilde{x}_a \\ \tilde{y}_a \end{pmatrix}, \quad (1)$$

where Σ_{ii} and $\Sigma_{ij}(i \neq j)$ are the normal and abnormal self-energies. The quantities E_a denote the quasiparticle energies obtained from a previous diagonalization of the bare nucleon–nucleon potential within the framework of the generalized Bogolyubov–Valatin transformation,

$$\Sigma_{11}(\tilde{E}_a) = \sum_{\tilde{b}\nu} \left(\frac{|V(a\tilde{b}\nu)|^2}{\tilde{E}_a - (\tilde{E}_b + \hbar\omega_\nu)} + \frac{|W(a\tilde{b}\nu)|^2}{\tilde{E}_a + (\tilde{E}_b + \hbar\omega_\nu)} \right), \quad (2)$$

$$\Sigma_{12}(\tilde{E}_a) = -\sum_{\tilde{b}\nu} V(a\tilde{b}\nu) W(a\tilde{b}\nu) \times \left(\frac{1}{\tilde{E}_a - (\tilde{E}_b + \hbar\omega_\nu)} - \frac{1}{\tilde{E}_a + (\tilde{E}_b + \hbar\omega_\nu)} \right), \quad (3)$$

with $\Sigma_{22}(\tilde{E}_a) = -\Sigma_{11}(-\tilde{E}_a)$.

Equation (1) is to be solved iteratively and simultaneously for all the involved quasiparticle states. At each iteration step, the original quasiparticle states a with occupation numbers u_a and v_a and quasiparticle energies E_a become fragmented into the several eigenstates $\tilde{a}$ of the energy-dependent eigenvalue problem of Eq. (1). For each positive eigenvalue $\tilde{E}_a$, there is a corresponding solution with eigenvalue $-\tilde{E}_a$. As in HFB theory, only positive solutions have to be included in the iterative procedure. In Eqs. (1)–(3), the phonon energies are denoted by $\hbar\omega_\nu$, and $V(a\tilde{b}\nu)$ or $W(a\tilde{b}\nu)$ label the particle-vibration vertex coupling the unperturbed quasiparticle a, with the configuration composed of the eigenstates $\tilde{b}$ and of the phonon ν. They are given by

$$V(a\tilde{b}\nu) = h(ab\nu)(u_a\tilde{v}_b - v_a\tilde{u}_b), \quad (4)$$
$$W(a\tilde{b}\nu) = h(ab\nu)(u_a\tilde{u}_b + v_a\tilde{v}_b).$$

The basic particle-vibration vertex $h(ab\nu)$ is calculated as explained in [1]. The unperturbed quasiparticle energies and occupation factors, resulting from mean field calculations, are denoted by E_a, u_a, and v_a, while $\tilde{E}_a$, $\tilde{u}_a$, and $\tilde{v}_a$ denote the corresponding renormalized quantities. The original quasiparticle strengths become fragmented over the different eigenstates $\tilde{a}$ with probability $\tilde{u}_a^2 + \tilde{v}_a^2$, while the renormalized occupation factors are obtained from the components of the eigenvectors, $\tilde{x}_a$ and $\tilde{y}_a$, according to the relations $\tilde{u}_a = \tilde{x}_a u_a + \tilde{y}_a v_a$, $\tilde{v}_a = -\tilde{y}_a u_a + \tilde{x}_a v_a$. The quantities $\tilde{u}_a$ and $\tilde{v}_a$ are related to the spectroscopic factors measured in one-nucleon stripping and pickup reactions, respectively. One can also define [18, 20] a renormalized state-dependent pairing gap through the relation $\tilde{\Delta}_a =$

$2\tilde{E}_a\tilde{u}_a\tilde{v}_a/(\tilde{u}_a^2+\tilde{v}_a^2)$, which in the limit of no fragmentation reduces to the usual BCS expression.[5)]

We have also included vertex corrections that renormalize the particle-vibration vertices V (and W) according to

$$\tilde{V}(a\tilde{b}\nu) = V(a\tilde{b}\nu) + \sum_{\tilde{c}\mu} \frac{X_{\tilde{b}\nu}^{\tilde{c}\mu} V(a\tilde{c}\mu)}{E_a - \tilde{E}_c - \hbar\omega_\mu}, \qquad (5)$$

where $X_{\tilde{b}\nu}^{\tilde{c}\mu}$ is the matrix element between the configurations $\tilde{c}\mu$ and $\tilde{b}\nu$.

In the calculations reported below, a Skyrme interaction (*Sly*4 parametrization, with $m_k \approx 0.7m$ [23]) was solely used to determine the properties of the bare single-particle states and the collective vibrations in the *ph* channel. On the other hand, in the *pp* (pairing) channel, the interactions used were the bare nucleon–nucleon v_{14} Argonne potential and the exchange of collective vibrations.

As seen from Fig. 3 of [16], Hartree–Fock theory is not able to account for the experimental quasiparticle energies of the low-lying states. Diagonalizing the Argonne v_{14} nucleon–nucleon potential in the Hartree–Fock basis, within the framework of the generalized Bogolyubov–Valatin approximation including scattering states up to 800 MeV above the Fermi energy (to achieve convergence) in a spherical box of radius equal to 15 fm, one obtains state-dependent pairing gaps. The resulting pairing gap (average value for levels around the Fermi energy) accounts for about half of the empirical pairing gap value (≈ 1.4 MeV) obtained from the odd–even mass difference.[6)] In keeping with this result, the quasiparticle spectrum, although being slightly closer to the experimental findings than that predicted by Hartree–Fock theory, displays large discrepancies with observations.

Making use of phonons which account for the experimental findings, the normal and abnormal self-energies were calculated, and Eq. (1) was solved. The average value of the resulting state-dependent pairing gap of ^{120}Sn is now close to the value $\Delta_{\rm exp} = 1.4$ MeV derived from the odd–even mass difference (cf. Fig. 4 of [16]). The peaks carrying the largest quasiparticle strength, for the orbitals around the Fermi energy, provide after the coupling an overall account of the lowest quasiparticle states measured in the odd systems ^{119}Sn and ^{121}Sn.

Successful examples of the application of this approach to light nuclei like ^{11}Li and ^{12}Be are reported in [25, 26]. At variance with the case of ^{120}Sn discussed above, the two-neutron correlations are essentially all due to the exchange of collective vibrations. This is due to two facts: (a) the small l-space available to the two loosely bound neutrons to correlate, which prevents them profiting from the bare interaction favoring the high-l $^1S_0$ scattering processes; (b) the softness of the nuclear response of the very extended, highly polarizable systems.

Moving to the *ph* channel, the situation is rather similar concerning the low-lying quadrupole vibration of ^{120}Sn calculated in the QRPA with standard effective nucleon–nucleon interactions like Gogny [27] or Skyrme forces supplemented by a zero-range density-dependent force in the pairing channel [28, 29]. While the energy is predicted too high, which may not be too important, the $B(E2)$ value is a factor of 2–3 too small, a result which calls for a better theory.

In fact, renormalizing the energy and the transition strength of the 2^+ phonon, following NFT [2], that is, considering the couplings of the type depicted in Fig. 2 of [16] (cf. also [30] and references therein), one obtains an increase in the $B(E2)$ transition probability which brings theory essentially into agreement with experiment.[7)]

The most important processes that renormalize the energy of the phonon are shown in Figs. 2*a* and 2*b* of [16]. While these two contributions tend to cancel each other in a normal system, this is not the case in a superfluid nucleus. In fact, the phonons are calculated in a Bogolyubov–Valatin-quasiparticle basis, and while the cancellation is strong in the *ph* channel, the opposite is true in the *pp* channel [32]. Other graphs that are also of fourth order in the particle-vibration coupling vertex, but contain intermediate

[5)] The formalism leading to Eq. (1) is equivalent to that presented in [18], which was based on Green's functions, and is closely connected to that of [22], which was based on the equation-of-motion method. To solve Eq. (1), we have diagonalized an equivalent energy independent matrix as explained in [22].

[6)] This result can be compared to a similar calculation performed with an effective mass equal to one, which gives $\Delta \approx 2.2$ MeV [24], a result which reflects the fact that the gap depends strongly on the density of levels at the Fermi energy.

[7)] We have only considered the renormalization of the 2^+ low-lying phonon, the properties of the other phonons participating in the renormalization processes being instead taken from experiment. For simplicity, the calculations were carried out by making use of a separable multipole–multipole interaction, including the modes with $\lambda^\pi = 2^+, 3^-, 4^+, 5^-$. The coupling constant of the quadrupole–quadrupole component was adjusted so that the bare quadrupole vibration displayed properties similar to those calculated by making use of effective interactions (i.e., $\hbar\omega_{2^+} = 2$ MeV and $B(E2\uparrow) = 700$ e^2 fm^4), while the other coupling constants were chosen so as to give an overall description of the measured energies and transition strengths of the low-lying states [31].

states with more than four quasiparticle states, lead to very small contributions. This is because these terms not only involve larger denominators, but also, due to their higher degree of complexity, give rise to contributions with "random" signs which tend to cancel each other. In keeping with the above discussion, the most important processes renormalizing the $B(E2)$ transition probability are those shown in Figs. 2*c*–2*f* of [16].

We have also calculated the static quadrupole moment Q of the 2^+ state, including the contributions from the processes shown in Fig. 6.27 of [1]. The resulting value of Q is rather small ($8\ e\ \mathrm{fm}^2$), in agreement with the experimental findings (10 ± 10 or $-5 \pm 10\ e\ \mathrm{fm}^2$ [33, 34]).

Because in the above calculations we have included only a partial set (although the most important for the physics under discussion) of the NFT graphs needed to provide a completely consistent description of single-particle and collective vibration renormalizations, the mixing of spurious states with the physical states has to be contemplated. Although it is difficult to give a precise estimate of the error induced by such undesired couplings, 30% effects have been found in the calculation of the energy of the one-phonon state [35].

The contributions of the same diagrams modify, often in sizeable way, the properties of the giant resonances [30, 36]. In particular, the spreading width is obtained, which is a redistribution of the total strength. Recently, we have calculated [37] the electric dipole strength distributions in the unstable neutron-rich oxygen isotopes ^{18,20,22}O. Low-lying strength is found, which exhausts between 5 and 10% of the TRK energy-weighted sum rule (EWSR), in rather good agreement with recent experimental data [38]. In [29, 39], predictions (the experimental data will soon be available, H. Emling, private communication) for the low-lying dipole strength in the nucleus ^{132}Sn are reported. This quantity is rather important for its role in determining the neutron capture rates in nuclei involved in the r-process. Below the giant dipole resonance region (below 12 MeV), about 10% of the EWSR is calculated. In all these cases, from the analysis of the transition densities (see, e.g., Fig. 1 in [29]), a noncollective character of the low-lying strength appears.

One can conclude that mean field theory and bare nucleon–nucleon potentials reproduce neither the experimental transition strengths nor the pairing gaps, let alone the density of quasiparticle states close to the ground state. Dressing the single-particle motion, the correlated particle–hole excitations of the mean field and the nucleon–nucleon interaction with collective surface vibrations bring the theory into overall agreement with experiment. In particular, about half of the pairing gap arises from the long-range component of the pairing interaction associated with the exchange of collective vibrations. To further clarify the interdependence of single-particle and collective degrees of freedom, future studies should, for example, concentrate on the role that this interdependence has on the nuclear masses, in particular, whether the explicit, simplified, inclusion of ground-state correlations and of the induced pairing interaction can reduce the present rms error of 0.674 MeV, with which one of the best presently available Hartree–Fock mass formulas [19] is able to reproduce the experimental findings.

REFERENCES

1. A. Bohr and B. R. Mottelson, *Nuclear Structure* (Benjamin, New York, 1974), Vol. II.
2. D. R. Bes *et al.*, Nucl. Phys. A **260**, 27 (1976).
3. D. R. Bes *et al.*, Nucl. Phys. A **260**, 77 (1976).
4. R. A. Broglia, B. R. Mottelson, D. R. Bes, *et al.*, Phys. Lett. B **64B**, 29 (1976).
5. D. R. Bes, G. G. Dussel, R. A. Broglia, *et al.*, Phys. Lett. B **52B**, 253 (1974).
6. G. G. Dussel and R. J. Liotta, Phys. Lett. B **37B**, 477 (1971).
7. A. B. Migdal, *Theory of Finite Fermi Systems and Applications to Atomic Nuclei* (Wiley, New York, 1967).
8. V. G. Soloviev, *Theory of Atomic Nuclei: Quasi-Particles and Phonons* (IOP, Bristol, 1992).
9. A. V. Avdeenkov and S. P. Kamerdzhiev, Yad. Fiz. **62**, 610 (1999) [Phys. At. Nucl. **62**, 563 (1999)].
10. S. Kamerdzhiev, E. Litvinova, and D. Zawitscha, Eur. Phys. J. A **12**, 285 (2001).
11. P. F. Bortignon, R. A. Broglia, D. R. Bes, and R. Liotta, Phys. Rep. **30C**, 305 (1977).
12. F. Barranco, M. Gallardo, and R. A. Broglia, Phys. Lett. B **198**, 19 (1987).
13. F. Barranco and R. A. Broglia, Phys. Rev. Lett. **59**, 2724 (1987).
14. P. F. Bortignon, R. A. Broglia, and D. R. Bes, Phys. Lett. B **76B**, 153 (1978).
15. J. Dukelsky, G. G. Dussel, and H. M. Sofia, J. Phys. G **8**, L191 (1982).
16. F. Barranco, R. A. Broglia, G. Colò, E. Vigezzi, and P. F. Bortignon, nucl-th/0304049v2.
17. F. Barranco *et al.*, Phys. Rev. Lett. **83**, 2147 (1999).
18. J. Terasaki, F. Barranco, R. A. Broglia, *et al.*, Nucl. Phys. A **697**, 126 (2002).
19. S. Goriely *et al.*, Phys. Rev. C **66**, 024326 (2002).
20. J. R. Schrieffer, *Theory of Superconductivity* (Addison-Wesley, Redwood, 1964).
21. C. Mahaux, P. F. Bortignon, R. A. Broglia, and C. H. Dasso, Phys. Rep. **120**, 1 (1985).
22. V. Van der Sluys *et al.*, Nucl. Phys. A **551**, 210 (1993).

23. E. Chabanat, P. Bonche, P. Haensel, *et al.*, Nucl. Phys. A **627**, 710 (1997). We have found it convenient to reduce the strength of the spin-orbit term by 15% in order to obtain a better overall agreement with the experimental data.
24. F. Barranco *et al.*, Phys. Lett. B **390**, 13 (1997).
25. F. Barranco, P. F. Bortignon, R. A. Broglia, *et al.,* Eur. Phys. J. A **11**, 385 (2001).
26. G. Gori, F. Barranco, E. Vigezzi, and R. A. Broglia, nucl-th/0301097.
27. G. Giambrone *et al.*, Nucl. Phys. A **726**, 3 (2003).
28. G. Colò, P. F. Bortignon, D. Sarchi, and E. Vigezzi, Acta Phys. Pol. B **34**, 2175 (2003).
29. G. Colò *et al.*, Nucl. Phys. A **722**, 111c (2003).
30. G. F. Bertsch, P. F. Bortignon, and R. A. Broglia, Rev. Mod. Phys. **55**, 287 (1983).
31. O. Beer *et al.*, Nucl. Phys. A **147**, 326 (1970); N. G. Jonsson *et al.*, Nucl. Phys. A **371**, 333 (1981).
32. P. F. Bortignon, R. A. Broglia, and C. H. Dasso, Nucl. Phys. A **398**, 221 (1983).
33. P. H. Stelson *et al.*, Phys. Rev. C **2**, 2015 (1970).
34. R. Graetzer *et al.*, Phys. Rev. C **12**, 1462 (1975).
35. D. R. Bes and J. Kurchan, *The Treatment of Collective Coordinates in Many-Body Systems. An Application of the BRST Invariance* (World Sci., Singapore, 1990).
36. P. F. Bortignon, A. Bracco, and R. A. Broglia, *Giant Resonances. Nuclear Structure at Finite Temperature* (Harwood Academic, New York, 1998).
37. G. Colò and P. F. Bortignon, Nucl. Phys. A **696**, 427 (2001).
38. A. Leistenschneider *et al.,* Phys. Rev. Lett. **86**, 5442 (2001).
39. D. Sarchi, P. F. Bortignon, and G. Colò, in press.

Physics of Atomic Nuclei, Vol. 67, No. 9, 2004, pp. 1645–1649. From Yadernaya Fizika, Vol. 67, No. 9, 2004, pp. 1672–1676.

Microscopic Description of Mixed-Symmetry States in Nearly Spherical Nuclei*

Ch. Stoyanov[1] and N. Lo Iudice[2]

Received January 21, 2004

Abstract—We adopt the quasiparticle-phonon model to investigate the phonon content and the proton–neutron symmetry of low-lying states recently discovered in nuclei around shell closure. The results are in overall agreement with experiments and consistent with the interacting boson model. © *2004 MAIK "Nauka/Interperiodica".*

1. INTRODUCTION

Considerable effort has been devoted to the study of low-lying spectra in heavy nuclei since the discovery of the magnetic dipole excitation in deformed nuclei [1], known as the scissors mode [2] (see for a review [3–6]). This is an isovector excitation existing only in deformed nuclei, characterized by a strong $M1$ decay to the ground state. In the algebraic IBM-2, it belongs to the class of F-spin mixed-symmetry states which are marked by weak $E2$ and strong $M1$ transitions to proton–neutron symmetric states [7]. The scissors mode was, actually, the only experimentally known mixed-symmetry excitation for many years.

Only recently was unambiguous experimental evidence in favor of such states in spherical or nearly spherical nuclei provided [8–10]. The discovery immediately stimulated theoretical investigations, especially within the microscopic models like nuclear shell model [11] and quasiparticle-phonon model (QPM) [12, 13].

The latest experiments were performed on ^{92}Zr [14, 15] with the purpose of testing the limit of F-spin symmetry in IBM. An analysis of the data based on a severely truncated shell model calculation was carried out and reached the conclusion that F-spin was badly broken in the lowest 2^+ state. This, in fact, turned out to be a neutron excitation and, as such, a linear combination of symmetric and mixed-symmetry IBM states.

The energy and collectivity of the low-lying states in nearly spherical nuclei change considerably with the mass number. These changes can be accounted for only by microscopic models. Moreover, the QPM, using a RPA phonon basis in a large configuration space, provides a more reliable test for F-spin symmetry breaking with respect to the shell model. Indeed, we will show here that the QPM not only gives a description of the low-lying states of all the nuclei explored experimentally, including the one supposed to be at the borderline of the F-spin domain, but also provides almost complete information about the phonon content and the proton–neutron symmetry properties of these states.

2. BRIEF OUTLINE OF THE QPM

The QPM intrinsic Hamiltonian has the form [16]

$$H = H_{\rm sp} + V_{\rm pair} + V_M^{ph} + V_{SM}^{ph} + V_M^{pp}. \qquad (1)$$

$H_{\rm sp}$ is a one-body Hamiltonian; $V_{\rm pair}$ is the monopole pairing; V_M^{ph} and V_{SM}^{ph} are, respectively, sums of separable multipole and spin-multipole particle–hole interactions; and V_M^{pp} is the sum of particle–particle multipole pairing potentials.

The building blocks of the QPM are the RPA phonons

$$Q^\dagger_{i\lambda\mu} = \frac{1}{2}\sum_{\tau=n,p}\sum_{jj'}\Big\{\psi^{i\lambda}_{jj'}[\alpha^\dagger_j\alpha^\dagger_{j'}]_{\lambda\mu} \qquad (2)$$
$$-(-1)^{\lambda-\mu}\varphi^{i\lambda}_{jj'}[\alpha_{j'}\alpha_j]_{\lambda-\mu}\Big\}_\tau .$$

They are superpositions of bilinear forms of the quasiparticle operators, $\alpha^\dagger_{jm}$ and α_{jm}, obtained from the particle operators ($a^\dagger_{jm}$, a_{jm}) through the canonical Bogolyubov transformation [16]. According to (2), the RPA basis includes collective as well as noncollective phonons.

*This article was submitted by the authors in English.

[1]Institute for Nuclear Research and Nuclear Energy, Sofia, Bulgaria; e-mail: stoyanov@inrne.bas.bg

[2]Dipartimento di Scienze Fisiche, Universitá di Napoli Federico II and INFN Sezione di Napoli, Napoli, Italy.

Table 1. The dependence of $M1$ and $E2$ transitions on the ratio $G^{(2)}/\kappa_0^{(2)}$ in ^{136}Ba

$G^{(2)}/\kappa_0^{(2)}$	$B(E2;\text{g.s.}\to 2^+_{\text{iv}})_{\text{RPA}}$, e^2 b^2	$B(M1;2^+_{\text{iv}}\to 2^+_{\text{is}})_{\text{RPA}}$, μ_N^2	$B(2^+)$
0	0.0032	0.042	0.58
0.85	0.011	0.24	22.6

Table 2. The values of $B(2^+)$ for ^{144}Nd [M_n and M_p represent the contribution of protons and neutrons, respectively, in (4)]

E, MeV	$B(2^+)$	M_n	M_p
2^+_1 0.695	3×10^{-3}	1.14×10^2	1.19×10^2
2^+_2 2.054	21.54	15.16	−23.49

The quasiparticle-phonon Hamiltonian is diagonalized using the trial wave function of total spin JM [17, 18]

$$\Psi_\nu(JM)=\Bigg\{\sum_i R_i(\nu J)Q^\dagger_{iJM} + \sum_{\substack{i_1\lambda_1\\ i_2\lambda_2}} P^{i_1\lambda_1}_{i_2\lambda_2}(\nu J)\left[Q^\dagger_{i_1\lambda_1\mu_1}\otimes Q^\dagger_{i_2\lambda_2\mu_2}\right]_{JM} + \sum_{\substack{i_1\lambda_1 i_2\lambda_2\\ i_3\lambda_3 I}} T^{i_1\lambda_1 i_2\lambda_2 I}_{i_3\lambda_3}(\nu J) \times\left[\left[Q^\dagger_{i_1\lambda_1\mu_1}\otimes Q^\dagger_{i_2\lambda_2\mu_2}\right]_{IK}\otimes Q^\dagger_{i_3\lambda_3\mu_3}\right]_{JM}\Bigg\}\Psi_0. \quad (3)$$

In computing the norm of the wave function as well as the necessary matrix elements, the exact commutation relations for the phonons [16–18] are used.

3. NUMERICAL DETAILS

The numerical details of the calculations are largely discussed in [13]. We adopt a one-body Woods–Saxon potential U and choose $f(r)=dU(r)/dr$ as radial component of the multipole fields entering into the particle–hole and particle–particle separable interaction. We fix the strengths $\kappa^{(2)}$ and $\kappa^{(3)}$ of the quadrupole–quadrupole and octupole–octupole particle–hole interaction by a fit of the energies of the first 2^+ and 3^- states. Only the quadrupole pairing interaction in the particle–particle channel is important for our purposes [13]. We set $G^{(2)}=G^{(2)}_{nn}=G^{(2)}_{pp}$ and $G^{(2)}_{np}=0$.

Table 3. Energies and structure of selected low-lying excited states in ^{94}Mo (only the dominant components are presented)

State		E, keV		Structure, %
T	J^π	Exp.	QPM	
Is.	$2^+_{1,\text{is}}$	871	860	93% $[2^+_{\text{is}}]_{\text{RPA}}$
	$2^+_{2,\text{is}}$	1864	1750	82% $[2^+_{\text{is}}\otimes 2^+_{\text{is}}]_{\text{RPA}}$
	$4^+_{1,\text{is}}$	1573	1733	82% $[2^+_{\text{is}}\otimes 2^+_{\text{is}}]_{\text{RPA}}$
Iv.	$1^+_{1,\text{iv}}$	3129	2880	90% $[2^+_{\text{is}}\otimes 2^+_{\text{iv}}]_{\text{RPA}}$
	$2^+_{1,\text{iv}}$	2067	1940	95% $[2^+_{\text{iv}}]_{\text{RPA}}$
	$2^+_{2,\text{iv}}$	2393	2730	27% $[2^+_{\text{is}}\otimes 2^+_{\text{iv}}]_{\text{RPA}}$
	$2^+_{3,\text{iv}}$	2740	3014	59% $[2^+_{\text{is}}\otimes 2^+_{\text{iv}}]_{\text{RPA}}$
	$4^+_{1,\text{iv}}$		3120	64% $[2^+_{\text{is}}\otimes 2^+_{\text{iv}}]_{\text{RPA}}$
	$3^+_{1,\text{iv}}$	2965	2940	87% $[2^+_{\text{is}}\otimes 2^+_{\text{iv}}]_{\text{RPA}}$
	1^+_2		3550	40% $[1^+_1]_{\text{RPA}}$

In order to test the isospin nature of the phonons, the following ratio is computed:

$$B(2^+)=\frac{|\langle 2^+||\sum_k^p r_k^2Y_{2\mu}(\Omega k)-\sum_k^n r_k^2Y_{2\mu}(\Omega k)||\text{g.s.}\rangle|^2}{|\langle 2^+||\sum_k^p r_k^2Y_{2\mu}(\Omega k)+\sum_k^n r_k^2Y_{2\mu}(\Omega k)||\text{g.s.}\rangle|^2}. \quad (4)$$

This ratio probes the isoscalar ($B(2^+)<1$) or isovector ($B(2^+)>1$) properties of the 2^+ state under consideration. The calculation shows that the first state is isoscalar and will be denoted by $[2^+_{\text{is}}]_{\text{RPA}}$. The properties of the second state, denoted by $[2^+_{\text{iv}}]_{\text{RPA}}$, depend critically on the ratio $G^{(2)}/\kappa_0^{(2)}$. The example of ^{136}Ba shown in Table 1 is illustrative of all nuclei. The ratio $B(2^+)$ increases dramatically with $G^{(2)}/\kappa_0^{(2)}$, showing that $[2^+_{\text{iv}}]_{\text{RPA}}$ changes from isoscalar to isovector.

Similar properties are exhibited by the $[2^+_{\text{is}}]_{\text{RPA}}$ and $[2^+_{\text{iv}}]_{\text{RPA}}$ states in ^{144}Nd (see Table 2).

Tables 1 and 2 show that, for an appropriate value of the ratio $G^{(2)}/\kappa_0^{(2)}(=0.8-0.9)$, the RPA basis contains a collective isoscalar $[2^+_{\text{is}}]_{\text{RPA}}$ and a slightly collective isovector $[2^+_{\text{iv}}]_{\text{RPA}}$ state. The two states are mutually coupled via a relatively strong $M1$ transition.

4. RESULTS

4.1. ^{94}Mo

Energies and phonon structure of the calculated excited states of ^{94}Mo are given in Table 3. The first

Table 4. $E2$ transitions connecting some excited states in ^{94}Mo calculated in the QPM (the experimental data are taken from [8, 9])

$B(E2; J_i \to J_f)$, e^2 fm^4	Exp.	QPM	IBM-2
	$\Delta T = 0$		
g.s. $\to 2^+_{1,\mathrm{is}}$	2030(40)	1978	2333
g.s. $\to 2^+_{2,\mathrm{is}}$	32(7)	35	0
$2^+_{2,\mathrm{is}} \to 2^+_{1,\mathrm{is}}$	720(260)	673	592
$4^+_{1,\mathrm{is}} \to 2^+_{1,\mathrm{is}}$	670(100)	661	592
	$\Delta T = 0$		
$2^+_{2,\mathrm{iv}} \to 2^+_{1,\mathrm{iv}}$		127	
$2^+_{3,\mathrm{iv}} \to 2^+_{1,\mathrm{iv}}$		266	
$1^+_{1,\mathrm{iv}} \to 2^+_{1,\mathrm{iv}}$	<690	374	556
$3^+_{1,\mathrm{iv}} \to 2^+_{1,\mathrm{iv}}$	250^{+310}_{-210}	368	582
	$(1.5^{+1.2}_{-0.6}) \times 10^3$		
$4^+_{1,\mathrm{iv}} \to 2^+_{1,\mathrm{iv}}$		274	
	$\Delta T = 1$		
g.s. $\to 2^+_{1,\mathrm{iv}}$	230(30)	150	151
g.s. $\to 2^+_{2,\mathrm{iv}}$	27(8)	18	0
g.s. $\to 2^+_{3,\mathrm{iv}}$	83(10)	10	0
$1^+_{1,\mathrm{iv}} \to 2^+_{1,\mathrm{is}}$	30(10)	13	49
$3^+_{1,\mathrm{iv}} \to 2^+_{1,\mathrm{is}}$	9^{+25}_{-8}	12	

$2^+_{1,\mathrm{is}}$ is dominantly a $[2^+_{\mathrm{is}}]_{\mathrm{RPA}}$ one-phonon isoscalar state, the second is an isoscalar two-phonon state, and the third is an isovector one-phonon state.

The $E2$ reduced transition probabilities are shown in Table 4. We notice the strong $E2$ transitions between isoscalar states differing by one $[2^+_{\mathrm{is}}]_{\mathrm{RPA}}$ phonon, fairly strong transitions between isovector states again differing by one RPA phonon, and very weak transitions between isovector to isoscalar states differing by an even number of phonons.

The $M1$ transitions are shown in Table 5. The measured $1^+_{1,\mathrm{iv}} \to$ g.s. and $1^+_2 \to$ g.s. $M1$ strengths are both reproduced by our calculation. The structure of these two states, however, is totally different. As shown in Table 3, the first one is basically a two-phonon isovector state, consistent with the IBM picture. The second 1^+_2 instead has a composite structure and contains a sizeable $[1^+]_{\mathrm{RPA}}$ with the dominant spin-flip quasiparticle configuration. This transition is outside the domain of the algebraic IBM.

Table 5. $M1$ transitions connecting some excited states in ^{94}Mo calculated in the QPM (the experimental data are taken from [8, 9])

$B(M1; J_i \to J_f)$, μ_N^2	Exp.	QPM		IBM-2
		g^s_{eff}		
		$0.7g^s_{\mathrm{free}}$	$0.0g^s_{\mathrm{free}}$	
	$\Delta T = 1$			
$1^+_{1,\mathrm{iv}} \to 2^+_{2,\mathrm{is}}$	0.43(5)	0.75	0.22	0.36
$2^+_{1,\mathrm{iv}} \to 2^+_{1,\mathrm{is}}$	0.48(6)	0.72	0.23	0.30
$2^+_{2,\mathrm{iv}} \to 2^+_{2,\mathrm{is}}$		0.10	0.034	
$2^+_{3,\mathrm{iv}} \to 2^+_{2,\mathrm{is}}$	0.35(11)	0.24	0.072	0.1
$3^+_{1,\mathrm{iv}} \to 2^+_{2,\mathrm{is}}$	$0.24^{+0.14}_{-0.07}$	0.34	0.10	0.18
$3^+_{1,\mathrm{iv}} \to 4^+_{1,\mathrm{is}}$	$0.074^{+0.044}_{-0.019}$	0.26	0.08	0.13
$4^+_{1,\mathrm{iv}} \to 4^+_{1,\mathrm{is}}$	0.8(2)	0.75	0.23	
	$\Delta T = 1$			
$1^+_{1,\mathrm{iv}} \to$ g.s.	0.16(1)	0.14	0.09	0.16
$1^+_{1,\mathrm{iv}} \to 2^+_{1,\mathrm{is}}$	0.007^{+6}_{-2}	6×10^{-4}	5×10^{-3}	0
$2^+_{2,\mathrm{iv}} \to 2^+_{1,\mathrm{is}}$	0.07	0.001	0.002	0
$2^+_{3,\mathrm{iv}} \to 2^+_{1,\mathrm{is}}$	0.03	0.013	0.005	0
$3^+_{1,\mathrm{iv}} \to 2^+_{1,\mathrm{is}}$	$0.01^{+0.012}_{-0.006}$	0.006	0.0025	0
	$\Delta T = 0$			
$1^+_{1,\mathrm{iv}} \to 2^+_{1,\mathrm{iv}}$	<0.05	3×10^{-6}	2×10^{-5}	0
$3^+_{1,\mathrm{iv}} \to 2^+_{1,\mathrm{iv}}$	$0.021^{+0.035}_{-0.014}$	2×10^{-5}	9×10^{-6}	0
	$0.09^{+0.07}_{-0.03}$			
$2^+_{2,\mathrm{is}} \to 2^+_{1,\mathrm{is}}$	0.06	0.006	0.004	0
$1^+_2 \to$ g.s.	0.046(18)	0.04	0.009	

The theoretical scheme of the $M1$ transitions is in remarkably good agreement with the experimental picture. We get strong transitions between members of the isovector and isoscalar groups having an equal number of phonons. We also obtain weak or very weak transitions between states of different isospin but with a different number of phonons and between states belonging to the same isospin group.

4.2. ^{92}Zr

The nucleus ^{92}Zr has two more neutrons than the semimagic ^{90}Zr. One could expect that the noncollective degrees of freedom are more pronounced in ^{92}Zr in comparison with those in ^{94}Mo. The comparison of the properties of low-lying states in both nuclei is presented in Table 6. The experimental data

Table 6. Some properties of 2^+ states in ^{94}Mo and ^{92}Zr

Transition	^{94}Mo	^{92}Zr
$B(E2; 2_1^+ \to \text{g.s.})$ [W.u.]	15.6	6.4
$B(E2; 2_2^+ \to \text{g.s.})$ [W.u.]	0.45	3.7
$B(M1; 2_2^+ \to 2_1^+)$ $[\mu_N^2]$	0.06	0.46

Table 7. Contribution of neutrons and protons to $[2^+]_{\text{RPA}}$ states of ^{92}Zr

State	Neutron		Proton	
$[2_1^+]_{\text{RPA}}$	60%		40%	
	main component	amplitude	main component	amplitude
	$(2d_{5/2})^2$	0.99	$(1g_{9/2})^2$	0.64
$[2_2^+]_{\text{RPA}}$	51%		49%	
	main component	amplitude	main component	amplitude
	$(2d_{5/2})^2$	−0.99	$(1g_{9/2})^2$	0.79

reveal the importance of the shell gap between proton orbitals $2p_{1/2}$ and $1g_{9/2}$ in the mass domain $A = 90$. The smaller value of $B(E2; 2_1^+ \to \text{g.s.})$ for ^{92}Zr reflects the dominance of the neutrons in the structure of 2_1^+ state, while the large $M1$ strength means that 2_2^+ is a candidate to be a one-phonon mixed-symmetry state. This is the first time that the 2_2^+ state of a nearly spherical nucleus could be identified as a one-phonon mixed-symmetry state [14]. On the other hand, the fact that the $M1$ strength is smaller than that in the nearby ^{94}Mo suggests an appreciable admixture with the symmetric component and, therefore, a nonnegligible F-spin symmetry breaking.

The calculated properties of the $[2^+]_{\text{RPA}}$ excited states are presented in Table 7. We obtain a neutron dominance in the $[2_1^+]_{\text{RPA}}$ and a comparable proton–neutron contribution in the $[2_2^+]_{\text{RPA}}$. The main neutron and proton components are in-phase in the $[2_1^+]_{\text{RPA}}$ state and out of phase in $[2_2^+]_{\text{RPA}}$. These features lead to large $B(M1; 2_2^+ \to 2_1^+)$. A relatively strong $E2$ transition connects the ground to the $[2_2^+]_{\text{RPA}}$ state. The calculated $B(E2; 2_2^+ \to \text{g.s.})$ is 2.2 W.u. This reveals that the isoscalar correlations are important in the structure of the $[2_2^+]_{\text{RPA}}$ state. The quite small value of $B([2_2^+]_{\text{RPA}})$ [Eq. (4)] $(\ll 1)$ provides an additional indication of such an isoscalar admixture. All the above properties lead to the conclusion that the nucleus ^{92}Zr is on the verge of the F-spin symmetry domain.

Table 8. Energies and structure of the selected low-lying excited states in ^{92}Zr (only the contributions of components under consideration are presented)

State	E, keV		Structure, %
	Exp.	QPM	
2_1^+	934	1017	$93\%\ [2_1^+]_{\text{RPA}}$
2_2^+	1847	1945	$90\%\ [2_2^+]_{\text{RPA}} + 2.5\%\ [2_1^+ \otimes 2_1^+]_{\text{RPA}}$
2_3^+	2067	2008	$4\%\ [2_2^+]_{\text{RPA}} + 19\%\ [2_3^+]_{\text{RPA}} + 65\%\ [2_1^+ \otimes 2_1^+]_{\text{RPA}}$

Table 9. The strength of $E2$ transitions connecting some excited states in ^{92}Zr calculated in QPM (the effective charge $e^*_{\text{eff}} = 0.1$ is used in the calculation)

Transition	Exp.	QPM
$B(E2; 2_1^+ \to \text{g.s.})$ [W.u.]	6.4(6)	6.5
$B(E2; 2_2^+ \to \text{g.s.})$ [W.u.]	3.7(8)	2.1
$B(E2; 2_3^+ \to \text{g.s.})$ [W.u.]		0.00018
$B(E2; 2_2^+ \to 2_1^+)$ [W.u.]	0.3(1)	0.39
$B(E2; 2_3^+ \to 2_1^+)$ [W.u.]		6.8

The structure of several 2^+ states calculated within the QPM is shown in Table 8. The first 2^+ is a one-phonon collective state. The second 2^+ is dominated by the one-phonon $[2_2^+]_{\text{RPA}}$, while the third 2^+ includes a large fraction of the proton–neutron symmetric two-phonon collective component. This structure determines the values of $E2$ and $M1$ transition probabilities. The computed strengths of the $E2$ and $M1$ transitions are shown in Tables 9 and 10. They are in good agreement with the measured ones. This confirms the conclusion made in [14] that, in ^{92}Zr, the second 2^+ is a one-phonon state. On the other hand, it strongly suggests that the proton–neutron symmetry is broken considerably in this state.

Another test of the structure of 2^+ excited states is obtained by calculating the corresponding *g-factors*. Only the gyromagnetic factor of the lowest 2^+ has been measured. Its value is $g(2_1^+) = -0.18(1)\mu_N$. The corresponding calculated value is $g(2_1^+) = -0.20\mu_N$. This comparison leads to the conclusion that the structure of low-lying quadrupole excitations is described quite well within the QPM.

The experimental data show a state with quadrupole structure at 3.26-MeV excitation energy. This 2^+ state is connected through a strong $M1$ transition with the 2_1^+ state ($B(M1; 2_{3.26}^+ \to 2_1^+) = 0.16(2)\mu_N^2$).

Table 10. The strength of $M1$ transitions connecting some excited states in ^{92}Zr calculated in the QPM

Transition	Exp.	QPM, $g^s_{\rm eff} = 0.7$
$B(M1; 1^+_1 \to \text{g.s.})\ [\mu^2_N]$	0.094(4)	0.069
$B(M1; 2^+_2 \to 2^+_1)\ [\mu^2_N]$	0.46(15)	0.68

The energy of the state (3.26 MeV) is close to the energy of the unperturbed three-phonon configuration $[[2^+_1 \otimes 2^+_1]_{IK} \otimes 2^+_2]_{2^+}$. According to the experimental energy of the first and second 2^+ states, the energy of the three-phonon configuration has to be around 3.7–3.8 MeV. This structure leads to a strong $M1$ decay to the 2^+_1 state. Such a transition belongs to the group of *boson forbidden* transitions discussed in detail in [18]. It is similar to the $M1$ transition connecting the ground and the 1^+_1 states dominated by the $[2^+_1 \otimes 2^+_2]_{1^+}$. If the structure of $2^+_{3.26\,\text{MeV}}$ state is dominated by the three-phonon component $[[2^+_1 \otimes 2^+_1]_{IK} \otimes 2^+_2]_{2^+}$, the value of $B(M1; 2^+_{3.26} \to 2^+_1)$ has to be close to the value of $B(M1; 1^+_1 \to \text{g.s.})$. We have estimated the transition probability assuming that the structure of the $2^+_{3.26\,\text{MeV}}$ state is exhausted completely by the $[[2^+_1 \otimes 2^+_1]_{IK} \otimes 2^+_2]_{2^+}$ component. The estimated strength is $B(M1; 2^+_{[[2^+_1 \otimes 2^+_1]_{IK} \otimes 2^+_2]_{2^+}} \to 2^+_1) = 0.14\mu^2_N$, close to the experimental value. We conclude that the excited 2^+ state at 3.26 MeV is a good candidate to be a three-phonon state.

5. CONCLUSIONS

According to our findings, the low-lying excitations observed recently in several nuclei near either proton or neutron shell closure are adequately described within the QPM as multiphonon states composed solely of the two lowest RPA $[2^+]_{\rm RPA}$ phonons. The first of the RPA phonons undergoes a strong isoscalar $E2$ decay to the ground state and is, therefore, symmetric with respect to proton–neutron exchange. The second occurs at low energy only for a sufficiently strong quadrupole pairing interaction and decays through a strong isovector $E2$ transition. It is therefore proton–neutron nonsymmetric.

The resulting low-lying QPM states can be classified according to the number of phonons and the proton–neutron symmetry. Indeed, states with the same symmetry, differing by a collective RPA phonon, are connected by appreciable, often strong, $E2$ transitions. On the contrary, nonsymmetric states with an equal number of phonons are coupled by strong $M1$ transitions.

The level and transition scheme is in excellent agreement with the experiments and fully consistent with the IBM picture. Indeed, the symmetric QPM states can be put in one-to-one correspondence with the $F = F_{\rm max}$ IBM states. The nonsymmetric ones are the QPM counterpart of the IBM $F = F_{\rm max} - 1$ mixed-symmetry states. The QPM approach appears to be suitable also for describing the low-lying spectra of nuclei at the borderline of the F-spin symmetry domain. In the case of ^{92}Zr, recently studied experimentally, our QPM calculation confirms the F-spin breaking but suggests that such a breaking occurs mainly in the second 2^+ and to a less extent in the first one, contrary to the conclusions drawn on the grounds of an analysis based on a severely truncated shell model space. We suggest the measurement of several key transitions and magnetic moments which should conclusively clarify the issue of F-spin symmetry breaking in this nucleus.

ACKNOWLEDGMENTS

The present work was partly supported by the Italian Ministry of Research and Technology (MURST) through the PRIN01 funds and by the Bulgarian Science Foundation.

REFERENCES

1. D. Bohle *et al.*, Phys. Lett. B **137B**, 27 (1984).
2. N. Lo Iudice and F. Palumbo, Phys. Rev. Lett. **41**, 1532 (1978).
3. A. Richter, Prog. Part. Nucl. Phys. **34**, 261 (1995), and references therein.
4. U. Kneissl, H. H. Pitz, and A. Zilges, Prog. Part. Nucl. Phys. **37**, 349 (1996), and references therein.
5. N. Lo Iudice, Part. Nucl. **28**, 556 (1997).
6. N. Lo Iudice, Riv. Nuovo Cimento **23**, 9 (2000).
7. T. Otsuka, A. Arima, and F. Iachello, Nucl. Phys. A **309**, 1 (1978).
8. N. Pietralla *et al.*, Phys. Rev. Lett. **83**, 1303 (1999).
9. N. Pietralla *et al.*, Phys. Rev. Lett. **84**, 3775 (2000).
10. C. Fransen *et al.*, Phys. Lett. B **508**, 219 (2001).
11. A. F. Lisetskiy *et al.*, Nucl. Phys. A **677**, 1000 (2000).
12. N. Lo Iudice and Ch. Stoyanov, Phys. Rev. C **62**, 047302 (2000).
13. N. Lo Iudice and Ch. Stoyanov, Phys. Rev. C **65**, 064304 (2002).
14. V. Werner *et al.*, Phys. Lett. B **550**, 140 (2002).
15. N. Pietralla *et al.* (in press).
16. V. G. Soloviev, *Theory of Atomic Nuclei: Quasiparticles and Phonons* (Institute of Phys. Publ., Bristol, 1992).
17. M. Grinberg and Ch. Stoyanov, Nucl. Phys. A **573**, 231 (1994).
18. V. Yu. Ponomarev *et al.*, Nucl. Phys. A **635**, 470 (1998).

Physics of Atomic Nuclei, Vol. 67, No. 9, 2004, pp. 1650–1655. From Yadernaya Fizika, Vol. 67, No. 9, 2004, pp. 1677–1682.

Collective Excitations and a Backbending Phenomenon in ^{156}Dy*

J. Kvasil[1], R. G. Nazmitdinov[2], and A. S. Sitdikov[3]

Received January 21, 2004

Abstract—We propose a self-consistent practical method to study collective excitations in rotating nuclei within the cranking + random phase approximation approach. It consists in solving the cranking Hartree–Bogolyubov equations for the modified Nilsson potential + monopole pairing forces. Further, the mean field results are used to construct collective vibrations treated in the random phase approximation (RPA). Special attention is paid to fulfill all conservation laws in the RPA to separate spurious and physical solutions. We demonstrate that the backbending in ^{156}Dy can be explained as a result of the disappearance of collective γ vibrations of the positive signature in the rotating frame. © *2004 MAIK "Nauka/Interperiodica".*

1. INTRODUCTION

The backbending phenomenon has been a subject of interest in nuclear physics for more than three decades [1]. It is widely accepted that the phenomenon is caused by the rotational alignment of angular momenta of a nucleon pair occupying a high-j intruder orbital near the Fermi surface. The alignment breaks a Cooper pair and leads to a sudden increase in the kinematical moment of inertia $\mathcal{J} = I/\Omega$ along the yrast level sequence as a function of rotational frequency Ω.

The mainstream of microscopic analysis of the backbending has been carried out in terms of various cranking Hartree–Fock–Bogolyubov (CHFB) calculations. In medium-heavy and heavy nuclei, the studies are based on the pairing plus quadrupole–quadrupole interaction (cf. [2]) and on effective forces such as the Gogny [3] and the Skyrme interactions [4]. It should be noted that there also exist a few calculations of the backbending in lighter nuclei such as ^{48,50}Cr in the shell model framework [5]. In this paper, we attempt to shed light upon the role of collective excitations in the backbending phenomenon.

The application of the shell model to heavy nuclei loses it feasibility due to a large number of relevant basis states. The CHFB approach, being a mean field theory, violates fundamental symmetries such as the particle number and the angular momentum conservation laws. However, a correct description of the backbending requires dealing with states that have good quantum numbers. The RPA is one of the effective methods to restore broken symmetries. In the case of broken symmetries, the RPA separates out the collective excitation associated with each broken symmetry as a zero-energy or *spurious* RPA mode, with an inertial parameter fixed by the approximation (cf. [6]). Furthermore, the RPA provides a consistent way to take into account quantum fluctuations around the mean field solution. In fact, the contribution of quantum fluctuations to the total energy modifies the moment of inertia [7, 8] and, consequently, the analysis of this contribution could bring new insight into the backbending phenomenon. It should be emphasized that it is quite important to achieve self-consistency between the mean field and the single-particle orbitals and total energy minimization at the stage of the application of the RPA. In addition, for detailed analysis of experimental data that manifest a complex interplay between single-particle and collective dynamics, it is important to start with a reliable single-particle basis.

The practical application of the RPA for nonseparable effective forces such as the Gogny or Skyrme interactions in rotating nuclei requires too large a configuration space. Moreover, different parametrizations of effective forces do not provide a well-established single-particle spectrum. A self-consistent mean field based upon phenomenological cranking Nilsson or Saxon–Woods potentials with pairing forces is still quite competitive from the above point of view. These potentials allow one to construct also a self-consistent residual interaction neglected at the mean field level. The RPA with separable multipole–multipole interaction based on these phenomenological potentials is an effective tool for the analysis

*This article was submitted by the authors in English.

[1]Institute of Particle and Nuclear Physics, Charles University, Praha, Czech Republic; e-mail: kvasil@ipnp.troja.mff.cuni.cz

[2]Departament de Física, Universitat de les Illes Balears, Palma de Mallorca, Spain; Bogolyubov Laboratory of Theoretical Physics, Joint Institute for Nuclear Research, Dubna, Moscow oblast, 141980 Russia.

[3]Kazan State Power Engineering University, Kazan, Russia.

1063-7788/04/6709-1650$26.00

of low-lying collective excitations of rotating nuclei (cf. [9, 10]). In this paper, we propose that a shape transition, when one of the low-lying collective modes disappears, could lead to the backbending. Our goal is to clarify this issue by using the RPA with separable interaction and comparing the result of our analysis with existing experimental data for ^{156}Dy.

The paper is organized as follows. In Section 2, we introduce our mean field and RPA model. Section 3 is devoted to analysis of experimental data within the framework of our model. The conclusions are drawn in Section 4.

2. THE CRANKING + RPA MODEL

2.1. The Effective Mean Field

We start with the cranking Hamiltonian in the form

$$H_\Omega = H - \sum_{\tau=N,P} \lambda_\tau \hat{N}_\tau - \hbar\Omega I_1 + H_{\rm int}. \quad (1)$$

Here, $H = H_0 + H_{\rm add}$, where $H_0 = \sum_i^A h_0(i)$ is a spherical Nilsson Hamiltonian with

$$h_0 = \frac{\mathbf{p}^2}{2m} + \frac{m}{2}\omega_0^2 r^2 - \hbar\omega_{00}[2\kappa \mathbf{l}\cdot\mathbf{s} + \kappa\mu(\mathbf{l}^2 - \langle \mathbf{l}^2\rangle_N)]. \quad (2)$$

Here, κ and μ are the Nilsson parameters [11], and $\omega_0 = \omega_0(\beta,\gamma)$ and $\hbar\omega_{00} = 41A^{-1/3}$ MeV are oscillator frequencies (β and γ are quadrupole deformation parameters defined below). In the cranking model with the standard Nilsson potential, the value of the moment of inertia is largely overestimated due to the presence of the velocity dependent $\mathbf{l}^2$ term. This shortcoming can be overcome by introducing the additional term $H_{\rm add} = \sum_i^A h_{\rm add}(i)$ with

$$h_{\rm add} = -(\boldsymbol{\nabla}_p V)\cdot m\boldsymbol{\Omega}\times\mathbf{r} = -\Omega m\left(x_2\frac{\partial}{\partial p_3} - x_3\frac{\partial}{\partial p_2}\right)V(\mathbf{r},\mathbf{p}) = \Omega m\omega_{00}\kappa\left[2\left(r^2 s_1 - x_1 \mathbf{r}\cdot\mathbf{s}\right) + \mu\left(2r^2 - \frac{\hbar}{m\omega_{00}}\left(N+\frac{3}{2}\right)\right)l_1\right]. \quad (3)$$

This term restores the local Galilean invariance of the Nilsson potential in the rotating frame (see [12] for details). As a result, the kinematical and dynamical moment of inertia calculated in the mean field approximation become much closer to the experimental values.

Since in ^{156}Dy the backbending occurs in the positive parity yrast band, it is enough to consider only the positive parity residual interaction. The interaction is taken in a separable form

$$H_{\rm int} = -\sum_\tau G_\tau P_\tau^+ P_\tau - \frac{1}{2}\kappa\left[\sum_{r,m} Q_m^{(r)2} + M^{(+)2}\right]. \quad (4)$$

Here, τ = neutron or proton particle number; $P^+ = \sum_k c_k^+ c_{\bar{k}}^+$; and c_k^+ and c_k are creation and annihilation single-particle operators, respectively. The index k labels a complete set of oscillator quantum numbers ($|k\rangle = |Nljm\rangle$) and the index $\bar{k}$ denotes the time-conjugated state. The index r indicates the signature quantum number ($r = \pm 1$) (see [9]). The quadrupole operators Q_m are defined by

$$\hat{Q}_m^{(r)} = \frac{i^{2+m+(r+3)/2}}{\sqrt{2(1+\delta_{m0})}}\left(\hat{Q}_{2m} + (-1)^{(r+3)/2}\hat{Q}_{2-m}\right), \quad m = 0,1,2. \quad (5)$$

The monopole interaction is defined by the positive signature operator $M^{(+)} = r^2 Y_0$. Single-particle matrix elements of any one-body Hermitian operator $F = \sum_{kl} f_{kl} c_k^+ c_l$ (P,Q,M) are determined by the signature, time-reversal, and Hermitian conjugation properties of the operator (cf. [9]). The choice of the constants G and κ will be discussed below.

Using the generalized Bogolyubov transformation for quasiparticles (for example, for the positive signature quasiparticle, we have $\alpha_i^+ = \sum_k \mathcal{U}_{ki} c_k^+ + \mathcal{V}_{\bar{k}i} c_{\bar{k}}$) and the variational principle (see details in [9]), we obtain the Hartree–Bogolyubov (HB) equations for the positive signature quasiparticle energies ε_i,

$$\begin{pmatrix} h(1) & \triangle \\ \triangle & h(2)\end{pmatrix}\begin{pmatrix}\mathcal{U}_i \\ \mathcal{V}_i\end{pmatrix} = \varepsilon_i \begin{pmatrix}\mathcal{U}_i \\ \mathcal{V}_i\end{pmatrix}. \quad (6)$$

It is sufficient to solve the HB equations only for the positive signature, since the negative signature eigenvalues and eigenvectors are obtained from the positive ones.

For the present discussion, we need to know only the structure of matrix elements $h(1)$ and Δ, which are the following:

$$(h(1))_{kl} = \delta_{kl}\varepsilon_{kl}^0 + \langle k|h_{\rm add}|l\rangle - \hbar\Omega\langle k|I_1|l\rangle - \kappa(\langle M\rangle\langle k|\hat{M}|l\rangle + \langle Q_0\rangle\langle k|\hat{Q}_0|l\rangle + \langle Q_2^{(+)}\rangle\langle k|\hat{Q}_2^{(+)}|l\rangle), \quad (7)$$

$$\Delta_{kl} = -\delta_{kl} G_\tau \langle P_\tau\rangle. \quad (8)$$

Here, ε_{kl}^0 are eigenstates of the spherical Nilsson Hamiltonian, and $\langle\ldots\rangle$ means the averaging over the HB vacuum state of the rotating system.

We define the quadrupole deformation β, γ using the parametrization

$$m\omega_0^2\beta\cos\gamma = \kappa\langle Q_0\rangle, \qquad (9)$$
$$m\omega_0^2\beta\sin\gamma = -\kappa\langle Q_2^{(+)}\rangle.$$

It results in the following definition of oscillator frequencies along the principal axes:

$$\omega_i^2 = \omega_0^2\left[1 - 2\beta\sqrt{\frac{5}{4\pi}}\cos\left(\gamma - \frac{2\pi}{3}i\right)\right], \qquad (10)$$
$$i = 1, 2, 3.$$

In addition, we use the volume conservation constraint $\omega_1\omega_2\omega_3 = \omega_{00}^3$. We recall that, in the limit of the harmonic oscillator, the use of the double stretched coordinate representation allows one to represent a three-dimensional oscillator determined by the frequencies [Eq. (10)] as a spherical-oscillator-type potential again, i.e., $x_i'' = (\omega_i/\omega_0)x_i \Rightarrow V_{\text{def.osc}}(\mathbf{r}'') = m\omega_0^2 r''^2/2$.

2.2. Collective Excitations

We introduce the following boson-like operators: $b_{k\bar{l}}^+ = \alpha_k^+\alpha_{\bar{l}}^+$, $b_{kl}^+ a = \alpha_k^+\alpha_l^+$, $b_{\bar{k}\bar{l}}^+ = \alpha_{\bar{k}}^+\alpha_{\bar{l}}^+$. These two-quasiparticle operators are treated in the quasiboson approximation (QBA) as elementary bosons; i.e., all commutators between them are approximated by their expectation values with the uncorrelated HB vacuum. The first equality introduces the positive signature boson, while the other two determine the negative signature ones. The corresponding commutation relations can be found in [9]. The positive and negative boson spaces are not mixed, since the corresponding operators commute. In this approximation, any single-particle operator F can be expressed as $F = \langle F\rangle + F^{(1)} + F^{(2)}$, where the second and third terms are linear and bilinear order terms in the boson expansion. We recall that, in the QBA, one includes all second order terms in the boson Hamiltonian such that $(F - \langle F\rangle)^2 = F^{(1)}F^{(1)}$.

Although in the double stretched representation the residual interaction formally has the same form as in (4), its structure is different. For example, the operators Q_0'' and $Q_2''^{(+)}$ expressed via nonstretched coordinates have the following forms:

$$Q_0'' = \left(1 - \frac{1}{2}\sqrt{\frac{5}{\pi}}\beta\cos\gamma\right)Q_0 \qquad (11)$$
$$- \frac{5}{4\pi}\beta\cos\gamma M^{(+)} + \frac{1}{2}\sqrt{\frac{5}{\pi}}\beta\sin\gamma Q_2^{(+)},$$
$$Q_2''^{(+)} = \left(1 + \frac{1}{2}\sqrt{\frac{5}{\pi}}\beta\cos\gamma\right)Q_2^{(+)}$$
$$- \frac{5}{4\pi}\beta\cos\gamma M^{(+)} + \frac{1}{2}\sqrt{\frac{5}{\pi}}\beta\sin\gamma Q_0.$$

The RPA Hamiltonian is diagonalized by solving the equations of motion

$$[\hat{H}_\Omega, \hat{P}_\lambda]_{\text{RPA}} = i\hbar\omega_\nu^2\hat{X}_\lambda, \qquad (12)$$
$$[\hat{H}_\Omega, \hat{X}_\lambda]_{\text{RPA}} = -i\hbar\hat{P}_\lambda, \quad [\hat{X}_\Omega, \hat{P}_\lambda]_{\text{RPA}} = i\hbar\delta_{\lambda\lambda'}$$

for each signature separately. Here, $\hat{X}_\lambda$ and $\hat{P}_\lambda$ are generalized coordinates and linear momenta of a given intrinsic state with the energy $\hbar\omega_\lambda$. The equations of motion (12) lead to the determinant of the secular equations $\mathcal{F}(\omega_\lambda) = \det(\mathbf{R} - 1/2\kappa)$, which is the fifth and the second order for the positive and negative signature, respectively (cf. [9]).

The zeros of the function $\mathcal{F}(\omega_\lambda) = 0$ yield the RPA eigenfrequencies ω_λ. Since the mean field violates the rotational invariance and particle number conservation law, among the RPA eigenfrequencies, there exist few spurious solutions. Introducing the operator $\Gamma^+ = (\hat{I}_2^{(1)} - i\hat{I}_3^{(1)})/\sqrt{2\langle I_1\rangle}$, we can separate the "spurious" rotational mode $\omega_\lambda = \Omega$ from the vibrational ones of the negative signature part of the full Hamiltonian,

$$H(r = -1) \qquad (13)$$
$$= 1/2\sum_{\lambda(\omega_\lambda\neq 0,\Omega)}(\hat{P}_\lambda^2 + \hbar^2\omega_\lambda^2\hat{X}_\lambda^2) + \hbar\Omega(\Gamma^+\Gamma + 1/2).$$

The other solutions with zero frequency are associated with the rotation around the first axis and the particle number conservation law, since

$$[\hat{H}, \hat{I}_1] = [\hat{H}, \hat{N}_\tau] = 0, \quad \tau = n, p. \qquad (14)$$

The first equation allows one to determine the Thouless–Valatin moment of inertia, while the second one gives the nucleus mass [13, 14]. As a result, for the positive signature RPA solutions, we have

$$H(r = +1) \qquad (15)$$
$$= \frac{1}{2}\sum_{\lambda(\omega_\lambda\neq 0)}\left(\hat{P}_\nu^2 + \hbar^2\omega_\lambda^2\hat{X}_\lambda^2\right)$$
$$+ \frac{1}{2}g_{I_1}\hat{I}_1^{(1)^2} + \frac{1}{2}\sum_\tau g_{N_\tau}\hat{N}_\tau^{(1)^2},$$

where $1/g_{N_\tau}$ and $1/g_{I_1}$ are the mass parameters for neutrons or protons and the Thouless–Valatin moment of inertia, respectively.

3. NUMERICAL RESULTS

3.1. Mean Field Solutions

For a three-dimensional harmonic oscillator, the variational principle with the volume conservation

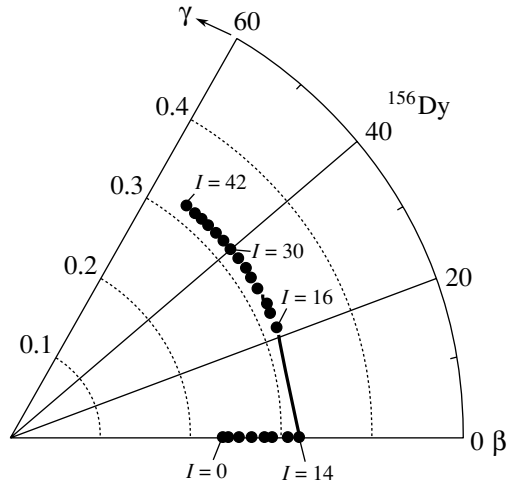

Fig. 1. The experimental dependence of quadrupole deformation parameters β and γ on the angular momentum I. These values were taken from [20], where they were determined from $E2$ transition probabilities along the yrast line.

condition leads to the self-consistent condition $\omega_1^2\langle x_1^2\rangle = \omega_2^2\langle x_2^2\rangle = \omega_3^2\langle x_3^2\rangle$ [15]. This condition fixes the self-consistent constant $\kappa_2 = (4\pi/5)(m\omega_0^2/\langle r''^2\rangle)$ for a residual interaction (quadrupole and monopole terms) in the oscillator potential [16].

At the minimum of the mean field, the expectation values of the operators Q_0 and $Q_2^{(+)}$ expressed in the double stretched coordinates [Eqs. (11)] are zeros,

$$\langle Q_0''\rangle = \langle Q_2''^{(+)}\rangle = 0. \tag{16}$$

We propose to use Eqs. (16) as the self-consistent HF conditions for equilibrium deformations β and γ in the yrast state $|\ \rangle$. Since the residual interaction consists of such a type of operators, with these conditions, we will fulfill the requirement that the residual interaction does not change the equilibrium deformation. The spin–orbit and l^2 terms would break these conditions; however, the violation is very weak.

In order to avoid solving highly nonlinear mean field equations, we use the experimental values of deformation parameters β and γ (see Fig. 1). These values are the input parameters for Eqs. (9), (10) and the HB equations (6). For the pairing field $\Delta_{kl} = \delta_{kl}\Delta_\tau(\Omega)$ in Eq. (6), we assume the phenomenological dependence of the pairing gap Δ_τ ($\tau = n, p$) on the rotational frequency Ω introduced in [17],

$$\Delta_\tau(\Omega) = \begin{cases} \Delta_\tau(0)\left[1 - \frac{1}{2}\left(\frac{\Omega}{\Omega_c}\right)^2\right] & \text{for } \Omega < \Omega_c, \\ \Delta_\tau(0)\frac{1}{2}\left(\frac{\Omega}{\Omega_c}\right)^2 & \text{for } \Omega > \Omega_c. \end{cases} \tag{17}$$

Here, $\Omega_c = 0.32$ MeV is a rotational frequency where the first band crossing (which is approximately the same for protons and neutrons) occurs for ^{156}Dy. The values of pairing gaps $\Delta_n(0) = 0.857$ MeV, $\Delta_p(0) = 0.879$ MeV (for ^{156}Dy) are obtained from the odd–even mass difference (see also [18]). The Nilsson parameters κ and μ are taken from systematic analysis for all deformed nuclei [11]. The calculations have been done for all shells up to $N = 8$. This configuration space exhausted 97% of the energy-weighted sum rule for quadrupole transitions.

To check the self-consistency of our mean field solutions, we calculate Eqs. (16) when all terms are included in the HB equations (6). In fact, the double stretched quadrupole moments are approximately zero for all values of the rotational frequency. The variation of the deformation parameters β and γ around the experimental (equilibrium) values results in a strong deviation of the double stretched quadrupole moments from zero values. We found also that the experimental values of β and γ correspond to the minimum of the total energy, but this minimum is very shallow for higher rotational frequencies.

3.2. Low-Lying Excited States

In order to analyze the low-lying excited states, we construct the Routhian function for each rotational band ($\nu =$ yrast, $\beta, \gamma, \ldots$),

$$R_\nu(\Omega) = E_\nu(\Omega) - \Omega I_1(\Omega). \tag{18}$$

Next, we define the experimental excitation energy in the rotating frame [19],

$$\omega_\nu(\Omega) = R_\nu(\Omega) - R_{\rm yr}(\Omega). \tag{19}$$

The experimental excitation energy [Eq. (19)] can be directly compared with the corresponding solutions $\hbar\omega_\lambda$ of the RPA secular equation. Experimental Routhianes R_ν have been obtained in [20] using experimental data from [21].

It is important to hold self-consistency in the RPA as well as in the mean field. In the pure oscillator, the self-consistent constant κ_2 warrants the fulfillment all conservation laws in the RPA for rotating nuclei [7]. We propose the following recipe to recover lost self-consistency for realistic calculations: we define our constants from the requirement of the fulfillment of the conservation laws Eqs. (14) and the separation of the rotational mode in the RPA. In other words, we force the separation between the spurious and the physical solutions. Otherwise, the physical solutions would be mixed with the spurious one.

We compare the positive signature experimental and calculated lowest excitation energies in Fig. 2. The lowest excited rotational bands are γ and β

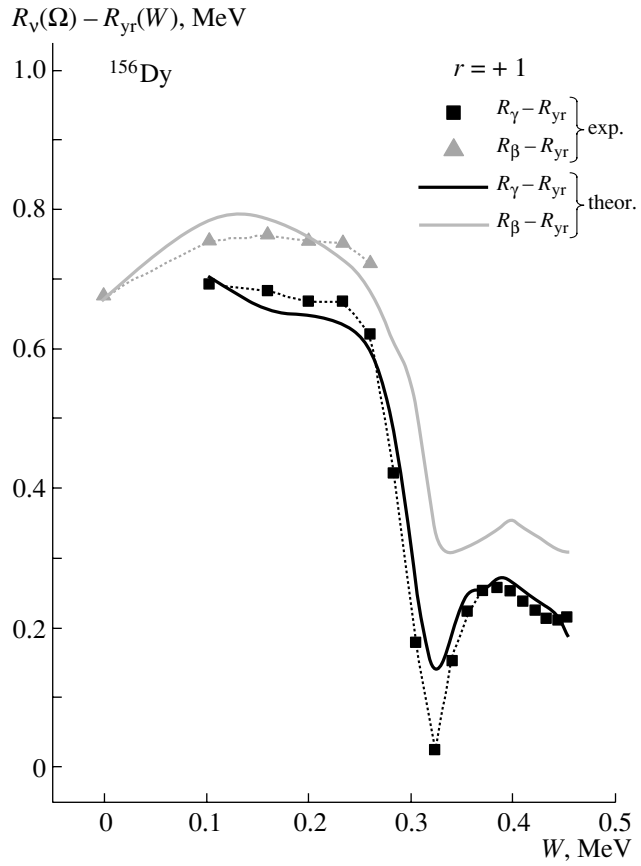

Fig. 2. The comparison of the lowest two experimental and calculated Routhians of positive signature in the dependence on rotational frequency Ω. The low-spin part of the lowest rotational band can be identified with the γ band and the second lowest band starts as β band. Experimental Routhians were obtained in [20] using the data from [21].

bands. The results demonstrate excellent agreement between theory and experiment. The lowest γ-vibrational frequency calculated for the positive signature states (even spins) becomes zero at $\Omega \sim 0.32$ MeV. Near this rotational frequency, backbending occurs in the considered case. The negative signature states describe quite well the γ-vibrational states with odd spins at low rotational frequencies. At higher rotational frequencies, these excitations correspond to wobbling excitations of the three axially deformed systems.

4. SUMMARY

Although the cranking + RPA approach has been well known for a long time, a reliable practical scheme for the analysis of vibrational states in rotating nuclei is still missing. In this paper, we further developed the effective approach [9] to describe numerically, at the same level of accuracy, both the yrast properties and the low-lying excitations. The approach is based on the cranking Nilsson model + monopole pairing forces to study mean field properties and the RPA to analyze the vibrational states. The key point of our approach is to hold the self-consistency at the mean field level and to restore mean field broken symmetries at the RPA. To this aim, we proposed the self-consistency conditions that should be fulfilled at the mean field level and in the RPA.

We solve the RPA equations of motion and obtain remarkable agreement with available experimental data for ^{156}Dy for low-lying excitations. We found that the disappearance of the positive signature γ-vibrational excitations in the rotating frame leads to backbending in this nucleus. It is a *novel* mechanism, in contrast to the standard explanation of the backbending phenomenon as a result of two-quasiparticle rotational alignment. The analysis of the backbending, based on this mechanism, in other nuclei is in progress. At low-rotational frequencies, we describe the low-lying states that belong to the γ band with odd spins as the negative signature γ-vibrational RPA excitations. We predict that, with the increase in the rotational frequency, these states can be associated with the wobbling excitations.

ACKNOWLEDGMENTS

This work was partly supported by the Czech grant agency under contract no. 202/02/0939 and by grant no. BFM2002-03241 from DGI (Spain). R.G.N. gratefully acknowledges support from the Ramón y Cajal programme (Spain).

REFERENCES

1. Z. Szymanski, *Fast Nuclear Rotation* (Clarendon, Oxford, 1980).
2. K. Enami, K. Tanabe, and N. Yoshinaga, Phys. Rev. C **59**, 135 (1999).
3. E. Carote, J. L. Egido, and L. M. Robledo, Phys. Rev. Lett. **80**, 4398 (1998).
4. P. Bonche, P. H. Heenen, and H. C. Flocard, Nucl. Phys. A **467**, 115 (1987).
5. E. Caurier *et al.*, Phys. Rev. Lett. **75**, 2466 (1995); G. Martinez-Pinedo *et al.*, Phys. Rev. C **54**, R2150 (1996).
6. P. Ring and P. Schuck, *The Nuclear Many-Body Problem* (Springer, New York, 1980).
7. R. G. Nazmitdinov, D. Almehed, and F. Dönau, Phys. Rev. C **65**, 041307(R) (2002).
8. D. Almehed, F. Dönau, and R. G. Nazmitdinov, J. Phys. G **29**, 2193 (2003).
9. J. Kvasil and R. G. Nazmitdinov, Sov. J. Part. Nucl. **17**, 265 (1986).
10. Y. R. Shimizu *et al.*, Rev. Mod. Phys. **61**, 131 (1989).

11. S. G. Nilsson and I. Ragnarsson, *Shapes and Shells in Nuclear Structure* (Cambridge Univ. Press, Cambridge, 1995).
12. T. Nakatsukasa *et al.*, Phys. Rev. C **53**, 2213 (1996).
13. D. J. Thouless and J. G. Valatin, Nucl. Phys. **31**, 211 (1962).
14. E. R. Marshalek and J. Weneser, Ann. Phys. (N.Y.) **53**, 569 (1969).
15. T. Troudet and R. Arvieu, Ann. Phys. (N.Y.) **134**, 1 (1981); E. R. Marshalek and R. G. Nazmitdinov, Phys. Lett. B **300**, 199 (1993).
16. H. Sakamoto and T. Kishimoto, Nucl. Phys. A **501**, 205 (1989).
17. R. Wyss, W. Satula, W. Nazarewicz, and A. Johnson, Nucl. Phys. A **511**, 324 (1990).
18. http://t2.lanl.gov/data/map.html.
19. R. G. Nazmitdinov, Sov. J. Nucl. Phys. **46**, 412 (1987).
20. R. Ch. Safarov and A. S. Sitdikov, Izv. Ross. Akad. Nauk, Ser. Fiz. **63**, 162 (1999).
21. http://www.nndc.bnl.gov.

Physics of Atomic Nuclei, Vol. 67, No. 9, 2004, pp. 1656–1663. From Yadernaya Fizika, Vol. 67, No. 9, 2004, pp. 1683–1690.

Effects of Dirac Sea on Giant Resonance States*

H. Kurasawa[1] and T. Suzuki[2]

Received January 21, 2004

Abstract—There are two approximations in relativistic models which keep the continuity equation of the baryon current without renormalization of the divergence. One is the no-free-term approximation (NFA) which neglects the divergent terms, but keeps the Pauli blocking terms coming from nucleon–antinucleon excitations in the RPA correlation functions. The other is the no-sea approximation (NSA) where antiparticle states are assumed to be empty with negative energies. It is shown that both approximations formally satisfy the Ikeda sum rule and the RPA theorem for the β_- and β_+ transition strengths also, but that the NFA requires negative strengths in the positive excitation energy region, while the NSA requires positive strengths in the negative excitation energy region, as a price of neglecting the renormalization of the divergence. © *2004 MAIK "Nauka/Interperiodica".*

1. INTRODUCTION

Nuclear ground states are explained phenomenologically very well by the relativistic mean field approximation, where antinucleon degrees of freedom are neglected [1]. For description of excited states in RPA, however, the nucleon space is proved not to be enough. In the nucleon space only, the continuity equation of the baryon current is violated [2–5]. Moreover, the Landau–Migdal (LM) parameters, F_0 and F_1, are not described correctly without antinucleon degrees of freedom [4]. This means that the center-of-mass motions, giant monopole states, nuclear magnetic moments, etc., which are expressed with these parameters [6], are not described correctly in the nucleon space only [7, 8].

In principle, the renormalization of the divergence is necessary to take into account the antinucleon excitations. To avoid the divergence problem without renormalization, two approximations are proposed. One is to keep the Pauli blocking terms coming from nucleon–antinucleon excitations in the RPA correlation function, while all divergent terms are simply neglected [2, 3]. We call this approximation the no-free-term approximation (NFA). The other is called the no-sea approximation (NSA) which assumes that the Dirac sea is empty and antinucleon states are particle states with negative energies [7, 8]. It has been shown that these two approximations keep the continuity equation [2–5, 7] and provide LM parameters which are consistent with the corresponding mean field approximation [4].

The purpose of the present paper is to show first that the Gamow–Teller (GT) sum rule, which is called Ikeda sum rule [9], also requires antinucleon degrees of freedom and is formally satisfied in the above two approximations. Second, the two approximations will be shown to satisfy the RPA theorem for the energy-weighted sum of the GT strengths. This theorem by Thouless [10] is known in the case of no-charge-exchange excitations, but will be shown to hold also in charge-exchange excitations with respect to the sum of the β_- and β_+ transition strengths. Finally, we will show, however, that there is a serious difficulty in the two approximations. The Ikeda sum rule and the RPA theorem are satisfied owing to the contribution from unphysical strengths which are negative in the NFA, and are positive, but distributed over the negative excitation energy region, in the NSA. Consequently, the total energy-weighted strength becomes negative in both approximations. This fact implies that renormalization of the divergence is not avoidable in relativistic models, even if they are phenomenological ones. We will show these results in an analytic way by calculating the GT strengths in nuclear matter.

In the following section, we will present the relativistic mean field correlation function for the GT excitations. Using it, we will discuss the Ikeda sum rule and RPA theorem in Section 3. The final section will be devoted to a brief discussion and conclusions.

*This article was submitted by the authors in English.

[1]Department of Physics, Faculty of Science, Chiba University, Chiba, Japan.

[2]Department of Applied Physics, Fukui University, Fukui, Japan, and RIKEN, Wako-shi, Japan; e-mail: suzuki@quantum.apphy.fukui-u.ac.jp

2. THE MEAN FIELD CORRELATION FUNCTION

We assume throughout the present paper that Dirac particles are bound in the Lorentz scalar and vector potentials, although the Lorentz vector potential does not appear explicitly in the present discussion. The Lorentz scalar potential is included in the nucleon effective mass M^*. Then, for the β_- excitation at $\mathbf{q}=0$ in $N>Z$ nuclei, the mean field correlation function for GT excitations in the particle–hole space is described as [5]

$$\Pi_{ph} = -4\int d^3p \frac{M^{*2}+p_y^2}{E_{\mathbf{p}}^2}\frac{\theta_{\mathbf{p}}^{(n)}-\theta_{\mathbf{p}}^{(p)}}{q_0+i\varepsilon}. \quad (1)$$

In the above equation, we have defined the abbreviations $E_{\mathbf{p}}=\sqrt{M^{*2}+\mathbf{p}^2}$ and $\theta_{\mathbf{p}}^{(i)}=\theta(k_i-|\mathbf{p}|)\,(i=p,n)$, k_p and k_n being the proton and neutron Fermi momenta, respectively. In addition to the particle–hole excitations, transitions from the Dirac sea to the Fermi sea are taken into account in the NFA. These transitions are forbidden, but are required for the RPA correlation function to satisfy the continuity equation of the baryon current. The correlation function for these excitations is described as [5]

$$\Pi_{\text{Pauli}} = 4\int d^3p \frac{\mathbf{p}^2-p_y^2}{E_{\mathbf{p}}^2} \quad (2)$$
$$\times\left(\frac{\theta_{\mathbf{p}}^{(p)}}{q_0-2E_{\mathbf{p}}+i\varepsilon}-\frac{\theta_{\mathbf{p}}^{(n)}}{q_0+2E_{\mathbf{p}}-i\varepsilon}\right).$$

Since the above function is density-dependent, there is no divergence problem.

In the NSA, the Dirac sea is considered to be empty and transitions from the Fermi sea to the antiparticle states with negative energies are taken into account. In this way, the NSA can avoid divergence and keep the continuity equation. For the β_- transitions, the correlation function for those transitions is given by changing the sign of the imaginary part of Eq. (2) as [5]

$$\Pi_{\text{no-sea}} = -4\int d^3p \frac{\mathbf{p}^2-p_y^2}{E_{\mathbf{p}}^2} \quad (3)$$
$$\times\left(\frac{\theta_{\mathbf{p}}^{(n)}}{q_0+2E_{\mathbf{p}}+i\varepsilon}-\frac{\theta_{\mathbf{p}}^{(p)}}{q_0-2E_{\mathbf{p}}-i\varepsilon}\right).$$

The correlation functions for the β_+ transitions are obtained by changing the sign of q_0 in Eqs. (1)–(3). In the case of β_- transitions, there are no backward amplitudes for particle–hole pairs, while, in the β_+ case, there are no forward amplitudes, but instead backward ones.

The response function $R(q_0)$ is defined with the above correlation functions as [3]

$$R(q_0)=\frac{1}{\pi}\frac{V}{(2\pi)^3}\text{Im}\Pi(q_0),$$

V standing for the volume of the system $(3\pi^2/2k_{\text{F}}^3)A$. In the NFA, $\Pi(q_0)$ is provided by the sum of Eqs. (1) and (2), while the one in the NSA is given by Eqs. (1) and (3). The total GT strength in the mean field approximation is obtained by integrating $R(q_0)$ over q_0. The contribution from the particle–hole states to the strength of the β_- transitions is

$$S_{ph}^{(-)} = \frac{1}{\pi}\frac{V}{(2\pi)^3}\lim_{\eta\to+0}\int_{-\eta}^{\infty}dq_0\text{Im}\Pi_{ph}(q_0) \quad (4)$$
$$= \frac{4V}{(2\pi)^3}\int d^3p\left(\theta_{\mathbf{p}}^{(n)}-\theta_{\mathbf{p}}^{(p)}\right)\frac{M^{*2}+p_y^2}{E_{\mathbf{p}}^2},$$

where the variable η is introduced, since $\text{Im}\Pi_{ph}(q_0)$ contains $\delta(q_0)$. For nuclei with $(k_n-k_p)/k_{\text{F}}\ll 1$, the above equation is written approximately as [5, 11, 12]

$$S_{ph}^{(-)} \approx \left(1-\frac{2}{3}v_{\text{F}}^2\right)2(N-Z), \quad (5)$$

where v_{F} denotes the Fermi velocity $k_{\text{F}}/E_{\text{F}}$.

In the present definition of the spin–isospin operators, the well-known Ikeda sum rule is described as[3)]

$$\langle|Q_+Q_-|\rangle-\langle|Q_-Q_+|\rangle = 2(N-Z) \quad (6)$$

with $Q_\pm=\sum_i^A\tau_{\pm i}\sigma_{yi}$. This sum rule is nothing but a result of the commutation relation: $[\tau_+\sigma_y,\tau_-\sigma_y]=2\tau_z$. Comparing Eq. (5) with the above equation, one can see that the GT strength in the nucleon sector of the relativistic model is quenched by a factor $\left(1-\frac{2}{3}v_{\text{F}}^2\right)$. This value is about 0.88 for $v_{\text{F}}=0.43$ from $M^*=0.6M$ and $k_{\text{F}}=1.36$ fm^{-1}. As shown below, the quenched amount is taken by the nucleon–antinucleon pair excitations. In the present model, there is no GT strength of the β_+ transitions in the particle–hole sector.

The total GT strength of the proton–antineutron (β_-) excitations in the NFA is given by Eq. (2) as

$$S_{\text{Pauli}}^{(-)} = -\frac{4V}{(2\pi)^3}\int d^3p\,\theta_{\mathbf{p}}^{(p)}\frac{\mathbf{p}^2-p_y^2}{E_{\mathbf{p}}^2}, \quad (7)$$

[3)] In most of the literature, the Ikeda sum rule value is quoted to be $3(N-Z)$, since the definition of $Q_\pm$ is different from the present one by a factor.

which is negative. One of the neutron–antiproton (β_+) excitations is obtained in the same way by changing the sign of q_0 in Eq. (2),

$$S^{(+)}_{\rm Pauli} = -\frac{4V}{(2\pi)^3}\int d^3p\theta^{(n)}_{\mathbf{p}}\frac{\mathbf{p}^2-p_y^2}{E^2_{\mathbf{p}}}, \qquad (8)$$

which is also negative.

From Eqs. (4), (7), and (8), we obtain the GT sum value in the mean field approximation of the NFA,

$$S^{(-)}_{ph} + S^{(-)}_{\rm Pauli} - S^{(+)}_{\rm Pauli} = 2(N-Z), \qquad (9)$$

which is just the Ikeda sum rule. Thus, the quenched amount of GT strength in the nucleon sector is taken by the nucleon–antinucleon pairs, and thus, the Pauli blocking terms are necessary for the NFA to satisfy the sum rule, although each strength of the proton–antineutron (β_-) and neutron–antiproton (β_+) excitations is negative.

In the NSA, the GT strength of the particle–hole pairs is the same as in the NFA, but the strengths from the antinucleon degrees of freedom are different. For the β_- transitions, the integration of Eq. (3) over negative excitation energy gives

$$S^{(-)}_{\text{no-sea}} = \frac{4V}{(2\pi)^3}\int d^3p\theta^{(n)}_{\mathbf{p}}\frac{\mathbf{p}^2-p_y^2}{E^2_{\mathbf{p}}},$$

which is equal to $-S^{(+)}_{\rm Pauli}$ as seen in Eq. (8). In the same way, we obtain $S^{(+)}_{\text{no-sea}} = -S^{(-)}_{\rm Pauli}$ for the total strength of the β_+ antinucleon–hole excitations in the NSA. In the NSA, each strength is positive, but the energy-weighted sum becomes negative. Although the strengths of the β_- and β_+ transitions in the NSA are different from those in the NFA, their difference satisfies the sum rule, as in Eq. (9).

Thus, the NFA and NSA formally satisfy the Ikeda sum rule, but with help of the unphysical GT strengths coming from antinucleon degrees of freedom which are taken into account for the continuity equation of the baryon current.

3. THE GT SUM RULE IN RELATIVISTIC RPA

In nonrelativistic models, the RPA correlations in the GT states are assumed to be induced by LM parameter g' [13, 14]. In the relativistic model, we also introduce g', which is provided in the nuclear Lagrangian as a contact term with the pseudovector coupling:

$$\mathcal{L} = \frac{g_5}{2}\bar\psi\Gamma^\mu_i\psi\bar\psi\Gamma_{\mu i}\psi, \quad \Gamma^\mu_i = \gamma_5\gamma^\mu\tau_i, \qquad (10)$$

$$g_5 = \left(\frac{f_\pi}{m_\pi}\right)^2 g'.$$

For the above Lagrangian, the RPA correlation function $\Pi_{\rm RPA}$ is written in terms of the mean field one Π as [5, 11, 12]

$$\Pi_{\rm RPA}(q_0) = \frac{\Pi(q_0)}{1+\chi_5\Pi(q_0)}, \quad \chi_5 = \frac{g_5}{(2\pi)^3}.$$

Then the RPA response functions for the β_- and β_+ transitions are given, respectively, by

$$R^{(\mp)}_{\rm RPA}(q_0) = \frac{1}{\pi}\frac{V}{(2\pi)^3}{\rm Im}\Pi_{\rm RPA}(\pm q_0).$$

3.1. The Non-Energy-Weighted GT Sum Rule

In NFA, the non-energy-weighted GT sum value in the RPA is given by [5]

$$S^{(0)}_{\rm RPA} \qquad (11)$$
$$= \lim_{\eta\to+0}\left\{\int_{-\eta}^{\infty} dq_0 R^{(-)}_{\rm RPA}(q_0) - \int_{\eta}^{\infty} dq_0 R^{(+)}_{\rm RPA}(q_0)\right\}.$$

In order to calculate the right-hand side, we expand $\Pi_{\rm RPA}$ in terms of χ_5,

$$S^{(0)}_{\rm RPA} = \frac{1}{\pi}\frac{V}{(2\pi)^3}\sum_{n=0}^{\infty}(-\chi_5)^n\lim_{\eta\to+0} I^{(0)}_n, \qquad (12)$$

where $I^{(0)}_n$ is defined as

$$I^{(0)}_n = \int_{-\eta}^{\infty} dq_0 {\rm Im}(\Pi(q_0))^{n+1} \qquad (13)$$
$$- \int_{\eta}^{\infty} dq_0 {\rm Im}(\Pi(-q_0))^{n+1}.$$

Due to the fact that $\Pi(\pm q_0)$ has no pole in the first quadrant of the complex plane, and the relationship $\Pi^*(-iq_0-\eta) = \Pi(iq_0-\eta)$, I_n can be expressed as

$$I^{(0)}_n = -{\rm Im}\int_C dq_0\left[(\Pi(q_0))^{n+1} - (\Pi(-q_0))^{n+1}\right], \qquad (14)$$

where C indicates the contour on $q_0 = Re^{i\theta}$ ($0 \le \theta \le \pi/2$). When $|q_0| \to \infty$, $\Pi(q_0)$ in the NFA behaves as

$$\Pi(q_0) = -\frac{2(2\pi)^3}{q_0}\frac{N-Z}{V}. \qquad (15)$$

Hence, the integration on the contour C gives

$$\int_C dq_0\Big(\Pi(\pm q_0)\Big)^{n+1} \qquad (16)$$

$$= \frac{i}{R^n}\left(\mp 2(2\pi)^3\frac{N-Z}{V}\right)^{n+1}\int_0^{\pi/2} d\theta e^{-in\theta} \to 0$$
$$(R\to\infty, n\geq 1).$$

From Eqs. (14) and (16), we finally obtain

$$I_n^{(0)} = 0 \quad (n\geq 1). \tag{17}$$

Thus, the GT sum value of the RPA in the NFA is equal to the one in the mean field approximation Eq. (9) and satisfies the Ikeda sum rule,

$$S_{\rm RPA} = \frac{1}{\pi}\frac{V}{(2\pi)^3}\lim_{\eta\to+0} I_0^{(1)} = 2(N-Z). \tag{18}$$

We can calculate in the same way the GT sum value of the RPA in the NSA, but performing the integration over negative energy,

$$S_{\rm RPA}^{(0)}$$
$$= \lim_{\eta\to+0}\left\{\int_{-\infty}^{\eta} dq_0 R_{\rm RPA}^{(-)}(q_0) - \int_{-\infty}^{-\eta} dq_0 R_{\rm RPA}^{(+)}(q_0)\right\}.$$

In this case, a closed contour with no pole is taken in the second quadrant. In this way, we can prove that the NSA also satisfies the Ikeda sum rule.

We have shown that the difference between total GT strengths for the β_- and β_+ transitions in the RPA is equal to the one in the mean field and both the NFA and the NSA satisfy the Ikeda sum rule. Of course, the distribution of the GT strengths is different from that in the mean field and depends on the value of the LM parameter g'. We will show below, however, unphysical GT strengths remain outside of the giant resonance region, as in the mean field.

In the RPA, the excitation energy of the giant GT resonance state is obtained from the dimesic function. For $(N-Z)/A \ll 1$, it is given by [11, 12]

$$\omega_0 \approx \frac{1-2v_{\rm F}^2/3}{1+2g_5\kappa/(3\pi^2)} g_5 \frac{8k_{\rm F}^3}{3\pi^2}\frac{N-Z}{2A}, \tag{19}$$

where κ comes from the coupling of the particle–hole states with the nucleon–antinucleon ones,

$$\kappa = -\left(P_{\bar N}(k_n,q_0) + P_{\bar N}(k_p,q_0)\right),$$
$$P_{\bar N}(k_i,q_0) = \frac{3}{4\pi}\int_0^{k_{\rm F}}\frac{d^3p}{E_{\mathbf p}^2}\frac{\mathbf{p}^2-p_y^2}{2E_{\mathbf p}+q_0}.$$

For $q_0 \ll M^*$, the above function $P_{\bar N}(k_i,q_0)$ becomes

$$P_{\bar N}(k_i,q_0) \approx P(k_{\rm F},0) \tag{20}$$
$$= E_{\rm F}^2\left(\frac{3}{2}v_{\rm F} - v_{\rm F}^3 - \frac{3}{4}\left(1-v_{\rm F}^2\right)\log\frac{1+v_{\rm F}}{1-v_{\rm F}}\right)$$
$$= k_{\rm F}^2\frac{v_{\rm F}^3}{5}\left(1+\frac{3}{7}v_{\rm F}^2+\ldots\right).$$

This equation shows that, for $v_{\rm F}=0.43$, the effect of the Pauli blocking term on the excitation energy is less than 0.5% and is negligible. When we neglect κ and $v_{\rm F}^2$, Eq. (19) is reduced to the nonrelativistic expression for the excitation energy of the giant GT resonance state obtained before [14].

The strength of the giant GT resonance state is given by the residue of the response function at $q_0 = \omega_0$,

$$S_{\rm GT} \approx \frac{1-2v_{\rm F}^2/3}{\left(1+2g_5\kappa/(3\pi^2)\right)^2}\cdot 2(N-Z). \tag{21}$$

Since the κ-dependent term from the Pauli blocking terms is negligible, the above equation shows that the GT state exhausts the sum value of the GT strengths in the nucleon space of the mean field.

The rest of the GT strengths in the NFA are distributed over the excitation energy region $q_0 \geq 2M^*$. The total strength of the β_- transitions in this region is given by

$$S_{\rm NFA}^{(-)} = \int_{2M^*} dq_0 R_{\rm RPA}(q_0) = \frac{V}{8\pi^4} \tag{22}$$
$$\times\int_{2M^*}^{2E_{{\rm F}p}} dq_0 \frac{I_{\rm Pauli}(k_p,q_0)}{(1+\chi_5\Pi_r(q_0))^2 + (\chi_5 I_{\rm Pauli}(k_p,q_0))^2},$$

while that of the β_+ transition is given by

$$S_{\rm NFA}^{(+)} = \int_{2M^*} dq_0 R_{\rm RPA}(-q_0) = \frac{V}{8\pi^4} \tag{23}$$
$$\times\int_{2M^*}^{2E_{{\rm F}n}} dq_0 \frac{I_{\rm Pauli}(k_n,q_0)}{(1+\chi_5\Pi_r(-q_0))^2 + (\chi_5 I_{\rm Pauli}(k_n,q_0))^2},$$

where $\Pi_r(q_0)$ stands for the real part of the RPA correlation function and $I_{\rm Pauli}(k_i,q_0)$ stems from the imaginary part,

$$I_{\rm Pauli}(k_i,q_0) \tag{24}$$
$$= -4\pi\int_0^{k_i} d^3p \frac{\mathbf{p}^2-p_y^2}{E_{\mathbf p}^2}\delta(q_0-2E_{\mathbf p})$$
$$= \begin{cases} -\dfrac{4\pi^2}{3}\dfrac{\left(q_0^2-4M^{*2}\right)^{3/2}}{q_0}, & 2M^* < q_0 < 2E_{{\rm F}i}, \\ 0, \quad \text{otherwise}, \end{cases}$$

with $E_{{\rm F}i} = \sqrt{M^{*2}+k_i^2}$. Thus, both total GT strengths in this region are negative, as seen from

the sign of $I_{\rm Pauli}(k_i, q_0)$. With help of the unphysical strengths, the RPA in the NFA satisfies the Ikeda sum rule.

The distribution of GT strengths in the NSA are also calculated in the same way as in the NFA. On the one hand, since the real part of the RPA correlation function is the same in the two approximations, the excitation energy and strength of the giant GT resonance state are predicted as in the NFA. On the other hand, the strengths of the region $|q_0| \geq 2M^*$ in the NSA are obtained by performing the integration of the response functions over negative energy, as we did before. The results are expressed in terms of those in the NFA as

$$S^{(-)}_{\rm NSA} = -S^{(+)}_{\rm NFA}, \quad S^{(+)}_{\rm NSA} = -S^{(-)}_{\rm NFA}. \qquad (25)$$

In this case, each total strength of the β_- and β_+ transitions is positive, but distributed over the negative energy region.

As a reference, in the figure, we show the response functions of the NFA in the high-excitation-energy region $|q_0| \geq 2M^*$. They are shown in units of nuclear volume V as a function of the excitation energy. The solid and dashed curves show the ones for the β_- and β_+ transitions, respectively. The values of parameters used here are shown in the figure. In this case, the excitation energy and strength of the giant GT resonance state are predicted to be 11.9 MeV and 89% of the Ikeda sum rule value, respectively, while the absolute value of the total strength for the β_- transition in the high-excitation-energy region is 11% of the sum rule value. This means that the sum of the energy-weighted β_- strength in the giant resonance and the high-excitation-energy region becomes negative. This is also true in the NSA.

3.2. The Energy-Weighted GT Sum Rule

In no-charge-exchange excitations, there is a famous theorem on the energy-weighted sum value of the excitation strengths in the RPA by Thouless [10]. According to the RPA theorem, the sum value is equal to the expectation value of the double commutator of the nuclear Hamiltonian with the excitation operator. Here, the expectation value is calculated by the ground state in the Hartree–Fock approximation. In this subsection, we will show that the same theorem holds for charge-exchange excitations with respect to the sum value of the β_- and β_+ transition strengths in the present model, although negative energy-weighted strengths appear in both the NFA and the NSA.

In the case of the NFA, the energy-weighted GT sum value is given by

$$S^{(1)}_{\rm RPA} = \frac{1}{\pi}\frac{V}{(2\pi)^3}\lim_{\eta\to 0}\left(\int_{-\eta}^{\infty} dq_0 q_0 {\rm Im}\Pi_{\rm RPA}(q_0) + \int_{\eta}^{\infty} dq_0 q_0 {\rm Im}\Pi_{\rm RPA}(-q_0)\right), \qquad (26)$$

where the first term on the right-hand side stands for the energy-weighted sum of the β_- transition strengths, while the second term is that of the β_+ ones. In the same way as in the previous subsection, we expand $\Pi_{\rm RPA}$ in terms of the coupling constant χ_5,

$$S^{(1)}_{\rm RPA} = \frac{1}{\pi}\frac{V}{(2\pi)^3}\sum_{n=0}^{\infty}(-\chi_5)^n \lim_{\eta\to+0} I^{(1)}_n, \qquad (27)$$

where $I^{(1)}_n$ is defined as

$$I^{(1)}_n = \int_{-\eta}^{\infty} dq_0 q_0 {\rm Im}(\Pi(q_0))^{n+1} + \int_{\eta}^{\infty} dq_0 q_0 {\rm Im}(\Pi(-q_0))^{n+1}. \qquad (28)$$

By the same arguments in the previous subsection, we can prove that

$$I^{(1)}_n = 0 \qquad (n \geq 2).$$

After calculating $I^{(1)}_0$ and $I^{(1)}_1$, finally we obtain the energy-weighted sum of the β_- and β_+ transition strengths in the RPA of the NFA,

$$S^{(1)}_{\rm RPA} = -\frac{V}{\pi^3}\int d^3p \frac{\mathbf{p}^2 - p_y^2}{E_{\mathbf{p}}}(\theta^{(n)}_{\mathbf{p}} + \theta^{(p)}_{\mathbf{p}}) + 4g_5\frac{(N-Z)^2}{V}. \qquad (29)$$

Next, we will show that Eq. (29) is equal to the expectation value of the double commutator of the Hamiltonian with the GT operator, when the expectation value is calculated by the ground state in the mean field. The nuclear field in the present model is written with the usual notation as

$$\psi(\mathbf{x}) = \int \frac{d^3p}{(2\pi)^{3/2}}\sum_{\alpha}(u_\alpha(\mathbf{p})\exp(i\mathbf{p}\cdot\mathbf{x})a_\alpha(\mathbf{p}) + v_\alpha(\mathbf{p})\exp(-i\mathbf{p}\cdot\mathbf{x})b^\dagger_\alpha(\mathbf{p})). \qquad (30)$$

The mean field Hamiltonian, the interaction, and the GT field operator are described, respectively, as

$$H_0 = \int d^3x \bar{\psi}(\mathbf{x})\left(-i\boldsymbol{\gamma}\cdot\boldsymbol{\nabla} + M^*\right)\psi(\mathbf{x}),$$

$$V = -\frac{g_5}{2}\int d^3x\bar{\psi}(\mathbf{x})\Gamma_i^\mu\psi(\mathbf{x})\bar{\psi}(\mathbf{x})\Gamma_{\mu i}\psi(\mathbf{x}),$$

$$F_\pm = \int d^3x\bar{\psi}(\mathbf{x})\gamma_5\gamma_y\tau_\pm\psi(\mathbf{x}).$$

The double commutator of the mean field Hamiltonian with the GT operator is easily calculated,

$$[F_+,[H_0,F_-]] = 4i\int d^3x\psi^\dagger(\mathbf{x})\gamma_0\left(\boldsymbol{\gamma}\cdot\boldsymbol{\nabla} - \gamma_y\frac{\partial}{\partial y}\right)\psi(\mathbf{x}).$$

Its expectation value of the ground state in the mean field becomes

$$\langle|[F_+,[H_0,F_-]]|\rangle = \frac{V}{\pi^3}\int d^3p\frac{\mathbf{p}^2 - p_y^2}{E_\mathbf{p}}(2-\theta_\mathbf{p}^{(p)}-\theta_\mathbf{p}^{(n)}). \quad (31)$$

The double commutator of V with the GT operator is calculated in the same way,

$$[F_+,[V,F_-]] = -\frac{g_5}{2}\int d^3x(\psi^\dagger(X_{\mu q})^\dagger\psi\psi^\dagger X_q^\mu\psi + \psi^\dagger f_{\mu q}\psi\psi^\dagger[f_+^2,X_{-q}^\mu]\psi + \psi^\dagger[f_+^2,X_{-q}^\mu]\psi\psi^\dagger f_{\mu q}\psi + \psi^\dagger X_q^\mu\psi\psi^\dagger(X_{\mu q})^\dagger\psi),$$

where we have used the abbreviations

$$f_q^\mu = \gamma_0\gamma_5\gamma^\mu\tau_q, \quad X_q^\mu = [f_q^\mu, f_-^2] \quad (q=\pm,0).$$

In the mean field approximation, the expectation value is calculated neglecting the exchange terms of the matrix elements. Keeping the direct terms only, we obtain

$$\langle|[F_+,[V,F_-]]|\rangle = g_5\int d^3x\langle|\psi^\dagger(X_+^2)^\dagger\psi\psi^\dagger X_+^2\psi|\rangle = g_5\frac{V}{(2\pi)^6} \times\left(4\int d^3p(\theta_\mathbf{p}^{(p)}-\theta_\mathbf{p}^{(n)})\right)^2 = 4g_5\frac{(N-Z)^2}{V}. \quad (32)$$

Thus, if we neglect the divergent term of Eq. (31), the sum of Eqs. (31) and (32) is just equal to the energy-weighted sum of the strengths for the β_- and β_+ transitions in the RPA given in Eq. (29),

$$S_{\mathrm{RPA}}^{(1)} = \langle|[F_+,[H_0+V,F_-]]|\rangle. \quad (33)$$

In the NSA, the nuclear field is given by replacing the creation operator $b_\alpha^\dagger$ of the antiparticles with the annihilation one in Eq. (30). Because of this change, on one hand, we obtain, instead of Eq. (31),

$$\langle|[F_+,[H_0,F_-]]|\rangle = -\frac{V}{\pi^3}\int d^3p\frac{\mathbf{p}^2 - p_y^2}{E_\mathbf{p}}(\theta_\mathbf{p}^{(p)}+\theta_\mathbf{p}^{(n)}),$$

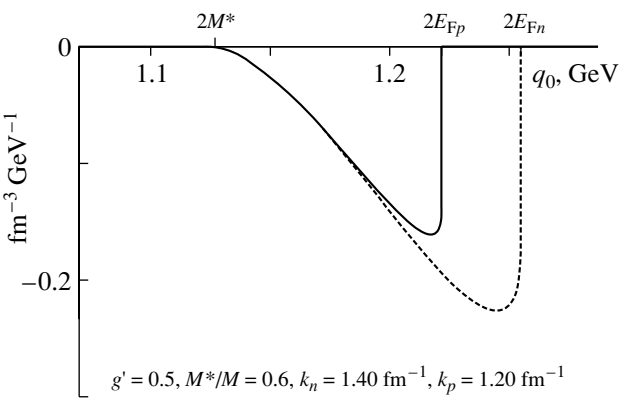

The RPA response function of the Gamow–Teller excitation in the high-excitation-energy region in units of the nuclear volume. For details, see text.

which does not contain the divergent term, but is negative. On the other hand, the expectation value of the double commutator as for V is the same as Eq. (32). Thus, in the NFA also, the energy-weighted sum of the GT strengths in the RPA is equal to the expectation value of the double commutator as in Eq. (33).

Formally, we have proved that the RPA theorem holds in charge-exchange excitations also with respect to the sum of the strengths for the β_- and β_+ transitions. In the present relativistic model, however, we have also shown that the energy-weighted sum value itself is negative in the NFA and NSA. Generally speaking, all previous calculations using the NFA and NSA have the same problem. In order to solve this problem, we definitely need the renormalization of the divergence.

4. DISCUSSIONS AND CONCLUSIONS

The relativistic model has been extensively used as a phenomenological model of nuclei for the past 30 years [1]. In particular, it explains very well the ground-state properties of nuclei with the mean field approximation, where antinucleon degrees of freedom are neglected [1]. In the RPA based on the mean field approximation, however, it is known that we cannot describe the excited states within the nucleon space only. If the configuration space is restricted to the nucleon sector, the continuity equation of the baryon current is violated. In order to keep the continuity equation without renormalization of the divergence, we should include Pauli blocking terms from nucleon–antinucleon excitations in the RPA correlation functions [2, 3]. We have called this approximation the NFA. It is also known that the NFA reproduces the correct LM parameters in the sense of the mean field approximation [4]. It is not obvious, however, that the addition of Pauli blocking terms

to the nucleon space is enough for the RPA to keep various other conservation laws.

In this paper, we have investigated whether or not the NFA satisfies the model-independent sum rule of the GT strengths. It is with respect to the difference between the total strengths of the β_- and β_+ transitions, and is usually called the Ikeda sum rule [9]. Since this sum rule is just a result of the commutation relation of the spin–isospin operators, any model should satisfy it. We have shown that the NFA satisfies the sum rule and the Pauli blocking terms are necessary. If the configuration space is limited to the nucleon one only, the sum rule value is exhausted only by about 88%. When adding the Pauli blocking terms to the RPA correlation function, the sum rule value is reproduced. This fact has been shown in an analytic way by calculating the GT strengths for nuclear matter.

The Ikeda sum rule has been also investigated in the NSA [7], where the Dirac sea is assumed to be empty, and the antinucleon states are treated as particle states with negative energy. It is known that, in this way also, one can avoid the divergence problem without violating the continuity equation. We have shown that the NSA also satisfies the Ikeda sum rule and predicts the same quenching of the GT strength in the giant resonance region. It has been shown, however, that each strength of the total β_- and β_+ transitions outside of the giant resonance region is different from those in the NFA.

The energy-weighted sum of the GT strengths in the RPA is also studied in the NFA and NSA. It has been shown that the sum of the energy-weighted strengths for the β_- and β_+ transitions is equal to the expectation value of the double commutator of the Hamiltonian with the GT operator, when the expectation value is calculated with the ground state in the mean field and the divergent terms are deleted. Thus, the well-known RPA theorem by Thouless [10] holds for charge-exchange excitations also.

We have shown formally that the NFA and NSA are consistent with the Ikeda sum rule and do not violate the RPA theorem. There is, however, a serious problem in both approximations, as a price for neglecting the divergence. The NFA and NSA require contributions from the unphysical GT strengths for the RPA to satisfy the Ikeda sum rule. The NFA needs negative strengths, while the NSA needs positive strengths, but in a negative excitation energy region. Moreover, the sum of the energy-weighted GT strengths is negative. Thus, it is not a justification of the approximation to satisfy the continuity equation only. So far, most of the nuclear observables are well reproduced phenomenologically without the renormalization. In order to solve the above problems, we definitely need the renormalization of the divergence in a future study.

It may depend on nuclear observables whether or not effects of the renormalization are important. In the previous studies [4], on one hand, it was shown that the LM parameter F_1 depends on antinucleon degrees of freedom, only through the Pauli blocking terms. These facts were shown by fully renormalized calculations in the σ–ω model [15]. As a result, some physical quantities which are dominated by F_1 can be described using an approximation with Pauli blocking terms. Indeed, for example, the nuclear current at $\mathbf{q} \to 0$, or nuclear magnetic moments and the center-of-mass motion were shown to be described well in the NFA and NSA [6, 7]. On the other hand, effects of the antinucleon degrees of freedom on the LM parameter F_0 are not represented by the Pauli blocking terms only, and the contribution from other nucleon–antinucleon excitations is more important, as shown in [4]. Another example is the Coulomb sum rule, where the renormalization provides us with a strong quenching of the sum rule value at high momentum transfer [15].

Thus, there may be some cases where the renormalization is not essential for description of the observables, but generally speaking, we should investigate in the future how effects of the renormalization change previous results in relativistic models, including the GT strengths discussed here.

We note finally that detailed discussions presented here are required not only from a theoretical point of view, but also from the recent experiment. It has been shown experimentally that the sum rule value is quenched by about 10% from the nonrelativistic analysis of the (p, n) reaction [16]. In nonrelativistic models, so far, all of the 10% quenching was assumed to be due to the coupling of the particle–hole states with Δ-hole states [17, 18]. If 6% quenching is due to the relativistic effects, however, it follows that only 4% stems from the contribution of the Δ degrees of freedom. This weak coupling of the particle–hole states with the Δ-hole states yields the extremely small value of LM parameter $g'_{N\Delta}$ which dominates the critical density of the pion condensation [19] and other spin-dependent response functions [20]. Thus, we need to discuss GT strengths carefully for the study of the spin-dependent structure of nuclei in detail.

REFERENCES

1. B. D. Serot and J. D. Walecka, Adv. Nucl. Phys. **16**, 1 (1986); P. Ring, Prog. Part. Nucl. Phys. **37**, 193 (1996).
2. S. A. Chin, Ann. Phys. (N.Y.) **108**, 301 (1977).

3. H. Kurasawa and T. Suzuki, Nucl. Phys. A **445**, 685 (1985).
4. H. Kurasawa and T. Suzuki, Phys. Lett. B **474**, 262 (2000).
5. H. Kurasawa and T. Suzuki, Phys. Rev. C **69**, 014306 (2004).
6. H. Kurasawa and T. Suzuki, Phys. Lett. B **165B**, 234 (1985); S. Nishizaki, H. Kurasawa, and T. Suzuki, Nucl. Phys. A **462**, 687 (1987).
7. J. F. Dawson and R. J. Furnstahl, Phys. Rev. C **42**, 2009 (1990).
8. Z. Ma, N. Van Giai, A. Wandelt, *et al.*, Nucl. Phys. A **686**, 173 (2001).
9. K. Ikeda, S. Fujii, and J. I. Fujita, Phys. Lett. **3**, 271 (1963).
10. D. J. Thouless, Nucl. Phys. **22**, 78 (1961).
11. H. Kurasawa, T. Suzuki, and N. Van Giai, Phys. Rev. Lett. **91**, 062501 (2003).
12. H. Kurasawa, T. Suzuki, and N. Van Giai, Phys. Rev. C **68**, 064311 (2003).
13. A. Bohr and B. R. Mottelson, Phys. Lett. B **100B**, 10 (1981).
14. T. Suzuki, Nucl. Phys. A **379**, 110 (1982); T. Suzuki and M. Kohno, Prog. Theor. Phys. **68**, 690 (1982).
15. H. Kurasawa and T. Suzuki, Nucl. Phys. A **490**, 571 (1988).
16. T. Wakasa *et al.*, Phys. Rev. C **55**, 2909 (1997); Phys. Lett. B **426**, 257 (1998); H. Sakai and K. Yako, Nucl. Phys. A **731**, 94 (2004).
17. T. Suzuki and H. Sakai, Phys. Lett. B **455**, 25 (1999).
18. A. Arima, W. Bentz, T. Suzuki, and T. Suzuki, Phys. Lett. B **499**, 104 (2001).
19. H. Kurasawa, T. Suzuki, and N. Van Giai, Nucl. Phys. A **731**, 114 (2004).
20. K. Kawahigashi, K. Nishida, A. Itabashi, and M. Ichimura, Phys. Rev. C **63**, 044609 (2001).

Physics of Atomic Nuclei, Vol. 67, No. 9, 2004, pp. 1664–1673. From Yadernaya Fizika, Vol. 67, No. 9, 2004, pp. 1691–1701.

Photonuclear Reactions: Modern Status of the Data*

B. S. Ishkhanov[1),2)] and V. V. Varlamov[2)]**

Received January 21, 2004

Abstract—Photonuclear reaction data play an important role in basic and applied research. Radiation shielding design, radiation transport analysis, activation analysis, astrophysical nucleosynthesis, safeguards and inspection technologies, human body radiotherapy absorbed dose calculations, beam monitoring in heavy-ion dissociation research at ultrarelativistic energies, etc., could be mentioned. However, there exist quite evident systematic discrepancies in both shapes and magnitudes between photonuclear cross sections measured in various laboratories. These discrepancies noticeably reduce the accuracy and reliability of data. A systematic overview of various types of data contained in the international database is given. The modern status of the data is discussed. The reasons for significant discrepancies between various photonuclear data are analyzed and methods to reduce them are suggested. © *2004 MAIK "Nauka/Interperiodica".*

INTRODUCTION

The absolute majority of data on photonuclear reaction cross sections in the energy range of giant dipole resonance (GDR) have been obtained [1–5] in experiments with bremsstrahlung (BR) and quasimonoenergetic photons produced by annihilation in flight of relativistic positrons (QMA). There are evident systematical discrepancies in both shapes and magnitudes between the data obtained not only in experiments of different types, but in experiments of the same type as well. The discrepancies are larger than statistical uncertainties and obviously depend on the experimental method explored. Though the majority of cross-section data were obtained quite long ago, they are included in the contemporary large database [6] and still extensively used. Thus, the current status of photonuclear research on the whole, as well as the accuracy and reliability of each set of data, becomes understandable only after a careful analysis of existing systematical disagreements and of the ways to take them into account. Large databases give a good possibility for such an analysis.

1. TWO MAIN TYPES OF PHOTONUCLEAR EXPERIMENTS

1.1. Experiments with Electron Bremsstrahlung Photons

The bremsstrahlung spectrum is a continuous one and, therefore, a direct measurement of a reaction cross section is not possible with it, but only a reaction yield $Y(E_{jm})$. The latter is a cross section $\sigma(k)$ with a threshold $E_{\rm th}$ depending on a photon energy k and folded with the photon spectrum $W(E_{jm},k)$ with the endpoint energy E_{jm}:

$$Y(E_{jm}) = \frac{N(E_{jm})}{\varepsilon D(E_{jm})} = \alpha \int\limits_{E_{\rm th}}^{E_{jm}} W(E_{jm},k)\sigma(k)dk. \quad (1)$$

Reaction cross section σ can be obtained from the experimental yield Y using one of the well-known mathematical methods (Penfold–Leiss, Tikhonov regularization, etc.). All of them have been developed especially to produce the effective photon spectrum (the apparatus function) that looks like (Fig. 1*b*) a sufficiently narrow line. However, a constructed apparatus function has a complex shape, which can produce additional uncertainties in shape, magnitude, and position of a cross section.

1.2. Experiments with Quasimonoenergetic Annihilation Photons

As an alternative to the procedure of solving inverse ill-posed problem (1), QMA experiments have been developed [5] [the majority of data have been obtained at Livermore (USA) and Saclay (France)]. They consist in producing annihilation photons with the energy $E_\gamma = E_{e^+} + 0.511$ MeV by fast positrons. Since annihilation photons always are accompanied by positron bremsstrahlung, a QMA experiment is carried out in three steps (Fig. 1—^{63}Cu$(\gamma,n)^{62}$Cu reaction [7]): (i) measurements of the yield $Y_{e^+}(E_j)$

*This article was submitted by the authors in English.

[1)]Physics Faculty, Moscow State University, Moscow, Russia.
[2)]Skobeltsyn Institute of Nuclear Physics, Moscow State University, Moscow, Russia.
**e-mail: varlamov@depni.sinp.msu.ru

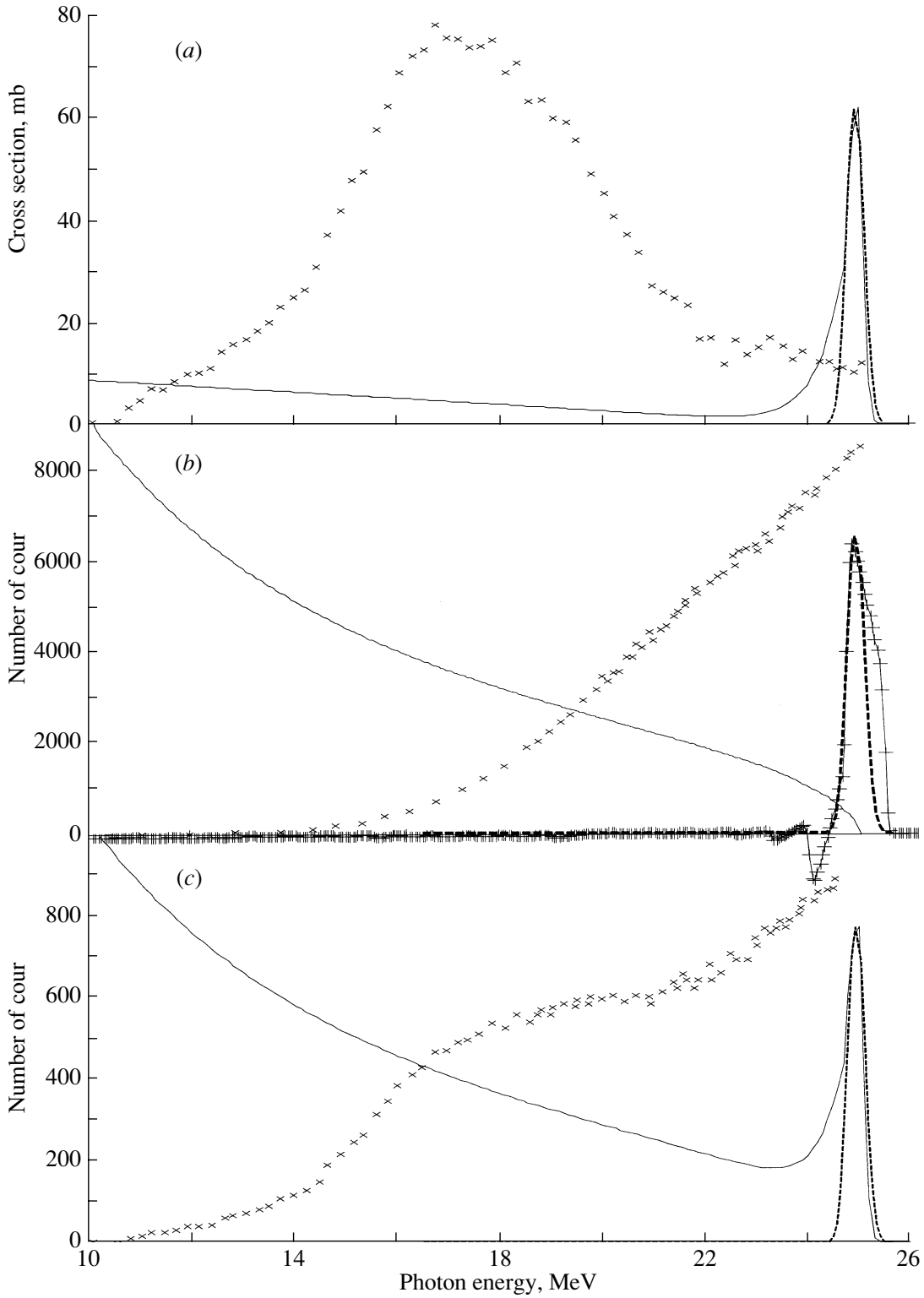

Fig. 1. Experimental yields [7] of ^{63}Cu(γ, n) ^{62}Cu reaction ($\times$), appropriate effective photon spectra (solid curves), and the apparatus function obtained by the reduction method (dashed curves): (*a*) the yield difference $Y_{e+}(E_j) - Y_{e-}(E_j) = Y(E_j) \approx \sigma(k)$ (2), i.e., the difference between spectra of photons produced by positrons and electrons, respectively; (*b*) the yield $Y_{e-}(E_j)$ and the electron bremsstrahlung spectrum [the apparatus function obtained by the Penfold–Leiss method is also presented (+)]; (*c*) the yield $Y_{e+}(E_j)$ and the spectrum of photons produced by positrons (the sum of bremsstrahlung and annihilation processes).

of the reaction induced by photons from both the annihilation and the bremsstrahlung of e^+; (ii) measurements of the yield $Y_{e^-}(E_j)$ of the reaction induced by photons from the e^- bremsstrahlung; (iii) the subtraction (the bremsstrahlung spectra is assumed to be identical for e^- and e^+)

$$Y_{e^+}(E_j) - Y_{e^-}(E_j) = Y(E_j) \approx \sigma(k). \qquad (2)$$

The difference (2) is interpreted as a reaction cross section "measured directly."

The following points should be mentioned: (i) There is no beam of QMA photons in reality: the QMA photons arise only as a difference of two real spectra. (ii) The apparatus function (Fig. 1*a*) of an experiment is obtained individually because it depends on conditions of both the measurements (i.e., on yields—Y_{e^+}, Y_{e^-}). (iii) The production of positron annihilation γ quanta is a result of a few successive processes [bremsstrahlung production ($e^- + A \to A + e^- + \gamma$); production of pairs ($\gamma + A \to A + e^- + e^+$); positron annihilation ($e^+ + e^- \to 2\gamma$)]. Due to this, the number of quasimonoenergetic photons appears to be small, and hence the statistical accuracy of measured yields, as well as their normalizations, is also low. (iv) An apparatus function has a complex shape and is spread over a wide energy range, so the result of (2) is really not a cross section, but again a yield.

2. MAIN DISCREPANCIES BETWEEN REACTION CROSS SECTIONS OBTAINED WITH BR AND QMA PHOTONS

As follows from the above discussion, conditions of these two types of experiments are different and this is the reason for a significant disagreement in their results.

2.1. Total Photoneutron Reaction (γ, xn) Cross-Section Shape (Structure, Resolution)

As a typical example of well-known discrepancies under discussion, photoneutron reaction $^{16}\mathrm{O}(\gamma, xn)$ total cross sections obtained in the BR [8] and QMA experiments [9, 10] can be pointed out. There are well-separated resonances in all three cross sections obtained with a high enough energy resolution (200 [8], 180–200 [9], and 200–300 keV [10]). However, all the QMA resonances have larger widths and smaller amplitudes than the appropriate BR ones. The QMA data look like smoothed versions of the BR data. Absolute values of the BR data [8] and the Saclay QMA data [9] are close: integrated cross sections for the same integration limits are 36.90 and 34.52 MeV mb, respectively, but the Livermore QMA data [10] [(1.12–1.20) × 27.64 MeV mb] became close enough to the other two only after additional normalization (the factor 1.12 will be discussed later).

An additional example of discrepancies concerned is a detailed comparison [11] of resonances in the $^{18}\mathrm{O}(\gamma, xn)$ reaction cross section obtained with BR [11] and QMA photons [12]: all the resonances have larger amplitudes ($\langle A_{\mathrm{BR}}/A_{\mathrm{QMA}}\rangle = 1.17$) and smaller widths ($\langle \Gamma_{\mathrm{QMA}}/\Gamma_{\mathrm{BR}}\rangle = 1.35$) in the BR cross sections than in the QMA cross sections. Integrated cross sections for the energy range 8–28 MeV are also different: $\sigma^{\mathrm{int}}_{\mathrm{BR}} = 187.12$ MeV mb and $\sigma^{\mathrm{int}}_{\mathrm{QMA}} = 167.33$ MeV mb (the ratio is again ~1.12).

The general systematics[3)] [13] of the disagreements is shown in Fig. 2 for a special parameter named "structureness" that describes as a whole the deviation of each reaction cross section from its significantly smoothed value (with a smearing parameter Δ about 1 MeV) for the whole energy range D:

$$S = \frac{1}{N}\sum_{i=1}^{N}\frac{(\sigma_i - \langle\sigma_i\rangle)^2}{\langle\langle\sigma\rangle\rangle^2}, \qquad (3)$$

where

$$\langle\sigma_i\rangle = \frac{1}{\Delta}\int\limits_{E_i-\Delta/2}^{E_i+\Delta/2}\sigma(k)dk, \quad \langle\langle\sigma\rangle\rangle = \frac{1}{D}\int\limits_{D}\sigma(k)dk$$

are averaged cross sections.

In Fig. 2, the ratios S/S_{L} are presented, where S values are calculated for data from various laboratories, whereas S_{L} is for the Livermore QMA data (some other QMA data are used also). Data clearly separate into two groups: BR ($\langle S/S_{\mathrm{L}}\rangle = 4.35$) and QMA ($\langle S/S_{\mathrm{L}}\rangle = 1.22$). This means that, in all the QMA laboratories, an estimation of energy resolution using the width of the annihilation line (in many cases 250–400, sometimes 500, more rarely 150–300 keV) does not give a real resolution: the QMA cross sections are oversmoothed. This is confirmed by the value $\langle S/S_{\mathrm{L}}\rangle = 4.22$ for data obtained in [14] using a tagged photon (TP) technique (the TP apparatus function is close to the Gauss shape).

Since in reality a QMA cross section (2) is only a yield (1), a real cross section can be obtained [15–18] only after an additional processing by the use of a real apparatus function and the reduction method [19, 20]. Actually, this is not a method of solving an inverse ill-posed problem (1) to unfold a cross section from a yield. The reduction method transforms data obtained with some experimental apparatus function (Fig. 1) into those which would have been measured

[3)] It contains more than 500 total photoneutron (γ, xn) cross sections for nuclei from ^{3}H to ^{238}U.

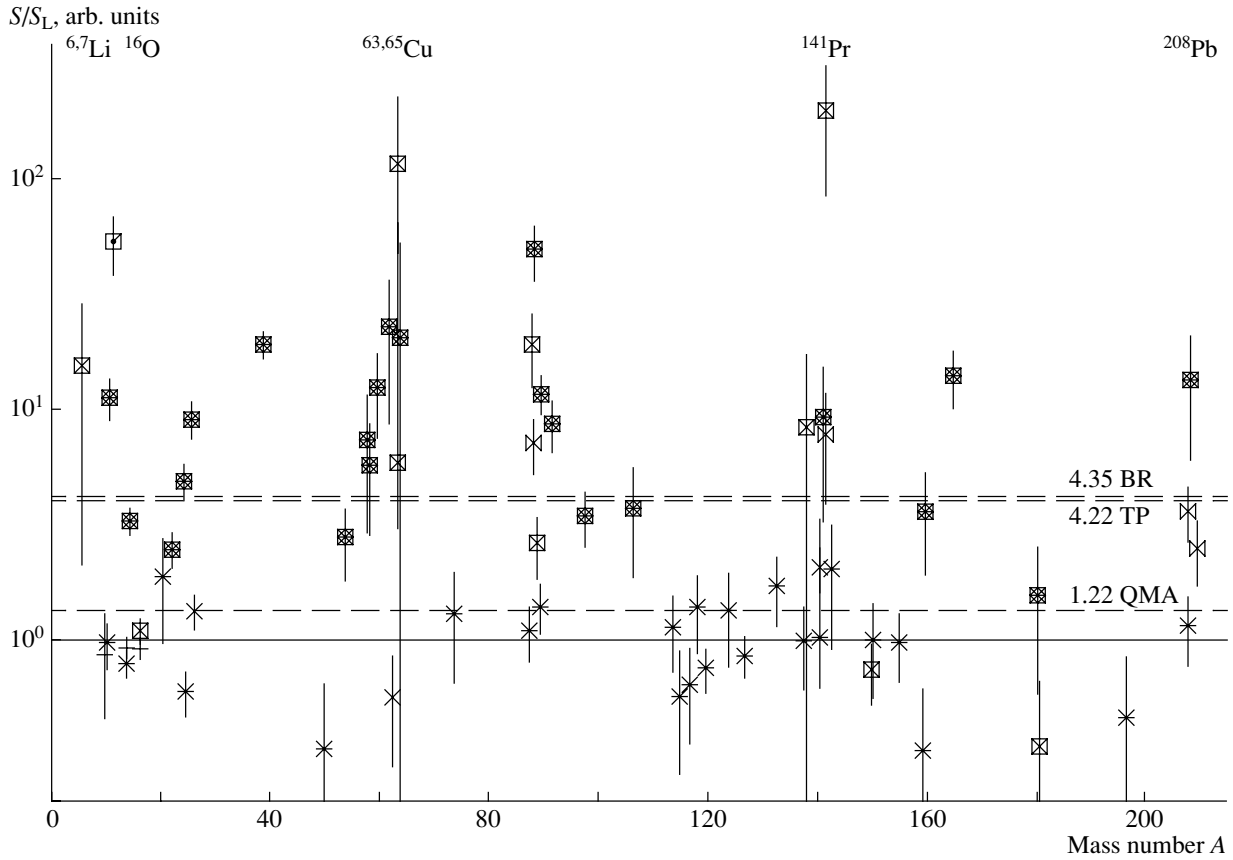

Fig. 2. The systematics of ratios S/S_L (see text) obtained for the total photoneutron reaction cross section data: BR data [(▩) Moscow, (⊠) Melbourne (Australia), (⊡) other]; QMA data [(×) Saclay (France), (+) Giessen (Germany), (×) other]; TP data [(⋈) Illinois (USA)].

by means of an apparatus function of another quality (the better, e.g., the Gauss line with an exactly known energy resolution). As a result, one gets the most reasonably achievable monoenergetic representation of a reaction cross section from a reaction yield.

A reaction yield (1) measured using an apparatus function A and written in an operator form reads

$$y = A\sigma + \nu. \tag{4}$$

Then after the simple transformation

$$Ry = R(A\sigma + \nu) = U\sigma + (RA - U)\sigma + R\nu = \sigma^{\text{eval}} \tag{5}$$

with a special operator R [18, 19],

$$R = U(\Sigma^{-1/2}A)^{-}\Sigma^{-1/2} = U(A^{*}\Sigma^{-1}A)^{-}A^{*}\Sigma^{-1}, \tag{6}$$

it can be transformed into the evaluated cross section

$$\sigma^{\text{eval}} = Ry = U\sigma + R\nu, \tag{7}$$

which represents the "measured" cross section with the apparatus function U of a needed quality.

The main result of processing using the reduction method is that the structure of a QMA cross section became much clearer and closer to that of a BR cross section. This is seen after processing of the QMA results (Fig. 3*e*) for $^{63}\mathrm{Cu}(\gamma, n)\,^{62}\mathrm{Cu}$ reaction [7] and a comparison for the same energy resolution of 210 keV of all three cross sections (2) obtained by the reduction method with the result of the BR experiment [21]. The inverse operation of smoothing of cross sections from Figs. 3*b*–3*d* gives [22] the real QMA result (Fig. 3*e*): the energy resolution is only ~1.3 MeV (i.e., 4 times worse than the estimated width of the annihilation line). The same processing of $^{197}\mathrm{Au}(\gamma, xn)$ reaction data [23] gives a real resolution value of 1.6 MeV (i.e., 3 times worse than the declared one).

2.2. Magnitude of a Total (γ, xn) Reaction Cross Section (Absolute Value)

Integrated cross section data. There are definite discrepancies between absolute values of data obtained at different laboratories using both the BR

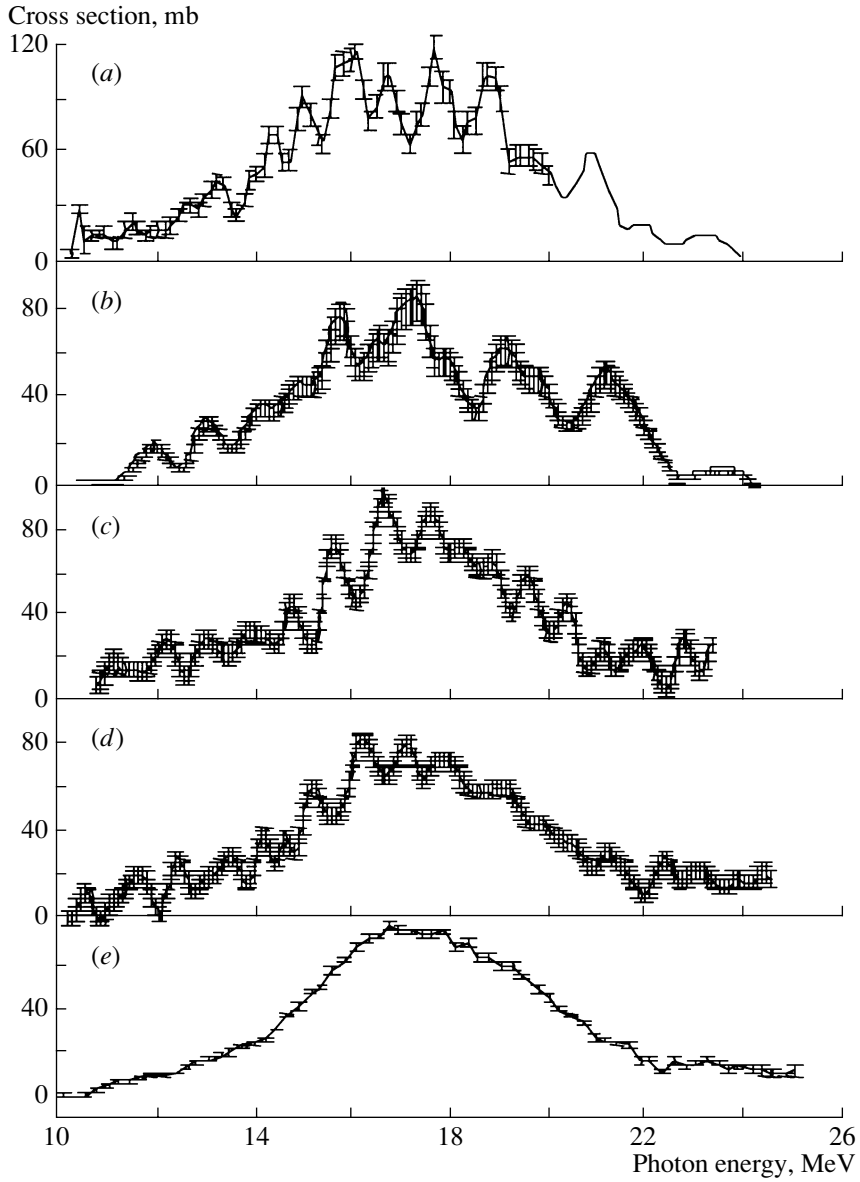

Fig. 3. Cross sections of ^{63}Cu$(\gamma, n)^{62}$Cu reaction obtained by various methods: (*a*) the BR experiment [21] (energy resolution 210 keV); (*b*) the result of processing of QMA yield (2) $Y_{e-}(E_j)$ [7] (the method of reduction for energy resolution 210 keV); (*c*) the result of processing of QMA yield (2) $Y_{e+}(E_j)$ [7] (the method of reduction for energy resolution 210 keV); (*d*) the result of processing of QMA yield difference (2) $Y_{e+}(E_j) - Y_{e-}(E_j) = Y(E_j) \approx \sigma(k)$ [20] (the method of reduction for resolution 210 keV); (*e*) the published [7] QMA yield difference (2) $Y_{e+}(E_j) - Y_{e-}(E_j) = Y(E_j) \approx \sigma(k)$ (the energy resolution 200–400 keV is declared).

and QMA photon beams. In addition to the data for ^{16,18}O presented above, other examples are presented in Table 1, where a comparison of the integrated QMA (γ, xn) reaction cross sections [1] from Livermore and Saclay is given. These four cases [1] are taken because of very close integration energy limits $E_\gamma^{\max}$ or vise versa—integrated cross section values σ^{int} (many other similar discrepancies can be found in [1] as well). One can easily estimate that, in all cases, the values from the Saclay experiments are higher than those from the Livermore ones by 6–16%.

A systematics of integrated cross sections. A systematics of ratios of integrated cross sections was obtained [13, 15, 16] for (γ, xn) reaction cross sections measured for energy ranges of incident photons between the thresholds of (γ, n) and $(\gamma, 2n)$ reactions. Specially calculated ratios $R_{\text{syst}}^{\text{int}} = \sigma_{\text{var.lab}}^{\text{int}}(\gamma, xn)/\sigma_{\text{L}}^{\text{int}}(\gamma, xn)$ of data from various laboratories to that from Livermore are presented in

Table 1. Comparison of the experimental QMA data on integrated (γ, xn) cross sections from Saclay (upper values) and Livermore (lower values)

Nucleus	^{51}V	^{75}As	^{90}Zr	^{165}Ho
$(E_\gamma^{\rm int})^{\max}$ [MeV]	27.8/27.8	26.2/29.5	25.9/27.6	26.8/28.9
$\sigma_{\rm S}^{\rm int}/\sigma_{\rm L}^{\rm int}$	$689/654 = 1.06$	$1306/1130 \geq 1.16$	$1309/1158 \geq 1.13$	$3667/3385 \geq 1.08$

Table 2. Recommended [23] normalization factors F to improve agreement of the Saclay and Livermore data

Nucleus	Rb	^{89}Sr	^{89}Y		^{90}Zr		^{91}Zr	^{92}Zr	^{93}Nb	^{94}Zr	^{127}I	^{197}Au	^{206}Pb	^{207}Pb	^{208}Pb		^{209}Bi
Lab.	S	S	S	L	S	L	L	L	S	L	S	S	L	L	L	S	L
F	0.85 ± 0.03	0.85 ± 0.03	0.82	1.0	0.88	1.0	1.0	1.0	0.85 ± 0.03	1.0	0.8	0.93	1.22*	1.22*	1.22*	0.93	1.22*

* The Livermore data increasing instead of the Saclay data decreasing.

Fig. 4. The results definitely confirm that, as a rule, the Livermore cross sections are smaller than the others: the values $R_{\rm syst}^{\rm int}$ are concentrated near the mean value $\langle R_{\rm syst}^{\rm int} \rangle = 1.12$ (just mentioned above). The QMA data from Saclay are more consistent with the data (both QMA and BR) of other laboratories.

Absolute values of reaction cross sections. Cross sections of photonuclear reactions on nuclei $^{\rm nat}$Zr, ^{127}I, ^{141}Pr, ^{197}Au, and $^{\rm nat}$Pb measured earlier at Livermore have been specially remeasured [24]. Remeasured data were used for a detailed comparison of absolute values of photoneutron cross sections in 14 nuclei (Table 2) with the aim to solve the evident problem of appreciable discrepancies between the data of different laboratories, primarily Livermore and Saclay. It was pointed out that "this comparison implies the Livermore experiment error either in the photon flux determination or in the neutron detection efficiency or in both." The major recommendations to put data into consistency were somewhat dual: (i) to decrease the Saclay data for various nuclei by factor $F = 0.8$–0.93 (Table 2); (ii) to increase the Livermore data for ^{206,207,208}Pb and ^{209}Bi (indicated by asterisks) by a factor of 1.22 to achieve agreement with data from experiments with tagged photons [14].

3. DISCREPANCIES BETWEEN CROSS SECTIONS OF PARTIAL PHOTONEUTRON REACTIONS (γ, n) AND $(\gamma, 2n)$ OBTAINED WITH QMA PHOTONS AT SACLAY AND LIVERMORE

Besides the discrepancies in $(\gamma, xn) = (\gamma, n) + (\gamma, np) + 2(\gamma, 2n)$ cross sections, there are certain discrepancies between cross section values of partial reactions (γ, n) and $(\gamma, 2n)$ [1]. It was found for 12 nuclei (^{89}Y, ^{115}In, ^{117,118,120,124}Sn, ^{133}Cs, ^{159}Tb, ^{165}Ho,^{181}Ta, ^{197}Au, ^{208}Pb) [25] that, while the integrated (γ, n) cross section from Saclay is higher than that from Livermore, the integrated $(\gamma, 2n)$ cross section is lower (Table 3). For example, the (γ, xn) data from Livermore and Saclay for the nucleus ^{159}Tb differ [1] only by 6%, but the (γ, n) data from Saclay are 37% higher than the corresponding Livermore data [25]. At the same time, the $(\gamma, 2n)$ data are lower by 47%.

These data were accurately recalculated [26] and supplemented with similar data for the other seven nuclei (^{51}V, ^{75}As, ^{90}Zr, ^{116}Sn, ^{127}I, ^{232}Th, ^{238}U). The complete systematics of integrated cross section ratios (Saclay/Livermore) for 19 nuclei is presented in Fig. 5. As a rule, the ratios of the (γ, n) data (squares) are noticeably larger than 1.0, but those for the $(\gamma, 2n)$ reaction (triangles) are less. On the basis of a detailed comparison [25] of (γ, n) and $(\gamma, 2n)$ data with the data from (e, n) and $(e, 2n)$ reactions measured for ^{181}Ta using both the neutron multiplicity sorting and the residual activity measurement methods [27–29], it was shown that discrepancies are produced by the difference in the neutron multiplicity sorting procedure. The Saclay procedure was not correct, and therefore the $(\gamma, 2n)$ data were underestimated [some events were interpreted as (γ, n) ones]. Correspondingly, the data for the (γ, n) reaction were overestimated.

The method to correct data [25, 26] is very simple and clear. Since $(\gamma, xn) = (\gamma, n) + 2(\gamma, 2n)$, the ratio $R = \sigma_{\rm S}(\gamma, xn)/\sigma_{\rm L}(\gamma, xn)$ must be used for joint correction of data from Saclay and Livermore. With this factor, one obtains the following expression of the corrected Saclay $(\gamma, 2n)$ cross section $\sigma_{\rm S}^*(\gamma, 2n)$:

$$R\sigma_{\rm L}(\gamma, 2n) = \sigma_{\rm S}^*(\gamma, 2n) = \sigma_{\rm S}(\gamma, 2n) \qquad (8)$$

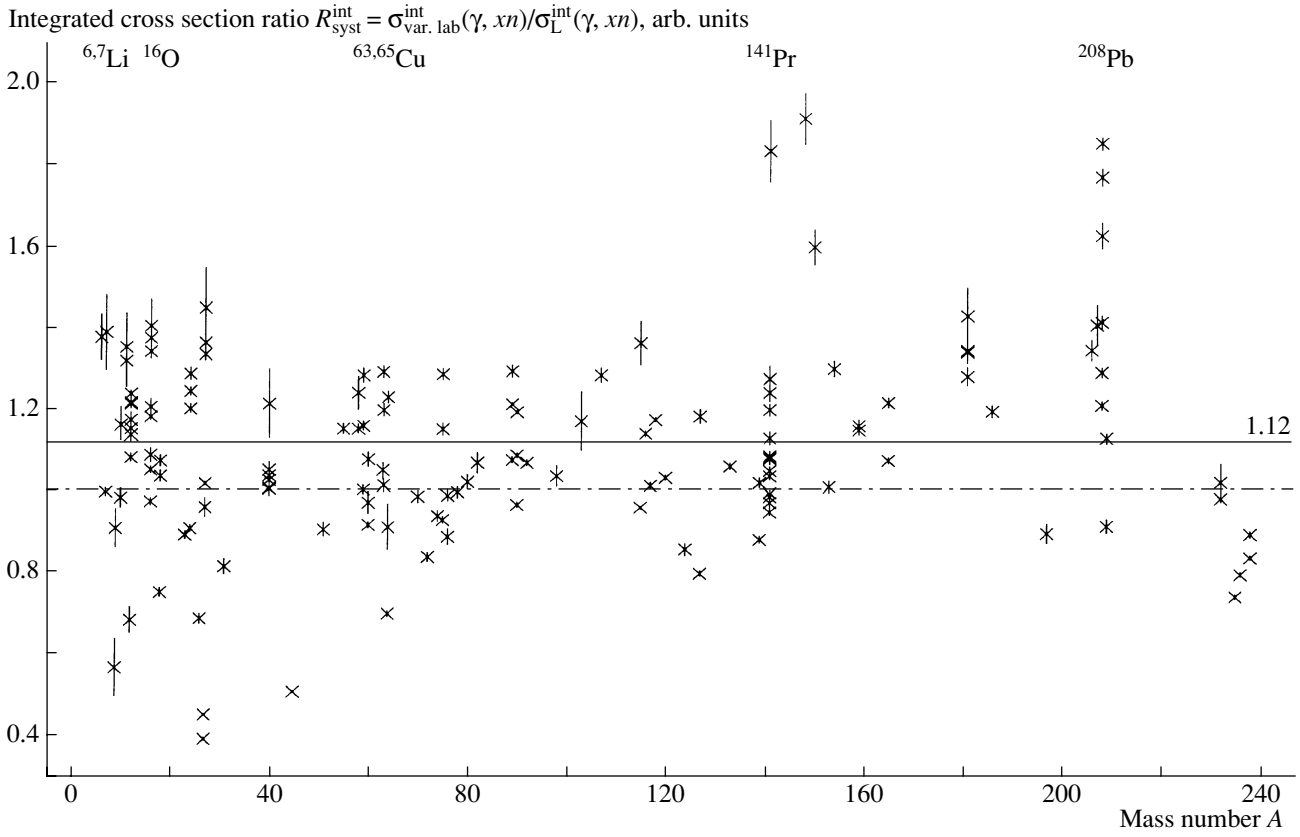

Fig. 4. The complete systematics [13, 15, 16] of ratios $R^{int}_{syst} = \sigma^{int}_{var.lab}(\gamma, xn)/\sigma^{int}_{L}(\gamma, xn)$ of the total integrated cross sections of photoneutron reaction in various nuclei obtained with various photon beams at various laboratories and with QMA photons at Livermore. The cross sections are calculated up to thresholds of $(\gamma, 2n)$ reaction. Solid line—the mean value $\langle R^{int}_{syst} \rangle = 1.12$; dashed line—$R^{int}_{syst} = 1.0$.

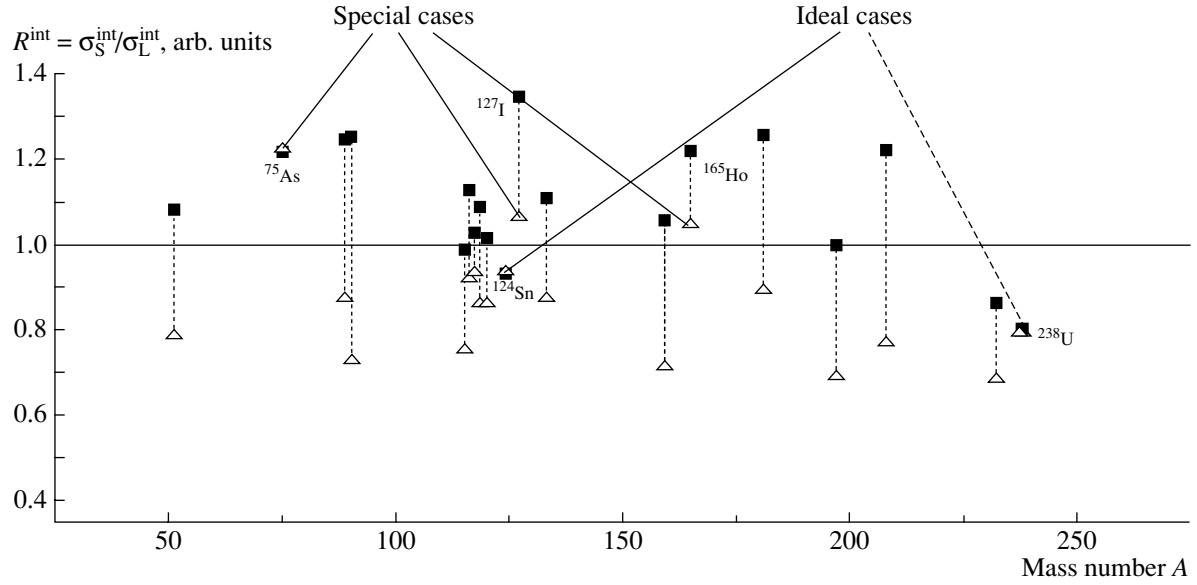

Fig. 5. The systematics [26] of values $R^{int}(n) = \sigma^{int}_{S}(\gamma, n)/\sigma^{int}_{L}(\gamma, n)$ (■) and $R^{int}(2n) = \sigma^{int}_{S}(\gamma, 2n)/\sigma^{int}_{L}(\gamma, 2n)$ (△). Special cases—$(\gamma, 2n)$ cross section ratios are more than 1.0. Ideal cases—(γ, n) and $(\gamma, 2n)$ cross section ratios are near. Special cases and ideal cases were processed individually [26].

$$+\frac{1}{2}(\sigma_S(\gamma,n)-R\sigma_L(\gamma,n)).$$

Expression (8) reflects the main idea described above: a part of the Saclay (γ,n) cross section $(\sigma_S(\gamma,n)-R\sigma_L(\gamma,n))/2$ is added ("transmitted back") to the Saclay $(\gamma,2n)$ cross section $\sigma_S(\gamma,2n)$. The Saclay (γ,n) cross section can be corrected by subtraction of the $R\sigma_L(\gamma,n)$ cross section for energies higher than the threshold of the $(\gamma,2n)$ reaction. At the same time, the left part of (8) means that the recalculated cross section $\sigma_S^*(\gamma,2n)$ must agree with the Livermore $(\gamma,2n)$ cross section multiplied by R, i.e., must be equal to $R\sigma_L(\gamma,2n)$.

The corrected cross section ratios for all 19 nuclei (Table 3) together with the integrated cross sections are presented in [26]. As an example, in Fig. 6, we show results of the joint correction of the Saclay and Livermore data for ^{208}Pb.

4. SUMMARY: MODERN STATUS OF WELL-KNOWN DATA

4.1. Important Conclusions

The problems discussed above clarify the "modern" status of well-known published photonuclear data. The value, accuracy, and reliability of all data could be understood only after a special analysis of systematic disagreements, which depend on the explored experimental method. The "modern" status of data under discussion means the following:

Owing to obvious discrepancies between various data, they should be used with caution and strongly individually; special attention has to be paid to the experimental method and data processing procedure explored in every particular case.

The QMA data are strongly oversmoothed (its real energy resolution is a factor of 3–4 worse than the declared one) in comparison with the BR data. The QMA data must be reprocessed using either the reduction method (4)–(7) or a similar one to take into account the real (not enough local) shape of an apparatus function (an effective photon spectrum).

The absolute values of (γ,xn) cross sections measured with the QMA photons at Livermore in general are smaller than those measured with the BR and QMA photons at various other laboratories. As a result, the data on (γ,xn) cross sections from Livermore for 19 nuclei listed above [26] must be corrected; i.e., they should be multiplied by appropriate coefficients $R^{\rm int}(\gamma,xn)=R^{\rm int}(\gamma,n)=\sigma_S^{\rm int}(\gamma,n)/\sigma_L^{\rm int}(\gamma,n)$ (Table 3), and for other nuclei, by $\langle R_{\rm syst}^{\rm int}\rangle = 1.12$ [13, 15, 16], at least.

Cross sections of the partial photoneutron reactions (γ,n) and $(\gamma,2n)$ from Saclay experiments are not correct due to exploiting an incorrect neutron multiplicity sorting procedure. They should be recalculated with expression (8).

Table 3. Ratio of integrated cross sections of (γ,n) and $(\gamma,2n)$ reactions before [1, 25] and after [26] correction

Nucleus	$\sigma_S^{\rm int}(\gamma,n)/\sigma_L^{\rm int}(\gamma,n)$ [both — MeV mb]		$\sigma_S^{\rm int}(\gamma,2n)/\sigma_L^{\rm int}(\gamma,2n)$ [both — MeV mb]	
	Before [1, 25]	After [26]	Before [1, 25]	After [26]
^{51}V	1.07*	1.00	0.79*	0.98
^{75}As	1.21*	1.00	1.22*	1.01
^{89}Y	1.33	1.00	0.75	1.05
^{90}Zr	1.26*	0.93	0.73*	1.05
^{115}In	1.09	1.00	0.55	1.02
^{116}Sn	1.10*	1.00	0.92*	0.98
^{117}Sn	0.97	1.00	0.46	0.96
^{118}Sn	1.06	1.00	0.49	0.93
^{120}Sn	0.99	1.00	0.59	0.97
^{124}Sn	0.82	1.00	0.75	1.02
^{127}I	1.34*	1.00	1.07*	0.99
^{133}Cs	1.24	1.00	0.65	1.04
^{159}Tb	1.37	1.00	0.68	0.94
^{165}Ho	1.20	1.00	1.03	1.03
^{181}Ta	1.68**	1.00	0.90	0.93
^{197}Au	1.18	1.00	0.62	1.06
^{208}Pb	1.54**	1.00	0.38	0.98
^{232}Th	0.84*	1.00	0.69*	0.94
^{238}U	0.81*	1.00	0.80*	1.01

* New data from [26].

** Incorrect initial data used.

The Livermore neutron multiplicity sorting procedure is correct. Therefore, the Livermore (γ,n) and $(\gamma,2n)$ cross sections are consistent with each other as well as with (γ,xn) cross sections, and both sets can be used, but again only after multiplication by coefficients $R^{\rm int}(\gamma,xn)$ or $\langle R_{\rm syst}^{\rm int}\rangle$.

4.2. Important Physical Consequences

The most important physical consequences are the following:

An intermediate GDR structure (peaks with widths on the order of hundreds of keV) exists; the BR data seem to be preferable for detailed study

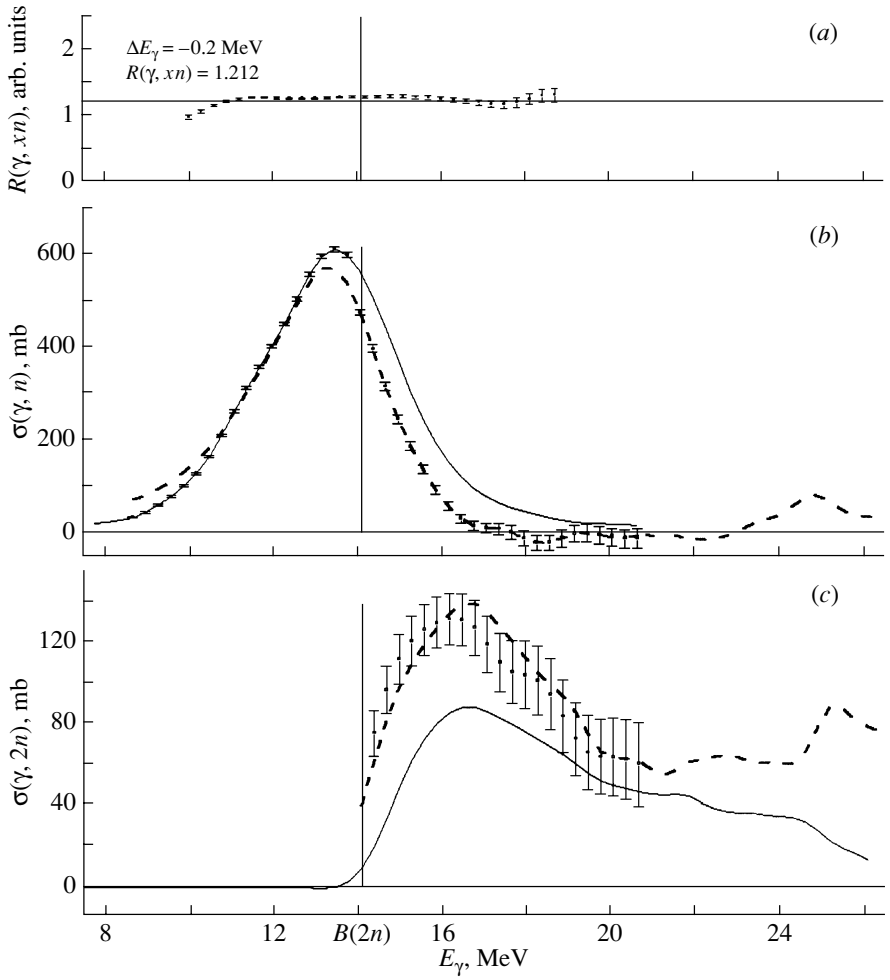

Fig. 6. Results of a joint correction [26] of the total and partial cross sections of photoneutron reactions for ^{208}Pb obtained at Saclay and Livermore: (a) ratios $R(E_\gamma)$ for (γ, xn) reaction cross sections; ΔE_γ and $R(\gamma, xn)$ are presented; (b) (γ, n) cross section [(solid curve) the initial Saclay data $\sigma_S(\gamma, n)$, (dots with error bars) the Saclay evaluated (8) data $\sigma^*_S(\gamma, n)$, (dashed curve) the Livermore evaluated data $R\sigma_L(\gamma, n)$]; (c) $(\gamma, 2n)$ reaction cross section data [(solid curve) the initial Saclay data $\sigma_S(\gamma, 2n)$, (dots with error bars) the Saclay evaluated data $\sigma^*_S(\gamma, 2n)$, (dashed curve) the Livermore evaluated data $R\sigma_L(\gamma, 2n)$].

of the GDR structure because the QMA data are strongly oversmoothed. The energy resolution ~ 1.3–1.6 MeV does not allow one to investigate properly the properties of resonance substructures having smaller width. An additional processing of the QMA data reveals that the GDR structure is close to that obtained from the BR data.

It appears that a statistical branch dominates a decay of GDR; the Saclay interpretation [30–33] of high-energy tails of (γ, n) cross sections as a contribution of high-energy neutrons from the GDR nonstatistical decay (this contribution is evaluated to be about 17–30%) seems to be very doubtful because of a small decrease in (γ, n) cross sections at energies higher than the $(\gamma, 2n)$ reaction threshold $B(2n)$; the corrections to the Saclay (γ, n) cross sections discussed above reduce them and put them in agreement with the Livermore data; i.e., the direct decay contribution is not more than 10–12%.

A large extravalue of the integrated cross section $\sigma^{\rm int}(\gamma, {\rm abs}) \approx (1.3$–$1.5) \cdot 60NZ/A$ (MeV mb) becomes questionable, being totally due to changing of the effective nucleon mass because of an influence of exchange forces [30–33]; errors in the Saclay procedure of neutron multiplicity sorting seriously affect the corresponding results for the total photoabsorption cross section evaluated by the use of the following combinations of cross section data: $(\gamma, {\rm abs}) = (\gamma, sn) + (\gamma, p)$ and $(\gamma, sn) = (\gamma, xn) - (\gamma, 2n)$; it is obvious that errors in $(\gamma, 2n)$ reaction data produce errors in both the (γ, sn) and the $(\gamma, {\rm abs})$ reaction data; the corresponding corrections reduce their values.

Some of the disagreements in the experimental data can be overcome by exploring methods similar to that described in the present paper; up to now, many data have been analyzed, evaluated, and put into consistency. However, new intensive really monoenergetic photon beams (High Intensity Gamma Source—HIGS [34] or similar) combined with effective measurement methods of photon flux, detector efficiency, neutron multiplicity sorting, etc., are needed to obtain really accurate and reliable experimental data for both shapes and magnitudes of total and partial cross sections of photoneutron reaction and photoabsorption, especially for medium and heavy nuclei.

ACKNOWLEDGMENTS

We acknowledge fruitful discussions with and help from Prof. I.M. Kapitonov and Drs. V.V. Chesnokov, N.N. Peskov, D.S. Rudenko, and M.E. Stepanov.

Investigations were carried out at the Centre for Photonuclear Experiments Data (MSU SINP Department of Electromagnetic Processes and Atomic Nuclei Interaction) and supported in part by the President of Russia, grant no. SS-1619.2003.2, and the Russian Foundation for Basic Research, project nos. 03-07-90434 and 04-02-16275.

REFERENCES

1. S. S. Dietrich and B. L. Berman, At. Data Nucl. Data Tables **38**, 199 (1988).
2. A. V. Varlamov, V. V. Varlamov, D. S. Rudenko, and M. E. Stepanov, INDC(NDS)-394, IAEA NDS (Vienna, Austria, 1999).
3. E. G. Fuller and H. Gerstenberg, *Photonuclear Data—Abstracts Sheets 1955–1982, NBSIR 83-2742* (USA Nat. Bureau Stand., 1986).
4. V. V. Varlamov, V. V. Sapunenko, and M. E. Stepanov, *Photonuclear Data 1976–1995, Index* (MSU Publ., Moscow, 1996).
5. B. L. Berman and S. C. Fultz, Rev. Mod. Phys. **47**, 713 (1975).
6. I. N. Boboshin, V. V. Varlamov, E. M. Ivanov, *et al.,* INDC(NDS)-427, IAEA NDS (Vienna, Austria, 2001), p. 49; http://depni.sinp.msu.ru/cdfe.
7. R. E. Sund, M. P. Baker, L. A. Kull, and R. B. Walton, Phys. Rev. **176**, 1366 (1968).
8. B. S. Ishkhanov, I. M. Kapitonov, E. V. Lazutin, *et al.*, Yad. Fiz. **12**, 892 (1970).
9. A. Veyssiere, H. Beil, R. Bergere, *et al.*, Nucl. Phys. A **227**, 513 (1974).
10. R. L. Bramblett, J. T. Caldwell, R. R. Harvey, and S. C. Fultz, Phys. Rev. **133**, B869 (1964); J. T. Caldwell, R. L. Bramblett, B. L. Berman, and R. R. Harvey, Phys. Rev. Lett. **15**, 976 (1965).
11. R. E. Pywell, M. N. Thompson, and B. L. Berman, Nucl. Instrum. Methods Phys. Res. **178**, 149 (1980).
12. J. G. Woodworth, K. G. McNeill, J. W. Jury, *et al.*, Phys. Rev. C **19**, 1667 (1979).
13. V. V. Varlamov, N. G. Efimkin, B. S. Ishkhanov, and V. V. Sapunenko, Vopr. At. Nauki Tekh., Ser. Yad. Konst., No. 1, 52 (1993).
14. L. M. Young, Ph. D. Thesis (University of Illinois, USA, 1972).
15. V. V. Varlamov, N. G. Efimkin, N. A. Lenskaja, and A. P. Chernjaev, Preprint No. 89-66/143, MSU INP (Moscow, 1989).
16. V. V. Varlamov and B. S. Ishkhanov, INDC(CCP)-433, IAEA NDS (Vienna, Austria, 2002).
17. N. G. Efimkin, B. S. Ishkhanov, Ju. P. Pyt'ev, and V. V. Varlamov, Preprint No. 91-35/239, MSU INP (Moscow, 1991).
18. N. G. Efimkin and V. V. Varlamov, in *Proceedings of the International Symposium on Nuclear Data Evaluation Methodology, BNL, USA, 12–16 Oct. 1992*, ISBN 981-02-1285-2 (World Sci., Singapore, 1993), p. 585.
19. Yu. P. Pyt'ev, *Methods for Experiment Analysis and Interpretation* (Moscow State Univ. Press, Moscow, 1990) [in Russian].
20. Yu. P. Pyt'ev, *Methods of Mathematical Modeling of Measuring-Computer-Aided Systems* (Nauka, Moscow, 2002) [in Russian].
21. B. S. Ishkhanov, I. M. Kapitonov, E. M. Lazutin, *et al.,* Vestn. Mosk. Gos. Univ., Ser. 3: Fizika, Astronomiya, No. 6, 606 (1970).
22. V. V. Varlamov, B. S. Ishkhanov, D. S. Rudenko, and M. E. Stepanov, Preprint No. 2002-19/703, MSU SINP (Moscow, 2003).
23. S. C. Fultz, R. L. Bramblett, J. T. Caldwell, and N. A. Kerr, Phys. Rev. **127**, 1273 (1962).
24. B. L. Berman, R. E. Pywell, S. S. Dietrich, *et al.,* Phys. Rev. C **36**, 1286 (1987).
25. E. Wolynec and M. N. Martins, Rev. Bras. Fis. **17**, 56 (1987).
26. V. V. Varlamov, N. N. Peskov, D. S. Rudenko, and M. E. Stepanov, Preprint No. 2003-2/715, MSU SINP (Moscow, 2003).
27. W. W. Gargaro and D. S. Onley, Phys. Rev. C **4**, 1032 (1971).
28. C. W. Soto Vargas, D. S. Onley, and L. E. Wright, Nucl. Phys. A **288**, 45 (1977).
29. W. R. Dodge, E. Hayward, and E. Wolinec, Phys. Rev. C **28**, 150 (1983).
30. R. L. Bergere, H. Beil, and A. Veyssiere, Nucl. Phys. A **121**, 463 (1968).
31. R. L. Bramblett, J. T. Caldwell, G. F. Auchampaugh, and S. C. Fultz, Phys. Rev. **129**, 2723 (1963).
32. R. Bergere, H. Beil, P. Carlos, and A. Veyssiere, Nucl. Phys. A **133**, 417 (1969).
33. H. Beil, R. Bergere, P. Carlos, and A. Lepretre, Nucl. Phys. A **227**, 427 (1974).
34. E. C. Schreiber, R. S. Canon, B. T. Crowley, *et al.,* Phys. Rev. C **61**, 061604 (2000).

Physics of Atomic Nuclei, Vol. 67, No. 9, 2004, pp. 1674–1681. From Yadernaya Fizika, Vol. 67, No. 9, 2004, pp. 1702–1709.

Electric Dipole Transitions in Neutron-Rich Nuclei*

T. Suzuki[1], H. Sagawa[2], and K. Hagino[3]

Received January 21, 2004

Abstract—The structure of neutron-rich nuclei in several isotopes is investigated by shell model calculations. We study the electric dipole ($E1$) transitions in C isotopes focusing on the interplay between the low-energy Pigmy strength and the giant dipole resonance (GDR). Reasonable agreement is obtained with available experimental data for the photoreaction cross sections in ^{12}C, ^{13}C, and ^{14}C with the inclusion of the quenching effects. A low-energy peak in the dipole strength in ^{15}C is associated with a single-particle motion of the $1s_{1/2}$ valence neutron relative to the ^{14}C core. The calculated transition strength below the GDR in C isotopes heavier than ^{15}C is found to exhaust about 50–80% of the cluster sum rule value and 12–16% of the classical Thomas–Reiche–Kuhn sum rule value. Next, we point out that the quadrupole and magnetic moments in the odd C isotopes strongly depend on configuration, which will be useful to determine the spin parities and the deformations of the ground states of these nuclei. The electric quadrupole ($E2$) transitions in even C isotopes are also studied. The isotopic dependence of the $E2$ transition strength is found to be reasonably well explained, although the calculated strength largely overestimates the unexpectedly small strength observed in ^{16}C. The $E1$ strength in ^{18}N and ^{19}N as well as in Ne isotopes is also investigated. © *2004 MAIK "Nauka/Interperiodica".*

1. INTRODUCTION

We have studied $E1$ strength in neutron-rich O isotopes by using the shell model [1] and found that the Pigmy strength exhausts about 10% of the Thomas–Reiche–Kuhn (TRK) sum rule and more than 40% of the cluster sum rule [2],

$$S_C = \frac{\hbar^2}{2m}\frac{9}{4\pi}\frac{(Z_1N_2 - Z_2N_1)^2}{AA_1A_2}, \qquad (1)$$

where $A_1 = N_1 + Z_1$ and $A_2 = N_2 + Z_2$. Calculated values of the Pigmy strength are in good agreement with the recent experimental observations in ^{20}O and ^{22}O [3].

Here, we extend our work on O isotopes and study the structure of neutron-rich C, N, and Ne isotopes by the shell model. The structure of C isotopes is studied in Section 2. The $E1$ strength in $^{12-19}$C is investigated with focus on the interplay between the low-energy Pigmy strengths and the giant dipole resonance (GDR). The configuration dependence of the quadrupole (Q) moments and magnetic (μ) moments in the odd C isotopes is also discussed. We also study the isotopic dependence and the magnitude of the $E2$ transition strengths in the even C isotopes. In Section 3, the $E1$ transition strength in N and Ne isotopes is studied. A summary is given in Section 4.

Ratios of the EWS of the strength up to $E_x = E_{\max}$ to the TRK sum rule values (experimental values taken from [6, 7] and calculated values are shown in the third and fourth column, respectively; experimental values compared to the calculated ones are represented in the last column)

A	$E_{\max}$, MeV	Experiment			Cal.	Exp./Cal.
		(γ, n)	(γ, p)	total		
^{12}C	30	0.24	0.40	0.64	0.91	0.70
	100			1.62		
	150			1.86		
^{13}C	30	0.50	0.22	0.72	0.98	0.73
^{14}C	30	0.53	0.08	0.61	1.04	0.59
				0.43 ± 0.06 ($T_<$)	0.58	0.74
				0.18 ± 0.04 ($T_>$)	0.45	0.40

*This article was submitted by the authors in English.

[1]Department of Physics, College of Humanities and Sciences, Nihon University, Tokyo, Japan; e-mail: suzuki@chs.nihon-u.ac.jp

[2]Center for Mathematical Sciences, the University of Aizu, Aizu Wakamatsu, Fukushima, Japan; e-mail: sagawa@u-aizu.ac.jp

[3]Yukawa Institute for Theoretical Physics, Kyoto University, Kyoto, Japan; e-mail: hagino@yukawa.kyoto-u.ac.jp

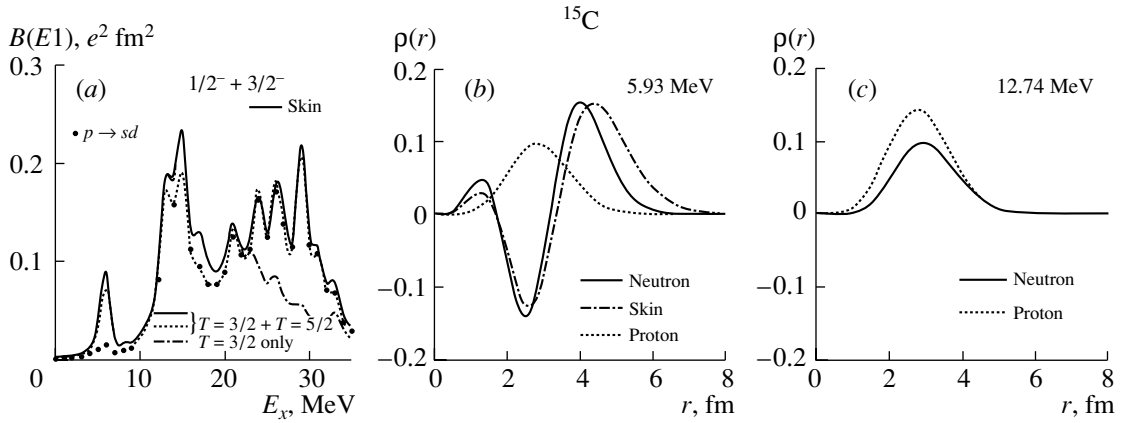

Fig. 1. (*a*) Calculated $B(E1)$ strength for ^{15}C with the use of the WBP10 interaction. The solid and dashed curves include the results of both $T = 3/2$ and $T = 5/2$ states, while the dash-dotted curve includes only those of $T = 3/2$ states. The solid curve is obtained with the effects of neutron skin. The dotted curve shows contributions from the $0p \to 1s0d$ transitions. (*b*) Neutron and proton transition densities for the Pigmy state at $E_x = 5.93$ MeV. The dash-dotted curve includes the neutron skin effects. (*c*) The same as in (*b*) for the GDR state at $E_x = 12.74$ MeV.

2. STRUCTURE OF C ISOTOPES

2.1. Electric Dipole Strength in C Isotopes

We study the $E1$ strength of C isotopes by shell model calculations with the use of the Warburton–Brown interaction (WBP10) [4]. A model space of $0s$–$0p$–$1s0d$–$1p0f$ shells including up to $3\hbar\omega$ excitations is taken for $^{12-14}$C. The $B(E1)$ transition strength is defined as

$$B(E1,\omega_n) = \frac{1}{2I_i+1}|\langle n||\hat{O}^{\lambda=1}||I_i\rangle|^2, \qquad (2)$$

where I_i is the angular momentum of the initial state and $|n\rangle$ is the nth excited 1^- state with the excitation energy $\hbar\omega_n$. The $E1$ transition operator is given by

$$\hat{O}^{\lambda=1}_\mu = -e\frac{Z}{A}\sum_i^N r_i Y_{1\mu}(\hat{r_i}) + e\frac{N}{A}\sum_i^Z r_i Y_{1\mu}(\hat{r_i}) \quad (3)$$

subtracting the center-of-mass motion. The transition strength is averaged by a weight factor of Lorenzian form with a width parameter of $\Gamma = 1$ MeV (see [5]). Calculated results of C isotopes are shown in [5]. The calculated and observed strength below $E_x \sim 15$ MeV in ^{13}C and ^{14}C is due to the excitation of the valence neutrons outside the ^{12}C core. Energies of the dipole states are rather well reproduced by our calculations, while further quenching is found to be necessary to explain the experimental magnitude of the strength. Comparison of the energy-weighted sum (EWS) to the TRK sum rule value is shown in the table, which indicates that the calculations including up to $3\hbar\omega$ excitations need further quenching by about 30–40% up to $E_x = 30$ MeV. A large fraction of the strength is pushed up beyond $E_x \sim 30$ MeV. When these quenchings are taken into account, the observed photoreaction cross sections are well explained (see [5] for details).

We now discuss ^{15}C. The calculated strength is shown in Fig. 1*a*. Contributions due to $0p \to 1s0d$ transitions are denoted by the dotted curve, which looks similar to the strength of ^{14}C. The low-energy peak at $E_x \sim 6$ MeV in the strength of ^{15}C, therefore, comes from the excitation of the $1s_{1/2}$ valence neutron to the $1p$ shell. Proton and neutron transition densities defined by

$$\rho_p(r) = \frac{N}{A}M_p(r), \quad \rho_n(r) = -\frac{Z}{A}M_n(r) \qquad (4)$$

with

$$M_{n(p)}(r) \qquad (5)$$
$$= \sum_{\mu,f}|\langle\phi_f(r)|e\sum_{i\in n(p)} r_i Y_{1\mu}(\hat{r}_{i,n(p)})|\phi_{\rm g.s}(r)\rangle|^2$$

are shown in Figs. 1*b* and 1*c* for a Pigmy state and a GDR state, respectively. For the Pigmy state at $E_x = 5.93$ MeV, the neutron and proton transition densities contribute coherently in the large radial region at $r \geq 4$ fm. The $\rho_n(r)$ is mainly caused by the $1s_{1/2} \to 1p_{3/2}$ transition. Here, the neutron motion and the proton motion represented by $M_n(r)$ and $M_p(r)$, respectively, are opposite in sign; that is, the contribution is isovector. Note that the isovector and isoscalar transition densities are defined by

$$\rho_{\rm iv}(r) = -\frac{1}{2}(M_n(r) - M_p(r))$$

and

$$\rho_{\rm is}(r) = \frac{N-Z}{2A}(M_n(r) + M_p(r)),$$

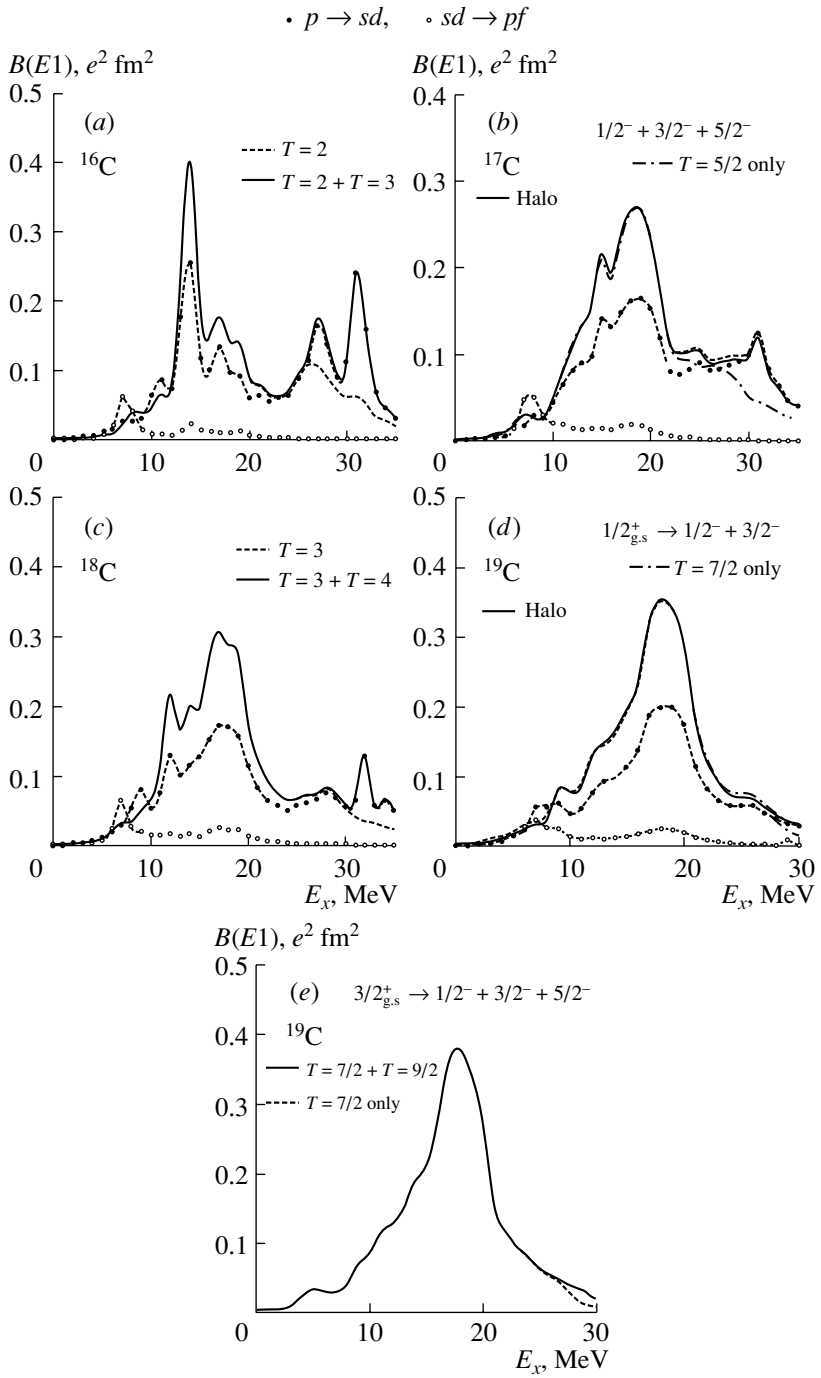

Fig. 2. Calculated $B(E1)$ strength for C isotopes with $N = 10-13$ with the use of the WBP10 interaction and the configurations of $1\hbar\omega$ excitations. The solid curve (a, c, e) includes the results of both $T_<$ and $T_>$ states, while the dashed or dash-dotted curves include only those of $T_<$ states. Closed and open circles represent contributions from the $0p \to 1s0d$ and $1s0d \to 1p0f$ transitions, respectively. (b) The solid curve includes the halo effects. (d) The ground state is taken to be $1/2^+$; the solid curve includes the halo effects. (e) The ground state is taken to be $3/2^+$.

respectively. The strength of the resonance amounts to about half of the strength given by Eq. (1) for ^{14}C and the valence neutron as the two clusters. Thus, the Pigmy mode can be considered as the single-particle motion of the valence $1s_{1/2}$ neutron relative to the ^{14}C core. For the GDR state at $E_x = 12.74$ MeV, the coherent isovector contribution at $r \sim 3$ fm is the dominant one.

The calculated $E1$ strength for $^{16-19}$C is shown in Fig. 2 (see [5] for details). Here, we add a comment

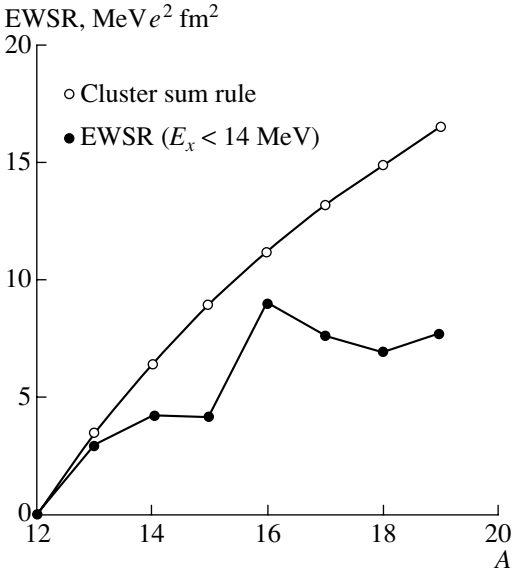

Fig. 3. Ratios of the calculated EWS up to $E_x = 14$ MeV to the cluster sum rule values in the C isotopes.

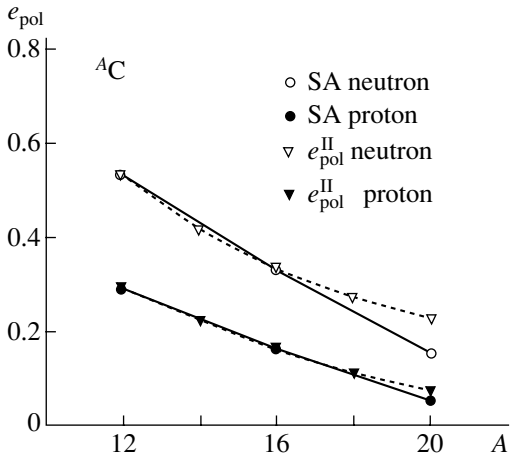

Fig. 4. Isotope dependence of the neutron and proton polarization charges $e^{(SA)}_{pol}$ obtained by HF + RPA method [8]. Those denoted by e^{II}_{pol} are given by parametrized formula (6).

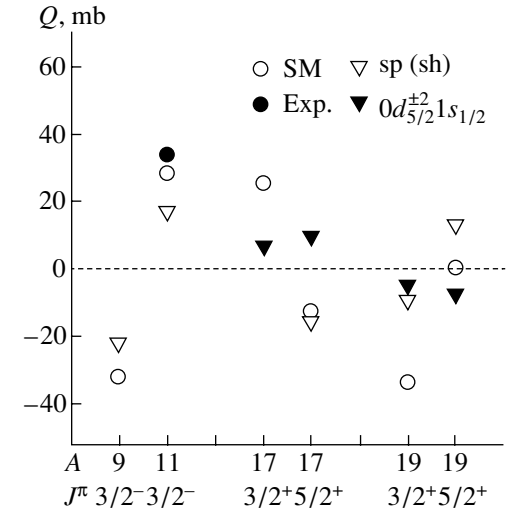

Fig. 5. Q moments for the odd C isotopes. Open circles denote the results of the shell model calculations obtained with the use of $e^{(SA)}_{pol}$. Open triangles denote single-particle or single-hole values, while closed triangles give results of the $0d^{\pm2}_{5/2}1s_{1/2}$ configuration. These values include the effects of the polarization charges, e^{II}_{pol}. The closed circle is the experimental value for ^{11}C [9].

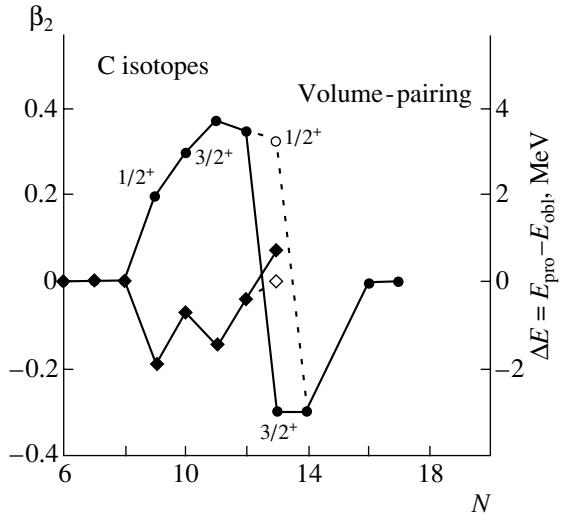

Fig. 6. Neutron number dependence of the deformation of C isotopes. Closed (open) circles are obtained by using the volume-pairing (density-dependent pairing) force. Closed (open) diamonds show the energy difference between prolate and oblate deformations obtained for the volume (density-dependent) pairing force.

that the $0p \to 1s0d$ and the $1s0d \to 1p0f$ transitions contribute destructively in the low-energy region below $E_x \sim 10$ MeV and that the Pigmy mode does not develop well in these isotopes. We find a coherent enhancement of the low-energy peak at $E_x \sim 12$ MeV in ^{16}C as in the GDR region in $^{16-19}$C. The separation of the Pigmy mode and the GDR becomes obscure in heavier isotopes, $^{17-19}$C. The calculated EWS values below $E_x = 14$ MeV, as well as the cluster sum rule values, are shown in Fig. 3. The ratio EWS/S_C amounts to about 80% for ^{16}C and decreases to ~50% in heavier isotopes.

2.2. Q Moments, μ Moments, and E2 Transitions

We study electromagnetic moments and transitions in C isotopes by the shell model calculations.

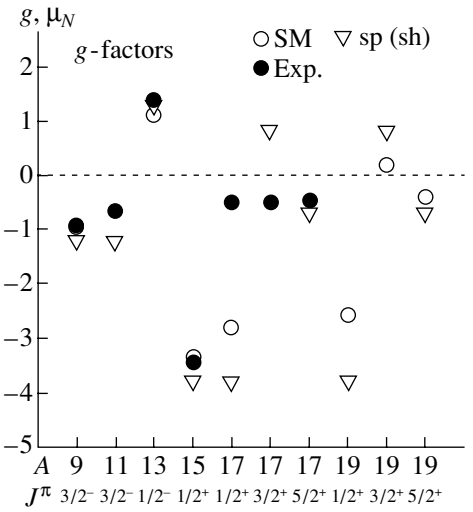

Fig. 7. Magnetic moments for the odd C isotopes. Open circles show the results of the shell model calculations, while closed circles give experimental values [14–16]. In case of the $3/2^+$ state in ^{17}C, the calculated g-factor coincides with the observation [11]. Open triangles denote the single-particle or single-hole values.

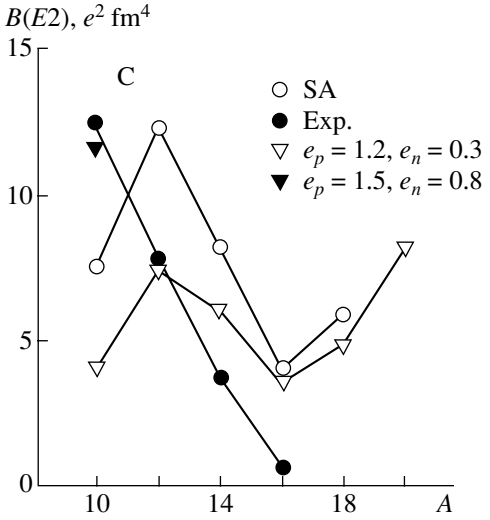

Fig. 8. $B(E2)$ values for the $2_1^+ \to 0_{g.s}$ transitions in even C isotopes. Open circles show the results of the shell model calculation with the use of the polarization charges $e^{\rm II}_{\rm pol}$ given by Eq. (6). Open and closed triangles are obtained with $e_p = 1.2$, $e_n = 0.3$ and $e_p = 1.5$, $e_n = 0.8$, respectively. Closed circles denote experimental values [17, 18].

We first discuss the Q moments. The WBP10 interaction is adopted within the $0\hbar\omega$ space with the inclusion of effective charges. State-dependent polarization charges, $e^{\rm (SA)}_{\rm pol}$ [8], given by the microscopic particle vibration coupling model (Hartree–Fock + random phase approximation) are used. The polarization charge can be parametrized as

$$e^{\rm II}_{\rm pol}/e = a\frac{Z}{A} + b\frac{N-Z}{A} + \left(c + d\frac{Z}{A}\frac{N-Z}{A}\right)\tau_z \qquad (6)$$

with $a = 0.82$, $b = -0.25$, $c = 0.12$, and $d = -0.36$ to reproduce the values of $e^{\rm (SA)}_{\rm pol}$ for ^{12}C and ^{16}C. They are shown in Fig. 4. Both the neutron (ν) and proton (π) polarization charges decrease as the neutron excess increases.

The Q moments obtained by using these polarization charges are shown in Fig. 5. Open circles denote results of the shell model calculations with the use of $e^{\rm (SA)}_{\rm pol}$. Single-particle or single-hole values with the use of $e^{\rm II}_{\rm pol}$ are given by open triangles. The configurations for ^{9}C and ^{11}C are $\nu p_{3/2}$ and $\nu p^{-1}_{3/2}$, respectively. The configurations for ^{17}C and ^{19}C are $\nu d_{5/2}1s^2_{1/2}$ and $\nu d^{-1}_{5/2}$ ($\nu d^5_{5/2}$), respectively, for the $5/2^+$ state. For the $3/2^+$ state of ^{17}C, a case for a single-particle configuration of $\nu d_{3/2}$ is given.

Closed triangles are obtained for $\nu d^{\pm 2}_{5/2}1s_{1/2}$ configuration with the use of $e^{\rm II}_{\rm pol}$. The $\nu d^2_{5/2}(J=2)1s_{1/2}$ and $\nu d^{-2}_{5/2}(J=2)1s_{1/2}$ are possible simple configurations for ^{17}C and ^{19}C, respectively, as the $\nu d^3_{5/2}$ or $\nu d^3_{5/2}1s^2_{1/2}$ configuration corresponding to the middle of the $d_{5/2}$ shell results in the vanishing of the Q moments. The Q moments are given by $\mp\frac{2}{5}e^n_{\rm pol}Q_{\rm sp}(d_{5/2})$ for $3/2^+$ and $\mp\frac{4}{7}e^n_{\rm pol}Q_{\rm sp}(d_{5/2})$ for $5/2^+$ for the $\nu d^{\pm 2}_{5/2}(J=2)1s_{1/2}$ configuration. Here, $e^n_{\rm pol}$ is the neutron polarization charge and $Q_{\rm sp}(d_{5/2})$ is the single-particle value of the Q moment for $d_{5/2}$. Note that the signs of the Q moments for ^{17}C and ^{19}C are opposite.

The shell model values of the Q moments are obtained by the admixtures among these configurations, and their magnitudes are usually enhanced compared to those of the simple configurations. Nevertheless, the difference of the signs between ^{17}C and ^{19}C can be understood from those of the simple configurations.

A deformed Skyrme HF + BCS calculation [10] shows that ^{17}C is prolate, while ^{19}C is oblate, though the deformation surfaces are rather soft and there are also energy minima on the opposite deformation sides (see Fig. 6). In the case of $3/2^+$ or $5/2^+$, this seems to be consistent with our shell model calculations which show the change of the sign of the Q moments in ^{17}C and ^{19}C. The spin of the ground state of ^{17}C has been assigned as $3/2^+$ [11]. The spin of ^{19}C is assigned as

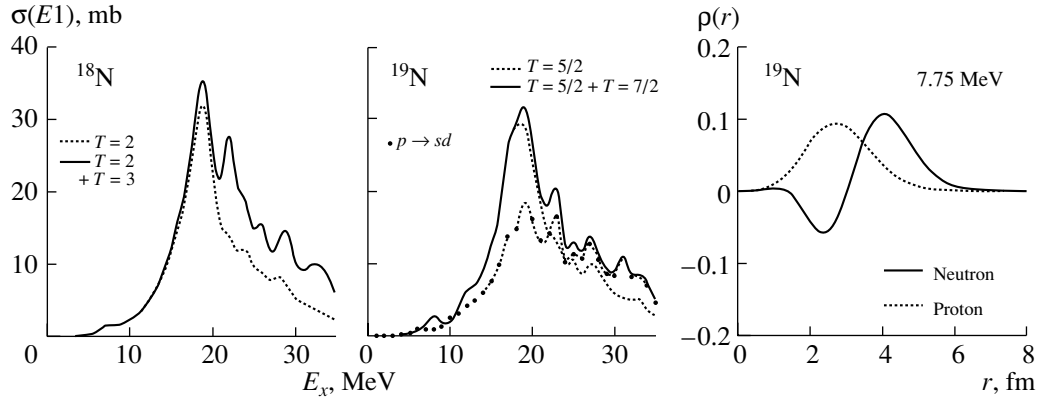

Fig. 9. Calculated photoreaction cross sections for ^{18}N and ^{19}N with the use of the WBP10 interaction. The dotted curve shows contributions from the $0p \to 1s0d$ transitions. Neutron and proton transition densities for the Pigmy state at $E_x = 7.75$ MeV are shown in the right panel.

$1/2^+$ in the Coulomb breakup reactions [12], while it was not determined in [13].

Calculated values for the magnetic (μ) moments are shown in Fig. 7. Here, $g_s^{\rm eff}/g_s^{\rm free} = 0.9$ is used for neutrons. The values of the μ moments are found to be sensitive to the configurations as in the case for the Q moments, which is useful to find out the spin parities and the deformations of the ground states of these nuclei.

Let us now discuss the $E2$ transitions in the even C isotopes. Calculated and experimental $B(E2)$ values for the $2_1^+ \to 0_{\rm g.s}^+$ transitions are shown in Fig. 8. The shell model values obtained with the use of $e_{\rm pol}^{\rm II}$ are larger than the experimental values except for ^{10}C, for which larger effective charges of $e_p = 1.5$ and $e_n = 0.8$ are needed. For $^{12-16}$C, the isotopic dependence of the observed values [17, 18] is well explained by that of $e_{\rm pol}^{\rm II}$, but their magnitudes are smaller than the calculated ones. In particular, the observed $B(E2)$ value is quite small for ^{16}C [18], which suggests some exotic structure as yet unknown in the isotopes. Other models [19] also fail to reproduce this abnormally small $B(E2)$ value. It would also be interesting to find out whether the $B(E2)$ value increases for ^{18}C as the calculation predicts. This increase comes from that of the neutron contribution.

3. N AND Ne ISOTOPES

We investigate the $E1$ strength in N and Ne isotopes. Photoreaction cross sections for ^{18}N and ^{19}N obtained by the shell model calculations are shown in Fig. 9. The photoreaction cross section is given by

$$\sigma(\omega) = \frac{16\pi^3}{9\hbar c}\omega\frac{dB(E1,\omega)}{d\omega}, \qquad (7)$$

where $B(E1,\omega)$ is the averaged transition strength by a Lorentzian. The Pigmy peak is found at $E_x \sim 8$ MeV for ^{19}N. The transition densities are also shown in Fig. 9 for the Pigmy state at $E_x = 7.75$ MeV. The main contribution for the neutron transition density comes from the $0d_{5/2} \to 1p_{3/2}$ transition. A coherence of the neutron and proton contributions is found at $r \geq 3$ fm.

The $E1$ strength and deformation properties of even Ne isotopes are studied. A deformed HF + BCS calculation with pairing effects (SkM^* interaction with volume pairing) [10] leads to deformations in the Ne isotopes. ^{20}Ne and ^{22}Ne are found to be prolate

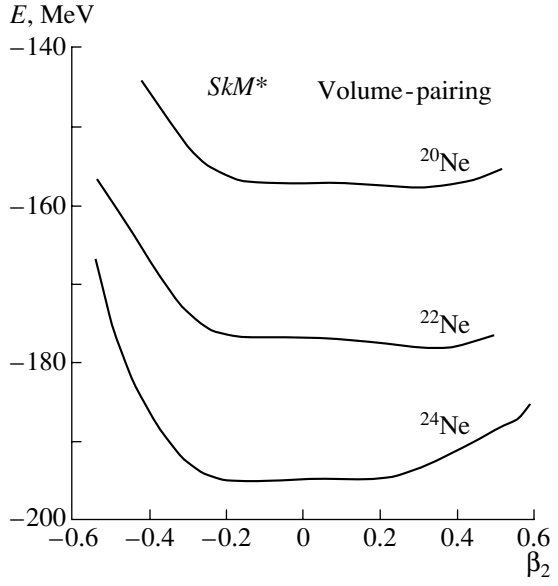

Fig. 10. The energy surfaces for the ground states of even Ne isotopes obtained by the HF + BCS calculation with a Skyrme interaction SkM^* together with the volume-type delta-pairing interaction.

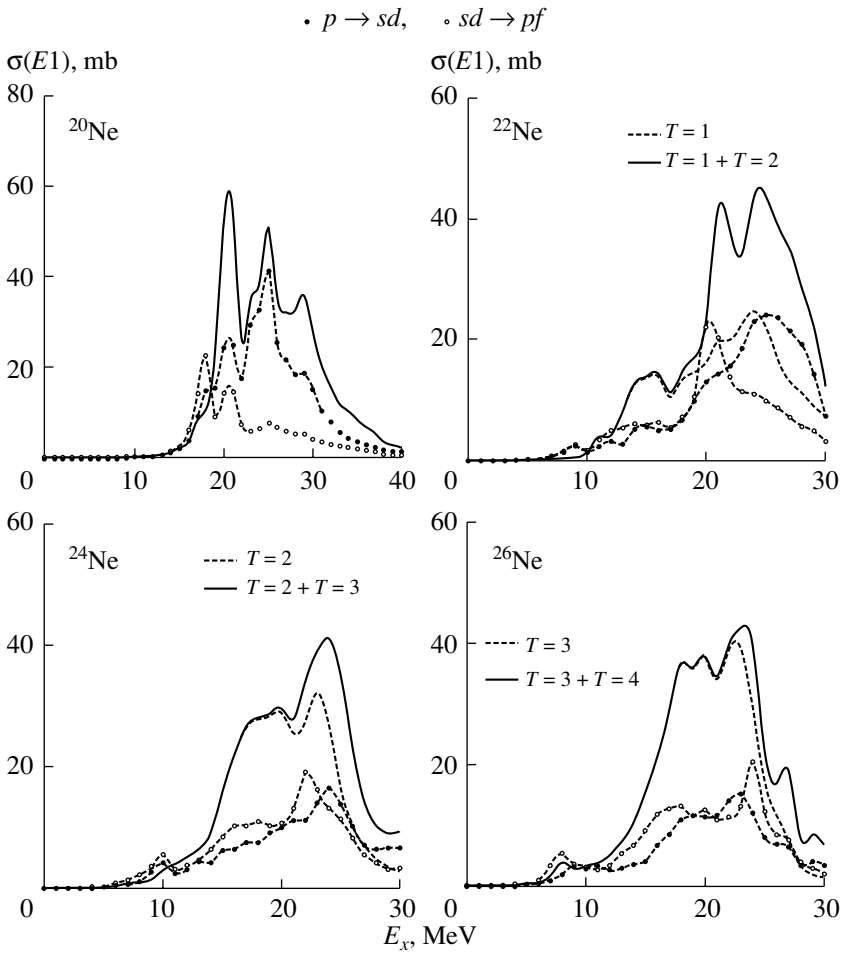

Fig. 11. Calculated photoreaction cross sections for Ne isotopes with the use of the WBP10 interaction and the configurations of $1\hbar\omega$ excitations. The solid curve includes the results of both $T_<$ and $T_>$ states, while the dashed curve includes only those of $T_<$ states. Closed and open circles represent contributions from the $0p \to 1s0d$ and $1s0d \to 1p0f$ transitions, respectively.

with $\beta = 0.29$ and $\beta = 0.33$, respectively, while ^{24}Ne is found to be oblate with $\beta = -0.14$, as shown in Fig. 10. The deformation properties for $^{26-32}$Ne are investigated in [20]. The deformation surface for ^{26}Ne is found to be rather soft.

Calculated photoreaction cross sections are shown in Fig. 11 for $^{20-26}$Ne. We find Pigmy modes in ^{22}Ne at $E_x \sim 15$ MeV and in ^{26}Ne at $E_x \sim 8$ MeV. The two-peak structures seen in Fig. 11 for ^{20}Ne, ^{22}Ne, and ^{24}Ne could be attributed to the deformation effects.

4. SUMMARY

We have studied Pigmy and GDR in C isotopes. For $^{12-14}$C, the shell model calculations explain well the observed photoreaction cross sections at $E_x \leq 30$ MeV with the quenching effects. In ^{15}C, a Pigmy resonance is found at $E_x \sim 6$ MeV, which can be assigned as a single-particle motion of the valence $1s_{1/2}$ neutron relative to the ^{14}C core. For $^{15-19}$C, the EWS of the $E1$ strength below $E_x = 14$ MeV amounts to 50–80% of the cluster sum rule. The separation between the Pigmy and the GDR modes becomes obscure in heavier isotopes.

We point out the configuration dependence of the Q moments and μ moments in the odd C isotopes, which can be attributed to the shell effects. This dependence can be used to determine the spin parities as well as the deformation properties of the ground states of the isotopes. The isotope dependence of the $B(E2)$ values in even C isotopes is found to be rather well explained, while the experimental values are found to be smaller in $^{12-16}$C, in particular, in ^{16}C, where the observed $B(E2)$ value almost vanishes. This suggests an exotic structure of ^{16}C still to be discovered.

Finally, we have studied the $E1$ strength in N and Ne isotopes. Pigmy modes are found in ^{19}N, ^{22}Ne, and ^{26}Ne. The two-peak structure in the GDR in

$^{20-24}$Ne would be attributed to the deformation effects.

ACKNOWLEDGMENTS

This work was supported in part by a grant-in-aid to promote advanced scientific research from the Ministry of Education, Culture, Sports, Science, and Technology.

REFERENCES

1. H. Sagawa and T. Suzuki, Phys. Rev. C **59**, 3116 (1999).
2. Y. Alhassid, M. Gai, and G. F. Bertsch, Phys. Rev. Lett. **49**, 1482 (1982); H. Sagawa and M. Honma, Phys. Lett. B **251**, 17 (1990).
3. A. Leistenschneider *et al.*, Phys. Rev. Lett. **86**, 5442 (2001).
4. E. K. Warburton and B. A. Brown, Phys. Rev. C **46**, 923 (1992); B. A. Brown, A. Etchegoyen, and W. D. M. Rae, OXBASH, Oxford, Buenos-Aires, Michigan State, Shell Model Program, MSU-NSCL, Report No. 524 (1986).
5. T. Suzuki, H. Sagawa, and K. Hagino, Phys. Rev. C **68**, 014317 (2003).
6. D. J. McLean, M. N. Thompson, D. Zubanov, *et al.*, Phys. Rev. C **44**, 1137 (1991).
7. J. Ahrens, H. Borchert, K. H. Czock, *et al.*, Nucl. Phys. A **251**, 479 (1975).
8. H. Sagawa and K. Asahi, Phys. Rev. C **63**, 064310 (2001).
9. *Table of Isotopes*, Ed. by R. B. Firestone *et al.* (Wiley, New York, 1996).
10. T. Suzuki, H. Sagawa, and K. Hagino, in *Proceedings of the International Symposium on Frontiers of Collective Motions (CM2002)* (in press); H. Sagawa, T. Suzuki, and K. Hagino, Nucl. Phys. A **722**, 183 (2003).
11. H. Ogawa *et al.*, Eur. Phys. J. A **13**, 81 (2002).
12. D. Bazin *et al.*, Phys. Rev. C **57**, 2156 (1998); T. Nakamura *et al.*, Phys. Rev. Lett. **83**, 1112 (1999); V. Maddalena *et al.*, Phys. Rev. C **63**, 024613 (2001).
13. Rituparna Kanungo, I. Tanihata, Y. Ogawa, *et al.*, Nucl. Phys. A **677**, 171 (2000).
14. K. Matsuta *et al.*, Nucl. Phys. A **588**, 153c (1995).
15. P. Raghaven, At. Data Nucl. Data Tables **42**, 189 (1989).
16. K. Asahi *et al.*, AIP Conf. Proc. **570**, 109 (2001).
17. S. Raman *et al.*, At. Data Nucl. Data Tables **36**, 1 (1987).
18. N. Imai *et al.*, Phys. Rev. Lett. **92**, 062501 (2004).
19. Y. Kanada-En'yo and H. Horiuchi, Prog. Theor. Phys. Suppl. **142**, 205 (2001).
20. P.-G. Reinhard, D. J. Dean, W. Nazarewicz, *et al.*, Phys. Rev. C **60**, 014316 (1999).

Physics of Atomic Nuclei, Vol. 67, No. 9, 2004, pp. 1682–1687. From Yadernaya Fizika, Vol. 67, No. 9, 2004, pp. 1710–1715.

Low-Lying Dipole Excitations in Nuclei in the Mass Regions of the New Dynamical Symmetries*

M. Scheck[1)], P. von Brentano[2)], C. Fransen[2)], A. Gade[2)], H. von Garrel[1)], J. Jolie[2)], U. Kneissl[1)], C. Kohstall[1)], A. Linnemann[2)], N. Pietralla[2)], H. H. Pitz[1)], F. Stedile[1)], S. Walter[1)], and V. Werner[2)]**

Received January 21, 2004

Abstract—Experimental indications for the nuclear phase transitions described by the new symmetries $E(5)$ and $X(5)$ are discussed for the stable Ba, Nd, and Gd isotopes. Their low-lying dipole excitations, systematically investigated at the bremsstrahlung facility of the 4.3-MV Stuttgart Dynamitron accelerator, provide indications for the phase transitional behavior, including the proposed critical point candidates.

1. MOTIVATION

The dynamical symmetries of the interacting boson approximation (IBA) [1] are well established. The limits can be associated with different nuclear shapes: $U(5)$ describing spherical vibrators, $SU(3)$ for axially symmetric rotors, and $O(6)$ for the γ-soft nuclei.

In the last few years, new ideas were developed to describe the shape transitions between these limits. With the Bohr Hamiltonian [2] the geometric collective approach leads to the new symmetries $E(5)$ [3] and $X(5)$ [4]. These symmetries describe the critical points of quantum phase transitions in a finite nuclear system. The $X(5)$ symmetry describes the critical point of the phase transition from $U(5)$ to $SU(3)$. This phase transition is of first order. Therefore, both phases (spherical vibrator, axially symmetric rotor) may coexist (see Fig. 1). Candidates which show the predicted properties of the $X(5)$ symmetry (e.g., $E_{4_1^+}/E_{2_1^+} = 2.91$, $E_{0_2^+}/E_{2_1^+} = 5.67$) are ^{150}Nd [5], ^{154}Gd, and especially ^{152}Sm [6]. The other phase transition from spherical vibrator $U(5)$ to $O(6)$ γ-soft nuclei is of second order and described by the $E(5)$ symmetry. The ^{134}Ba nucleus is proposed to fulfill the spectral properties [7] (e.g., $E_{4_1^+}/E_{2_1^+} = 2.20$, $E_{0_2^+}/E_{2_1^+} = 3.03$).

The question to be investigated in the present contribution is whether this transitional behavior can be observed in the systematics of low-lying dipole excitations too. Low-lying electric dipole excitations are, e.g., the so-called two-phonon excitations [8] in spherical nuclei and the excitations of the bandheads of the different octupole bands ($K = 0$ and $K = 1$) in deformed nuclei. Strong low-lying magnetic dipole excitations occur in deformed nuclei, e.g., the $M1$ scissors mode [9, 10].

2. EXPERIMENTAL METHOD

Because of the small angular momentum transfer and its strength selectivity, the scattering of real photons is an excellent tool for the investigation of dipole excitations in stable nuclei. Using a photon spectrum with a continuous energy distribution produced by bremsstrahlung, the dipole excitations in an energy

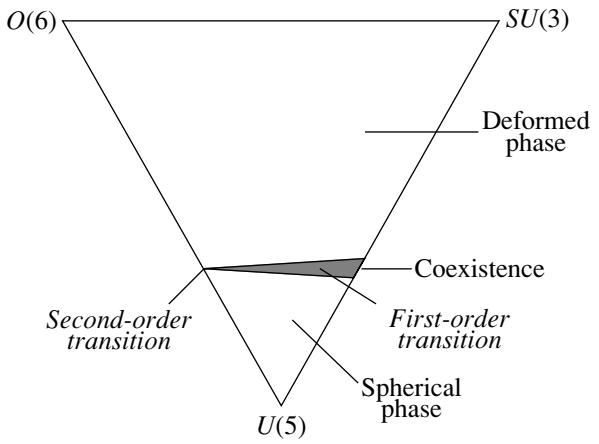

Fig. 1. The Casten triangle showing the classical IBA limits. The phase transitional regions are pointed out.

*This article was submitted by the authors in English.

[1)]Institut für Strahlenphysik, Universität Stuttgart, Stuttgart, Germany.
[2)]Institut für Kernphysik, Universität zu Köln, Köln, Germany.
**e-mail: scheck@ifs.physik.uni-stuttgart.de

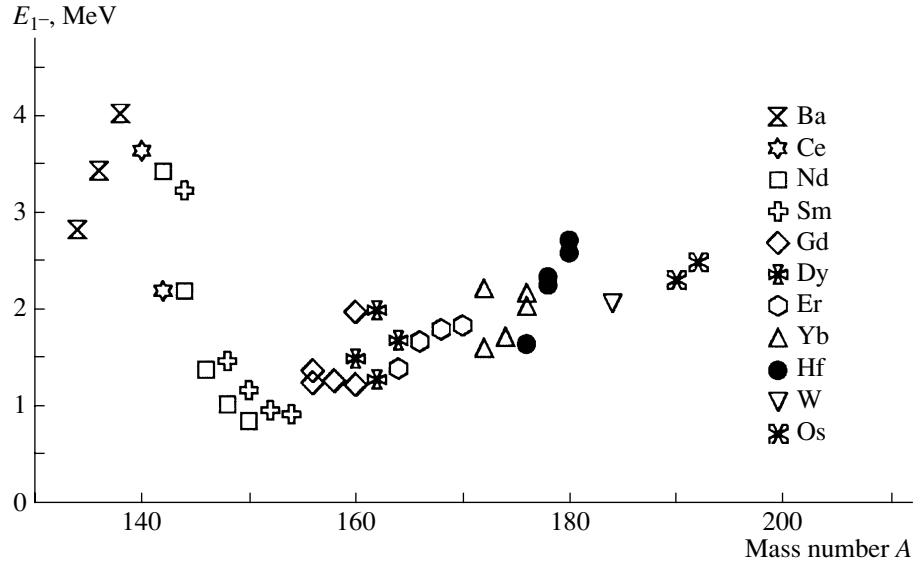

Fig. 2. The excitation energy of the lowest-lying 1^- states plotted as a function of the mass number. Remarkable is the minimum at $A \approx 150$, where the nuclei of the $X(5)$ symmetry are expected.

range up to the endpoint of the bremsstrahlung spectrum can be measured simultaneously. Therefore, one gets the excitation energy E_γ and the integrated scattering cross section for the level

$$I_{S,f} = g \left(\frac{\pi\hbar c}{E_\gamma}\right)^2 \frac{\Gamma_0\Gamma_f}{\Gamma}\frac{W(\theta)}{4\pi}, \qquad (1)$$

$$g = \frac{2J+1}{2J_0+1}.$$

Here, Γ_i and Γ are the partial and total decay widths; $W(\theta)$ is the normalized angular distribution, which can be determined by the comparison of spectra measured at different angles to the incoming photon beam. In the case of an even–even nucleus, the so-called spin factor g is equal to 3 for a dipole excitation. The reduced ground-state transition width $\Gamma_0^{\rm red}$ for a dipole transition $\Gamma_0^{\rm red} = \Gamma_0/E_\gamma^3$ is related to the reduced electric or magnetic dipole transition probabilities $B(\Pi 1)$. Furthermore, it is possible to determine the spins and to assign the parities of the excited states. More detailed descriptions can be found in the preceding article [11].

3. DIPOLE EXCITATIONS IN THE MASS REGION OF THE $X(5)$ SYMMETRY

In this paper, we want to concentrate on the mass region from $N \geq 82$ as representatives of $U(5)$ spherical vibrators to $N \approx 100$ as representatives of the $SU(3)$ axially symmetric rotors, including the critical point candidates ^{150}Nd, ^{152}Sm, ^{154}Gd with $N = 90$ of the new $X(5)$ symmetry. In the following, the development of $E1$ and $M1$ transitions shall be in the limelight.

3.1. E1 Transitions

The shape transitional behavior was already observed in the early 1970s, when the giant dipole resonance (GDR) was investigated thoroughly. In the neodymium and samarium isotopic chains, the onset of the deformation splitting takes place in the proposed critical point candidates ^{150}Nd and ^{152}Sm [12, 13].

For the low-lying $E1$ strength in Fig. 2, the excitation energies of the first 1^- states are plotted as a function of the mass number. In spherical nuclei around the $N = 82$ neutron shell closure, these levels have rather high excitation energies up to 4 MeV, which drop rapidly with the onset of the deformation. A minimum is obvious at the critical point candidates. At larger mass numbers, we see slightly increasing energies until the observed $E1$ strength breakdown at mass numbers of about $A \approx 180$ (see Fig. 3).

To understand this feature, the internal structure of the first 1^- states has to be considered. In the vicinity around the closed shell, the first 1^- state is of two-phonon character, where the first 2^+ quadrupole and the first 3^- octupole phonons couple nearly harmonically ($E_{2^+} + E_{3^-} \approx E_{1^-}$). This coupling leads to a quintuplet of states with spins and parities 1^- to 5^-, of which in nuclear resonance fluorescence (NRF) experiments only the 1^- state is excited. The drop in the excitation energies of the 2^+ and 3^- phonons explains the drop in the excitation energy of the first 1^- state upon stepping away from the closed shell. In the middle of the shell, the first excited 1^- states are given by the bandheads of the $K = 0$ octupole bands.

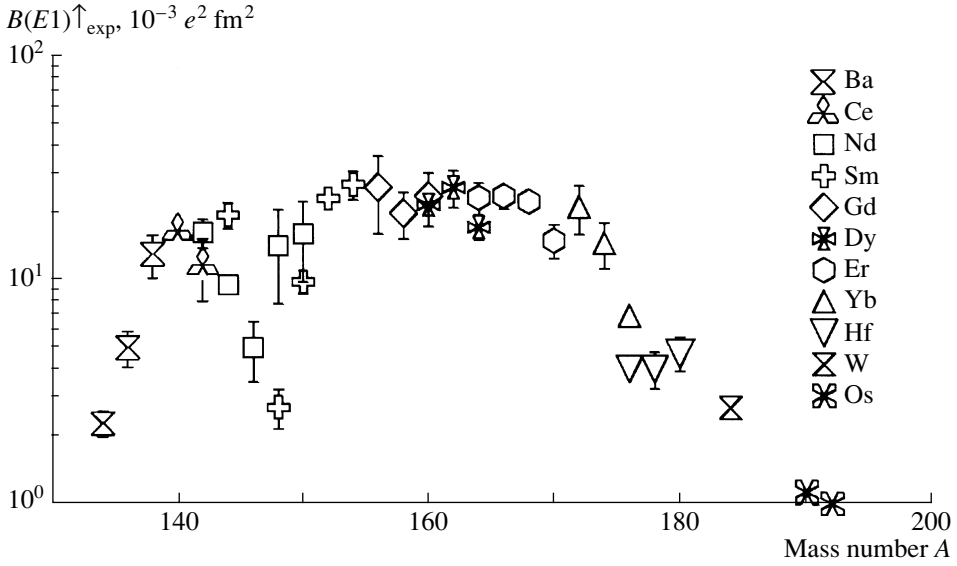

Fig. 3. $B(E1)\uparrow$ strength of the lowest 1^- states in even–even nuclei in the mass region $A = 134$–192.

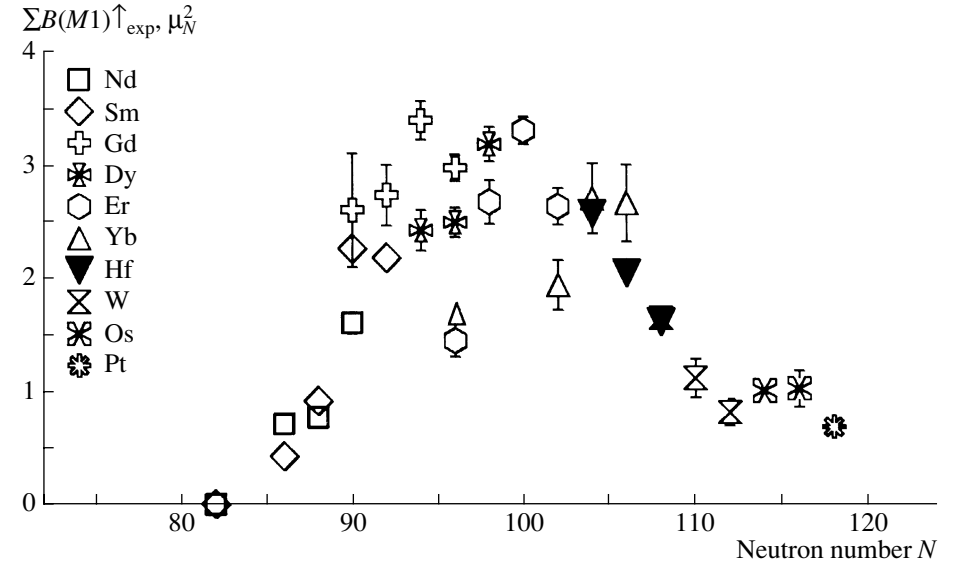

Fig. 4. The total $B(M1)$ strengths of the Scissors Mode in even–even rare-earth nuclei.

The $B(E1)\uparrow$ strengths are shown in Fig. 3. The closed-shell nuclei show strong transitions from the first 1^- state which decrease upon stepping away from the closed shell. The strength rises again and reaches a saturation while crossing the critical point candidates ^{150}Nd and ^{152}Sm.

3.2. M1 Transitions

The low-lying magnetic dipole strength below 4 MeV is ascribed to the scissors mode. The systematics of $M1$ strength summed over the fragments of the scissors mode in the mass region above the $N = 82$ shell closure is shown in Fig. 4.

In the spherical $N = 82$ isotones, no $M1$ transitions are observed. With the onset of and increase in deformation, the $B(M1)\uparrow$ values increase proportionally to the square of the deformation parameter δ. This fact is known as the δ^2 law [14]. From the point where the deformation remains constant, we reach a region of saturation. The $B(M1)\uparrow$ strength remains constant at a value of $\sum B(M1)\uparrow \approx 2.7\mu_N^2$. It is not astonishing that this is the case for the $N = 90$ nuclei: ^{152}Sm and ^{154}Gd.

The next question to be investigated is the behavior of the fragmentation of the $M1$ strength in isotopic chains undergoing the phase transition. In this paper,

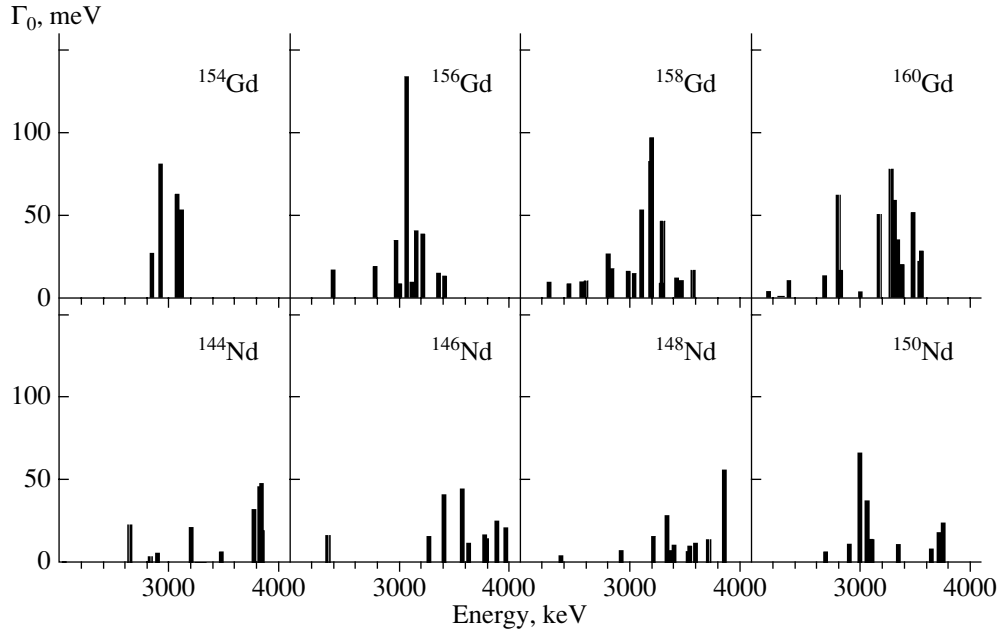

Fig. 5. The distribution of $M1$ strength in nuclei of the Nd and Gd isotopic chains, including the critical point candidates ^{150}Nd and ^{154}Gd.

the neodymium [15, 16] and gadolinium [17] isotopic chains are chosen as examples. Their $M1$ strength distributions are plotted in Fig. 5. The data, except for ^{154}Gd, have been obtained from NRF measurements.

The nearly spherical isotope ^{144}Nd shows a more random distribution of weak $M1$ transitions. Towards the critical point candidate ^{150}Nd, the strength increases and the fragments accumulate. The center of the distribution shifts to 3 MeV. A similar distribution is visible in the other critical point candidate ^{154}Gd. After the phase transition, the center of the distribution shifts to higher energies, and the number of fragments increases. This easily can be understood by the increasing number of valence nucleons and, therefore, the increasing number of possible configurations.

4. DIPOLE EXCITATIONS IN THE MASS REGION OF THE $E(5)$ SYMMETRY

The mass region below the $N = 82$ isotones provides us with an example of the second-order phase transition from $U(5)$ spherical vibrators to $O(6)$ γ-soft nuclei. Especially the barium and xenon isotopic chains are well-applicable examples of this phase transition. Of special interest is ^{134}Ba fulfilling the spectral properties for $E2$ transitions of the new $E(5)$ critical point symmetry. That is not really surprising, because ^{134}Ba usually was treated as a typical representative of $O(6)$ γ-soft nuclei and often compared to ^{196}Pt.

The (γ, γ') spectra of the stable barium isotopes [18–20] from the closed shell nucleus ^{138}Ba to the critical point candidate ^{134}Ba are plotted in Fig. 6. Peaks belonging to transitions from the photon flux calibration standard ^{27}Al are marked. Further peaks stemming from the transition from the 1^- two-phonon states or from the 1^+ scissors mode states are marked too. It is better to discuss the distribution of the reduced ground-state transition widths for the dipole transitions (shown on the right part of Fig. 6).

The transition strengths from the 1^+ states increase, as expected, with the deformation. The $M1$ strength in the critical point candidate ^{134}Ba ($\sum B(M1)\uparrow = 0.56(4)\mu_N^2$) is comparable to that in the $O(6)$ representative ^{196}Pt ($\sum B(M1)\uparrow = 0.69(7)\mu_N^2$) [21].

The data of the 1^- two-phonon states of the barium isotopes are summarized in the table. Addition-

Properties of the 1^- two-phonon states in the even–even barium isotopes

Isotope	E_{1^-}, keV	E_{2^+}, keV	E_{3^-}, keV	$E_{2^+} + E_{3^-}$, keV	$B(E1)\uparrow$, $10^{-3}\,e^2\,\mathrm{fm}^2$
138	4026	1436	2881	4317	13.0(28)
136	3436	819	2532	3351	5.39(33)
134	2824	605	2255	2860	2.30(30)

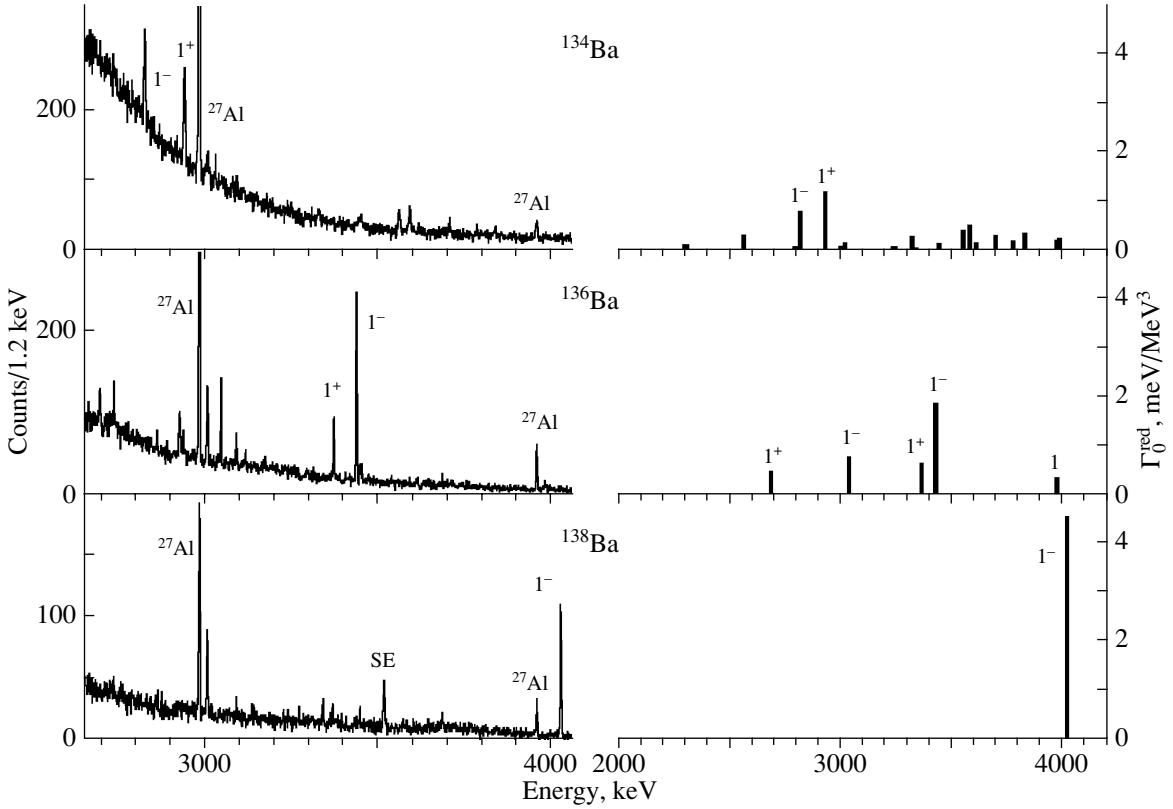

Fig. 6. Left part: NRF spectra of the even–even barium isotopes measured at the Stuttgart bremsstrahlung facility. The lines marked with ^{27}Al are used to calibrate the photon flux. Right part: The distribution of dipole excitations in stable even–even barium isotopes.

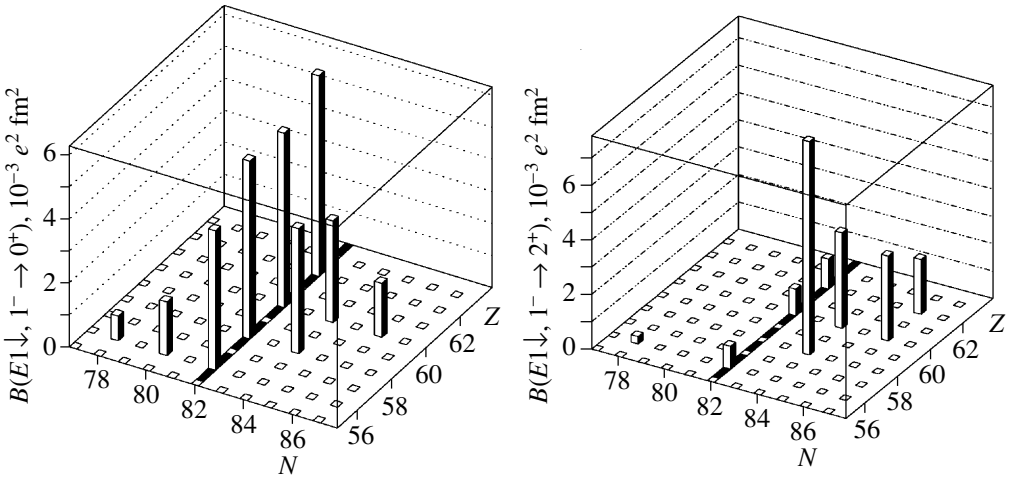

Fig. 7. $B(E1)\downarrow$ transition strengths from the $[2^+ \otimes 3^-]_{1^-}$ two-phonon state either to the ground state (left side) or to the first excited 2^+ level (right side). The magic neutron number is marked with the black bar.

ally, the energies of the first 2^+ quadrupole and the 3^- octupole phonons and their total energy are given.

The small difference between the total energies of the 2^+ and 3^- phonons and the excitation energies of the two-phonon 1^- state suggests only small anharmonicities in the coupling. Furthermore, a decrease in the $B(E1)\uparrow$ strength by stepping from the closed shell isotope ^{138}Ba to the critical point isotope ^{134}Ba is obvious. This result will now be discussed in a

more general systematics of two-phonon excitations around the $N = 82$ shell closure (see Fig. 7).

For the transitions from the $[2^+ \otimes 3^-]_{1^-}$ state to the ground state, we see, as before in the barium isotopic chain, strong transition for the $N = 82$ isotones which drops by moving away from it by pairs of neutrons. The transitions to the first 2^+ level show an opposite behavior: weak transitions on the closed shell and strong ones beside. Within the quasiparticle–phonon nuclear model (QPM) [22], this can be explained by the dipole core polarization effect. This effect mixes the pure two-phonon configurations with the low-energy tail of the giant dipole resonance. A detailed discussion can be found in [8].

Recapitulating the second-order phase transition, obviously there is a lack of available data. The stable barium isotopes have only been measured down to the critical point candidate ^{134}Ba. The other two existing more γ-soft stable barium isotopes ^{130,132}Ba could not be investigated in NRF experiments at present. Due to their low natural abundance, enriched targets, even of low enrichment, are too expensive.

An alternative can be measurements of the neighboring stable xenon isotopes ($Z = 54$). This isotopic chain consists of seven stable even–even isotopes, from $N = 82$ to $N = 70$. The experimental challenge is the gaseous nature of xenon. NRF measurements have been made possible by the development of a high-pressure gas target [23], which consists of a thin-wallet titanium sphere, able to stand pressures of 140 bar. The first measurements, performed at the bremsstrahlung facility in Stuttgart, showed encouraging results.

5. CONCLUSIONS

In the present article, we have seen that the low-lying dipole excitations showed a transitional behavior for the first-order phase transition from the spherical vibrators to the axially symmetric rotors at the proposed critical point candidates. For the second-order phase transition from spherical vibrators to the γ-soft nuclei, not enough data are available at present. Ongoing measurements of the gaseous xenon isotopes will provide more data in this very interesting mass region.

ACKNOWLEDGMENTS

We thank all the colleagues from Darmstadt, Dubna, Gent, Karlsruhe, Moscow, Rossendorf, and Sofia. The financial support by the Deutsche Forschungsgemeinschaft (DFG) under contract nos. Kn154/36, Br 799/10 is gratefully acknowledged.

REFERENCES

1. A. Arima and F. Iachello, *The Interacting Boson Model* (Cambridge Univ. Press, London, 1985).
2. A. Bohr, K. Dan. Vidensk. Selsk. Mat. Fys. Medd. **26** (14) (1952).
3. F. Iachello, Phys. Rev. Lett. **85**, 3580 (2000).
4. F. Iachello, Phys. Rev. Lett. **87**, 052502 (2001).
5. R. Krücken *et al.*, Phys. Rev. Lett. **88**, 232501 (2002).
6. R. Casten and V. Zamfir, Phys. Rev. Lett. **87**, 052503 (2001).
7. R. Casten and V. Zamfir, Phys. Rev. Lett. **85**, 3584 (2000).
8. W. Andrejtscheff *et al.*, Phys. Lett. B **506**, 239 (2001).
9. N. Lo Iudice and F. Palumbo, Phys. Rev. Lett. **41**, 1532 (1978).
10. D. Bohle *et al.*, Phys. Lett. B **137B**, 27 (1984).
11. U. Kneissl *et al.*, Prog. Part. Nucl. Phys. **37**, 349 (1996).
12. P. Carlos *et al.*, Nucl. Phys. A **172**, 437 (1971).
13. P. Carlos *et al.*, Nucl. Phys. A **225**, 171 (1974).
14. W. Ziegler *et al.*, Phys. Rev. Lett. **65**, 2515 (1990).
15. T. Eckert *et al.*, Phys. Rev. C **56**, 1256 (1997).
16. H. H. Pitz *et al.*, Nucl. Phys. A **509**, 587 (1990).
17. H. H. Pitz *et al.*, Nucl. Phys. A **492**, 411 (1989).
18. R. D. Herzberg *et al.*, Nucl. Phys. A **592**, 211 (1995).
19. N. Pietralla *et al.*, Phys. Rev. C **58**, 796 (1998).
20. H. Maser *et al.*, Phys. Rev. C **54**, R2129 (1996).
21. P. von Brentano *et al.*, Phys. Rev. Lett. **76**, 2029 (1996).
22. V. G. Soloviev, *Theory of Atomic Nuclei: Quasiparticles and Phonons* (IOP, Bristol, Philadelphia, 1992).
23. R. Reifarth *et al.*, Phys. Rev. C **66**, 064603 (2002).

Physics of Atomic Nuclei, Vol. 67, No. 9, 2004, pp. 1688–1695. From Yadernaya Fizika, Vol. 67, No. 9, 2004, pp. 1716–1723.

Nuclear Physics Aspects of the Astrophysical *p*-Process*

Zs. Fülöp[**,***], **Gy. Gyürky**[***], **and E. Somorjai**

ATOMKI, Debrecen, Hungary

Received January 21, 2004

Abstract—An overview is given on the experimental nuclear physics aspects of the astrophysical *p*-process that is responsible for the production of the heavy proton-rich nuclei known as *p*-nuclei. The nuclear physics input of the *p*-process scenario involves the knowledge of radiative capture cross sections, mostly calculated by the Hauser–Feshbach statistical model. Our experiments test the reliability of the model calculations in the proton-rich region as well as provide experimental information on the cross sections relevant to the *p*-process. © *2004 MAIK "Nauka/Interperiodica"*.

1. INTRODUCTION

Although the nucleosynthesis of heavy elements is well described by neutron capture via the *s*- and *r*-processes, there are some isotopes—called *p*-nuclei—not reachable by the above processes. The aim of this paper is to give an account of the nuclear physics problems behind the nucleosynthesis of the *p*-nuclei. A short introduction to the present status of light- and heavy-element nucleosynthesis can be found in [1].

The stable neutron-deficient isotopes of the elements with charge number $Z \geq 34$ are classically referred to as *p*-nuclei. They have been observed only in the solar system and here they represent 0.1 to 1% of the abundance of the bulk isotopes, made predominantly of the more neutron-rich *s*- and *r*-nuclei. The stellar process synthesizing the *p*-nuclei is called the *p*-process. Several models have been developed for describing the *p*-process. There are differences in the details (astrophysical site, temperature, time scale, reactions involved, etc.); however, the generally accepted main process involves subsequent (γ, n) reactions starting from *s*- and *r*-nuclei and driving the nuclei towards the neutron-deficient region [2–4]. Along this isotopic path, the binding energy of neutrons gradually becomes larger. As a result, the (n, γ) and (γ, n) reactions become equilibrated, the reaction flow slows down, and, at some point, it is deflected by (γ, α) and/or (γ, p) reactions. At these branching points, the matter tends to accumulate. The branching points are the *p*-nuclei themselves (lower mass region) or their progenitors (heavier mass region). It is also expected that the *rp*-process has a contribution to the production of *p*-nuclei [5].

A recent overview on the *p*-process can be found in [6]. In the following sections, the contribution of experimental nuclear physics to the understanding of the *p*-process is described.

2. EXPERIMENTAL NEEDS

The modeling of *p*-process nucleosynthesis requires a large network of thousands of nuclear reactions involving stable nuclei as well as unstable, proton-rich nuclides. The relevant astrophysical reaction rates (calculated from the cross sections) are inputs to this network; therefore, their knowledge is essential for the *p*-process calculations. While there are compilations of neutron capture data along the line of stability above the iron region, there are still very few charged-particle cross sections determined experimentally, despite big experimental efforts in recent years. Thus, the *p*-process rates involving charged projectiles are still based mainly on (largely untested) theoretical cross sections obtained from modern Hauser–Feshbach statistical model calculations [7, 8].

Therefore, the primary aim of the present *p*-process studies is the test of statistical model calculations in the mass and energy range relevant to the astrophysical *p*-process. Because of technical reasons, instead of (γ, α) or (γ, p) experiments, usually the inverse (α, γ) or (p, γ) cross sections are determined experimentally. However, due to the fast developments of high-intensity gamma sources, it is expected that, in the near future, the first gamma-induced charged-particle-emitting reactions in the *p*-process region can be investigated.

Because in many cases the cross sections are determined by the activation method (Section 2.2), the

*This article was submitted by the authors in English.

**e-mail: fulop@atomki.hu

***Bolyai fellow.

accuracy in the half-lives of the residual nuclei also plays an important role. Since the reliability of the statistical model calculations depends on the input parameters, experimental determination of optical alpha potentials is desirable at astrophysical energies. All those aspects will be described below, indicating the experimental approaches, the arising problems, and their possible solutions.

2.1. Cross Section Determination via In-Beam Gamma Spectroscopy

The most straightforward method of determining the charged-particle radiative capture cross section is in-beam gamma spectroscopy. Since the expected cross sections at sub-Coulomb energies are rather low, high beam intensity, enriched and stable targets, and high-efficiency gamma detectors are needed. Also, the determination of target thickness is crucial; usually, the PIXE, XRF, and RBS methods are used for this purpose.

As an example of in-beam gamma spectroscopy, the pioneering work [9] on the reaction ^{70}Ge(α, γ)^{74}Se is discussed in detail.

2.1.1. ^{70}Ge(α, γ)^{74}Se. The experiment on the ^{70}Ge(α, γ)^{74}Se reaction has been performed at the MGC cyclotron in ATOMKI, Debrecen, and the Dynamitron Tandem accelerator in Bochum from $E = 5.0$ up to 7.8 MeV, using a He^{++} beam. Single gamma and $\gamma\gamma$ coincidence measurements have also been performed using high-efficiency HPGe detectors. For reducing the background yield (predominantly caused by high-energy gamma rays and neutrons from the ^{13}C(α, n)^{16}O reaction), thin gold foil was used as a target backing and a liquid N_2 shroud close to the target served against carbon deposition. The evaporated ^{70}Ge-enriched (86.5%) target had a thickness of 36 μg/cm^2. An average target current of 1 pμA has been used without any target deterioration. The accumulated charge for the gamma-ray spectra varied between 120 μC and 62 mC, depending on the bombarding energy. An electric field of 300 V was applied to eliminate the effect of secondary electrons on beam integration. The measurements were repeated at several bombarding energies on the gold backing without a target to identify clearly the peaks belonging to the ^{74}Se nucleus. Coulomb excitation was used extensively throughout the measurement series for monitoring the target stability. Only the $E_\gamma = 635$ keV gamma transition from ^{74}Se, namely, the head of the $K^\pi = 0^+$ ground-state band, was clearly seen in all the spectra taken in the bombarding energy range. The total cross section of the reaction was obtained using the intensity of the $E_\gamma = 635$ keV peak only with a small correction due to a loss through another ground-state transition.

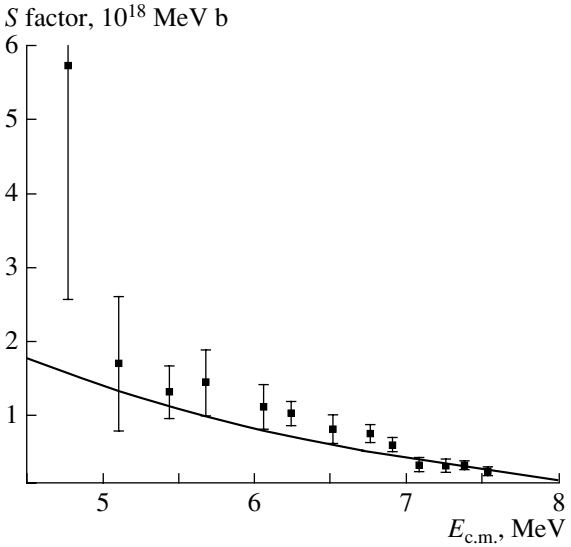

Fig. 1. The astrophysical S factor of the reaction ^{70}Ge(α, γ)^{74}Se. The solid curve is the SMOKER statistical model calculation [8]. Taken from [9].

The resulting S factor is in satisfactory agreement with the statistical model calculation, as is shown in Fig. 1.

2.2. Cross-Section Determination via Activation

It should be noted that, in other reactions, the in-beam cross-section determination can be much more complicated. In the case of the ^{88}Sr(p, γ)^{89}Y reaction [10], for example, there are more than ten secondary transitions contributing to the reaction yield; therefore, the resulting spectra are more complicated, an angular distribution determination being necessary for all the transitions. A possible solution to this problem is the activation method, where the irradiation is separated in time from the gamma detection. The advantage of this method is that capture reactions on different isotopes can be studied simultaneously using natural targets, and the in-beam background is reduced to the laboratory background that can be shielded well. On the other hand, because of the possible longer half-lives of the residual nuclei, new targets should be prepared for each irradiation, or longer cooling periods should be applied. The method can be used only in a limited range of residual nuclei: the residual nucleus must be radioactive, and the half-life should be reasonable; overly short- or long-lived isotopes cannot be measured. Also, the γ branching of the decay is a limiting factor.

As examples, the investigation of the Sr isotopic chain with the activation method [11] and the study

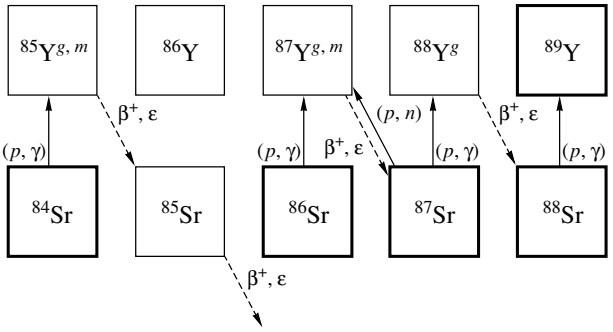

Fig. 2. Part of the chart of nuclides showing the investigated reactions and the decay scheme of reaction products. Stable nuclides are indicated by bold squares. Taken from [11].

of the ^{144}Sm(α, γ)^{148}Gd reaction [12] are described below.

2.2.1. ^{84,86,87}Sr(p, γ). The element Sr has four stable isotopes with mass numbers $A = 84$, 86, 87, and 88, having isotopic abundance of 0.56, 9.86, 7.00, and 82.58%, respectively. Only the (p, γ) cross section of the first three isotopes can be determined by activation because in the case of the ^{88}Sr(p, γ) reaction the product nucleus ^{89}Y is stable and its isomer is short-lived ($T_{1/2} = 16.06$ s). In the case of ^{84}Sr and ^{86}Sr, the partial cross sections leading to the isomer and ground state of the corresponding Y isotopes can be determined separately because of the different decay pattern of the isomeric and ground state. The relevant part of the chart of nuclides can be seen in Fig. 2, where the decay of the reaction products can also be seen. As mentioned above, the isotope ^{88}Sr, which cannot be investigated by activation, has the highest natural abundance of about 80%. Thus, in the case of natural targets, only 20% of the material is effective for the activation. However, the use of natural Sr targets has the advantage that the isotopic abundances are very well known and natural Sr is easily available in many chemical forms. In our measurements, we used natural SrF_2 targets, evaporated onto thick carbon backings. The fluorine content of the target causes no disturbance because in the investigated energy range there is no activity produced by proton bombardment on F and it has a low mass number; thus, it is well separated from Sr in Rutherford backscattering (RBS) spectra that were also measured during the irradiation in order to monitor the target stability. Carbon causes no disturbing long-lived activity, and due to its low mass number, the C edge lies far below the Sr and F peaks in the RBS spectra. The number of target atoms was determined by proton-induced x-ray emission (PIXE) at the PIXE setup of the ATOMKI. The results were checked by α-RBS determining the width of the Sr peak. Altogether more than thirty targets were prepared; some of them were only used for test runs.

Using natural Sr targets, the (p, γ) cross sections of ^{84}Sr, ^{86}Sr, and ^{87}Sr can be determined simultaneously in a single activation procedure. At $E_p = 2.67$ MeV bombarding energy, the ^{87}Sr(p, n)^{87}Y channel opens, which results in the same product nucleus as ^{86}Sr(p, γ). Consequently, above this energy, the cross section of the ^{86}Sr(p, γ) reaction cannot be deduced. However, this is the only disturbing proton-induced reaction channel on Sr isotopes which is open in the investigated energy range.

The resulting cross sections were compared with statistical model calculations. While good agreement was found between experiment and theory for the cross section of the reaction ^{84}Sr(p, γ)^{85}Y, the predictions for the other two reactions differ considerably from the experimental results.

2.2.2. ^{144}Sm(α, γ)^{148}Gd. The activation method can also be used when the residual nucleus is an alpha emitter. Here, the high efficiency and better figure of merit of the alpha detection allow a study involving heavier isotopes such as the ^{144}Sm(α, γ)^{148}Gd reaction [12].

Since the cross section here is determined via off-line detection of the alpha decay of ^{148}Gd residual nuclei, alpha activity of the target material (as well as the backing) is not desirable. Therefore, the well-known reductive evaporation of samarium oxide is not suitable, because the small contamination from lanthanum used for the reduction shows alpha activity. The electrophoresis method, however, provided samarium oxide targets free from disturbing alpha activity. The thickness of the samarium oxide–enriched (87 and 96%) targets varied between 20 and 350 μg/cm^2. The prepared targets were analyzed by RBS and PIXE. Figure 3 shows the diffusion-like RBS pattern of the loose structure of the samarium oxide grains on the backing in comparison with the metallic Sm produced by reductive evaporation. To increase the target stability during the bombardment, a very thin aluminum layer was evaporated onto the samarium oxide layer. A chamber containing a surface-barrier detector for the detection of the scattered α particles has been constructed for the irradiation. The yield of the scattered particles has been used to monitor the target stability during the irradiation process. An electric field of 300 V was applied again to eliminate the effect of secondary electrons on beam integration.

Poly-allyl-diglycol-carbonate (TASTRAK, England) etched track detectors have been used for the determination of the number of α particles emitted from the ^{148}Gd ($T_{1/2} = 74.6 \pm 3.0$ yr [13]) residual

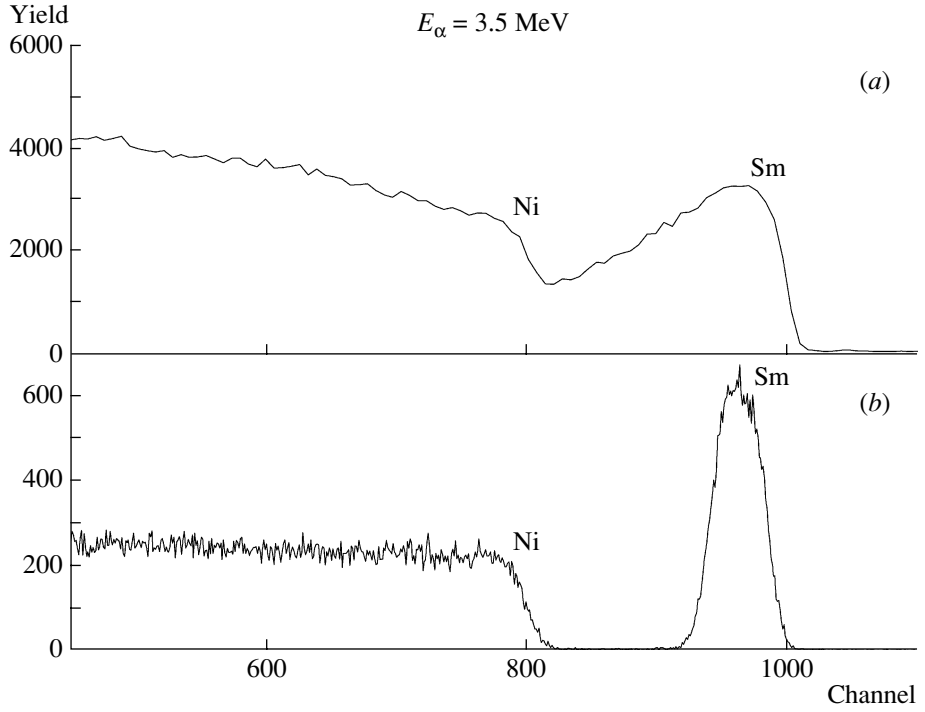

Fig. 3. RBS spectra from (*a*) samarium oxide (beaded surface) and (*b*) metallic Sm targets on nickel backing. Taken from [12].

nuclei. The track detectors enclosed the targets in 2π geometry in normal air conditions at room temperature, with the exposure time varying between two weeks and half a year. Track counting was done manually using an optical microscope. The separation of the 3.18-MeV α-particle tracks (^{148}Gd) from 2-MeV ones (background) was achieved by track size and shape comparison by visual inspection. The detection efficiency of the track detector and of the track counting method was taken into account to obtain the number of ^{148}Gd nuclei on the target. The alpha activity of unirradiated natural and enriched targets has also been measured to check the effect of contaminants. For confirmation of the experimental results, targets irradiated at the highest α energies of the bombarding energy region have also been measured by a surface barrier Si detector (600 mm^2) in an underground laboratory having a very low background (LNGS, Italy). The α spectra from a target before and after irradiation at $E_\alpha = 13.355$ MeV are shown in Fig. 4. The extracted activities agree with the ones from the track detectors.

The activation method implies knowledge of the half-life of the residual nucleus, and the error of the half-life in question directly affects the error in the reaction rate.

In order to determine the half-life, we started to measure the alpha decay of a weak ^{148}Gd/^{241}Am mixed source with a compact dedicated system [14]. The ^{148}Gd isotope was obtained from the Los Alamos National Laboratory, USA, as gadolinium (III) in a 0.1 M HCl solution. The source preparation was done at Niigata University by mixing and depositing ^{148}Gd and ^{241}Am on a platinum sheet. The source was covered by a thin gold layer. The α particles are detected by a Si photodiode in close geometry on air pressure. The data acquisition was a PC-based commercial system. To ensure the long-term stability, the electronics, as well as the data acquisition, was equipped with an uninterruptable power supply (UPS). The source stability and the electronics can be monitored by the yield of long-lived ^{241}Am. The data acquisition system was programmed to minimize the possibility of data loss. The daily results were summed up for periods of four weeks. From the decay curve of ^{148}Gd obtained so far, the preliminary result is $T_{1/2} = 70.9 \pm 1.0$ yr. The decay curve of ^{241}Am is also constructed with a least squares fit where the half-life is fixed to the literature data. The statistical analysis of both data sets shows that 65% of the data points are within a 1σ range of the fitted decay curve, fulfilling the required distribution pattern. In order to investigate the systematic errors, we also fitted the ratio of the ^{148}Gd/^{241}Am yields. Since the half-life of ^{241}Am is well established, we can give the half-life of ^{148}Gd from this decay curve after a correction for the known ^{241}Am half-life. The resulting decay curve is shown in Fig. 5. Since the ^{241}Am decay rate in the

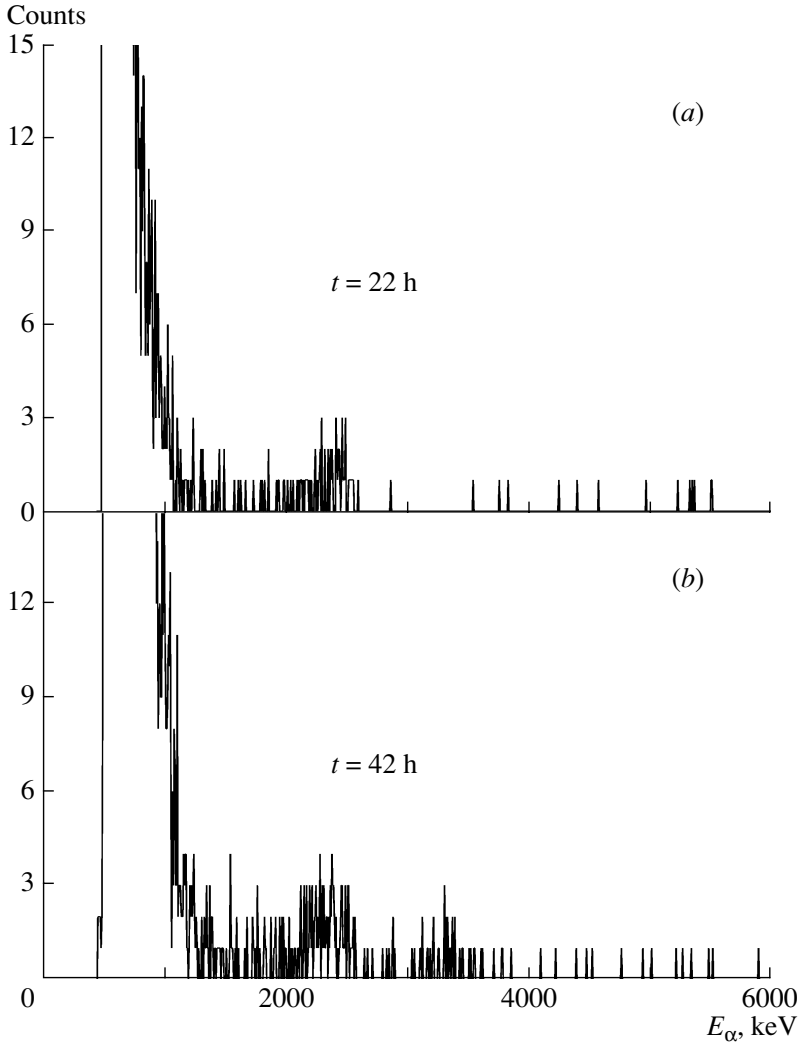

Fig. 4. The α-particle spectra from a target (a) before and (b) after irradiation. Taken from [12].

sample is 10 times less than that of ^{148}Gd, in this case the statistical error is dominated by the lower alpha yield from ^{241}Am. The obtained result ($T_{1/2} = 74.5 \pm 3.7$ yr) is consistent with the data based only on the ^{148}Gd decay, and both data support the validity of the accepted value.

In summary, to get a reliable cross-section value, sophisticated target preparation, detection methods, underground experiments, and independent half-life determination were needed. This shows the complexity of the p-process experiments, especially in the heavy-mass region. Nevertheless, the activation method should be used in general, and only in those cases where the activation does not work is the more complicated in-beam spectroscopy the answer.

The resulting S factor of the reaction ^{144}Sm(α, γ)^{148}Gd is shown in Fig. 6 together with statistical model calculations using different optical model potentials. An updated analysis of the data can be found in Fig. 20 of [6]. The results show clearly the need for more reliable optical potential parameters. The experimental efforts to retrieve those parameters from elastic scattering experiments are discussed in the following section.

2.3. Elastic Scattering Experiments

Of the many nuclear properties entering the statistical model calculation, the α-particle width is the dominating one. This particle width is obtained by employing an α + nucleus optical potential. The experimental determination of the α–nucleus potential at energies below the Coulomb barrier is limited in general because the experimental data show only small deviations from the Rutherford cross section, and the optical potentials have ambiguities.

The (γ, α) and (α, γ) reaction rates show a strong dependence on the chosen α-nucleus potential. Therefore, systematic folding potentials have

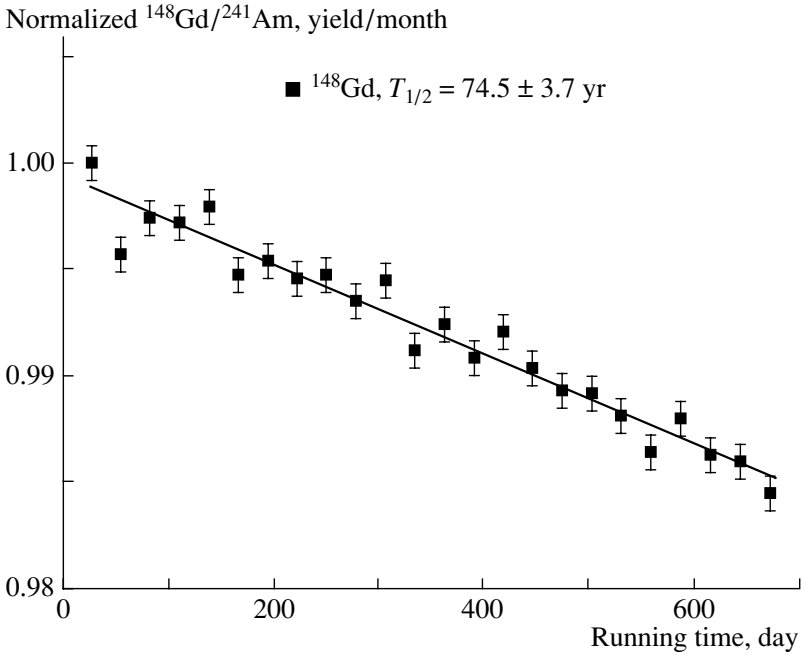

Fig. 5. The measured decay curve of ^{148}Gd/^{241}Am with an exponential least-squares fit. The result includes a correction for the known half-life of ^{241}Am. Taken from [14].

been determined by elastic α-scattering experiments on different proton-rich nuclei (^{144}Sm, ^{92}Mo, ^{112}Sn [17–19]). In those experiments, complete angular distributions have been measured, and the corresponding α-nucleus potentials for ^{144}Sm [17], ^{92}Mo [18], and ^{112}Sn [19] have been fully determined at the measured energies. These potentials can be used to predict (α, γ) reaction cross sections, and their inverse (γ, α) reaction rates can be calculated using detailed balance. To understand the systematic behavior of optical potentials, neutron-rich ^{124}Sn was also studied.

The angular distributions of the elastically scattered α particles were measured at the Cyclotron Laboratory ATOMKI, Debrecen. The highly enriched targets were set in the center of the 78-cm scattering chamber, and spectra were registered at angles between $20° \leq \vartheta_{\rm lab} \leq 170°$ in one-degree steps. For the measurement of the angular distribution, we used four silicon surface-barrier detectors mounted on an upper and a lower turntables, which could be moved independently. On each turntable, two detectors were mounted at an angular distance of 10°. Directly in front of the detectors, apertures were placed resulting in solid angles from $\Delta\Omega = 1.63 \times 10^{-4}$ to $\Delta\Omega = 1.55 \times 10^{-4}$. The ratios of the solid angles of the different detectors were determined by overlap measurements with an accuracy much better than 1%. Additionally, two detectors were mounted at the wall of the scattering chamber at fixed angles of $\vartheta = 15°$ and 165°, respectively. These detectors were used as monitoring detectors to normalize the measured angular distribution and to determine the precise position of the beam spot on the target. The solid angle of both monitoring detectors was $\Delta\Omega = 8.10 \times 10^{-6}$.

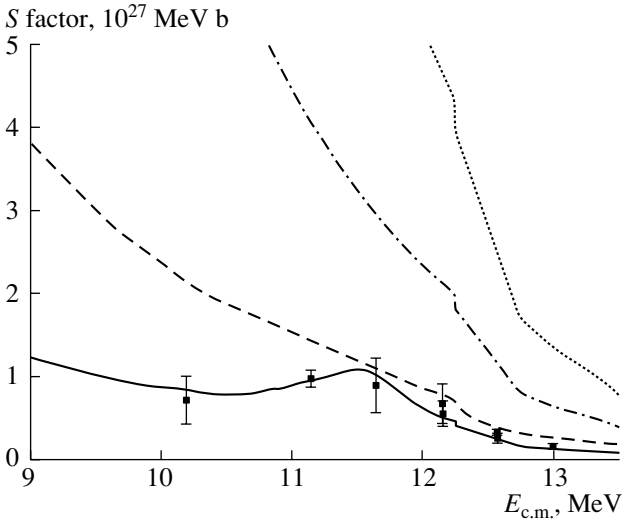

Fig. 6. The astrophysical S factor for ^{144}Sm(α, γ)^{148}Gd. The dash-dotted and dotted curves are the estimates obtained with the Hauser–Feshbach code MOST and the global α–nucleus optical potentials of [15] (as used in the code SMOKER) and [16], respectively. The solid curve is obtained with the MOST code and the energy-dependent optical potential developed in [12]. The dashed curve is from [17]. Taken from [12].

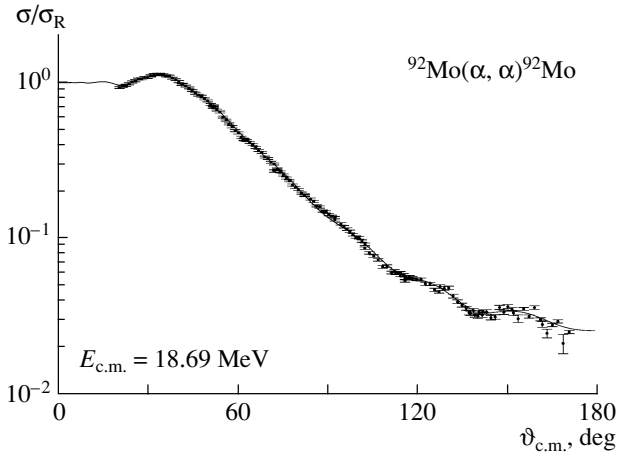

Fig. 7. Experimental cross section of ^{92}Mo(α, α)^{92}Mo at $E_{\text{c.m.}} \simeq 19$ MeV normalized to the Rutherford cross section. The curve is the result of optical model calculations. Taken from [18].

The angular calibration of the setup is of crucial importance for the precision of a scattering experiment at energies close to the Coulomb barrier because the Rutherford cross section depends sensitively on the angle as $\sin^{-4}(\vartheta/2)$. A small uncertainty of 0.1° in the determination of ϑ leads to a cross-section uncertainty of 2.0% (1.0%, 0.6%) at an angle $\vartheta = 20°$ (40°, 60°). The following methods were applied to measure the precise scattering angle ϑ:

The position of the beam on the target was continuously controlled by two monitoring detectors. The precise position of the beam spot was derived from the ratio of the count rates in both monitoring detectors, which were mounted at angles of 15° left and right relative to the beam axis. Typical corrections were smaller than one millimeter, leading to corrections in ϑ on the order of 0.1°.

The position of the four detectors was calibrated using the steep kinematics of ^{1}H(α, α)^{1}H scattering at forward angles ($10° < \vartheta_{\text{lab}} < 15°$).

Finally, we measured a kinematic coincidence between elastically scattered α particles and the corresponding ^{12}C recoil nuclei using a pure carbon backing as the target. One detector was placed at $\vartheta_{\text{lab},\alpha} = 70°$, and the signals from elastically scattered α particles on ^{12}C were selected by a TSCA. This TSCA output was used as a gate for the signals from another detector which was moved around the corresponding ^{12}C recoil angle $\vartheta_{\text{lab,recoil}} = 45.5°$. The maximum recoil count rate was found almost exactly at the expected angle.

The overall uncertainty of the angles ϑ in these experiments is about 0.1°. The above setup enables accurate angular distribution determination at low bombarding energies; consequently, improved optical model parameters can be given. A typical angular distribution pattern is shown in Fig. 7.

The experimental determination of relevant optical potential parameters is an important step to improve the reliability of the statistical model calculations.

3. OUTLOOK

To understand the nature of the astrophysical p-process, the various astrophysical scenarios should provide reliable abundance values for the p-nuclei. In lack of experimental data, that process involves extensive reaction rate calculations using cross sections based on the statistical model. Therefore the sensitivity of statistical model calculations to various input parameters (ground-state properties, level densities, gamma-strength functions, optical potentials) should be studied especially in the proton-rich region. A recent study reveals the sensitivity of the statistical model calculations to several input parameters in the case of (p, γ) cross sections for various Se isotopes [20]. Further cross-section experiments are needed to cover especially the heavy-ion region. In order to establish a reliable global alpha potential, further low-energy elastic scattering experiments are also needed. The first steps have been made towards an experimental nuclear database for the p-process, but the most difficult part—alpha capture cross sections close to the heaviest p-nuclei—is missing because of technical difficulties.

ACKNOWLEDGMENTS

This summary was supported by OTKA (nos. T034259, T042733, and F043408). Parts of this work were done in collaboration with Ruhr University, Bochum, Germany; Demokritos Institute, Athens, Greece; TU Darmstadt, Germany; University of Basel, Switzerland; CNS, Wako, Japan; Niigata University, Japan; and ULB, Brussels, Belgium.

REFERENCES

1. G. Wallerstein *et al.*, Rev. Mod. Phys. **69**, 995 (1997).
2. M. Arnould, Astron. Astrophys. **46**, 117 (1976).
3. S. Woosley *et al.*, Astrophys. J., Suppl. Ser. **36**, 285 (1978).
4. M. Rayet *et al.*, Astron. Astrophys. **227**, 271 (1990).
5. M. Schatz *et al.*, Phys. Rev. Lett. **86**, 3471 (2001).
6. M. Arnould *et al.*, Phys. Rep. **384**, 1 (2003).
7. S. Goriely, *Nuclei in the Cosmos V* (Frontières, Paris, 1998), p. 314.
8. T. Rauscher and F.-K. Thielemann, At. Data Nucl. Data Tables **79**, 47 (2001).
9. Zs. Fülöp *et al.*, Z. Phys. A **355**, 203 (1996).
10. S. Galanopoulos *et al.*, Phys. Rev. C **67**, 065801 (2003).
11. Gy. Gyürky *et al.*, Phys. Rev. C **64**, 065803 (2001).

12. E. Somorjai *et al.*, Astron. Astrophys. **333**, 1112 (1998).
13. L. K. Peker, Nucl. Data Sheets **59**, 393 (1990).
14. Zs. Fülöp *et al.*, Nucl. Phys. A **718**, 688 (2003).
15. F. M. Mann, *Hauser 5* (A Computer Code to Calculate Nuclear Cross Sections, Hanford Engineering HEDL-TME), 78-83 (1978).
16. V. Avrigeanu *et al.*, Phys. Rev. C **49**, 2136 (1994).
17. P. Mohr *et al.*, Phys. Rev. C **55**, 1523 (1997).
18. Zs. Fülöp *et al.*, Phys. Rev. C **64**, 065805 (2001).
19. D. Galaviz *et al.*, Nucl. Phys. A **719**, 111 (2003).
20. Gy. Gyürky *et al.*, Phys. Rev. C **68**, 055803 (2003).

Physics of Atomic Nuclei, Vol. 67, No. 9, 2004, pp. 1696–1700. From Yadernaya Fizika, Vol. 67, No. 9, 2004, pp. 1724–1728.

Weak Interaction Rates for Astrophysical Applications*

I. N. Borzov**

Institut d'Astronomie et d'Astrophysique, Université Libre de Bruxelles, Belgium

Received January 21, 2004

Abstract—An important effort has been developed in recent decades to measure the masses and β-decay rates of very neutron-rich nuclei at radioactive ion beam (RIB) facilities. However, major astrophysical applications involve a huge number of exotic species. Most of them cannot be synthesized in terrestrial laboratories and only theoretical predictions can fill the gap. We concentrate on the self-consistent predictions of the β-decay rates needed for stellar r-process modeling and for performing the RIB experiments. The continuum QRPA approach based on the self-consistent ground-state description in the framework of the density functional theory is briefly described. The model for the large-scale calculations of total β-decay half-lives accounts for the Gamow–Teller and first-forbidden transitions. Due to the shell configuration effect, the first-forbidden decays have a strong impact on the total half-lives of the r-process relevant nuclei at $N = 126$, $Z = 60–70$. The performance of existing global models for the nuclides near the r-process paths at $N = 126$ is critically analyzed and confronted with the recent RIB experiments in the region "east" of ^{208}Pb. © *2004 MAIK "Nauka/Interperiodica".*

1. THEORETICAL FRAMEWORK

Reliable prediction of the weak interaction rates based on the microscopic description of the β-strength function poses a certain challenge for nuclear theory. The nuclear models fitted to experimental data close to the β-stability line usually allow for a crude extrapolation to high isospin values. For the r-process calculations, self-consistent models are mandatory. The predictions of the β-decay rates based at least on the same ground-state description as the one used to calculate the nuclear masses provide more reliable extrapolation far from stability. This is essential in order to ensure the internal consistency of the nuclear structure and nucleosynthesis models.

The ultimate QRPA model of the β-decay properties should be based on the self-consistent mean-field and pairing potential and on the universal effective NN interaction which, in principle, are to be derived from a single nuclear energy–density functional (DF). So far, some restrictions exist in applications of the fully self-consistent approach. The parameters of the spin–isospin part of the DF are constrained by the values of the scalar parameters defining the ground state [1]. In the Landau limit, the spin–isospin parameter g' derived from the available Skyrme DFs turns out to be much lower than its empirical value [2]. Satisfactory spin-dependent DFs have not been developed yet for spin-unsaturated nuclei [1, 3]. However, for large-scale calculations, one can use the fact that the ground-state properties are rather insensitive to the spin and spin–isospin dependent components of the DF (except for the spin–orbit term). Then the scalar and spin–isospin components of the DF can be decoupled and the effective NN interactions in the scalar and spin–isospin channels can be introduced independently [4]. The DF + QRPA approach developed in such a way has an advantage of using the well-founded spin–isospin effective NN interaction of the finite Fermi system theory (FFS) [5].

We have followed the approach to the large-scale calculations of the allowed Gamow–Teller (GT) and first-forbidden (FF) decays developed in [6]. The specific features of the model are as follows:

1. The ground-state properties are treated self-consistently in the framework of the local energy–density functional theory. The Fayans' phenomenological DF [1] consisting of a normal and a pairing part is adopted. The DF3 version of the functional [4] contains the two-body spin–orbit and velocity-dependent effective NN interactions important for the full consistency, as well as the isovector spin–orbit force. The latter ensures a correct description of the single-particle levels near the "magic cross" at ^{132}Sn [7]. In [2, 6], we have studied also a possibility of the ground-state description given by the Skyrme *SkSC*17 [2] and *MSk*7 forces [8].

2. The pairing energy density depends on the anomalous nucleon density ν as $\varepsilon_{\text{pair}} = \nu F^{\xi} \nu^*/2$. Here, F^{ξ} is the effective NN interaction in the

*This article was submitted by the author in English.

** e-mail: iborzov@astro.ulb.ac.be

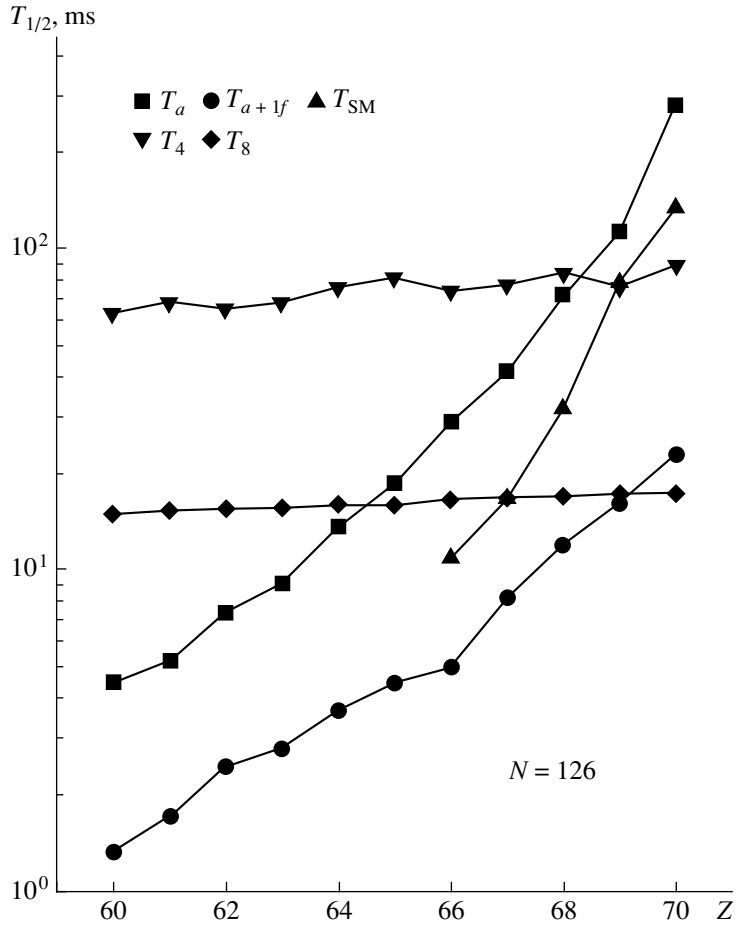

Fig. 1. The total half-lives for the $N = 126$ chain. Notation: a—allowed transitions; $a + 1f$—the first-forbidden transition included; SM, 4, 8—see text.

particle–particle (pp) channel chosen in the density-dependent form as $F^{\xi}(\mathbf{r}_{12}) = -4N_0^{-1} f^{\xi}(x)\delta(\mathbf{r}_{12})$, where $N_0 = 150$ MeV fm^3 is the inverse half-density of states at the Fermi surface in equilibrium nuclear matter; $X = (\rho_p + \rho_n)/2\rho_0$, where the $\rho_{p(n)}$ are the proton (neutron) densities; the $f^{\xi}(x)$ is expressed in a Skyrme-like form [1]. For density-dependent pairing, a local cutoff treatment of the pairing energy density [1] helps to avoid the problem of the choice of the cutoff energy. An efficient pairing regularization procedure has been suggested recently in [9].

3. For the excited states, the continuum QRPA (CQRPA) equations of the finite Fermi system theory [5] are solved with an exact treatment of the particle–hole (ph) continuum, pairing, and effective NN interaction in the ph and pp channels [10]. Thus, the $SO(8)$ quasispin symmetry of the QRPA problem is preserved.

4. The method to include the ph continuum for the $\Delta T = \pm 1$ excitations of superfluid nuclei [10] is similar to the one for $\Delta T = 0$ excitations [11]. It is based on exact treatment of the pairing in "valence λ space" ($\mu^{\tau} - \xi < \varepsilon_{\lambda} < \mu^{\tau} + \xi$), where μ^{τ} are the neutron and proton chemical potentials. Far from the Fermi surface, the ph propagator is the same as in the system with no pairing. It is calculated via the Green's functions constructed in the r space which allows the exact inclusion of the ph continuum.

5. The universal medium renormalization (beyond the QRPA-type correlations) of the spin–isospin fields is taken into account via the quasiparticle local charge operators $\hat{e}_{qi} = e_q[V_0^{JLS}]$; the so-called "quenching factor" is $Q = e_{qs}[\sigma\tau]^2 = (g_A/G_A)^2$. The smaller Q, the less strength contained in the low-energy part ($\omega < \varepsilon_{\mathrm{F}}$) of the spin–isospin response, and therefore the longer the β-decay half-lives.

6. A finite-range effective NN interaction in the ph channel is chosen in a $\delta + \pi + \rho$ form. The one-π and one-ρ exchange terms modified by the nuclear medium are important in describing the magnetic properties of nuclei and the nuclear spin–isospin responses. The competition between the one-pion at-

traction $g_\pi Q < 0$ and contact spin–isospin repulsion $g'_0 > 0$ determines the degree of "softness" of the pionic modes in nuclei that influences the β-decay half-lives.[1)]

The effective $T = 0$ NN interaction in the pp channel is assumed to be similar to a like-particle pairing. It cannot be neglected, as this would destroy the $SO(8)$ symmetry of the QRPA equations and cause unrealistic odd–even staggering of total β-decay half-lives. The CQRPA equations of the FFS allow a reasonable description of nuclear spin–isospin modes in the region far from the instability point in the pp channel [10].

7. Total β-decay half-life is calculated through the corresponding β-decay strength functions $S_{J^\pi}(\omega)$, where ω is the decay transition energy.[2)] The strength functions are found by solving the CQRPA equations for the following driving operators: $\boldsymbol{\sigma}$; γ_5, $[\boldsymbol{\sigma}\mathbf{r}]^{(J=0)}$; α, $\mathbf{r}$, $[\boldsymbol{\sigma}\mathbf{r}]^{(J=1)}$; $[\boldsymbol{\sigma}\mathbf{r}]^{(J=2)}$. Thus, for nonunique decays, the relativistic vector operator α and axial charge operator γ_5 should be included along with the spacelike operators. An efficient approximation used in global calculations of total half-lives is to replace α and γ_5 by space-dependent fields. The exact nonrelativistic relation for the matrix element of the timelike operator $\langle\alpha\rangle = \xi/\lambda_e \cdot \Lambda_1 \cdot \langle i\mathbf{r}\rangle$ can be applied which reflects the conservation of the nuclear vector current (CVC). In a fully self-consistent approach, a precise cancellation of all the terms except the averaged Coulomb potential takes place; thus, the translation factor Λ_1 reads $\xi\Lambda_1 = \omega_{if} + \bar{u}_C$.

For the timelike operator γ_5 and its spacelike counterpart $\boldsymbol{\sigma} \cdot \mathbf{r}$, no analogous exact relation exists due to the partial conservation of the axial current. On the basis of the chiral symmetry and soft-pion theorem, it has been argued that the $\langle\gamma_5\rangle$ vertex is amplified in the nuclear medium due to the meson-exchange currents and the effective NN interactions [17]. The self-consistent FFS sum rule approach [13] is used to approximate the operator γ_5 in an analogous way by the spacelike operator $\boldsymbol{\sigma} \cdot \mathbf{r}$ taking into account the medium corrections which are mainly due to the spin–orbit and velocity-dependent interactions [6]. With the resulting set of space-dependent external fields, large-scale calculations of the β-decay half-lives are feasible.

2. RESULTS

2.1. β Decay vs. (ν_e, e^-) Capture in $N = 126$ Region

Currently favored r-process scenarios—neutrino driven wind, shock-heated helium shells, and neutron star merger models—assume that the material ejected after the core collapse of a type II supernova is exposed to extreme fluxes of neutrinos of all flavors. All these models demand much shorter r-process time scales than the one of the canonical model obtained in the allowed transition approximation.

Though a rule of thumb is that the β^--decay half-lives become longer as closed (sub)shells are approached, the $T_{1/2}$ values are sensitive to the specific N, Z-shell sequence. The interplay of the low-energy GT and high-energy FF transitions may result in hindering the β-half-lives due to a phase-space amplification of the high-energy FF decays. In the previous microscopic large-scale calculations, the validity of the allowed transition approximation has not been analyzed, which needs to be critically revised. Within the proposed microscopic approach, both the GT and FF transitions are treated self-consistently and on the same footing. On this basis, systematic large-scale calculations of the GT and FF decays for the r-process relevant nuclei are performed.

In the important r-process region near $Z \approx 60$–80 and $N = 126$, the role of the FF decays is decisive. These nuclei undergo high-energy first-forbidden decays related to the $\nu 1i_{13/2} \to \pi 1h_{11/2}$ configuration. Our CQRPA calculations predict a strong high-energy $J^\pi = 1^-$ ($S = 1$) transition near $Z \approx 70$ and $N = 126$ with a β-decay energy of about 6 MeV, well above the GT transitions at 4 MeV corresponding to the $\nu 1h_{9/2} \to \pi 1h_{11/2}$ configuration. At the same time, the unperturbed β-decay energy of the main GT decay configuration $\nu 1i_{13/2} \to \pi 1i_{11/2}$ is low (about 1 MeV).

Our calculated half-lives are displayed in Fig. 1 together with the shell-model (SM) calculation [18] performed in the GT approximation. We see that the inclusion of the FF transitions made in [6] results in noticeably shorter half-lives in the $N = 126$ region. The deviation with the GT approximation amounts to typically a factor 5 to 10 and is more pronounced

[1)] So far, two basic sets of FFS parameters have been found to describe satisfactorily the spin–isospin nuclear properties: (A) $Q = 0.81$, $g' = 0.9$–1.0 derived from the magnetic moments, which allows for moderately soft π modes [12]; (B) $Q = 0.64$, $g' = 1.0$–1.1 derived from observed GT and $M1$ strength distributions [13, 14]. A strong quenching excludes the existence of soft π modes. The recent analysis of (p, n) reaction spectra at $E_p = 295$ MeV [15] and excitation energies up to $E_x < 50$ MeV gives some evidence for $Q = 0.93 \pm 0.05$, i.e., of a lower quenching than previously deduced in [13] from the old (p, n) data at $E_x < 30$ MeV [16]. The experimental uncertainties still remain large, and both sets will be applied in the calculations of the β-decay half-lives.

[2)] Notice, though the excitation energies in the daughter nuclei are used for the experimental decay schemes, the adequate variables within the RPA-type approaches are the β-decay transition energy ω relative to the parent nucleus ground state.

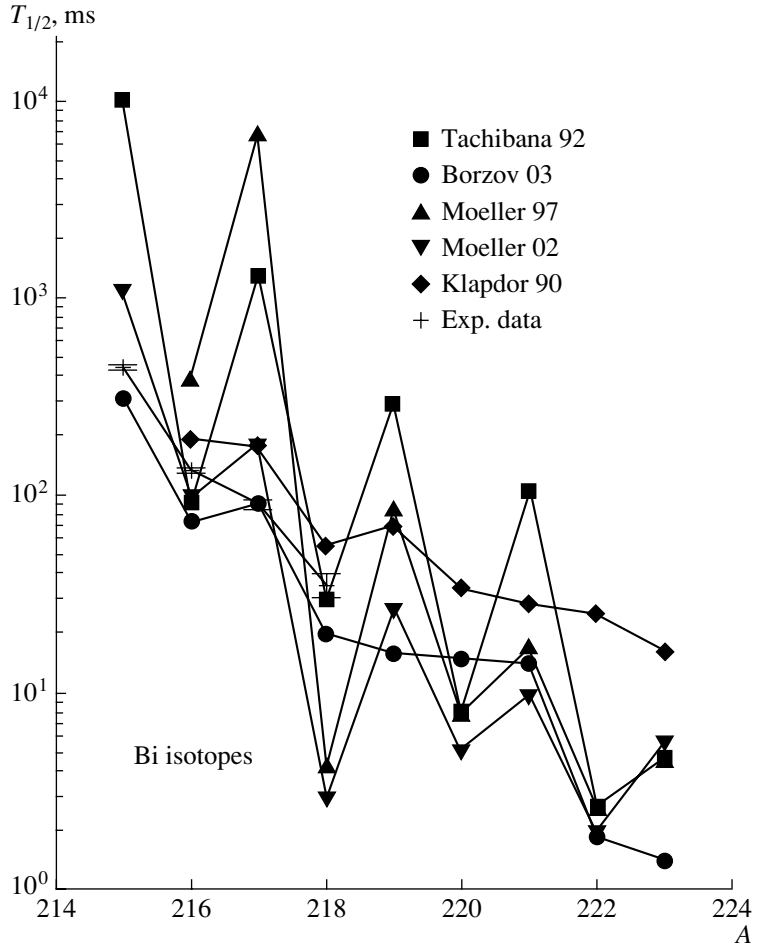

Fig. 2. The total half-lives for neutron-rich Bi isotopes.

for heavier nuclei approaching the closed proton shell at $Z = 82$. Note that the SM half-lives [18] (obtained for the GT decay with the SM-quenching factor $(g_A/G_A)^2 = 0.55$) would be shorter if the first-forbidden decays were included.

The shorter half-lives predicted for $N = 126$ imply an acceleration of the flow of matter through this "waiting point," both in the r-process standard scenario and in a neutrino wind model where the flow of matter to higher Z may speed up due to the combined effect of the β decays and charged-current electron neutrino captures. Shown in Fig. 1 are our calculated inverse (ν_e, e^-) rates at the neutrino temperature $T_\nu = 4$ MeV [2] (corrected for the forbidden transitions) and the RPA calculations by [19] for $T_\nu = 8$ MeV (the neutrino luminosity is $L_\nu \approx 10^{52}$ erg s^{-1}, and the distance from the center of the neutron star is $R = 100$ km).

One observes from Fig. 1 that, even at $T_\nu = 8$ MeV (with complete neutrino conversion $\nu_e \rightleftarrows \nu_{\mu,\tau}$ in effect [19]), the GT + FF β decays dominate over charged-current electron neutrino captures in this region of the r-process path (for the accepted values of L_ν, R, and T). The shorter β-decay half-lives obtained in the present work for the $N = 126$ region may change the estimate of the distance from the neutron star surface at which the neutrino–nucleus reactions occur and influence the picture of the r process both in the canonical and in neutrino wind scenarios.

2.2. β Decay in the Region "East" of ^{208}Pb

For the time being, the predictions in the $Z = 60-70$, $N = 126$ region cannot be verified experimentally. The current experiments [20] concern mostly the nuclei "east" of ^{208}Pb. In the region close to ^{208}Pb, the strong first-forbidden β decays are well known experimentally. The main problem that the models encounter lies in a near cancellation of the leading matrix elements for $J = 0, 1$ transitions, which results in a deviation of the electron spectra from a statistical shape.

In Fig. 2, we compare the measured half-lives [20] with the predictions from the existent global approaches [6, 21–24]. The total half-lives for the GT decay calculated within the FRDM + RPA model [23] overestimate the experimental ones by orders of magnitude. The scale of the odd–even effects predicted by [23] is generally too large because of the inconsistent treatment of the ground-state properties and pairing correlations and also due to the $T = 0$ pn effective interaction not being included in [23].

The results of statistical model (gt) [21] with a parametric description of the FF transitions vary significantly from the odd-A to even nuclei (Fig. 2). The results from the "microstatistical" (FRDM–RPA–gt) model [24] (in which the "gross-theory" calculations of the FF decay is combined with FRDM + RPA description of the GT decay) are closer to the experimental data. This model provides shorter total half-lives than the ones calculated for the GT decay in [23]. However, the obtained strong renormalization of the GT half-lives (for example, in ^{216}Bi) is hard to explain. It may well come from the inconsistency in the microscopic and "gross-theory" inputs within these hybrid models.

The QRPA calculations by [22] are overparametrized compared to the BCS–RPA calculations by [23], as the strengths of the separable ph and pp NN interactions are fitted to the experimentally known half-lives for each isotopic chain, which is a purely empirical procedure. As the odd–even behavior of the half-lives calculated in [22] is reasonable (the $T = 0$ paring has been included), such a procedure may provide a sound local extrapolation in the vicinity of experimentally known nuclei. As the FF transitions have not been included, the calculations by [22] overestimate the experimental half-lives in the region of Bi isotopes.

The results of the GT + FF calculation [6] show a fairly regular behavior with some underestimation of the experimental total half-lives (Fig. 2). The calculation may still be oversimplified in the specific region "east" of ^{208}Pb, especially if the $\Delta J = 0$ transitions dominate in the decay schemes. This is mainly due to the neglect of the velocity-dependent terms in the effective NN interaction and to the use of the Coulomb (ξ) approximation. However, the results are in a qualitative agreement with available experimental data on total half-lives.

In summary, the developed DF + CQRPA approach is based on the self-consistent description of the ground-state properties and on universal (A-independent) effective NN interaction. These features are of prime importance for large-scale applications. A strong impact of the high-energy FF transitions on the total β-decay half-lives in the region $Z = 60–70$, $N = 126$ is found. The present calculations provide guidance for new experiments in remote regions, in particular, in the region "east" of ^{208}Pb.

ACKNOWLEDGMENTS

I am grateful to OSTC, Belgium, for support within the PAI Program IAP P5/07 "Exotic Nuclei for Nuclear Physics and Astrophysics."

REFERENCES

1. S. A. Fayans *et al.*, Nucl. Phys. A **676**, 49 (2000).
2. I. N. Borzov and S. Goriely, Phys. Rev. C **62**, 035501 (2000).
3. M. Bender *et al.*, Phys. Rev. C **65**, 054322 (2002).
4. I. N. Borzov *et al.*, Z. Phys. A **355**, 117 (1996).
5. A. B. Migdal, *Theory of Finite Fermi Systems and Applications to Atomic Nuclei* (Nauka, Moscow, 1982; Interscience, New York, 1967).
6. I. N. Borzov, Phys. Rev. C **67**, 025802 (2003).
7. K. M. Mezilev *et al.*, Phys. Scr. **56**, 227 (1995).
8. S. Goriely *et al.*, At. Data Nucl. Data Tables **77**, 311 (2001).
9. A. Bulgac, Phys. Rev. C **65**, 051305 (2002).
10. I. N. Borzov and E. L. Trykov, Yad. Fiz. **33**, 52 (1990) [Sov. J. Nucl. Phys. **52**, 33 (1990)].
11. A. P. Platonov and E. E. Saperstein, Nucl. Phys. A **486**, 63 (1988).
12. I. N. Borzov, E. E. Saperstein, S. V. Tolokonnikov, and S. A. Fayans, Fiz. Élem. Chastits At. Yadra **12**, 848 (1981) [Sov. J. Part. Nucl. **12**, 338 (1981)].
13. N. I. Pyatov and S. A. Fayans, Fiz. Élem. Chastits At. Yadra **14**, 953 (1983) [Sov. J. Part. Nucl. **14**, 401 (1983)].
14. I. N. Borzov, S. V. Tolokonnikov, and S. A. Fayans, Yad. Fiz. **40**, 1151 (1984) [Sov. J. Nucl. Phys. **40**, 732 (1984)].
15. T. Wakasa *et al.*, Phys. Rev. C **55**, 2909 (1997).
16. C. Gaarde, Nucl. Phys. A **396**, 127c (1983).
17. K. Kubodera *et al.*, Phys. Rev. Lett. **40**, 755 (1978).
18. G. Martinez-Pinedo, Nucl. Phys. A **668**, 357c (2000).
19. A. Hektor *et al.*, Phys. Rev. C **61**, 055803 (2000).
20. H. De Witte, A. N. Andreev, and I. N. Borzov (Leuven–CERN Collab.), Phys. Rev. C **69**, 044305 (2004).
21. T. Tachibana *et al.*, Prog. Theor. Phys. **84**, 641 (2000).
22. M. Hirsch *et al.*, At. Data Nucl. Data Tables **51**, 244 (1992).
23. P. Möller *et al.*, At. Data Nucl. Data Tables **66**, 131 (1997).
24. P. Möller, B. Pfeiffer, and K.-L. Kratz, Phys. Rev. C **67**, 055802 (2003).

Physics of Atomic Nuclei, Vol. 67, No. 9, 2004, pp. 1701–1708. From Yadernaya Fizika, Vol. 67, No. 9, 2004, pp. 1729–1736.

Nuclear Structure with the Dinuclear Model*

G. G. Adamian[1),2)], N. V. Antonenko[1)], R. V. Jolos[1)], Yu. V. Palchikov[1)], W. Scheid[3)], and T. M. Shneidman[1)]

Received January 21, 2004

Abstract—The dinuclear system concept is applied to the explanation of the structure of nuclei. The appearance of a low-lying band with negative parity states near the ground-state band in actinides and other nuclei is described by oscillations of the dinuclear system in the mass-asymmetry coordinate. The results for the parity splitting and electric multipole moments in alternating parity bands of these nuclei are in agreement with experimental data. The ground-state band and the superdeformed band of ^{60}Zn are interpreted as being caused by α-particle and Be clusterizations, respectively. Hyperdeformed nuclei are assumed as dinuclear systems which could directly be built up in heavy-ion collisions. Signatures of hyperdeformed states in such reactions could be γ transitions between these states and their decay into the nuclei forming the hyperdeformed nucleus. © *2004 MAIK "Nauka/Interperiodica"*.

1. INTRODUCTION

The dinuclear system (DNS) is a configuration with two touching nuclei which preserve their individuality and exchange nucleons and/or clusters [1]. Such configurations are also denoted as quasimolecular or bicluster configurations and nuclear molecules [2]. Well-known examples with light nuclei are the Be configuration built up by two α particles and the nuclear molecular resonances in the reactions ^{12}C on ^{12}C up to ^{58}Ni on ^{58}Ni. The concept of the dinuclear system has manifold applications in the calculation of fusion cross sections for very heavy nuclei and of the mass and charge distributions in quasifission [3]. For example, in the production of superheavy elements, the DNS is first formed in the reaction between two heavy ions, and then the touching nuclei exchange nucleons up to the moment when the system crosses the inner fusion barrier and an excited compound nucleus is formed.

In this article, we discuss applications of the DNS concept for the description of nuclear structure effects. First, in Section 2, we introduce the basic facts about the description of the dinuclear configuration within the dinuclear system model. Then, in Section 3, we explain the parity splitting of rotational bands in actinides and other nuclei with vibrations of the dinuclear system in the mass-asymmetry coordinate. With the same type of vibrations, we interpret the ground-state and superdeformed bands of ^{60}Zn in Section 4. In Section 5, we study the question of whether hyperdeformed states can be assumed as dinuclear molecular resonances and propose experiments to produce hyperdeformed nuclei in heavy-ion reactions.

2. DESCRIPTION OF THE DINUCLEAR CONFIGURATION

The main coordinates of the DNS model are the relative coordinate R between the nuclei (clusters) and the mass and charge asymmetry coordinates defined as $\eta = (A_1 - A_2)/(A_1 + A_2)$ and $\eta_Z = (Z_1 - Z_2)/(Z_1 + Z_2)$, where A_1, A_2 and Z_1, Z_2 are the mass and charge numbers of the nuclei, respectively. The mass and charge multipole moments of the DNS shape can be calculated with the expression

$$Q_{\lambda,\mu} = \sqrt{\frac{16\pi}{2\lambda+1}} \int \rho(\mathbf{r}) r^\lambda Y_{\lambda,\mu}(\Omega) d\tau, \qquad (1)$$

where $\rho(\mathbf{r})$ is the sum of the mass or charge densities of the nuclei forming the DNS: $\rho(\mathbf{r}) = \rho_1(\mathbf{r}) + \rho_2(\mathbf{r} + \mathbf{R})$ (frozen density approximation). In order to get a correspondence of the DNS coordinates with a multipole expansion of the shape of the DNS, we expand the nuclear surface with deformation parameters β_λ: $\tilde{R} = R_0(1 + \beta_0 Y_{00} + \beta_1 Y_{10} + \beta_2 Y_{20} + \ldots)$, where R_0 is the spherical equivalent radius. Equating the multipole moments calculated with the deformation parameters and with the parameters of the DNS,

$$Q_{\lambda,0}(\beta_\lambda) = Q_{\lambda,0}(\eta, R), \qquad (2)$$

*This article was submitted by the authors in English.

[1)]Bogolyubov Laboratory of Theoretical Physics, Joint Institute for Nuclear Research, Dubna, Moscow oblast, 141980 Russia.

[2)]Institute of Nuclear Research, Tashkent, Uzbekistan.

[3)]Institut für theoretische Physik der Justus-Liebig-Universität, Giessen, Germany; e-mail: werner.scheid@theo.physik.uni-giessen.de

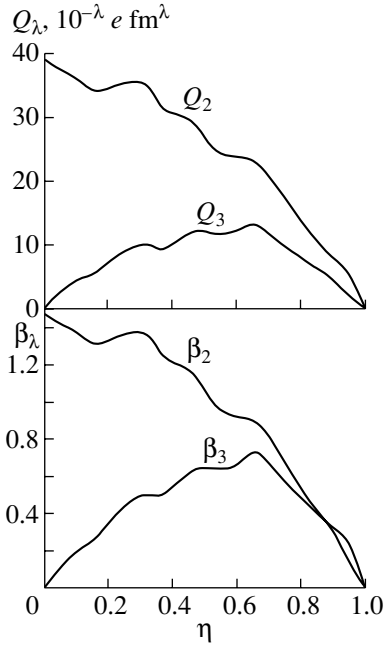

Fig. 1. Dependence of Q_2 and Q_3 (upper part) and of β_2 and β_3 (lower part) on the mass asymmetry η for the compound nucleus ^{152}Dy.

we obtain a relation between these parameters which is shown in Fig. 1 for two touching nuclei forming the ^{152}Dy system [4]. The same figure also gives the dependence of the charge multipole moments $Q_{20} = Q_2$ and $Q_{30} = Q_3$ on the mass-asymmetry coordinate. Since the deformations of the DNS nuclei are functions of η, this dependence has some oscillations.

The potential of the DNS is strongly repulsive for smaller distances and hinders the nuclei amalgamating together in the relative coordinate. Under the assumption of a small overlap of the nuclei, the potential energy is usually semiphenomenologically calculated [4],

$$U(R,\eta,I) = B_1 + B_2 + V(R,\eta,I) - B_{12}. \quad (3)$$

Here, B_i ($i = 1, 2$, negative) are the asymptotic experimental binding energies of the nuclei, and $V(R,\eta,I)$ is the interaction between the nuclei,

$$V(R,\eta,I) = V_{\rm C}(R,\eta) + V_N(R,\eta) + V_{\rm rot}(R,\eta,I), \quad (4)$$

consisting of the Coulomb potential, the nuclear part, and the centrifugal potential $V_{\rm rot} = \hbar^2 I(I+1)/(2\Im)$. The nuclear part is calculated by a double folding procedure with a Skyrme-type effective density-dependent nucleon–nucleon interaction taken from the theory of finite Fermi systems. The potential $U(R,\eta,I)$ is related to the binding energy B_{12} of the compound nucleus. Also, deformations of the clusters are taken into account by assuming the clusters to be in a pole-to-pole orientation.

The moment of inertia of the DNS can be assumed in the sticking limit

$$\Im = \Im_1 + \Im_2 + \mu R^2, \quad (5)$$

where μ is the reduced mass of relative motion and the moments of inertia $\Im_i$ ($i = 1, 2$) of the nuclei are calculated in the rigid-body approximation ($\Im_i = \Im_i^r$).

3. PARITY SPLITTING IN ACTINIDES AND OTHER NUCLEI

The appearance of a low-lying band with negative parity states near the positive parity ground-state band of even–even actinide nuclei such as Ra, Th, U, and Pu is caused by reflection-asymmetric shapes of these nuclei [5, 6]. The negative parity states are shifted upwards with respect to the positive parity states. This effect is denoted as parity splitting. The band with negative parity and the parity splitting can be explained by considering the dynamics in the octupole deformation degree of freedom [7] or by assuming vibrations in the mass-asymmetry degree of freedom [8, 9]. The later type of approach is based on a cluster interpretation of the low-lying positive and negative parity states and can be formulated in the dinuclear model. This approach will be used in the following to explain the parity splitting and to calculate electric multipole transition moments observed in alternating parity bands in actinides and other nuclei.

Instead of a parametrization of the nuclear shape in terms of quadrupole, octupole, and higher multipole deformations, we use the mass-asymmetry coordinate η as the relevant collective variable. The ground-state wave function in η is thought of as a superposition of different cluster-type configurations including the mononucleus configuration at $|\eta| = 1$. Calculating the potential energy of the dinuclear system for these nuclei, we find an α-cluster configuration mixed to the ground-state wave function:

$$^A Z \to {}^{(A-4)}(Z-2) + \alpha \text{ particle}.$$

The mononucleus configuration can have a higher potential energy than the α-cluster configuration. The resulting potential is schematically depicted as a function of the mass-asymmetry coordinate in Fig. 2, where also the reflection-asymmetric shapes of the α-cluster configuration are shown. The mass asymmetry coordinates of the later configurations are $\eta_\alpha = \pm(1 - 8/A)$. Since the potential energy of configurations with a light cluster heavier than an α particle increases rapidly with decreasing $|\eta|$, we restricted our investigations of the ground-state band

to configurations with light clusters not heavier than Li, i.e., to cluster configurations near $|\eta| = 1$, and not overly high angular momenta.

It is convenient to substitute the coordinate η by the following coordinate:

$$x = \eta - 1 \text{ if } \eta > 0, \quad x = \eta + 1 \text{ if } \eta < 0.$$

Then the Schrödinger equation can be written as

$$\left(-\frac{\hbar^2}{2}\frac{d}{dx}\frac{1}{B_x}\frac{d}{dx} + U(x,I)\right)\psi_n(x,I) = E_n(I)\psi_n(x,I), \quad (6)$$

where $B_x = B_\eta$ is the effective mass. The potential energy is calculated with Eq. (3) by setting $U(x,I) = U(R = R_m, \eta, I)$ with the touching distance R_m between the clusters. Details of the calculation of $V_N(R_m,\eta)$ are given in [10]. The nuclear density distribution is approximated by the Fermi distribution with a radius parameter of 1.15 fm for the Ra–Pu region and with a diffuseness parameter $a =$ 0.48 fm for the densities of ^{4}He and ^{7}Li and $a = 0.56(B_n^{(0)}/B_n)^{1/2}$ fm for the heavy clusters, where B_n and $B_n^{(0)}$ are the neutron binding energies of the studied nucleus and of the heaviest isotope considered for the same element, respectively. For example, in the case of Ra, Th, and U isotopes, $B_n^{(0)}$ corresponds to the neutron binding energies of ^{226}Ra, ^{232}Th, and ^{238}U, respectively. To calculate the potential energy for $I \neq 0$, the moment of inertia $\Im$ in the centrifugal potential is expressed for cluster configurations with α and Li as light clusters as

$$\Im(\eta) = c_1\left(\Im_1^r + \Im_2^r + M\frac{A_1A_2}{A}R_m^2\right). \quad (7)$$

Here, $\Im_i^r$ are the rigid-body moments of inertia for the clusters of the DNS, $c_1 = 0.85$ for all considered nuclei [8, 9], and M is the nucleon mass. Single-particle effects like alignment of the single-particle angular momenta in the heavy cluster are neglected.

For $|\eta| = 1$, the moment of inertia is not known from the data because the experimental moment of inertia is a mean value between the moments of inertia of the mononucleus ($|\eta| = 1$) and of the cluster configurations arising due to oscillations in η. We assume $\Im(|\eta| = 1) = c_2\Im^r(|\eta| = 1)$, where $\Im^r$ is the rigid-body moment of inertia of the mononucleus calculated with deformation parameters and $c_2 = 0.1$–0.3 is a scaling parameter fixed by the energy of the first 2^+ state. For example, for the isotopes ^{220,222,224,226}Ra, we find $\Im(|\eta| = 1) = 12$, 17, 22, and 32 $\hbar^2$/MeV, respectively.

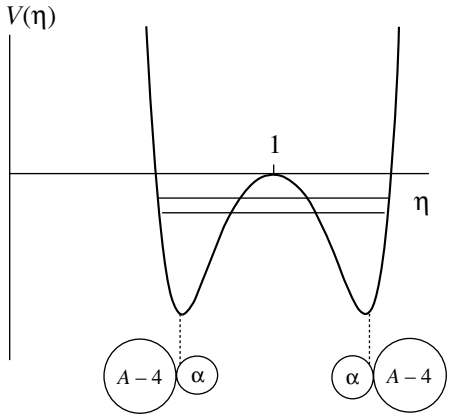

Fig. 2. Schematic picture of the potential in the mass asymmetry and of the two states with different parities (parallel lines, lower state with positive parity, higher state with negative parity).

Then a smooth parametrization of the potential $U(x,I)$ is chosen:

$$U(x,I) = \sum_{k=0}^{4} a_{2k}(I)x^{2k}. \quad (8)$$

The parameters $a_{2k}(I)$ with $k > 0$ are determined by the calculated potential values for $x = x_\alpha$ and $x = x_{\mathrm{Li}}$. The value $a_0(I = 0)$ is taken so that the ground-state energy $E_0(I = 0)$ is zero after the solution of the Schrödinger equation. In the majority of cases, this procedure leads to a value $U(x = 0, I = 0) = a_0(I = 0)$ close to $E_0(I = 0) = 0$. However, for ^{222}Th and ^{220,222}Ra, we varied the inertia coefficient $B_x = B_\eta$ in Eq. (6) in the range $B_\eta = (10$–$20) \times 10^4 M$ fm^2 to obtain the correct value of $E_0(I = 0) = 0$.

The mass B_η can be estimated by relating the mass-asymmetry coordinate η to the octupole deformation coordinate β_3. Such a relation between η, R, and β_3 was derived in [4]:

$$\beta_3 = \sqrt{\frac{7}{4\pi}}\frac{\pi}{3}\eta(1-\eta^2)\frac{R^3}{R_0^3}, \quad (9)$$

where R_0 is the spherical equivalent radius of the corresponding compound nucleus. If we take the value of $B_{\beta_3} = 200\ \hbar^2$/MeV known from the literature, then we obtain $B_\eta \approx (d\beta_3/d\eta)^2 B_{\beta_3} = 9.3 \times 10^4 M$ fm^2, compatible with the one used in the calculations.

We calculated the parity splitting for even–even isotopes of the actinides Ra, Th, U, and Pu and of the nuclei Ba, Ce, and Nd for different values of nuclear spin I [8, 9]. Figure 3 gives a comparison of experimental and calculated energies of states of the alternating parity bands in $^{232-238}$U. The experimental data are taken from [11, 12]. Also, the results for

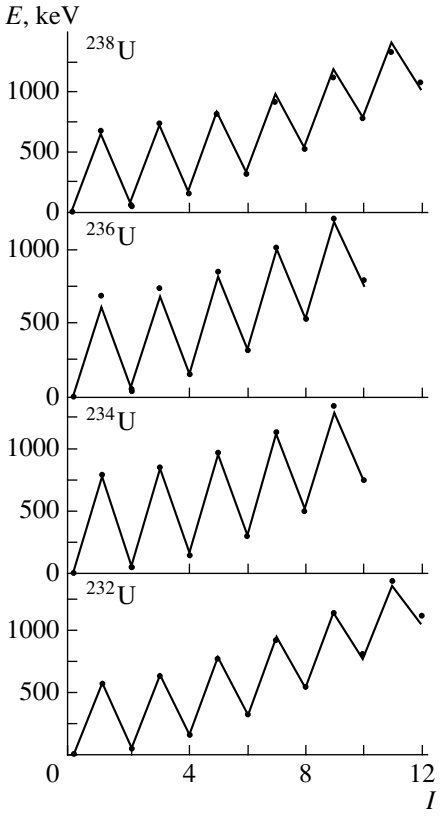

Fig. 3. Experimental (points) and theoretical (lines) rotational spectra for ^{232,234,236,238}U.

the other isotopes agree well with the experimental data, with the largest deviations being in the lightest Ra and Th isotopes.

The ground-state wave function has a maximum in the vicinity of $|\eta| = 1$ even when the potential energy has minima at $|\eta| = \eta_\alpha$ because these minima of maximal 0.8 MeV are rather shallow. With increasing angular momentum, the barrier at $x = 0$ separating the minima at $|x| = x_\alpha$ increases and the maxima of the wave function shift closer to the minima of the potential, i.e., to the α-cluster configuration. In the ground state of ^{226}Ra, we find a weight of the α-cluster configuration, estimated as that contribution to the norm of the wave function located at $|x| \geq x_\alpha$, of about 5×10^{-2}, which is close to the calculated spectroscopic factor [13].

A good test for the quality of the calculations is the reduced matrix elements of the electric multipole moments $Q(E1), Q(E2)$, and $Q(E3)$. The electric multipole operators can be obtained for the DNS and result in the expressions [4, 9]

$$Q_{10} = 2D_{10} = e\frac{A}{2}(1-\eta^2)R_m\left(\frac{Z_1}{A_1} - \frac{Z_2}{A_2}\right), \quad (10)$$

$$Q_{20} = e\frac{A}{4}(1-\eta^2) \quad (11)$$
$$\times R_m^2\left((1-\eta)\frac{Z_1}{A_1} + (1+\eta)\frac{Z_2}{A_2}\right)$$
$$+ Q_{20}(1) + Q_{20}(2),$$

$$Q_{30} = e\frac{A}{8}(1-\eta^2) \quad (12)$$
$$\times R_m^3\left((1-\eta)^2\frac{Z_1}{A_1} - (1+\eta)^2\frac{Z_2}{A_2}\right)$$
$$+ \frac{3}{2}R_m((1-\eta)Q_{20}(1) - (1+\eta)Q_{20}(2)),$$

where the charge quadrupole moments $Q_{20}(i)$ of the clusters $i = 1, 2$ are calculated with respect to their centers of mass. The charge-to-mass ratios Z_1/A_1 and Z_2/A_2 are functions of η. For the α particle, this ratio is equal to 0.5. For small values of $|x|$, we parametrize the ratio Z/A of the light cluster as follows: Z/A is equal to the value of the mononucleus for $|x| < x_\alpha$ and $Z/A = 0.5$ for $|x| \geq x_\alpha$ as for the α cluster.

In the calculations, we used effective charges e^{eff} instead of the unit charge e. We set the effective charge for $E1$ transitions to be $e_1^{\text{eff}} = e(1+\chi)$ with an average state-independent value of the $E1$ polarizability coefficient $\chi = -0.7$. This renormalization regards a coupling of the mass-asymmetry mode to the giant dipole resonance. For quadrupole transitions, we set $e_2^{\text{eff}} = e$, although an effective charge of $1.35e$ describes the experimental data better. Octupole transitions are treated with $e_{3,\text{proton}}^{\text{eff}} = 1.2e$ and $e_{3,\text{neutron}}^{\text{eff}} = 0.8e$ by assuming effects from the coupling of the mass-asymmetry mode with higher lying isovector and isoscalar octupole excitations. Figure 4 shows the result for the reduced electric quadrupole transition moment of ^{226}Ra as a function of nuclear spin in comparison with experimental data (from [14]). The obtained values are in qualitative agreement with the known experimental data for Q_λ^{exp} with some exceptions, e.g., in the case of ^{220,222}Ra.

The calculation of the spectrum of ^{223}Ra with an odd number of neutrons leads to a doubling of the states for fixed spin I. This is shown in comparison with experimental energies in Fig. 5. The positive parity state for a fixed spin I is situated lower in energy than the corresponding negative parity state. Calculated matrix elements for $E1$ transitions ($K^-I \to K^+I$) are also presented in Fig. 5.

4. GROUND-STATE AND SUPERDEFORMED BANDS OF ^{60}Zn

The ^{60}Zn nucleus can be thought of as consisting of a double magic ^{56}Ni plus an α particle. The

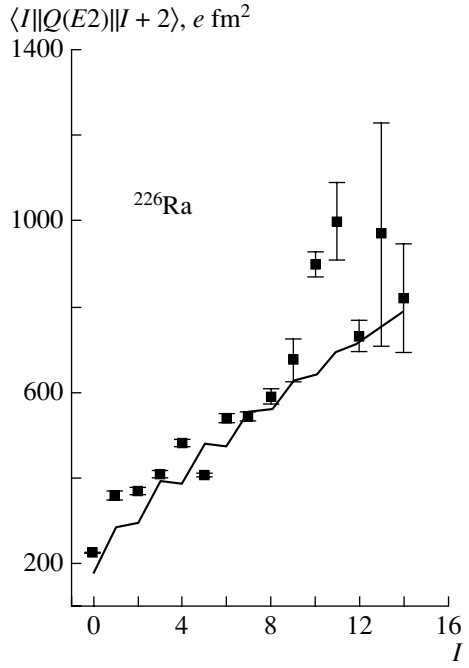

Fig. 4. Reduced matrix elements of the electric quadrupole operator (solid curve) for ^{226}Ra in comparison with experimental data (squares).

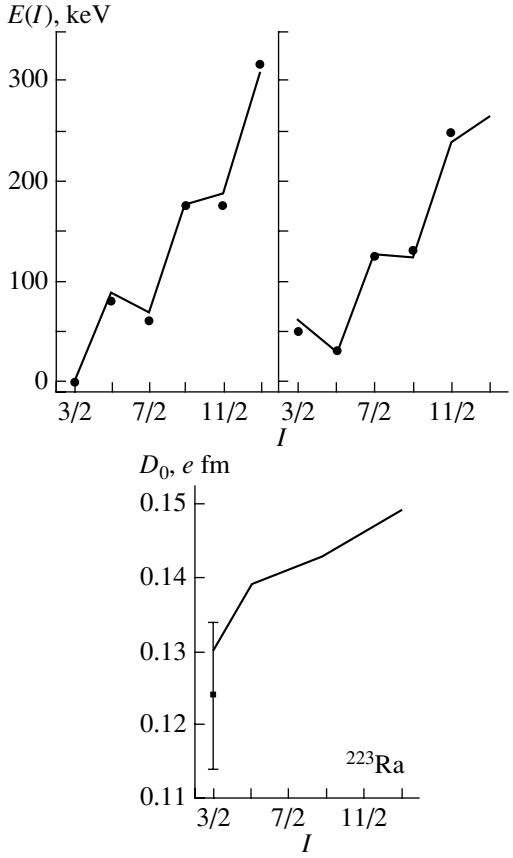

Fig. 5. Calculated spectrum and dipole matrix elements of ^{223}Ra in comparison with experimental data (dots and square with error bar).

threshold for the α decay of ^{60}Zn is only 2.7 MeV higher than the ground state of ^{60}Zn. Therefore, it is possible that the ground-state band of ^{60}Zn contains an α component which was used by Buck *et al.* [15] for the description of the ground-state band of ^{60}Zn. Also, a superdeformed band has been observed [16] which decays into the states of the ground-state band in the spin region $I = 8-12$. The moment of inertia in the superdeformed band takes the values $(692-795)M$ fm^2 depending on spin. These values are close to the sticking moment of inertia of the ^{52}Fe + ^{8}Be cluster configuration, which is $750M$ fm^2. In addition, the threshold energies for the decay of ^{60}Zn into ^{52}Fe+^{8}Be (10.8 MeV) and ^{48}Cr + ^{12}C (11.2 MeV) are close to the extrapolated value of the superdeformed band head, which is approximately 7.5 MeV. Therefore, it is justified to assume that two sets of cluster states exist in ^{60}Zn, namely, the states of the ground-state band containing the α-cluster configuration as an important component and the states of the superdeformed band with a Be-cluster configuration [17].

For the description of the ^{60}Zn nucleus, we take the dinuclear model discussed in Sections 2 and 3 where the mass-asymmetry coordinate η is used for the presentation of the various clusterizations of the nuclear system. The wave function in η can be thought of as a superposition of different cluster-type configurations including the mononucleus configuration with $|\eta| = 1$. The relative contribution of each cluster component to the total wave function is determined by the collective Hamiltonian given in Eq. (6).

In Fig. 6, we show the potential energy $U(x, I = 0)$ of ^{60}Zn. The potential at the α minimum is 4.5 MeV deeper than the energy of the mononucleus at $x = 0$. The next important minima correspond to ^{8}Be and ^{12}C cluster configurations with the values 5.1 and 9.0 MeV of the potential, respectively. Using the calculated values of the potential at the α, ^{6}Li, ^{8}Be, ^{10}B, ^{12}C (and so on) clusterizations, we obtained the shown steplike potential. To minimize the number of free parameters, we took the widths of all the barriers and minima separately equal to each other. These two widths were determined with the energy of the experimentally known 3^- state.

The potential energy for $I \neq 0$ depends on the moments of inertia $\Im(\eta)$. For cluster configurations $(x \neq 0)$, they are set equal to the dinuclear moment of inertia calculated under the sticking condition as

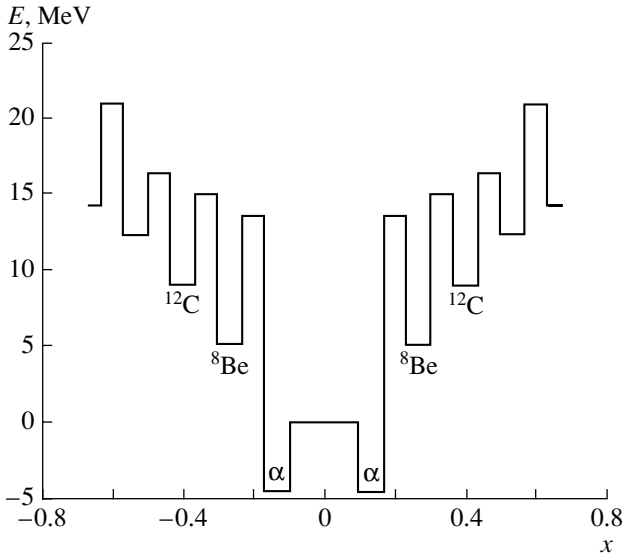

Fig. 6. Potential energy of ^{60}Zn as a function of x.

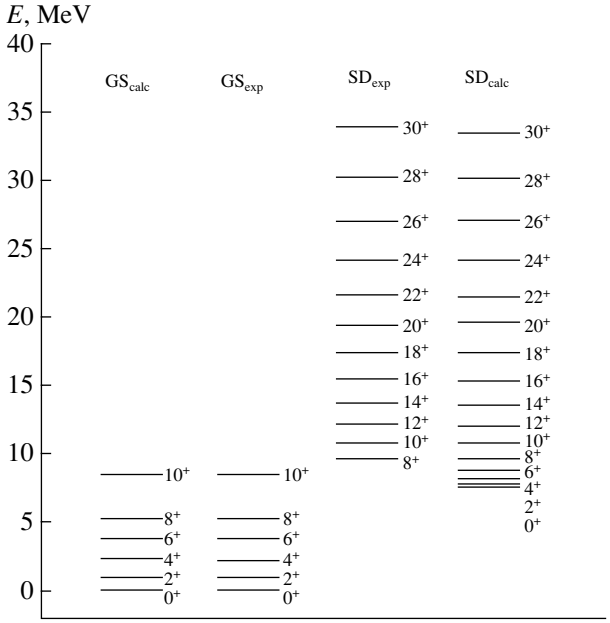

Fig. 7. Experimental and calculated energies of the states of the ground-state (GS) and superdeformed (SD) bands of ^{60}Zn. The experimental data are taken from [16].

given in Eq. (5). The ground-state band is described by a soft rotor with a moment of inertia $\Im(|\eta| = 1)$ linearly depending on spin I for $I \leq 8$. Thus, the known energies of the states of the ground-state band are fitted. The experimental energy of the $I = 10$ state is higher than the value that can be obtained by extrapolating the data for the lower spins. This is a shell effect which is taken into account with an additional energy shift of the states with $I \geq 10$. For the estimation of the mass parameter B_x in Eq. (6), see [17].

The calculated spectra for the ground-state and superdeformed bands are shown in Fig. 7. The energies of the superdeformed band are described quite well, including a variation of inertia with spin. In our calculation, this variation is reproduced because at spin values $I = 20$ the superdeformed band is crossed by the ground-state band and becomes the yrast band above $I = 20$.

Let us consider the decay of the superdeformed states into the ground-state band. We calculated the branching ratios of the intensities of the $E2$ transitions with $\Delta I = 2$. In the experiment only decays of the $18^+_{\rm SD}$, $16^+_{\rm SD}$, and $14^+_{\rm SD}$ states into the superdeformed states were observed. We obtained for the corresponding ratios in our calculations $I(18^+_{\rm SD} \to 16^+_{\rm GS})/I(18^+_{\rm SD} \to 16^+_{\rm SD}) = 0.02$, $I(16^+_{\rm SD} \to 14^+_{\rm GS})/I(16^+_{\rm SD} \to 14^+_{\rm SD}) = 0.07$, and $I(14^+_{\rm SD} \to 12^+_{\rm GS})/I(14^+_{\rm SD} \to 12^+_{\rm SD}) = 0.18$. For the ratio $I(12^+_{\rm SD} \to 10^+_{\rm GS})/I(12^+_{\rm SD} \to 10^+_{\rm SD})$, where the lowest experimental 10^+ state is treated as the $10^+_{\rm GS}$ state, the experimental value is 0.54 [16] and the calculated one is 0.42. For the ratio $I(10^+_{\rm SD} \to 8^+_{\rm GS})/I(10^+_{\rm SD} \to 8^+_{\rm SD})$, the experimental value is 0.60 [16] and the calculated one 0.63.

In addition to the positive parity states, the dinuclear model predicts the existence of negative parity states [17]. However, no experimental information about collective negative parity states in ^{60}Zn is known except the 3^- state at an excitation energy of 3.504 MeV. According to our calculations, an appreciable shift (of about 2 MeV) of the negative parity states is obtained for the ground-state band, whereas the parity splitting practically disappears in the superdeformed band.

5. HYPERDEFORMED NUCLEI AS NUCLEAR MOLECULES

Nuclear molecular states were first observed in the ^{12}C–^{12}C collision by Bromley *et al.* and then seen up to the system Ni + Ni by Cindro *et al.* [2]. The question arises whether heavier nuclear systems have excited states with the properties of molecular (or cluster) states. Such states could be the hyperdeformed (HD) states which are explained by a third minimum in the potential energy surfaces (PES) of the corresponding nuclei. An interesting observation in shell model calculations was made that the third minimum of the PES of actinide nuclei belongs to a molecular configuration of two touching nuclei (clusters) [18]. We showed that dinuclear systems have quadrupole moments and moments of inertia

like those measured for superdeformed states and estimated for HD states [4].

If hyperdeformed states can be considered as nuclear molecular resonance states, it should be possible to excite them by forming a hyperdeformed configuration in the scattering of heavy ions. In the following, we discuss the systems $^{48}\mathrm{Ca} + {}^{140}\mathrm{Ce}$ and $^{90}\mathrm{Zr} + {}^{90}\mathrm{Zr}$ as possible candidates for exploring the properties of hyperdeformed states [19]. The charge quadrupole moments of $(40-50) \times 10^2\ e\ \mathrm{fm}^2$ and the moments of inertia of $(160-190)\ \hbar^2/\mathrm{MeV}$ of the dinuclear configurations $^{48}\mathrm{Ca} + {}^{140}\mathrm{Ce}$ and $^{90}\mathrm{Zr} + {}^{90}\mathrm{Zr}$ are close to those estimated for hyperdeformed states.

First, we calculated the potentials $V(R, \eta, L = I)$ with Eq. (4) as a function of the relative distance for various angular momenta. These potentials are shown in Fig. 8. They have a minimum around 11 fm at a distance $R_m \approx R_1 + R_2 + 0.5$ fm, where R_1 and R_2 are the radii of the nuclei. The depth of this molecular minimum decreases with growing angular momentum and vanishes for $L > 100$ in the considered systems.

The potential pocket has virtual and quasibound states situated above and below the barrier, respectively. Approximating the potential in the neighborhood of the minimum by a harmonic oscillator potential, we can easily estimate the positions of one to three quasibound states with an energy spacing of $\hbar\omega \approx 2.2$ MeV for $L > 40$. For example, in the $^{90}\mathrm{Zr} + {}^{90}\mathrm{Zr}$ system, we find the lowest quasibound state for $L = 50$ lying 1.1 MeV above the potential minimum.

We assume that the quasibound states are HD states and propose to produce these states in heavy-ion reactions of ^{48}Ca on ^{140}Ce and ^{90}Zr on ^{90}Zr. The following conditions should be fulfilled: (i) The quasibound states should be directly excited by tunneling through the potential barrier in R, including the centrifugal potential; i.e., the DNS should have no extra excitation energy. (ii) The DNS should stay in the potential minimum without changing the mass and charge asymmetries. Spherical and stiff nuclei (magic and double magic nuclei) fulfill the second condition.

The cross section for penetrating the barrier and populating quasibound states can be written as

$$\sigma(E_{\mathrm{c.m.}}) = \frac{\pi\hbar^2}{2\mu E_{\mathrm{c.m.}}} \sum_{L=L_{\min}}^{L_{\max}} (2L+1) T_L(E_{\mathrm{c.m.}}). \quad (13)$$

Here, $E_{\mathrm{c.m.}}$ is the incident energy in the center-of-mass system, and $T_L(E_{\mathrm{c.m.}})$ is the transmission probability through the entrance barrier, which can be approximated by a parabola with frequency ω':

$$T_L(E_{\mathrm{c.m.}}) \quad (14)$$

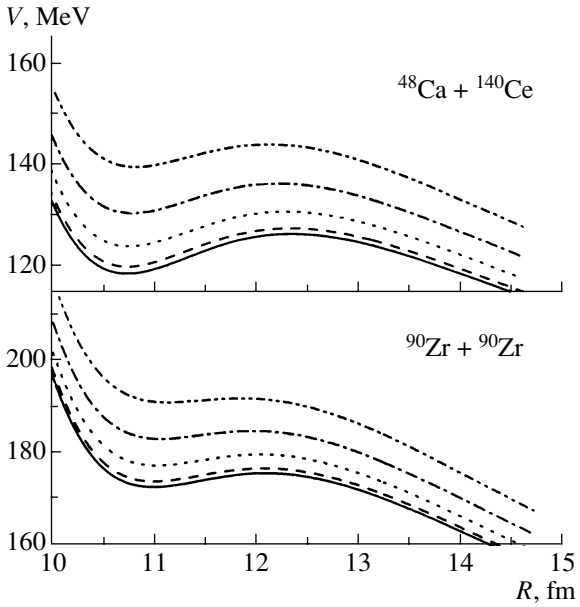

Fig. 8. The potential $V(R, L)$ for the systems $^{48}\mathrm{Ca} + {}^{140}\mathrm{Ce}$ and $^{90}\mathrm{Zr} + {}^{90}\mathrm{Zr}$ as a function of R for $L = 0, 20, 40, 60, 80$ shown by solid, dashed, dotted, dash-dotted, and dash-dot-dotted curves, respectively.

$$= 1/\left(1 + \exp[2\pi(V(R_b, \eta, L) - E_{\mathrm{c.m.}})/(\hbar\omega')]\right).$$

The barrier is at R_b. The angular momentum quantum numbers $L_{\min}$ and $L_{\max}$ in Eq. (13) fix the interval of angular momenta contributing to the excitation of HD states. The range of partial waves leading to the excitation of quasibound states constitutes the so-called molecular window known in the theory of nuclear molecules with light heavy ions [2].

In the reaction ^{48}Ca on ^{140}Ce, cold and long-living DNS states can be formed at an incident energy $E_{\mathrm{c.m.}} = 147$ MeV and $90 < L < 100$, and in the reaction ^{90}Zr on ^{90}Zr at $E_{\mathrm{c.m.}} = 180$ MeV and $40 < L < 50$. For both reactions, we estimate a cross section of about 1 μb with Eq. (13). Also other reactions, namely, $^{48}\mathrm{Ca} + {}^{144}\mathrm{Sm}$ ($E_{\mathrm{c.m.}} = 149$ MeV, $80 < L < 90$), $^{48}\mathrm{Ca} + {}^{142}\mathrm{Nd}$ ($E_{\mathrm{c.m.}} = 148$ MeV, $80 < L < 90$), and $^{38}\mathrm{Ar} + {}^{140}\mathrm{Ce}$, ^{142}Nd, ^{144}Sm ($E_{\mathrm{c.m.}} = 137$, 141, and 145 MeV, respectively, $80 < L < 90$), can be thought to be applied for a possible observation of cluster-type HD states.

The spectroscopic investigation of the HD structures is difficult because of the small formation cross section and the high background produced by fusion–fission, quasifission, and other reactions. However, the latter processes have characteristic times much shorter than the lifetime of the HD states, which is of the order of 10^{-16} s. The HD states are characterized by γ transitions between the HD states and by their decay into the nuclei by which they are formed.

Therefore, if these signatures would be observed in heavy-ion experiments, it would be unique proof of the idea that HD states are cluster-type states and further that quasimolecular configurations also exist in heavier nuclear systems.

REFERENCES

1. V. V. Volkov, Izv. Akad. Nauk SSSR, Ser. Fiz. **50**, 1879 (1986); *Deeply Inelastic Nuclear Reactions* (Énergoizdat, Moscow, 1982) [in Russian].
2. W. Greiner, J. Y. Park, and W. Scheid, *Nuclear Molecules* (World Sci., Singapore, 1995).
3. G. G. Adamian, N. V. Antonenko, A. Diaz-Torres, and W. Scheid, in *Proceedings of the Symposium on Nuclear Clusters: from Light Exotic to Superheavy Nuclei, Rauischholzhausen, Germany, 2002*, Ed. by R. Jolos and W. Scheid (EP Systema, Debrecen, 2003).
4. T. M. Shneidman, G. G. Adamian, N. V. Antonenko, *et al.*, Nucl. Phys. A **671**, 119 (2000).
5. I. Ahmad and P. A. Butler, Annu. Rev. Nucl. Part. Sci. **43**, 71 (1993).
6. P. A. Butler and W. Nazarewicz, Rev. Mod. Phys. **68**, 349 (1996).
7. E. Garrote, J. L. Egido, and L. M. Robledo, Phys. Rev. Lett. **80**, 4398 (1998).
8. T. M. Shneidman, G. G. Adamian, N. V. Antonenko, *et al.,* Phys. Lett. B **526**, 322 (2002).
9. T. M. Shneidman, G. G. Adamian, N. V. Antonenko, *et al.,* Phys. Rev. C **67**, 014313 (2003).
10. G. G. Adamian, N. V. Antonenko, R. V. Jolos, *et al.*, Int. J. Mod. Phys. E **5**, 191 (1996).
11. http://www.nndc.bnl.gov/nndc/ensdf/.
12. J. F. C. Cocks *et al.*, Nucl. Phys. A **645**, 61 (1999).
13. Yu. S. Zamiatin *et al.*, Fiz. Élem. Chastits At. Yadra **21**, 231 (1990) [Sov. J. Part. Nucl. **21**, 537 (1990)].
14. H. J. Wollersheim *et al.*, Nucl. Phys. A **556**, 261 (1993).
15. B. Buck, A. C. Merchant, and S. M. Perez, Phys. Rev. C **61**, 014310 (2000).
16. C. E. Svensson *et al.*, Phys. Rev. Lett. **82**, 3400 (1999); private communication.
17. G. G. Adamian, N. V. Antonenko, R. V. Jolos, *et al.*, Phys. Rev. C **67**, 054303 (2003).
18. S. Cwiok, W. Nazarewicz, J. X. Saladin, *et al.*, Phys. Lett. B **322**, 304 (1994).
19. G. G. Adamian, N. V. Antonenko, N. Nenoff, and W. Scheid, Phys. Rev. C **64**, 014306 (2001).

Physics of Atomic Nuclei, Vol. 67, No. 9, 2004, pp. 1709–1714. From Yadernaya Fizika, Vol. 67, No. 9, 2004, pp. 1737–1742.

Superdeformation as Cluster State*

G. G. Adamian[1),2)], N. V. Antonenko[1)], R. V. Jolos[1)], Yu. V. Palchikov[1)], W. Scheid[3)], and T. M. Shneidman[1)]**

Received January 21, 2004

Abstract—A cluster approach is applied to describing the decay-out phenomenon of the yrast superdeformed states for mass region $A \approx 190$. © *2004 MAIK "Nauka/Interperiodica".*

1. INTRODUCTION

The intensities of the rotational $E2$ γ transitions within a superdeformed (SD) band show a remarkable feature. Transitions follow the band down with practically constant intensity. At some spins, the whole level-population intensity of the SD band drops practically to zero within two transitions. This phenomenon is said to be the decay out of the SD band [1–5]. The sudden disappearance of the SD bands at low spin $I = 6-14$ in the $A = 190$ region and at $I = 24-32$ in the $A \approx 150$ region together with unobserved decay path has raised many questions concerning the mechanism involved in the decay-out problem [6]. It has been suggested that the decay out is probably due to the mixing with the normal deformed (ND) states in the ordered or chaotic regimes. However, the numerical calculations have been more or less schematic with a lot of parameters and assumptions. We will apply the cluster approach to describing the ND and SD bands and the decay-out phenomenon.

2. CLUSTER APPROACH

The important modes of nuclear excitations are related to a motion in charge $\eta_Z = (Z_2 - Z_1)/(Z_2 + Z_1)$ and mass $\eta = (A_2 - A_1)/(A_2 + A_1)$ asymmetry coordinates, where Z_1 (A_1) and Z_2 (A_2) are the charge (mass) numbers of a light and heavy nucleus of the dinuclear system (DNS) [7–11], two touching nuclei or clusters. These relevant collective variables describe a partition of nucleons between the nuclei forming the DNS. The potential energy as a function of η_Z (η) has a few minima corresponding to different clusterizations of the whole system. The characteristics of the states in these minima are close to those of the ND and SD bands. The wave function in η_Z may be thought of as a superposition of different cluster-type configurations, including the mononucleus configuration with $|\eta_Z| = 1$, the α-cluster ^{4}He configuration with $|\eta_Z| = 1 - 4/Z$, the ^{8}Be-cluster configuration with $|\eta_Z| = 1 - 8/Z$, the ^{12}C-cluster configuration with $|\eta_Z| = 1 - 12/Z$, and other cluster ($Z = Z_1 + Z_2$) configurations. The relative contribution of each cluster component to the total wave function is determined by solving the stationary Schrödinger equation

$$H|\Psi(I)\rangle = E(I)|\Psi(I)\rangle, \tag{1}$$

where the collective Hamiltonian is

$$H = -\frac{\hbar^2}{2}\frac{d}{d\eta_Z}\frac{1}{B_{\eta_Z}}\frac{d}{d\eta_Z} + U(\eta_Z, I), \tag{2}$$

with the inertia coefficient B_{η_Z} and the potential $U(\eta_Z, I)$. The potential $U(\eta_Z, I)$ in Eq. (2) is taken as a dinuclear potential energy for $|\eta_Z| < 1$ [8, 12],

$$U(\eta_Z, I) = B_1(\eta_Z) + B_2(\eta_Z) + V(R = R_m, \eta_Z, I). \tag{3}$$

Here, the internuclear distance $R = R_m = R_1 + R_2 + 0.5$ fm is the touching distance between the clusters. Since the N/Z equilibrium occurs in the DNS, the potential energy U is minimized with respect to the mass asymmetry η for each fixed charge asymmetry η_Z. The quantities B_1 and B_2 (which are negative) are the experimental binding energies of the clusters forming the DNS at a given charge asymmetry η_Z. The quantity $V(R, \eta_Z, I)$ in (3) is the nucleus–nucleus interaction potential [12]:

$$V(R, \eta_Z, I) = V_C(R, \eta_Z) + V_N(R, \eta_Z) + V_{rot}(R, \eta_Z, I) \tag{4}$$

*This article was submitted by the authors in English.

[1)]Bogolyubov Laboratory of Theoretical Physics, Joint Institute for Nuclear Research, Dubna, Moscow oblast, 141980 Russia.
[2)]Institute of Nuclear Research, Tashkent, Uzbekistan.
[3)]Institut für theoretische Physik der Justus-Liebig-Universität, Giessen, Germany.
**e-mail: adamian@thsun1.jinr.ru

1063-7788/04/6709-1709$26.00

with the Coulomb V_C, the centrifugal $V_{rot} = \hbar^2 I(I+1)/(2\Im(\eta, R))$, and the nuclear interaction V_N potentials. Calculating the potential energy for α-, ^{7}Li-, ^{8}Be-, ^{11}B-, ^{12}C-, ^{15}N-, and ^{16}O-cluster configurations by formula (3), we interpolated the potential at discrete points by the stepwise potential [11].

To calculate the potential energy for $I \neq 0$, we need the moment of inertia $\Im(\eta_Z) = \Im(\eta_Z, R_m)$ [10]. As was shown in [8], the highly deformed states are well described as the cluster systems and their moments of inertia are about 0.85 of the rigid-body limit. Following this, we assume that the moment of inertia of the cluster configurations can be expressed as

$$\Im(\eta_Z) = c_1 \left(\Im_1^r + \Im_2^r + m_0 \frac{A_1 A_2}{A} R_m^2 \right). \quad (5)$$

Here, $\Im_i^r$ ($i = 1, 2$) are rigid-body moments of inertia for the clusters in the DNS, $c_1 = 0.85$ for all considered nuclei, and m_0 is the nucleon mass. The rigid-body moments of inertia are calculated with deformation parameters from [13]. For $|\eta_Z| = 1$, the value of the moment of inertia is not known from data because the experimental moment of inertia is a mean value between the moment of inertia of the mononucleus ($|\eta_Z| = 1$) and the moments of inertia of the cluster configurations arising due to the oscillations in $|\eta_Z|$. We assume that $\Im(|\eta_Z| = 1) = c_2 \Im^r(|\eta_Z| = 1)$, where $\Im^r$ is the rigid-body moment of inertia of the mononucleus and c_2 is a scaling parameter which is fixed by the energy of the first 6^+ state of the ND band. In the yrast ND band, the states with $I \geq 6$ are assumed to be rotational ones. We set $c_2 = 0.07$ for all nuclei under consideration.

The method of calculation of the inertia coefficient $B_{\eta_Z} = (d\eta/d\eta_Z)^2 B_\eta$ (where B_η is a mass parameter in the mass-asymmetry coordinate) used for the cluster configurations is given in [14]. Since the scale of variation of η_Z is large, the η dependence of the inertia coefficient is taken into consideration. Our calculations show that B_{η_Z} is a smooth and weak function of total charge number Z for $Z = 80$ and 82. For all considered nuclei, we set $B_{\eta_Z} = 19.2 \times 10^4 m_0$ fm^2 and $12.8 \times 10^4 m_0$ fm^2 for ^{8}Be- and ^{12}C-cluster configurations, respectively. For the ND wells of all nuclei considered, we set $B_{\eta_Z} = 7.5 \times 10^4 m_0$ fm^2. With this B_{η_Z}, the value of $U(|\eta_Z| = 1, I = 0)$ was chosen so as to obtain the correct values of binding energies $E(I = 0)$ of the ground states [10].

3. RESULTS OF CALCULATIONS

3.1. Potential Energy

For ^{190,192,194}Hg nuclei, the potential energy has a few important minima corresponding to mononucleus and ^{8}Be- and ^{12}C-cluster configurations. The DNS with α cluster has a potential energy a little larger than the energy of mononucleus at $|\eta_Z| = 1$. At values of $|\eta_Z|$ corresponding to the ^{7}Li- and ^{11}B-cluster configurations, the potential energy has maxima. The states of the ND bands have a significant contribution of an α-cluster component. The states of the ground and excited SD bands are described mainly as ^{8}Be- and ^{12}C-cluster configurations, respectively [9]. The SD bands lie at high energy and are isolated in a well-defined minimum at the point where they decay out to the ND states. At a given spin, the SD state is viewed as a zero-point vibration in the SD well. Since different cluster configurations have different moments of inertia, the barrier separating the SD and ND minima smoothly decreases with spin, but it remains relatively sizeable for the spins corresponding to the rapid escape from the SD minimum to the ND minimum. This indicates rather pure SD states until the lowest observed member of each SD band. The interaction between the SD states and ND states is suppressed by the small tunneling through the barrier. The origin of the spin dependence of the interaction between the pure SD and ND states is clear in the cluster approach [15].

3.2. Energy Spectra

Spectra of the yrast ND and SD bands for the nucleus ^{194}Hg are shown in Fig. 1. One can see that, in the ND band, there is an appreciable shift of the negative parity states with respect to the positive-parity states that is parity splitting. In the SD bands, the parity splitting almost disappears. The negative-parity states in the ground SD band were not found in the experiments. It should be mentioned that our consideration provides the possibility of considering the ground SD band as a mirror symmetric cluster configuration with two α particles on the opposite sides of heavy core like $^{194}\mathrm{Hg} = \alpha - ^{186}\mathrm{Os} - \alpha$ instead of asymmetric configuration $^{194}\mathrm{Hg} = ^{186}\mathrm{Os} - ^8\mathrm{Be}$. We checked that the energies and moments of inertia of these symmetric and asymmetric cluster configurations were almost the same. Thus, it is very interesting to consider in more detail in the experiment with the aim of finding out whether the negative-parity ground SD states exist or not [11].

Taking into consideration the absence of parameters for fitting in our cluster approach, the description of the experimental data is pretty good. Since the calculated spectra are purely rotational, the deviation from the experiment seems to be caused by the influence of other degrees of freedom (vibrations, the coupling with internal degrees of freedom). If there is a doubt about the spin and parity of the measured

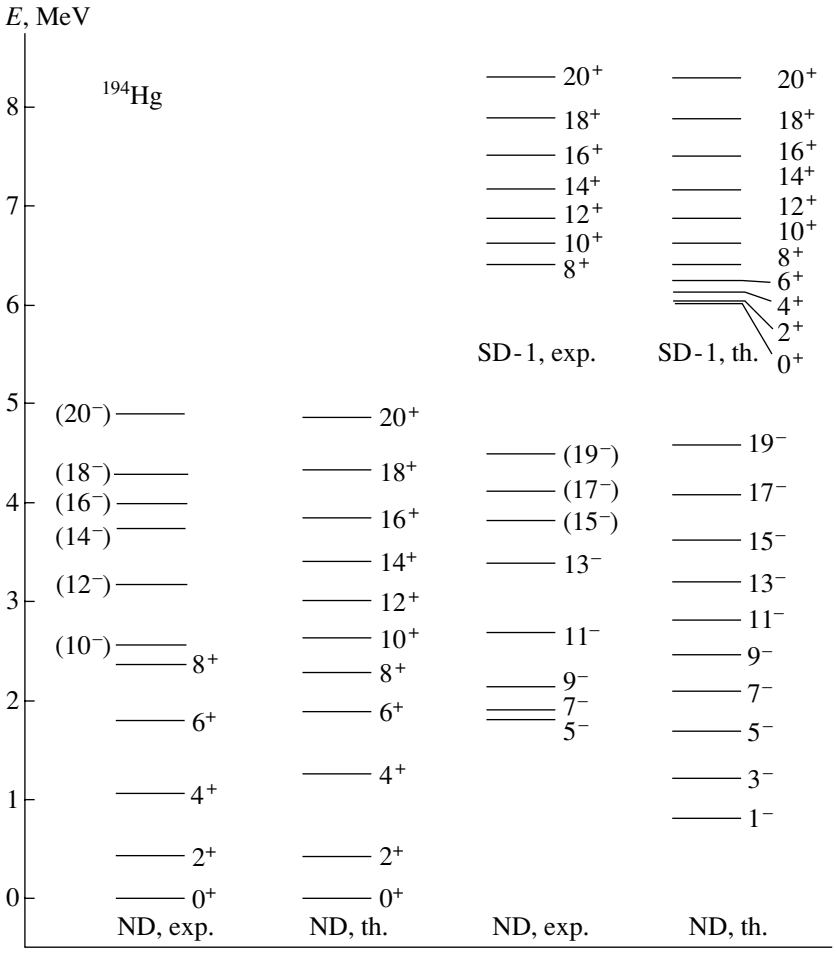

Fig. 1. Experimental (exp.) and calculated (th.) energies of the states of the ground ND and ground SD (SD-1) bands in ^{194}Hg. Experimental data are taken from [3].

level, its notation is given in parentheses in Fig. 1. Some of these levels are in good correspondence with the calculated ones. The yrast SD bands are well defined as rotational bands and, thus, better described in our approach than the ND bands.

For the ^{194}Hg nucleus, the experimental levels of the excited SD bands are in agreement with the calculated ones (Fig. 2). The calculated transition quadrupole moments Q_t in the ground and first excited SD bands are also in satisfactory agreement with the experimental data for ^{190,192,194}Hg nuclei.

3.3. Crossing of SD and ND Bands

In Fig. 3, the energies of the ground and excited ND states in the α-cluster well, as well as the yrast SD state in the ^{8}Be well, are shown as a function of even spin for the isotopes of mercury. The energy of the SD level is lower than the energy of the nearest neighboring ND level at large spins. With decreasing spin, the energy interval between these states decreases, and at some spin I, the ND states become more energetically favorable than the SD state. In all nuclei under consideration, this spin is close to the experimental spin I_{out} ($I_{\text{out}} = 10$ for ^{192,194}Hg and $I_{\text{out}} = 14$ for ^{190}Hg), where the decay out happens. The SD band crosses the first excited ND band, from which the collective transition to the ND band is expected to be very weak due to the competition with statistical quasicontinuum transitions.

Figure 4 shows that a significant increase in the component c^2 of the SD state in the ND well takes place around the crossing point of the SD band with the nearest neighboring ND band. The reason for this steep rise of the ND admixture c^2 of the SD states is the relative position (interference) of the SD and ND levels. A decrease in the barrier between the SD and ND wells with spin smoothly influences only the value of c^2.

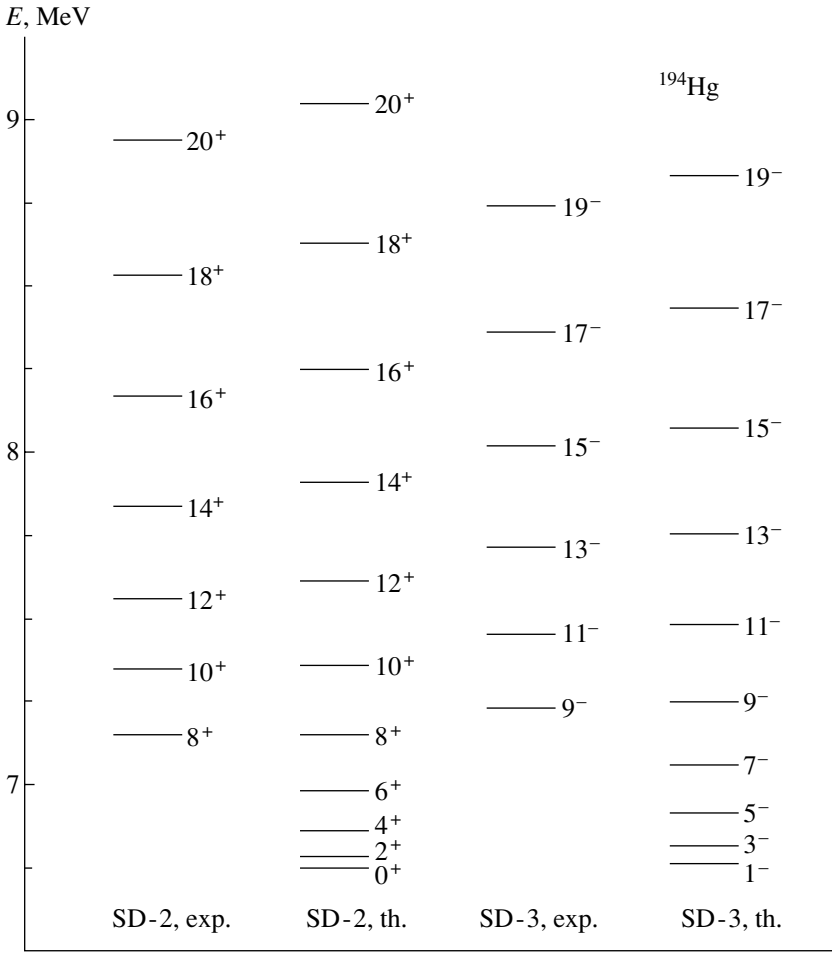

Fig. 2. Experimental (exp.) and calculated (th.) energies of the states of the excited SD bands (SD-2 and SD-3) in ^{194}Hg. Experimental data are taken from [1, 3].

3.4. Probability of Decay Out

In spite of the relatively small ND admixture of the SD state (for example, $c^2 = 2.4 \times 10^{-2}$ for ^{194}Hg), the decay out occurs through this component because the decay width $\Gamma_{\rm ND}$ in the ND well is much larger than the decay width $\Gamma_{\rm SD}$ in the SD well. The ratio $\Gamma_{\rm SD}/\Gamma_{\rm ND}$ drops sharply as spin decreases. $\Gamma_{\rm SD} = \hbar B(E2)E_\gamma^5$ is determined by collective rotational electromagnetic (nonstatistical) quadrupole transitions in the SD well. The in-band $E2$ transition rate falls rapidly because of the growing fractional decrease in E_γ and E_γ^5 dependence. In order to determine $\Gamma_{\rm ND}$, only statistical $E1$ transitions were considered for the decay between the ND states, since they are expected to dominate (with respect to the collective $E2$ and statistical $M1$ transitions) due to the high excitation energy of the SD states above the yrast line (≈ 4 MeV). The latter comes from fact that the moment of inertia for the SD shape is larger than the one for the ND states and the SD states become more excited with respect to the ND yrast line with decreasing spin I. The statistical $E1$ decay is governed by the level densities and the giant dipole resonance strength function based on the energy-weighted sum rule. The $E1$ width is approximated by the analytical expression $\Gamma_{\rm ND} = 3c_{E1}T^5$ [16], where $T = (U/a)^{1/2}$, the excitation energy $U = E(I) - \hbar^2 I(I+1)/(2\Im^r(|\eta| = 1)) - 2\Delta$ [17], the level density parameter $a = 22.58$ MeV^{-1} [15, 17], the backshift parameter $2\Delta = 24/A^{1/2}$, and

$$c_{E1} = 4!\frac{e^2}{\hbar c}\frac{1}{m_0c^2}\frac{\Gamma_R}{E_R}\frac{NZ}{A}.$$

The $E1$ giant resonance parameter is chosen as $E_R = 78/A^{1/3}$ MeV and $\Gamma_R = 4.4$ MeV [15]. The increase in $\Gamma_{\rm ND}$ with decreasing I is evident.

The total probability $P_{\rm out}$ that the state in the SD well decays into the state in the ND well is calculated

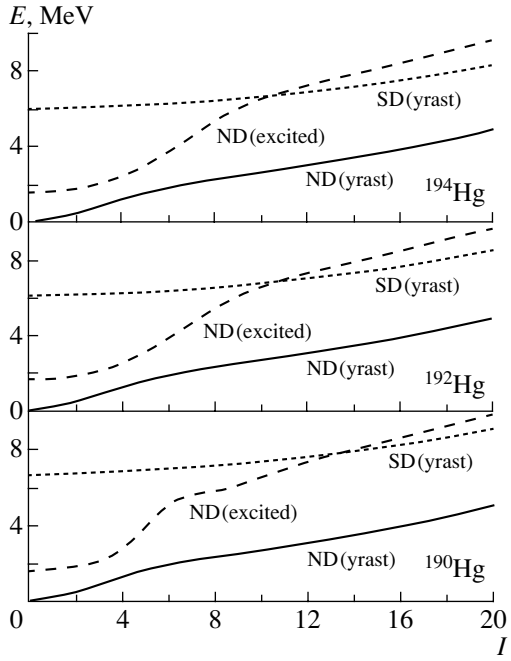

Fig. 3. The energies of the ground (solid curve) and the first excited (dashed curve) ND positive-parity states, and the ground SD state (dotted curve) as functions of spin I for the isotopes of mercury.

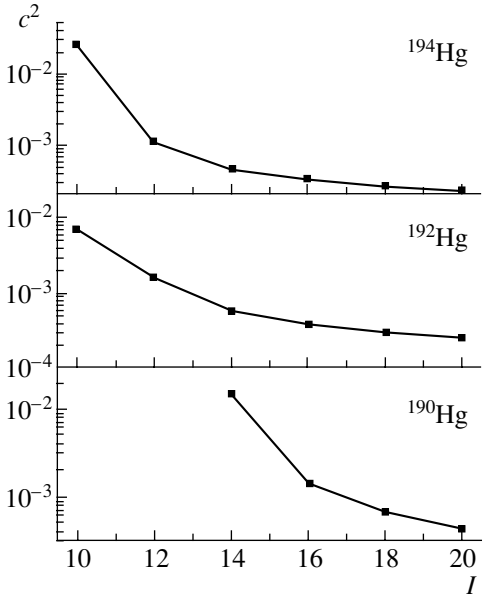

Fig. 4. The calculated ND admixture c^2 of the yrast SD state as a function of spin for ^{190,192,194}Hg nuclei. The experimental decay-out spins are $I_{\rm out} = 14$, 10, and 10 for ^{190}Hg, ^{192}Hg, and ^{194}Hg, respectively [3–5].

as follows:

$$P_{\rm out} = \frac{c^2\Gamma_{\rm ND}}{c^2\Gamma_{\rm ND} + (1-c^2)\Gamma_{\rm SD}}, \qquad (6)$$

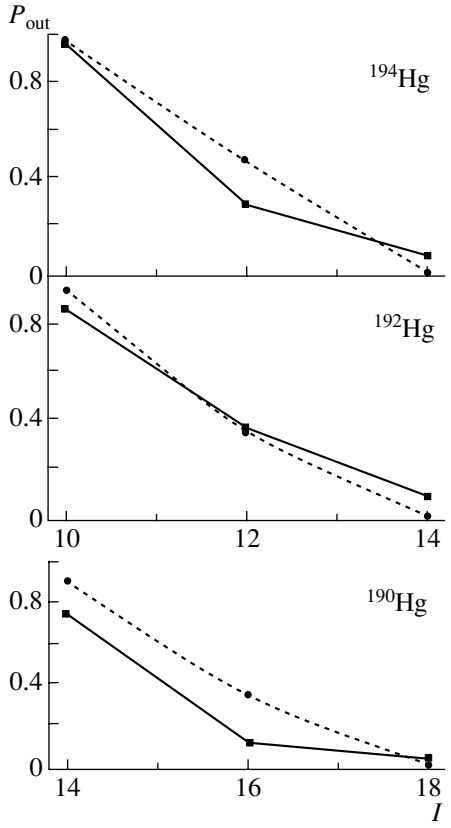

Fig. 5. The calculated (solid circles) probability $P_{\rm out}$ that the SD state decays into the ND states as a function of spin I for different isotopes of mercury. Experimental data (solid squares) are taken from [3–5]. The solid and dashed lines are to guide the eye.

where c^2 is the fraction of the wave function with the dominant SD component in the ND well. Here, the SD state has the partial width $(1-c^2)\Gamma_{\rm SD}$ to decay in the next SD state and the partial width $c^2\Gamma_{\rm ND}$ to decay in the lower energy ND states.

One can see in Fig. 5 that the calculated total probabilities $P_{\rm out}$ are in good agreement with the experimental ones. This is an indication of validity of the cluster approach. The increase in $P_{\rm out}$ is mainly due to the increase in c^2 for the ^{190,192,194}Hg nuclei.

The origin of the decay out from the excited SD band is expected to be the same as for the decay out from the yrast SD band. It is still unclear to us the nature (α cluster or two-quasiparticle-like structures) of the excited ND band which is crossed with the excited SD band. Another open question is whether the mechanism underlying the transition from the ground and excited SD bands to the ND states in mass regions with $A \approx 130$, 140, and 150 is the same as in mass-190 region. With the cluster approach, we recently reproduced the experimental data for the SD band of the ^{60}Zn nucleus [11]. In this

case, the one-step discrete collective $E2$ γ rays to the ND yrast states carry a large fraction of the decay out of the ground SD state since the width of collective $E2$ transitions in the ND well is much larger than the statistical one because of the small level densities.

4. SUMMARY

We conclude that the cluster approach provides a good description of the spectra and decay out of the ground SD bands in the mass-190 region. Our analysis indicates that the sudden decay out of the SD band (^{8}Be-cluster configuration) into the ND band (related to the α-particle clusterization) is because of the crossing of the SD band with the nearest neighboring excited ND band. Near the band-crossing point, the statistical $E1$ decay to the ND configurations competes successfully against the collective $E2$ decay along the SD band. The main reasons for the decay out at the crossover point are (i) the perceptible square of the amplitude of the SD wave function component in the ND well and (ii) the reduction of the in-band SD collective $E2$ decay rate and the increase in the ND statistical $E1$ transition rate due to the large excitation energy of the SD state with respect to the ND yrast line.

The decay width of a light cluster is one of the most important physical quantities to identify a cluster-like structure. During γ emission, the SD cluster states can decay into two fragment clusters. Therefore, one can identify the SD states by measuring the rotational γ quanta in coincidence with the decay fragments of the DNS. If the SD state is a cluster state, we should observe pronounced yields of the light clusters like α particles, ^{8}Be (two correlated α particles), and ^{12}C. The spectroscopic investigation of the SD states turns out not to be easy because of the low cross sections.

ACKNOWLEDGMENTS

This work was supported in part by DFG (Bonn), Volkswagen-Stiftung (Hannover), and the Russian Foundation for Basic Research (Moscow).

REFERENCES

1. X.-L. Han and C.-L. Wu, At. Data Nucl. Data Tables **73**, 43 (1999); http://www.nndc.bnl.gov/nndc/ensdf/.
2. T. Lauritsen *et al.*, Phys. Rev. Lett. **89**, 282501 (2002); **88**, 042501 (2002).
3. T. L. Khoo *et al.*, Phys. Rev. Lett. **76**, 1583 (1996); G. Hackman *et al.*, Phys. Rev. Lett. **79**, 4100 (1997).
4. A. N. Wilson *et al.*, Phys. Rev. C **54**, 559 (1996); B. Crowell *et al.*, Phys. Rev. C **51**, R1599 (1995).
5. P. Fallon *et al.*, Phys. Rev. C **51**, R1609 (1995); A. Korichi *et al.*, Phys. Lett. B **345**, 403 (1995); P. Willsau *et al.*, Nucl. Phys. A **574**, 560 (1994).
6. E. Vigezzi, R. A. Broglia, and T. Dossing, Phys. Lett. B **249**, 163 (1990); Nucl. Phys. A **520**, 179 (1990); T. L. Khoo *et al.*, Nucl. Phys. A **557**, 83 (1993); S. Aberg, Phys. Rev. Lett. **82**, 299 (1999); C. A. Stafford and B. R. Barrett, Phys. Rev. C **60**, 051305 (1999); J.-Z. Gu and H. A. Weidenmueller, Nucl. Phys. A **660**, 197 (1999); J. Libert, M. Girod, and J.-P. Delaroche, Phys. Rev. C **60**, 054301 (1999); R. Kruecken *et al.*, Phys. Rev. C **64**, 064316 (2001).
7. V. V. Volkov, Phys. Rep. **44**, 93 (1978); W. Greiner, J. Y. Park, and W. Scheid, *Nuclear Molecules* (World Sci., Singapore, 1995).
8. T. M. Shneidman *et al.*, Nucl. Phys. A **671**, 119 (2000).
9. G. G. Adamian *et al.*, Acta Phys. Pol. B **34**, 2147 (2003).
10. T. M. Schneidman *et al.*, Phys. Lett. B **526**, 322 (2002); Phys. Rev. C **67**, 014313 (2003).
11. G. G. Adamian *et al.*, Phys. Rev. C **67**, 054303 (2003).
12. G. G. Adamian *et al.*, Int. J. Mod. Phys. E **5**, 191 (1996).
13. S. Raman, C. W. Nestor, and P. Tikkanen, At. Data Nucl. Data Tables **78**, 1 (2001).
14. G. G. Adamian, N. V. Antonenko, and R. V. Jolos, Nucl. Phys. A **584**, 205 (1995).
15. R. Kruecken *et al.*, Phys. Rev. C **55**, 1625 (1997); R. Kruecken, Phys. Rev. C **62**, 061302(R) (2000); A. Dewald *et al.*, Phys. Rev. C **64**, 054309 (2001).
16. T. Dossing and E. Vigezzi, Nucl. Phys. A **587**, 13 (1995).
17. A. V. Ignatyuk, *Statistical Properties of Excited Atomic Nuclei* (Énergoizdat, Moscow, 1983) [in Russian].

Physics of Atomic Nuclei, Vol. 67, No. 9, 2004, pp. 1715–1720. From Yadernaya Fizika, Vol. 67, No. 9, 2004, pp. 1743–1748.

Integral Equations in the Fock–Bargmann Space and the Generator-Coordinate Method*

G. F. Filippov[1)], Yu. A. Lashko[1)], S. V. Korennov[1),2)], and K. Katō[3)]**

Received January 21, 2004

Abstract—In the generator-coordinate method, the norm kernel built as a Slater determinant of the Brink–Bloch orbitals plays a role of unity for the complete set of orthonormalized states defined in the Fock–Bargmann space and satisfying the Pauli exclusion principle. The closure condition is then written as the Hilbert–Schmidt expansion of the norm kernel and can be derived by a simple algebraic procedure. A basis of eigenstates of the norm kernel is shown to be a powerful tool in resonating-group calculations.

1. INTRODUCTION

The purpose of the present work is to construct a complete orthonormalized basis in the generator-coordinate method (GCM) and then use it in solving the Hill–Wheeler equations. Moreover, the basis can be applied in the resonating-group method (RGM) calculations. Further details and references can be found in [1].

Both the GCM and the Hill–Wheeler equations are well known. Here, we recall only the points important for further discussion. A remarkable feature of the GCM is that it reduces a many-body problem to a study of just a few degrees of freedom reproducing important modes of motion. Their importance is first determined on the basis of physical considerations.

Some of the difficulties appearing in the GCM calculations and ways to overcome them can be clearly illustrated by a simple yet realistic example of the interaction between a neutron and ^{4}He nucleus. Generalizations are then straightforward.

2. GENERATOR-COORDINATE METHOD

An application of the GCM begins with the construction of a generator (trial) function

$$\Psi(\mathbf{R};\{\mathbf{r}_i\}),$$

where $\mathbf{R}$ is a vector generator parameter introduced to describe the relative motion of one of the nucleons and the center of mass of the rest of them; $\mathbf{r}_i$ are single-particle position vectors. The generator function is considered to be known. In the following, it is assumed to have the form of a Slater determinant of the five-particle system constructed of s orbitals (α-particle nucleons),

$$\phi_0(\mathbf{r}) = \pi^{-3/4}\exp\left(-\frac{\mathbf{r}^2}{2}\right),$$

and the modified Bloch–Brink orbital $\phi(\mathbf{R},\{\mathbf{r}\})$ for the valence neutron [2],

$$\phi(\mathbf{R},\{\mathbf{r}\}) = \pi^{-3/4}\exp\left(-\frac{\mathbf{r}^2}{2}+\sqrt{2}(\mathbf{R}\cdot\mathbf{r})-\frac{\mathbf{R}^2}{2}\right).$$

Being a Slater determinant, the generator function

$$\Psi(\mathbf{R};\{\mathbf{r}_i\}) = \det||\phi_k(\mathbf{r}_i)|| \qquad (1)$$

is antisymmetric with respect to permutations of nucleonic coordinates. The basis functions generated by (1) satisfy the Pauli principle as well. We shall not show the explicit form of this Slater determinant here to keep things simple, but later some constructions derived from it will be demonstrated.

Now, following the GCM procedure, we calculate the norm kernel (overlap),

$$I(\mathbf{R};\mathbf{S}) = \int \Psi(\mathbf{R};\{\mathbf{r}_i\})\Psi(\mathbf{S};\{\mathbf{r}_i\})d\tau, \qquad (2)$$

as well as the Hamiltonian $\hat{H}$ kernel for the system studied,

$$H(\mathbf{R};\mathbf{S}) = \int \Psi(\mathbf{R};\{\mathbf{r}_i\})\hat{H}\Psi(\mathbf{S};\{\mathbf{r}_i\})d\tau.$$

Integration is taken over all single-particle vectors.

In the GCM, the wave functions $F(\{\mathbf{r}_i\})$ have the form

$$F(\{\mathbf{r}_i\}) = \int C(\mathbf{R}^*)\Psi(\mathbf{R};\{\mathbf{r}_i\})d\mu_{\mathrm{B}}.$$

*This article was submitted by the authors in English.

[1)]Bogolyubov Institute for Theoretical Physics, National Academy of Sciences of Ukraine, Kiev, Ukraine.
[2)]Université Libre de Bruxelles, Brussels, Belgium.
[3)]Hokkaido University, Sapporo, Japan.
**e-mail: gfilippov@bitp.kiev.ua

The problem is now reduced to the Hill–Wheeler equation for the coefficients $C(\mathbf{R}^*)$,

$$\int \{H(\mathbf{R};\mathbf{S})C(\mathbf{S}^*) - E\cdot I(\mathbf{R};\mathbf{S})C(\mathbf{S}^*)\}d\tilde{\mu}_{\mathrm{B}} = 0. \tag{3}$$

Equation (3) follows from the variational principle for the functional

$$J = \int\int C(\mathbf{R}^*)\{H(\mathbf{R};\mathbf{S}) - E\cdot I(\mathbf{R};\mathbf{S})\}C(\mathbf{S}^*)d\mu_{\mathrm{B}}d\tilde{\mu}_{\mathrm{B}}. \tag{4}$$

In the present approach, we search for the coefficients, or rather functions, $C(\mathbf{R})$ in the form of an expansion over a complete orthonormalized basis of states $\{\psi_n(\mathbf{R})\}$ satisfying the Pauli exclusion principle. We set

$$C(\mathbf{R}) = \sum_n C_n\psi_n(\mathbf{R}).$$

The basis is defined so that

$$I(\mathbf{R},\mathbf{S}) = \sum_n \Lambda_n\psi_n(\mathbf{R})\psi_n(\mathbf{S}). \tag{5}$$

The latter condition has a simple physical meaning. The quantity $I(\mathbf{R},\mathbf{S})$ is not only the norm kernel but also the density matrix (of mixed states, to be exact), which can always be diagonalized. Later we will show how to do this, but for now let us note only that the Hamiltonian kernel can be represented in the form

$$H(\mathbf{R},\mathbf{S}) = \sum_n\sum_{\tilde{n}} \psi_n(\mathbf{R})\langle n|\hat{H}|\tilde{n}\rangle\psi_{\tilde{n}}(\mathbf{S}), \tag{6}$$

which leads to the following form of the functional (4):

$$J = \sum_n\sum_{\tilde{n}} C_n\left(\langle n|\hat{H}|\tilde{n}\rangle - E\cdot\Lambda_n\delta_{n,\tilde{n}}\right)C_{\tilde{n}}.$$

As a result, after variation of J, instead of the Hill–Wheeler equation (3), we arrive at a set of linear algebraic equations for the coefficients C_n,

$$\sum_{\tilde{n}=0}^{\infty}\left(\langle n|\hat{H}|\tilde{n}\rangle - E\cdot\Lambda_n\delta_{n,\tilde{n}}\right)C_{\tilde{n}} = 0, \tag{7}$$

$$n = 0, 1, 2, \ldots,$$

which we call the set of equations of the algebraic version of the resonating-group method. The ways to solve these coupled equations were already shown and the results were published. So we would rather discuss the construction of the basis set $\{\psi_n(\mathbf{R})\}$, since this is a nontrivial matter when the number of dynamic degrees of freedom is relatively large.

3. ORTHONORMALIZED GCM BASIS

It appears that it is much simpler to construct this complete orthonormalized set of states $\{\psi_n(\mathbf{R})\}$ allowed by the Pauli principle in the Fock–Bargmann space [3–6], where, in fact, complex vectors $\mathbf{R}$ and $\mathbf{S}$ are defined.

A wave function, originally defined in the usual coordinate space, has its map in the Fock–Bargmann space. This map is an entire function of its variable, in our case, the complex vector $\mathbf{R}(\mathbf{S})$: it has no irregularities except at infinity.

The Fock–Bargmann map $\psi(\mathbf{R})$ of a function $\phi(\mathbf{r})$ is obtained by the integral transform with the kernel

$$\Phi(\mathbf{R},\mathbf{r}) = \frac{1}{\pi^{3/4}}\exp\left(-\frac{\mathbf{r}^2}{2} + \sqrt{2}(\mathbf{R}\cdot\mathbf{r}) - \frac{\mathbf{R}^2}{2}\right),$$

which is nothing but the modified Bloch–Brink orbital.

Thus, the map is found after a threefold integration,

$$\psi(\mathbf{R}) = \int \Phi(\mathbf{R},\mathbf{r})\phi(\mathbf{r})d\mathbf{r}.$$

The original function can be restored by means of the inverse transform,

$$\phi(\mathbf{r}) = \int \Phi(\mathbf{R}^*,\mathbf{r})\psi(\mathbf{R})d\mu_{\mathrm{B}},$$

which is a sixfold integration with the Bargmann measure $d\mu_{\mathrm{B}}$,

$$\mathbf{R} = \frac{\boldsymbol{\xi} + i\boldsymbol{\eta}}{\sqrt{2}}, \qquad d\mu_{\mathrm{B}} = \exp\{-(\mathbf{R}\cdot\mathbf{R}^*)\}\frac{d\boldsymbol{\xi}d\boldsymbol{\eta}}{(2\pi)^3}.$$

In the applications of the GCM, the maps of functions appear to be remarkably simpler than many-particle originals, which justifies the whole idea of the use of the Fock–Bargmann space.

To construct the complete basis of allowed states to solve of the generator-coordinate problem, we have to find an expanded form of the norm kernel (the density matrix), Eq. (5). If $I(\mathbf{R},\mathbf{S})$ is considered as the symmetric kernel of an integral equation, this expansion acquires the meaning of the Hilbert–Schmidt expansion, and it is not that easy to find it.

Only a few of us have not been surprised, realizing that a differential equation can be reduced to a simpler algebraic one by the Laplace transform. Similarly, we were excited understanding that, if the expression $I(\mathbf{R},\mathbf{S}^*)$ is treated as the kernel of an integral equation for the Fock–Bargmann map of the allowed basis functions, the eigenfunctions of this kernel are obtained instantly. The reason is that the kernel is reduced to a set of degenerate (separable) kernels and each of them presents an easy-to-solve problem.

The transform leading to the norm kernel has been known to us and other people for a while. However, the interpretation of $I(\mathbf{R},\mathbf{S})$ as a kernel of an integral equation with the Bargmann measure (thus, defined in the Fock–Bargmann space) is given here for the first time. Like Moliere's character, we just realized we spoke prose all the time.

4. FOCK–BARGMANN SPACE

We now turn to some basic features of the Fock–Bargmann space in comparison with the conventional coordinate space, as well as to examples of some simple functions and operators and their Fock–Bargmann maps.

In the coordinate space, the basis functions of the one-dimensional harmonic oscillator (h.o.) are expressed in terms of Hermite polynomials, i.e.,

$$\phi_n(x) = \frac{1}{\sqrt{2^n n!\sqrt{\pi}}} H_n(x) \exp\left(-\frac{x^2}{2}\right), \quad n = 0, 1, 2, \ldots,$$

while the closeness condition for these functions reads

$$\delta(x-y) = \sum_{n=0}^{\infty} \phi_n(x)\phi^*(y).$$

In the Fock–Bargmann space, the h.o. basis functions are the eigenfunctions of the operator

$$\hat{H}_{\rm osc} = z\frac{d}{dz} + \frac{1}{2}$$

and take the form

$$\psi_n(z) = \frac{1}{\sqrt{n!}} z^n, \qquad n = 0, 1, 2, \ldots,$$

where z is a complex variable. The closeness condition becomes

$$\exp(zz^*) = \sum_{n=0}^{\infty} \psi_n(z)\psi_n(z^*).$$

Naturally, the functions $\psi_n(z)$ are orthonormalized:

$$\int_{-\infty}^{\infty}\int_{-\infty}^{\infty} \psi_n(z)\psi_{n'}(z^*) d\mu_{\rm B} = \delta_{n,n'}.$$

The Bargmann measure here reads

$$d\mu_{\rm B} = \exp(-zz^*)\frac{d\xi d\eta}{2\pi}, \quad z = \frac{\xi + i\eta}{\sqrt{2}}.$$

In the coordinate space, the continuum of the plane waves

$$\phi_k(x) = \frac{1}{\sqrt{2\pi}} \exp ikx, \quad -\infty < k < \infty,$$

satisfies the following closeness condition

$$\delta(x-y) = \frac{1}{2\pi}\int_{-\infty}^{\infty} \exp[ik(x-y)]dk.$$

The same condition in the Fock–Bargmann space,

$$\exp(zz^*) = \frac{1}{\pi^{1/2}} \times \int_{-\infty}^{\infty} \exp\left(-k^2 - i\sqrt{2}(z - z^*, k) + \frac{z^2 + z^{*2}}{2}\right) dk,$$

follows the form of plane waves,

$$\phi_k(R) = \frac{1}{\pi^{1/4}} \exp\left(-\frac{k^2}{2} - i\sqrt{2}Rk + \frac{R^2}{2}\right), \quad -\infty < k < \infty. \tag{8}$$

The function (8) is the eigenfunction of the momentum operator

$$\hat{k} = -\frac{i}{\sqrt{2}}\left(z - \frac{\partial}{\partial z}\right)$$

defined in the Fock–Bargmann space.

One more example of a function of the continuum is the eigenfunction of the coordinate operator

$$\phi_x(z) = \frac{1}{\pi^{1/4}} \exp\left(-\frac{x^2}{2} + \sqrt{2}z\, x - \frac{z^2}{2}\right), \quad -\infty < x < \infty.$$

It satisfies the equation

$$\hat{x}\phi_x(z) = x\phi_x(z),$$

where

$$\hat{x} = \frac{1}{\sqrt{2}}\left(z + \frac{\partial}{\partial z}\right).$$

The corresponding closeness condition takes the familiar, for the Fock–Bargmann space, form

$$\exp(zz^*) = \frac{1}{\pi^{1/2}} \times \int_{-\infty}^{\infty} \exp\left(-x^2 + \sqrt{2}(z + z^*, x) + \frac{z^2 + z^{*2}}{2}\right) dx.$$

In all these examples, one utilizes the kernel of the (one-dimensional) Bargmann transform between the two spaces,

$$\Phi(x,z) = \frac{1}{\pi^{1/4}} \exp\left(-\frac{x^2}{2} + \sqrt{2}zx - \frac{z^2}{2}\right).$$

Therefore, in particular, there holds the following definition of the map of the h.o. eigenfunction in terms of its original:

$$\psi_n(z) = \int_{-\infty}^{\infty} \Phi(x,z)\phi_n(x)dx.$$

In general,

$$\psi(z) = \int_{-\infty}^{\infty} \Phi(x,z)\phi(x)dx.$$

Finally, the inverse transform requires the Bargmann measure,

$$\phi(x) = \int \Phi(x,z)\psi(z)d\mu_{\rm B}.$$

5. HILBERT–SCHMIDT EXPANSION

Coming back to the $^4\mathrm{He}+n$ system, we consider its norm kernel (2),

$$I(\mathbf{R},\mathbf{S}) = \exp(\mathbf{R}\cdot\mathbf{S}) - \exp\left(-\frac{1}{4}(\mathbf{R}\cdot\mathbf{S})\right).$$

If the GCM vector parameters $\mathbf{R},\mathbf{S}$ are analytically continued to the complex space,[4)] then $I(\mathbf{R},\mathbf{S})$ becomes that unity which is resolved by the Pauli-allowed basis states in the closeness condition. The complete basis itself can be found as a solution of the integral equation

$$\Lambda\phi(\mathbf{R}) \qquad (9)$$
$$= \int \left\{\exp(\mathbf{R}\cdot\mathbf{S}) - \exp\left(-\frac{1}{4}(\mathbf{R}\cdot\mathbf{S})\right)\right\}\phi(\mathbf{S}^*)d\tilde{\mu}_{\rm B}.$$

At first glance, Eq. (9) does not look promising to search for its eigenvalues Λ_n and eigenvectors $\phi_n(\mathbf{R})$. But if we do one more step and expand the kernel,

$$I(\mathbf{R},\mathbf{S}) = \sum_{n=0}^{\infty}\left\{1-\left(-\frac{1}{4}\right)^n\right\}\frac{1}{n!}(\mathbf{R}\cdot\mathbf{S})^n, \quad (10)$$

we suddenly realize that this is the Hilbert–Schmidt expansion, and the eigenvalues are

$$\Lambda_{(n,0)} = 1-\left(-\frac{1}{4}\right)^n,$$

while the orthonormalized (with the Bargmann measure) eigenfunctions are contained in the expressions

$$\frac{1}{n!}(\mathbf{R}\cdot\mathbf{S})^n = \sum_{l,m}\phi_{(n,0),l,m}(\mathbf{R})\phi_{(n,0),l,m}(\mathbf{S}).$$

[4)]This continuation means a transition to the phase space, as the number of independent parameters is doubled.

Note that every basis function $\phi_{(n,0),l,m}(\mathbf{R})$ belongs to the irreducible representation $(\lambda,\mu)=(n,0)$ of the $SU(3)$ group and that

$$\int \frac{1}{n!}(\mathbf{R}\cdot\mathbf{R}^*)^n d\mu_{\rm B} = \frac{(n+1)(n+2)}{2},$$

where the value on the right-hand side is the dimensionality of this representation. Here, n is the number of h.o. quanta of the relative motion of ^{4}He and the neutron, l is the orbital momentum, and m is its projection.

The normalized basis functions with $l=m=0$ take the form

$$\phi_{(2k,0),0,0}(\mathbf{R}) = \frac{1}{\sqrt{(2k+1)!}}\mathbf{R}^{2k}.$$

One can easily check their orthogonality. The closeness condition for these functions reads

$$\frac{\sinh(|\mathbf{R}||\mathbf{S}|)}{|\mathbf{R}||\mathbf{S}|} - \frac{\sinh(|\mathbf{R}||\mathbf{S}|/4)}{|\mathbf{R}||\mathbf{S}|/4}$$
$$= \sum_{k=1}^{\infty}\left(1-\frac{1}{4^{2k}}\right)\phi_{(2k,0),l=0}(\mathbf{R})\phi_{(2k,0),l=0}(\mathbf{S}).$$

The eigenvalues $\Lambda_{(n,0)}$ depend on the $SU(3)$ symmetry indices only. As n increases, they are limited to unity, but at low values of n the corresponding eigenfunctions are affected by the Pauli principle. Note that, at $\Lambda_0=0$, the state ϕ_0 is forbidden.

There is an alternative interpretation of the expansion (10). It can be treated as the diagonal form of the density matrix of the "mixed" states of the system and can be used in quantum-statistical applications.

Let us take another example. The system $^6\mathrm{He}+n$ requires an additional pair of vectors, $\mathbf{u}$ and $\tilde{\mathbf{u}}$, to describe possible excitations of the ^{6}He cluster. The norm kernel for this system takes the form

$$I(\mathbf{R},\mathbf{S}) = (\mathbf{u}\cdot\tilde{\mathbf{u}})^2\Big\{\exp(\mathbf{R}\cdot\mathbf{S}) \qquad (11)$$
$$-\exp\left(-\frac{1}{6}(\mathbf{R}\cdot\mathbf{S})\right)\Big\} - (\mathbf{u}\cdot\tilde{\mathbf{u}})(\mathbf{u}\cdot\mathbf{S})(\mathbf{R}\cdot\tilde{\mathbf{u}})$$
$$\times\exp\left(-\frac{1}{6}(\mathbf{R}\cdot\mathbf{S})\right).$$

At all even $n=2k$, the integral equation yields two states with zero angular momentum,

$$\phi_{(2k+2,0),l=0}(\mathbf{R},\mathbf{u}) = \frac{1}{\sqrt{2(2k)!(2k+3)}}$$
$$\times\left\{\mathbf{u}^2\cdot\mathbf{R}^{2k} - \frac{2k}{2k+1}[\mathbf{u}\times\mathbf{R}]^2\cdot\mathbf{R}^{2k-2}\right\},$$

$$\Lambda_{(2k+2,0)} = 1+\frac{14k-1}{6^{2k}},$$

$$\phi_{(2k-2,2),l=0}(\mathbf{R},\mathbf{u}) = \sqrt{\frac{2}{2(2k+1)!(2k+1)}}[\mathbf{u}\times\mathbf{R}]^2\cdot\mathbf{R}^{2k-2},$$

$$\Lambda_{(2k-2,2)} = 1 - \frac{8}{6^{2k}}.$$

Again, the functions appear to be so simple that it is a pleasure to show them explicitly.

All these functions are antisymmetric with respect to permutations of the nucleons. It can be proven with an explicit definition of the antisymmetrization operator in the Fock–Bargmann representation. However, it will not be discussed here.

One more remark. When there are three pairs of vector parameters, as in the $^6\mathrm{He}+{}^6\mathrm{He}$ case, there appears the $SU(3)$ degeneracy; that is, different eigenfunctions of a nucleus have the same quantum numbers introduced above. The case of degenerate kernels is also tractable by a standard algebraic procedure. There, the degree of degeneracy becomes the order of the algebraic set of equations one needs to solve.

6. HAMILTONIAN KERNEL

The kernel of a Hamiltonian $\hat{H}$ is defined as an integral

$$H(\mathbf{R},\mathbf{S}) = \int \Psi(\mathbf{R};\{\mathbf{r}_i\})\hat{H}\Psi(\mathbf{S};\{\mathbf{r}_i\})d\tau.$$

It can also be expanded over the eigenfunctions of the kernel (10), but the expansion will be nondiagonal,

$$H(\mathbf{R},\mathbf{S}) = \sum_n\sum_{\tilde{n}}\phi_n(\mathbf{R})\langle n|\hat{H}|\tilde{n}\rangle\phi_{\tilde{n}}(\mathbf{S}),$$

where the matrix elements is

$$\langle n|\hat{H}|\tilde{n}\rangle = \int\int \phi_n(\mathbf{R}^*)H(\mathbf{R},\mathbf{S})\phi_{\tilde{n}}(\mathbf{S}^*)d\mu_{\mathrm{B}}d\tilde{\mu}_{\mathrm{B}}. \quad (12)$$

The integrations in (12) are taken analytically.

7. GENERAL CASE

In the most general case, the eigenfunctions of the norm kernel (a Slater determinant of overlaps of Brink–Bloch orbitals) are labeled by the number of h.o. quanta ν, the $SU(3)$ Elliott's indices (λ,μ), $SU(3)$ multiplicity label $\alpha_{(\lambda,\mu)}$ (when necessary), the orbital momentum l and its projection m, and an additional quantum number α_l (if necessary). We denote a set of all these numbers as n, with Λ_n, $\psi_n(\mathbf{R})$ being the corresponding eigenvalue and eigenfunction of the norm kernel. The eigenvalues depend on ν and (λ,μ) (and, possibly, on $\alpha_{(\lambda,\mu)}$). The set of eigenfunctions $\psi_n(\mathbf{R})$ of the norm kernel is orthonormalized (with the Bargmann measure). If there is no $SU(3)$ degeneracy, the set can be found in a simple algebraic way. Otherwise, one needs to solve an integral equation with a degenerate kernel.

The Bargmann transform kernel can be expanded in a way similar to Eq. (5):

$$\Phi(\mathbf{R},\mathbf{r}) = \sum_n \sqrt{\Lambda_n}\psi_n(\mathbf{R})\phi_n(\mathbf{r}),$$

where $\phi_n(\mathbf{r})$ is the Pauli-allowed basis state and $\psi_n(\mathbf{R})$ is its Fock–Bargmann map. In actual calculations, one utilizes the facts that the latter is simpler than the former and that the matrix elements do not depend on a particular representation of the basis functions and the operators.

The Hill–Wheeler equation can naturally be written in the discrete representation of the basis $\{\psi_n(\mathbf{R})\}$. First, one has to find a matrix element of the Hamiltonian $\hat{H}$ between the generating functions and, then, to project this matrix element to the basis states.

The solution of the Hill–Wheeler equation $\Psi(\mathbf{R})$ is sought in the form

$$\Psi(\mathbf{R}) = \sum_n C_n\psi_n(\mathbf{R}),$$

where the unknown coefficients C_n satisfy the equations

$$\sum_{\tilde{n}}\langle n|\hat{H}|\tilde{n}\rangle C_{\tilde{n}} - E\Lambda_n C_n = 0. \quad (13)$$

The index n takes all values allowed by the Pauli principle.

This set of equations differs from the discrete representation of the Schrödinger equation in two ways.

Firstly, only the matrix elements between the Pauli-allowed states participate in the equations. Therefore, an additional (e.g., phenomenological) term projecting out the forbidden states is not needed. If it were present in (13), it would have no contribution.

Secondly, the last term on the left-hand side of Eq. (13) is proportional to the eigenvalue Λ_n of the norm kernel. This factor is due to antisymmetrization of the generating function $\Phi(\mathbf{R},\mathbf{r})$. It is convenient to rewrite the set as follows:

$$\sum_{\tilde{n}}\langle n|\hat{H}|\tilde{n}\rangle C_{\tilde{n}} + E(1-\Lambda_n)C_n - EC_n = 0, \quad (14)$$

where the second term $E(1-\Lambda_n)C_n$ is the one which is absent in the standard discrete representation of the Schrödinger equation. This term reproduces the action of the antisymmetrizer to the allowed states,

and the factors $E(1-\Lambda_n)$ can be treated as the matrix elements of this operator—an effective potential—in the diagonal representation of Pauli-allowed states. If in some channel the matrix elements are bound by unity from above, the effective potential is repulsive. Its intensity increases with E, but cannot be more than the energy. Since there are no forbidden states in the set (14), the effective repulsion has no reason to grow infinitely. Likewise, if the eigenvalues are bound by unity from below, the effective potential is attractive, which leads to some interesting spectral effects.

8. CONCLUSIONS

The following general ideas were illustrated by simple examples.

In the Fock–Bargmann representation, or the representation of entire functions, the norm kernel of the generator-coordinate method is a symmetric kernel of an integral equation. Its eigenfunctions are defined in the coordinate–momentum phase space and form a complete set of orthonormalized (with the Bargmann measure) basis states satisfying the Pauli exclusion principle. The eigenvalues have a finite limiting point and thus the integral equation is of a special kind. Our main conclusion is that, in the Fock–Bargmann representation, the kernel of the integral equation is always representable in the form of a sum of degenerate kernels classified with the use of $SU(3)$ symmetry indices. In the absence of an $SU(3)$ degeneracy, the eigenspectrum of the norm kernel directly follows its form. If there is an $SU(3)$ degeneracy, it is found as a solution of the integral equation which is reduced to a set of homogeneous algebraic equations with rank equal to the degree of $SU(3)$ degeneracy. In this way, following the requirements of the permutational symmetry, the basis states are consistently classified with the use of additional quantum numbers.

REFERENCES

1. G. F. Filippov, Yu. A. Lashko, S. V. Korennov, and K. Katō, Few-Body Syst. **33**, 173 (2003).
2. D. M. Brink, The Alpha-Particle Model of Light Nuclei, *Proceedings of the International School of Physics "Enrico Fermi," Course 37, Varenna, Italy* (Academic, New York, 1965).
3. V. A. Fock, Z. Phys. **49**, 339 (1928).
4. V. Bargmann, Commun. Pure Appl. Math. **14**, 187 (1961).
5. L. D. Faddeev and O. F. Yakubovsky, *Lecture on Quantum Mechanics for Student in Mathematics* (Leningrad State Univ., 1980) [in Russian].
6. A. M. Perelomov, *Generalized Coherent States and Their Applications* (Springer, Berlin, 1987).

Physics of Atomic Nuclei, Vol. 67, No. 9, 2004, pp. 1721–1725. From Yadernaya Fizika, Vol. 67, No. 9, 2004, pp. 1749–1753.

Trinucleon Cluster Structure at High-Excitation Energies in $A = 6$ Nuclei*

H. Akimune[1)], T. Yamagata[1)], S. Nakayama[2)], M. Fujiwara[3)], K. Fushimi[2)], K. Hara[3)], K. Y. Hara[1)], K. Ichihara[2)], K. Kawase[3)], K. Matsui[2)], K. Nakanishi[3)], A. Shiokawa[1)], M. Tanaka[4)], H. Utsunomiya[1)], and M. Yosoi[5)]**

Received January 21, 2004

Abstract—Trinucleon molecular structures in ^{6}He and ^{6}Be were investigated by using the ^{6}Li(^{7}Li, ^{7}Be)^{6}He reaction at 455 MeV and ^{6}Li(^{3}He, t)^{6}Be reaction at 450 MeV, respectively. Binary decays into $t + t$ from a broad state at $E_x = 18.0 \pm 1.0$ MeV in ^{6}He and into ^{3}He + ^{3}He from one at $E_x = 18.0 \pm 1.2$ MeV in ^{6}Be, respectively, were observed by measuring trinucleon cluster decays in coincidence with reaction particles. The branching ratios for binary decay were estimated to be about 0.7 for ^{6}He and ^{6}Be. These large branching ratios show that a trinucleon cluster state exists as an isobaric partner around $E_x = 18$ MeV in ^{6}He and ^{6}Be. © *2004 MAIK "Nauka/Interperiodica".*

1. INTRODUCTION

Over many years, an enormous amount of effort has been devoted to understanding excitation energy spectra of light nuclei. Both the molecular-like picture and the independent particle picture are essentially important to understand the structure of light nuclei. For example, the microscopic $\alpha + d$ cluster model successfully describes the low-lying states of ^{6}Li. For high-lying resonance states, one naive question naturally arises: Are there any resonances including ^{3}He or ^{3}H particles acting as a cluster? Such resonant states are known to exist at low excitation energies [1, 2]. Trinucleon cluster states were predicted by Thompson and Tang [3], who claimed that the "molecular" resonance with two trinucleon clusters should exist in the $A = 6$ triad, ^{6}He, ^{6}Li, and ^{6}Be.

In the past, trinucleon resonances were experimentally reported in ^{6}Li and ^{6}Be on the basis of radiative capture reactions [4–6] and of a phase shift analysis on the ^{3}He + ^{3}H and ^{3}He + ^{3}He elastic scattering data [7, 8]. In the case of ^{6}Li, Ventura *et al.* [5] found evidence for the $^{33}P_2$ resonance at $E_x = 18.3$ MeV. On the other hand, Vlastou *et al.* [7] reported that the $^{33}P_2$ and $^{33}P_0$ resonances exist at 21.0 and 21.5 MeV, respectively. Concerning the $^{33}P_2$ resonance in ^{6}Li, there was a serious discrepancy by about 3 MeV in excitation energy. Recently, a similar conclusion was theoretically reported by Ohkura *et al.* [9]. However, the precision of the extracted level parameters in [10] is still a subject of some objection [11].

In the case of ^{6}Be, contradictory results were also reported about the trinucleon cluster resonance. Ventura *et al.* assigned a broad resonance at $E_x = 23$ MeV in ^{6}Be to be the $^{33}F_3$ resonance from the radiative capture reaction of ^{3}He on ^{3}He [6]. However, Vlastou *et al.* did not observe this state in the phase shift analysis of elastic scattering of polarized ^{3}He on ^{3}He, but they observed the $^{33}F_4$, $^{33}F_2$, and $^{33}F_3$ resonances located at $E_x = 23.4$, 26.2, and 26.7 MeV, respectively [8]. Thus, experimental information on the trinucleon clustering in $A = 6$ nuclei appears highly contentious.

Recently, we investigated the $t + t$ molecular state in ^{6}He via the ^{6}Li(^{7}Li, ^{7}Be)^{6}He reaction at 455 MeV by measuring binary triton decay in coincidence with ^{7}Be particles [12]. We observed the $t + t$ cluster state at $E_x = 18$ MeV in ^{6}He. From the basis of the isospin symmetry, the analog of the resonance in ^{6}He is expected to exist around $E_x = 18$ MeV in ^{6}Be. In this work, the trinucleon cluster state in ^{6}He and ^{6}Be were sought via the ^{6}Li(^{7}Li, ^{7}Be)^{6}He reaction at 455 MeV and ^{6}Li(^{3}He, t)^{6}Be reaction at 450 MeV, respectively. Unbound states with $t + t$ and ^{3}He + ^{3}He cluster

*This article was submitted by the authors in English.

[1)]Department of Physics, Konan University, Kobe, Japan.
[2)]Department of Physics, University of Tokushima, Tokushima, Japan.
[3)]Research Center for Nuclear Physics, Osaka University, Osaka, Japan.
[4)]Kobe Tokiwa College, Kobe, Japan.
[5)]Department of Physics, Kyoto University, Kyoto, Japan.
**e-mail: akimune@konan-u.ac.jp

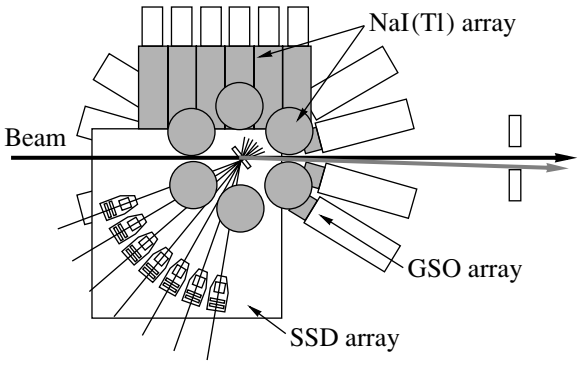

Fig. 1. Schematic diagram of the experimental setup used for detecting charged particles and γ rays.

configurations are expected to binary decay into t and ^{3}He. The trinucleon cluster states in ^{6}He and ^{6}Be are uniquely deduced by measuring trinucleon cluster decay particles in coincidence with reaction particles. The (^{7}Li, ^{7}Be) reaction is a probe which distinguishes the spin-nonflip ($\Delta S = 0$) and spin-flip ($\Delta S = 1$) isovector excitations by measuring ^{7}Be particles in coincidence with the deexcitation γ rays in ^{7}Be [13]. Therefore, the spin nature of trinucleon cluster states in ^{6}He is expected to be investigated. The trinucleon cluster state observed in ^{6}Be will be compared with that in ^{6}He and the structure with a trinucleon cluster configuration in the $A = 6$ isobars will be discussed.

2. EXPERIMENT AND RESULTS

The experiment was performed at the RCNP cyclotron facility of Osaka University with a $^7Li^{3+}$ beam of 65 MeV/nucleon and $^3He^{2+}$ beam of 150 MeV/nucleon. The target used was a self-supporting foil of an enriched ^{6}Li isotope (95.2%) with a thickness of 0.7 mg/cm^2. Spectra for the ^{6}Li(^{7}Li, ^{7}Be) and ^{6}Li(^{3}He, t) reactions were measured with the magnetic spectrometer Grand Raiden [14]. The angular acceptance of the spectrometer was $\pm$20 mrad horizontally and vertically. The ^{7}Be particles and tritons were detected using a focal-plane detector system, which consisted of two multiwire drift chambers backed by a ΔE–E plastic-scintillator telescope. Charged particles from the excited states in ^{6}He and ^{6}Be formed in the ^{6}Li(^{7}Li, ^{7}Be) and ^{6}Li(^{3}He, t) reactions were detected using an array of eight surface-barrier-type Si solid-state detector (SSD) telescopes. The thickness of the ΔE detectors was 500 μm. Each ΔE detector was backed by a 300-μm-thick E detector. Those telescopes were located at intervals of 10° from 90° to 160° ($\phi = 0°$) and at a distance of 25 cm from the target. The time-of-flight technique was utilized for particle identification for the decay particles.

Gamma rays from the first excited state in a ^{7}Be ($E_x = 0.43$ MeV, $J^\pi = 1/2^-$) projectile were detected using an array of 18 NaI(Tl) scintillator blocks ($2 \times 2 \times 6.5$ in.), 6 NaI(Tl) scintillator cylinders ($3 \oslash \times 6.5$ in.), and 10 GSO scintillator blocks ($1 \times 2 \times 2$ in.) surrounding the target. The 0.43-MeV γ ray was used to distinguish $\Delta S = 1$ excitations from $\Delta S = 0$ excitation [13]. The detection efficiency of γ rays was $(10 \pm 4)\%$ for 1.33-MeV γ rays from a ^{60}Co γ-ray source. Figure 1 shows the schematic diagram of the setup used for the charged particle and γ-ray detection.

Figure 2*a* shows the singles spectrum for the ^{6}Li(^{7}Li, ^{7}Be)^{6}He reaction at 65 MeV/nucleon. Three broad resonances were observed at $E_x = 5$, 15, and 25 MeV. These resonances have been observed in the ^{6}Li(n, p) reaction [15] and the ^{6}Li(^{7}Li, ^{7}Be) reaction [13, 16, 17]. The resonances at $E_x \simeq 5$ and 25 MeV were assigned by Nakayama *et al.* to be the soft dipole resonance [13] and the analog of the dipole resonance caused by an excitation of the α cluster in the ^{6}Li nucleus [18], respectively. The coincidence spectrum in the ^{6}Li(^{7}Li, ^{7}Be $+ t$)^{3}H reaction obtained by gating on the binary triton-decay events is shown in Fig. 2*b*. Only one broad peak was observed at $E_x = 18 \pm 1.0$ MeV. The width (full width at half maximum, FWHM) was 9.5 ± 1.0 MeV. The triple coincidence spectrum in the ^{6}Li(^{7}Li, ^{7}Be $+ t + \gamma$)^{3}H reaction obtained by gating on the 0.43-MeV γ ray from ^{7}Be ejectiles ($\Delta S = 1$ excitation) is also shown in Fig. 2*b* by the dashed line. The peak energy for $\Delta S = 1$ excitation is shifted towards higher excitation energies by about 2 MeV. Figure 2*c* shows a two-dimensional scatter plot of ^{7}Be–t coincidence events. Here, energies of tritons were expressed in the energies of the rest system for ^{6}He, taking into account the recoil effect. The coincidence events corresponding to triton decay are clearly separated from other charged particle decay, such as proton, deuteron, and alpha decay. Figure 2*d* shows a two-dimensional scatter plot of ^{7}Be–t coincidence events for $\Delta S = 1$ transitions. The solid curve in Fig. 2*b* shows the result of a peak fitting procedure with the Breit–Wigner one-level formula [19]. The details of this procedure will be discussed in the next section.

Figure 3*a* shows the singles spectrum for the ^{6}Li(^{3}He, t)^{6}Be reaction at 150 MeV/nucleon. One broad resonance was also observed at $E_x = 25$ MeV. The coincidence spectrum in the ^{6}Li(^{3}He, $t +^3$ He)^{3}He reaction obtained by gating on the binary triton-decay events is shown in Fig. 3*b*.

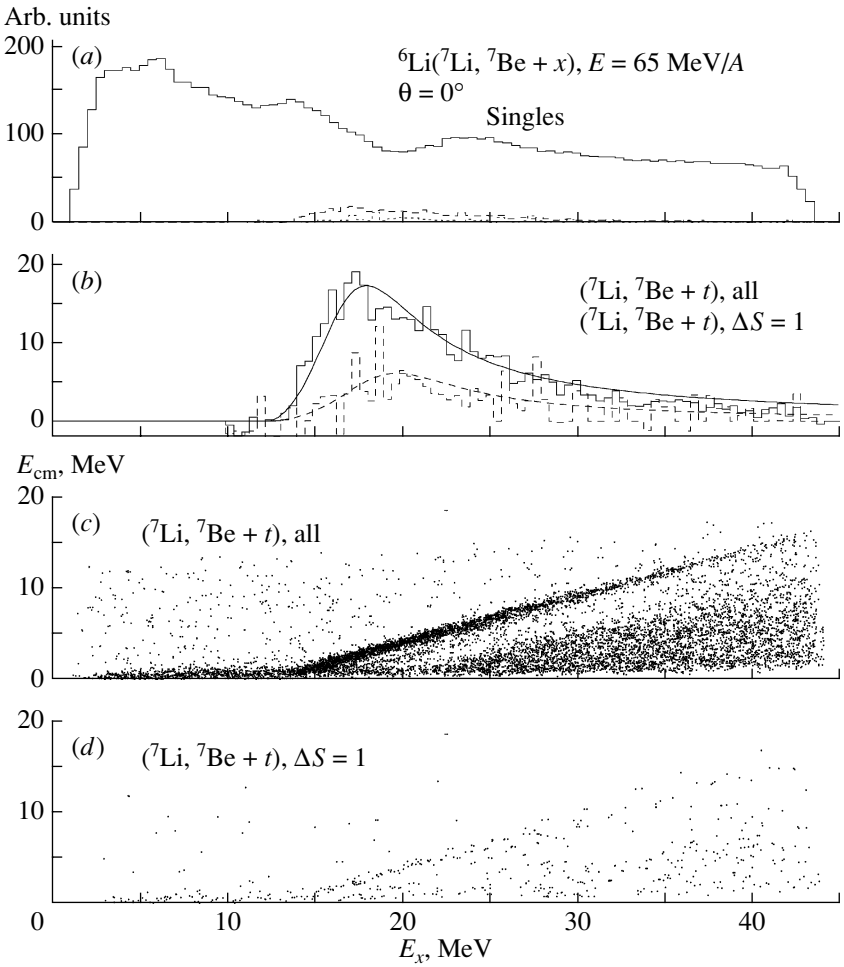

Fig. 2. (a) Singles spectrum for the ^{6}Li(^{7}Li, ^{7}Be) reaction at 65 MeV/A. A gated spectrum for the binary triton decay is also shown in the figure. (b) Coincidence spectrum for the ^{6}Li(^{7}Li, ^{7}Be + t)^{3}H reaction. The solid and dashed histograms are the experimental data. The solid and dashed curves show the peak shapes calculated with the Breit–Wigner one-level formula. (c) Two-dimensional scatter plot for coincidence events. The horizontal and vertical axes are the excitation energy in ^{6}He and the energy of tritons, respectively. (d) Two-dimensional scatter plot for t–γ coincidence events. Coincidence gates for 0.43-MeV γ rays and decay tritons are applied to select the $\Delta S = 1$ states in ^{6}He.

Only a broad peak was observed at $E_x = 18 \pm 1.2$ MeV. The width (full width at half maximum) was 9.2 ± 1.3 MeV. Figure 3c shows a two-dimensional scatter plot of t–^{3}He coincidence events.

3. DISCUSSION

In order to deduce the resonant parameters, the spectral shapes of the 18-MeV resonances shown in Figs. 2b and 3b were fitted by using the Breit–Wigner one-level formula. We assumed the triple differential cross section $d^3\sigma(E_x)/d\Omega_{^7\mathrm{Be}}d\Omega_t dE_x$ as

$$\frac{d^3\sigma(E_x)}{d\Omega_{^7\mathrm{Be}}d\Omega_t dE_x} \propto \frac{\Gamma_3}{(E_x - E_R)^2 + (\Gamma/2)^2},$$

where E_R, Γ, and Γ_3 are the resonance energy, the total width, and the partial width for triton or ^{3}He decay, respectively. The width Γ_3 is expressed as [20]

$$\Gamma_3 = \frac{2\hbar}{R}\left(\frac{2E}{\mu}\right)^{1/2}\theta^2 P_l,$$

where R, E, μ, θ^2, and P_l are the interaction radius of two trinucleon clusters, the decay-particle energy in the c.m. system, a reduced mass, a dimensionless reduced width, and the penetrability with an angular momentum l, respectively. The interaction radius is given by $R = r_0(A_1^{1/3} + A_2^{1/3})$ with $r_0 = 1.4$ fm. The total Γ is expressed as $\Gamma = \Gamma_3 + \Gamma'$, where Γ' is a partial width for neutron, proton, or other particle decay. Since the neutron-decay threshold energy for ^{6}He (0.97 MeV) and the proton-decay threshold energy for ^{6}Be (-1.37 MeV) are much lower than the peak

Experimental excitation energy E_x, width (FWHM), reduced width, and $\Gamma_\downarrow$

Channel	E_x, MeV	FWHM, MeV	θ	$\Gamma_\downarrow$, MeV
$t+t$, total	18.0 ± 1.0	9.5 ± 1.0	1.0 ± 0.4*	3.5*
$t+t$, $\Delta S = 1$	20.5 ± 1.5	11.0 ± 1.7	1.0 ± 0.4*	3.5*
^{3}He + ^{3}He, total	18.0 ± 1.2	9.2 ± 1.3	1.0 ± 0.4*	3.5*

* Fixed in the fits.

position of $E_x = 18$ MeV, the width Γ' was assumed to be constant within the resonance region.

As shown in Figs. 2*b* and 3*b*, the shape of the coincidence spectrum is well reproduced with the Breit–Wigner one-level formula assuming $l = 1$. In the table, parameters for the resonances in this work are summarized. When we use the resonance parameters in the table, the branching ratio R for trinucleon decay

$$R = \int \frac{d^2\sigma}{d\Omega dE}\frac{\Gamma_3}{\Gamma}dE \Big/ \int \frac{d^2\sigma}{d\Omega dE}dE$$

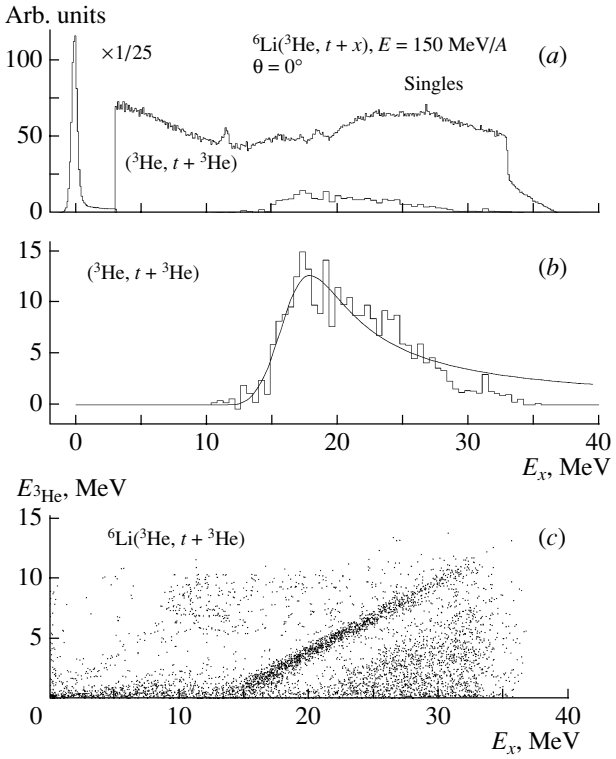

Fig. 3. (*a*) Singles spectrum for the ^{6}Li(^{3}He, t) reaction at 150 MeV/A. (*b*) Coincidence spectrum for the ^{6}Li(^{3}He, $t+^3$ He)^{3}He reaction. (*c*) Two-dimensional scatter plot for coincidence events. The horizontal and vertical axes are the excitation energy in ^{6}He and the energy of ^{3}He, respectively.

amounts to 70% for ^{6}He and ^{6}Be.

The centroid energy of the $t+t$ resonance excited via $\Delta S = 1$ channel is located at 20 MeV. This value is higher by $\sim$2 MeV than the centroid energy of the sum of $\Delta S = 1$ and 0. If we assume that this resonance is the ^{33}P state of two trinucleons, three total angular momenta, $J^\pi = 0^-$, 1^-, and 3^+, are possible. The shift in excitation energy might be attributed to the enhancement of a specific J^π state in $\Delta S = 1$ excitation. However, although the (^{3}He, t) reaction at 150 MeV/A at $\theta = 0°$, $\Delta S = 1$ excitation is dominant, the centroid energy of the ^{3}He + ^{3}He resonance is very close to the sum of $\Delta S = 1$ and 0 excitations in the $t+t$ resonance.

4. SUMMARY

Binary decays into $t+t$ from a broad state at $E_x = 18.0 \pm 0.4$ MeV in ^{6}He and into ^{3}He + ^{3}He from one at $E_x = 18.0 \pm 0.6$ MeV in ^{6}Be, respectively, were observed by measuring trinucleon cluster decays in coincidence with reaction particles. The branching ratios for the binary decay were estimated to be 0.7 for ^{6}He and ^{6}Be. This large branching ratio shows that a trinucleon cluster state exists as an isobaric partner around $E_x = 18$ MeV in ^{6}He and ^{6}Be.

ACKNOWLEDGMENTS

This experiment was performed at RCNP, Osaka University, under programs E172, E184, and E190. We are grateful to the RCNP cyclotron crew for preparing a stable and clean beam.

REFERENCES

1. Y. M. Shin *et al.*, Phys. Lett. B **55B**, 297 (1975).
2. M. F. Werby *et al.*, Phys. Rev. C **8**, 106 (1973).
3. D. R. Thompson and Y. C. Tang, Nucl. Phys. A **106**, 591 (1968).
4. S. L. Blatt *et al.*, Phys. Rev. **176**, 1147 (1968).
5. E. Ventura *et al.*, Phys. Lett. B **46B**, 364 (1973); Nucl. Phys. A **173**, 1 (1971), and references therein.
6. E. Ventura *et al.*, Nucl. Phys. A **219**, 157 (1974).

7. R. Vlastou *et al.*, Nucl. Phys. A **292**, 29 (1977).
8. R. Vlastou *et al.*, Nucl. Phys. A **303**, 368 (1978).
9. H. Ohkura, T. Yamada, and K. Ikeda, Prog. Theor. Phys. **94**, 47 (1995).
10. A. Mondragón and E. Hernández, Phys. Rev. C **41**, 1975 (1990).
11. D. R. Tilley *et al.*, Nucl. Phys. A **708**, 3 (2002).
12. H. Akimune *et al.*, Phys. Rev. C **67**, 051302(R) (2003).
13. S. Nakayama *et al.,* Phys. Rev. Lett. **85**, 262 (2000).
14. M. Fujiwara *et al.*, Nucl. Instrum. Methods Phys. Res. A **422**, 484 (1999).
15. F. P. Brady *et al.*, J. Phys. G **10**, 363 (1984).
16. S. Nakayama *et al.,* Phys. Rev. Lett. **87**, 122502 (2001).
17. J. Jänecke *et al.*, Phys. Rev. C **54**, 1070 (1996).
18. T. Yamagata *et al.*, in *Proceedings of the Tours Symposium on Nuclear Physics V* (in press).
19. J. M. Blatt and V. F. Weisskopf, *Theoretical Nuclear Physics* (Wiley, New York, 1952), p. 391.
20. C. E. Rolfs and W. S. Rodney, *Cauldrons in the Cosmos* (Univ. Chicago Press, Chicago, 1988), p. 178.

Physics of Atomic Nuclei, Vol. 67, No. 9, 2004, pp. 1726–1730. From Yadernaya Fizika, Vol. 67, No. 9, 2004, pp. 1754–1758.

Nontrivial Manifestation of Clustering in Fission of Heavy Nuclei at Low and Middle Excitations*

Yu. V. Pyatkov[1)], V. V. Pashkevich[2)], W. H. Trzaska[3)], G. G. Adamian[2)], N. V. Antonenko[2)], D. V. Kamanin[4)], V. A. Maslov[4)], V. G. Tishchenko[4)], and A. V. Unzhakova[4)]

Received January 21, 2004

Abstract—An analysis of the preferable fission path manifesting itself as a fine structure of the total kinetic energy–mass distribution of the fission fragments compelled us to put forward an absolutely new shape of the fissioning system on the descent from the fission barrier. It is a multicomponent nuclear molecule constituted by two magic clusters and a torus-like neck between. © *2004 MAIK "Nauka/Interperiodica"*.

The main subject of the analysis in the present work will be the fine structure (FS) of the total kinetic energy–mass (TKE-M) and total kinetic energy–charge (TKE-Z) distributions of the fission fragments (FF) formed in the reaction $^{233}\mathrm{U}(n_{\mathrm{th}}, f)$. In our work [1], the procedure of revealing the fine structure of the TKE-M distribution of the FF is described in detail and a resultant map is obtained. The most typical and pronounced structures found for the first time are shown in Fig. 1*a*.

An initial mass–energy distribution of the FF has been obtained on a single-arm time-of-flight (TOF) spectrometer installed at the research reactor of the Moscow Engineering Physics Institute [2]. In total, about 10^7 events of fission have been processed. The procedure of revealing the FS consisted of two stages. At the first stage, the identification of statistically significant points (peaks) with a locally increased yield in the TKE-M matrix, distinct from those produced by proton even–odd staggering, was carried out. At the second stage, the allocated points were combined into the image according to criteria proposed in [1].

We have got strong support for the reliability of the structure under discussion from the data obtained for the reaction $^{238}\mathrm{U} + d$ (65 MeV) (Fig. 1*b*) at the HENDES facility installed in the accelerator laboratory of the University of Jyväskylä (Finland) [3]. It should be stressed that the primary FF masses measured in this case (due to the TOF–TOF method used) originated from the decays of the middle-excited system heavier than the previous one by 6 amu. Nevertheless, very similar structures are observed in both cases. The right-side tails of the structures asymptotically approach the same masses 128 and 132 amu associated with the magic and doubly magic Sn nuclei, respectively.

For concentration of attention on the curve to be analyzed, it is plotted separately in Fig. 2*a*. We have saved in Figs. 2 and 3 the designations proposed earlier in [1]. Points of bifurcation of structures are marked by closed circles. The "tails," which are normally less pronounced than the statistically dominating curves, are detached from these curves by vertical strokes. To facilitate the discussion, we labeled the curves or/and their parts (detached by vertical strokes or closed circles placed onto curves). Each label consists of a maximum of three components. For instance, the label $1a^2$ means part "2" of the curve "*a*" from the family "*1*."

In order to exclude any influence of the Coulomb factor $Z_L Z_H$ (the labels L and H indicates light and heavy fragments, respectively) on the shape of a curve, we shall replace the TKE axis with the axis of $Z_L Z_H/\mathrm{TKE} \sim d$, where d is proportional to the distance between the centers of the fragments at a scission point under the assumption of solely Coulomb interaction between the nascent fragments. It is necessary to specify what is understood as the "scission point" in this case. Following [4], it is supposed that, with some probability, the system can tunnel into the valley of the separated fragments at any stage of a descent along the chosen potential valley, i.e.,

*This article was submitted by the authors in English.

[1)]Moscow Engineering Physics Institute, Moscow, Russia; e-mail: yvp_nov@mail.ru

[2)]Bogolyubov Laboratory of Theoretical Physics, Joint Institute for Nuclear Research, Dubna, Moscow oblast, 141980 Russia.

[3)]Department of Physics of University of Jyväskylä; Helsinki Institute of Physics, Helsinki, Finland.

[4)]Flerov Laboratory of Nuclear Reactions, Joint Institute for Nuclear Research, Dubna, Moscow oblast, 141980 Russia.

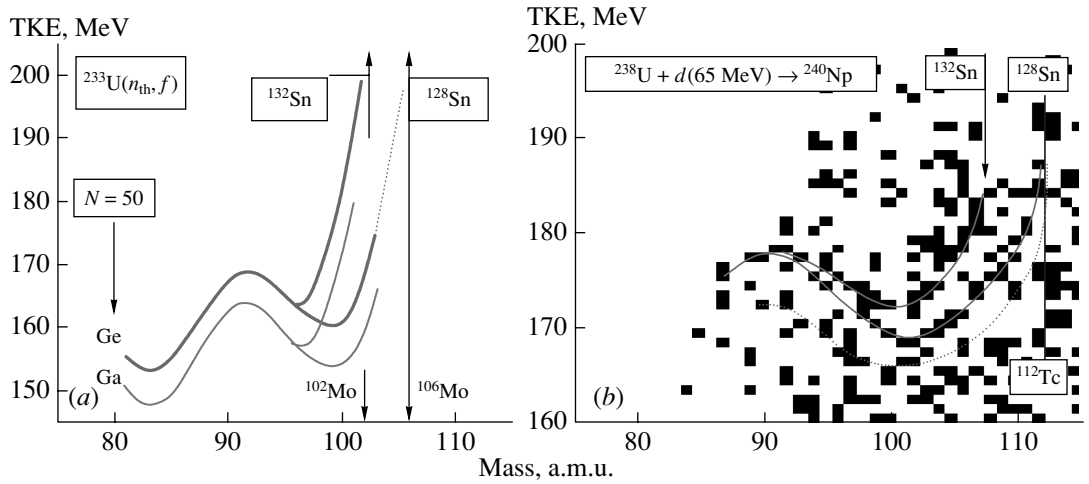

Fig. 1. Most pronounced fine structures revealed in the TKE-M distributions for FF originated from the reactions ^{233}U(n_{th}, f) (*a*) and ^{238}U + d (65 MeV) (*b*).

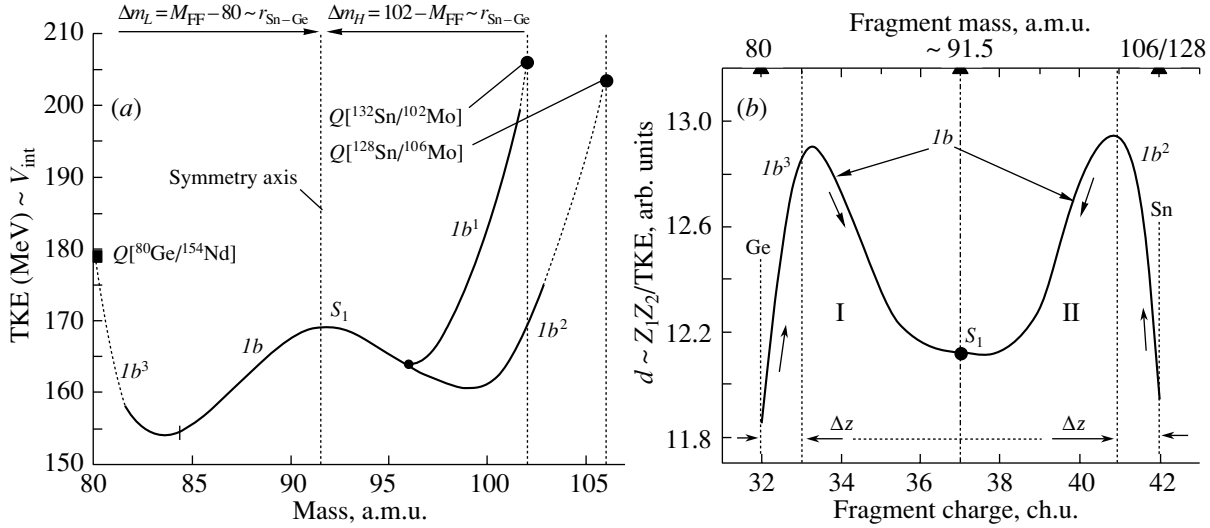

Fig. 2. Images of the fission path in the frame of Sn–Ge fission mode: in the TKE-M space (*a*), the same image in the charge–elongation coordinates (*b*).

any point of descent could turn out to be "a scission point."

Suggested transformation from TKE to $d(Z)$ is convenient to execute with the use of a map of the fine structure on the Z–TKE plane represented in Fig. 3. Initial data were obtained at the Cosi-Fun-Tutte spectrometer [5]. The curve $1b^3$–$1b$–$1b^2$ of the increased yields transformed into new coordinates is shown in Fig. 2*b*. From this figure, one could conclude that the curve $d(Z)$ consists of two approximately identical parts (designated by the Roman numerals I and II) located symmetrically about the axis $Z \sim 37$ ch.u., which corresponds to a value of the mass of ~ 91 amu taking into account the known dependences $\langle A \rangle (Z, \text{TKE})$ (average mass of the isotope distribution as a function of TKE) [6]. At small values of d (compact prescission configurations), a straight line $d = \text{const}$ crosses the dependence $d(Z)$ at two points; i.e., fragments in the vicinity of both $Z \sim 32$ ch.u. (Ge) and $Z \sim 42$ ch.u. (Mo is a fragment complementary to the nucleus of Sn) are born.

Considering the shape of the curve $d(Z)$, one can conclude that, from $Z = 32$ ch.u. and to the charge value corresponding to the maximum at part I, an increase in the charge of the light fragment by the value $\Delta z = Z - 32$ is approximately proportional to the gain of the elongation d. In other words, the difference Δz, as well as the corresponding difference of the mass $\Delta m = M - 80$, can serve as a measure of the distance between the centers of the nascent

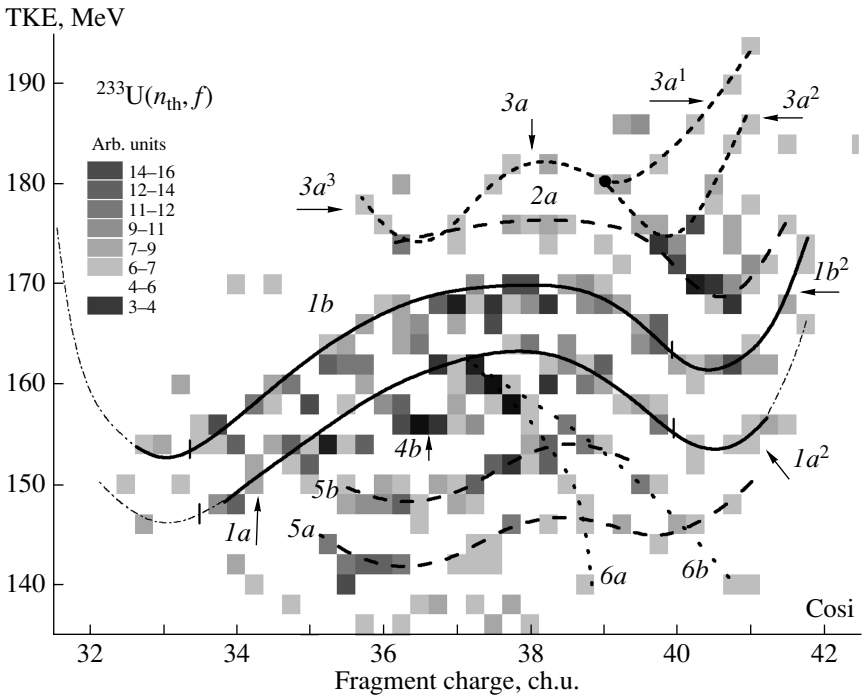

Fig. 3. Fine structure in the TKE–Z distribution of the fragments from the reaction ^{233}U(n_{th}, f).

fragments. For the right half (II) of the curve $d(Z)$, similar differences are expressed as

$$\Delta z' = 42 - Z, \quad \Delta m' = 106 - M,$$

and, by virtue of the symmetry of the curve $d(Z)$,

$$\Delta z \sim \Delta z', \quad \Delta m \sim \Delta m'.$$

The connection revealed with the help of Fig. 2*b* allows one to put forward the following interpretation of the line *1b*–*1b*^{2} of the increased yields (Figs. 1, 3).

Within the framework of the dicluster concept of fission modes developed in [7], the shape evolution of the fissioning system on the descent along a certain valley of the potential energy surface (PES) is reduced to the transformation of the neck joining the mode-forming clusters, keeping unchanged, in the first approximation, their composition and shape. We mean in this case the nuclei of Ge and Sn. As most of the charge of an initial fissioning nucleus is concentrated in them (the ratio of charges inside clusters and outside them is as large as 82 : 10), one could expect that the interaction potential of the nascent fragments V_{int} is determined mostly by the interaction of these clusters. The interaction energy V_{int} of the prefragments at the moment of scission transforms after scission into the observable value of TKE (to within the prescission component of TKE), and the value Δz as shown above is proportional to the distance r between charging centers of the nascent fragments, i.e.,

$$\text{TKE} \sim V_{int}, \quad \Delta z \sim r, \qquad (1)$$

$$\Delta m \sim r.$$

Taking relations (1) into account, one could expect a geometrical similarity between the discussed line of the FS and the graph of the nuclear–nuclear potential $V_{Ge-Sn}(r)$ as a function of the distance between the mode-forming clusters of Ge and Sn, which is indeed observed. The characteristic form of a nucleus–nuclear potential with a potential "pocket" and a hump (Fig. 4) is confidently reproduced by the curve *1b*–*1b*^{2} in Fig. 2*a*. Lacking the opportunity to present a more detailed analysis, we should only remark here that the salient W-like shape of each FS curve under discussion represents a sum of two slightly different copies of quite the same Ge–Sn interaction potential.

The curves in Fig. 4 calculated by the double-folding method [8] reproduce surprisingly well both the distance of ~ 5 MeV between the adjacent curves *1a*, *1b* (Fig. 3) and the positions of their maxima on the energy axis.

The nonmonotonic behavior of d as a function of Δz in Fig. 2*b* becomes clear now. In the vicinity of a bottom of the potential "pocket" caused by the essential contribution of a nuclear component of the interaction with an increase in the distance r between interacting nuclei, the potential V_{int} grows, while, due to the Coulomb interaction only (namely, in this approximation, d is calculated), the energy of interaction should fall monotonically, i.e., d should grow.

Thus, the symmetry of the curve $d(Z)$ can mean that, since the minimal values of d are at the same

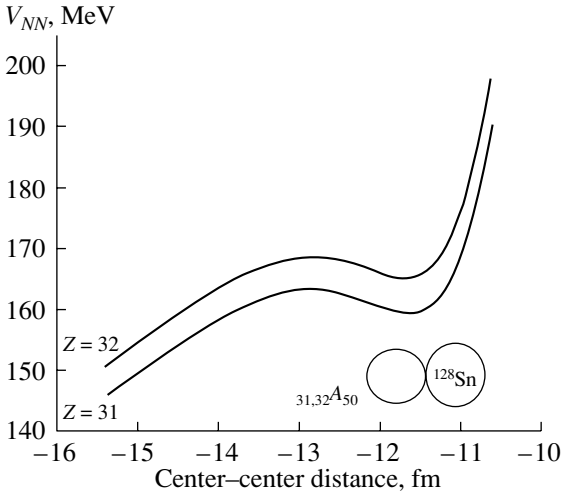

Fig. 4. Calculated energy of interaction between magic nucleus of ^{128}Sn and also magic nuclei of Ge and Ga (neutron shell $N = 50$).

elongation (within the framework of the same prescission shape), light fragments with two different charges Z_1 and Z_2 are born:

$$Z_1 \approx Z_{\mathrm{Ge}} + \Delta z, \qquad (2)$$
$$Z_2 \approx Z_{\mathrm{Mo}} - \Delta z = Z_{\mathrm{U}} - (Z_{\mathrm{Sn}} + \Delta z),$$

where Δz, as follows from Fig. 2*b*, is approximately identical in both variants of formation of the light fragment.

As the neutron-to-proton ratio N/Z in the fragments differs insignificantly from its value in the fissioning nucleus ("unchanged charge density hypothesis"), the approximate equalities (2) in a rough approach are also true for the masses of the fragments:

$$M_1 \approx M_{\mathrm{Ge}} + \Delta m, \qquad (3)$$
$$M_2 \approx M_{\mathrm{Mo}} - \Delta m = M_{\mathrm{U}} - (M_{\mathrm{Sn}} + \Delta m).$$

By virtue of the importance of the approximate equalities (3), we shall directly formulate the established law of formation of the fragments in the fission mode under consideration.

At each stage of elongation of a fissioning system, light fragments of two types are born which are approximately equidistant on the charge (mass) axis from the light and heavy mode-forming clusters, respectively. It means alternatively either the light fragment consisting of the cluster of Ge and a piece of the neck or the complementary one to the fragment consisting of the cluster of Sn and the same piece of the neck. At the minimal elongation (maximal TKE) corresponding to "cold" fission if it is energetically allowed, the mode-forming clusters themselves are born (not necessarily with identical probabilities).

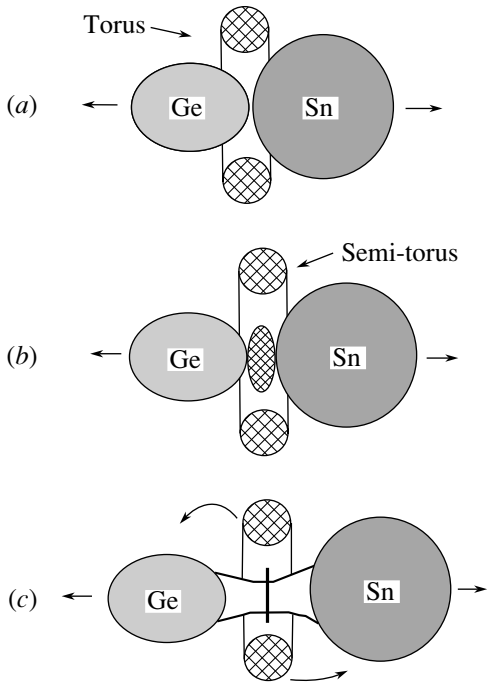

Fig. 5. Presumable shapes of the fissioning system in the framework of Ge–Sn fission mode for the most compact configuration (*a*), some greater elongation (*b*), prescission phase (*c*).

A movement synchronous on Z of the two points (representing the charges of the fragments) along the two equivalent parts I, II of the curve $d(Z)$ (Fig. 2*b*) from the same starting point on d towards the point of symmetry S_1 (directions of movement of the points are shown by the arrows) can serve as the visual pattern of the revealed law of formation of the fragments.

Let us try to imagine now the probable shape of the fissioning system in a fission valley consistent with the revealed laws of formation of the fragments. The phase of transformation of a continuous fissioning system into a nuclear molecule is presented in Fig. 5. The constituents of a molecule are two mode-forming clusters (nuclei of Ge and Sn) and a torus consisting of nucleons which have not joined any cluster. The most compact shape is presented in Fig. 5*a*. While the distance between the clusters increases, the central fragment of a nuclear molecule starts to be formed in an undense area that arises (Fig. 5*b*).

As is well established for the light systems, a pronounced cluster (molecule-like) structure arises in the excited states of nuclei. The common feature for the states characterized by the regarded cluster structure is that the excitation energy is close to the threshold of dissociation into separate clusters ("threshold rule" [9]).

In the considered case, an "attempt" by a weakly bound cluster, for example, Ge, to tear off a molecule

results in its reorganization. It is quite expectable that the central fragment of a molecule "pasted" by the nuclear interaction to the clusters of Ge and Sn will be stretched until the waist in the neck is organized and a rupture appears to occur (Fig. 5*c*). The nucleons of the torus will join the complementary heavy fragment. Accordingly, if the cluster of Sn "initiates" the process of scission, the nucleons of the torus will join a fragment including the cluster of Ge and its part of the central fragment (neck). Such choice is illustrated by the round arrows in Fig. 5*c*.

Moving clusters of Ge and Sn apart is accompanied by filling of the space between their edges by the nucleons from the torus down to transition of all of these nucleons into the neck. A proposed scenario automatically provides a concretion of the left and the right branches of the curve $d(Z)$ (Fig. 2*b*) at the point S_1 of the value Z_S of the charge of the light fragment equal to

$$Z_S \sim [Z_{\mathrm{U}} - (Z_{\mathrm{Ge}} + Z_{\mathrm{Sn}})]/2.$$

The shape of the "neck" (in habitual terms) of the fissioning system (Fig. 5) seems to be extremely extravagant; however, the close prototype suggested for a rather long time, namely, the nuclei in the form of a bubble [10]. The investigation of such noncompact nuclei taking into account the shell corrections has been continued in the works [11, 12]. The "nuclear bubbles" (or "semibubble" if the nucleon density in the center of such a nuclear system is distinct from zero [13]) are analyzed as one of the possible ways of reducing the Coulomb energy of the protons of a nucleus.

By analogy to the term "semibubble," the neck shape of the system presented in Fig. 5*b* can be called a "semitorus." The physical reason for its probable occurrence as well as in the case of a nuclear bubble is the way of reducing the Coulomb energy of the system.

The main conclusions that could be inferred from the analysis above are as follows:

(i) The fine structures revealed for the first time in the TKE-*M* distributions of the FF originated from the reactions $^{233}\mathrm{U}(n_{\mathrm{th}}, f)$ and $^{238}\mathrm{U} + d$ (65 MeV) presumably map the history of evolution of the fissioning system in the frame of the distinct fission mode onto the experimentally observed elongation–mass-asymmetry space. In other words, we observe a trajectory in this space being an image of the fission mode based on the magic nuclei of Ge and Sn as the mode-forming clusters.

(ii) The evolution scenario linked with the typical trajectory revealed needs a very special shape of the decaying system for being realized. It is a multicomponent nuclear molecule formed by two clusters (nuclei of Ge and Sn in the mode under discussion) and a torus (semitorus) between them consisting of the residual nucleons.

ACKNOWLEDGMENTS

We are grateful to Prof. F. Gönnenwein for his kind permission to use the data obtained at the Cosi-Fun-Tutte spectrometer and for stimulating discussions.

This work is supported in part by the CRDF (grant no. MO-011-0).

REFERENCES

1. Yu. V. Pyatkov *et al.*, Nucl. Instrum. Methods Phys. Res. A **488**, 381 (2002).
2. A. A. Alexandrov *et al.*, Nucl. Instrum. Methods Phys. Res. A **303**, 323 (1991).
3. W. H. Trzaska *et al.*, AIP Conf. Proc. **392**, 1059 (1997).
4. J. F. Berger *et al.*, Nucl. Phys. A **428**, 23c (1984).
5. R. Shekhmamet'ev *et al.*, in *Proceedings of the International Conference on Nuclear Data for Science and Technology, Triest, Italy, 1977*, p. 655.
6. V. Quade *et al.*, Nucl. Phys. A **487**, 1 (1988).
7. Yu. V. Pyatkov *et al.*, Nucl. Phys. A **624**, 140 (1997).
8. G. G. Adamian *et al.*, Int. J. Mod. Phys. E **5**, 191 (1996).
9. K. Ikeda, in *Proceedings of the V International Conference on Clustering Aspects in Nuclear and Subnuclear Systems, Kyoto, Japan*, 1988, p. 277.
10. H. A. Wilson, Phys. Rev. **69**, 538 (1946).
11. K. Dietrich *et al.*, Phys. Rev. Lett. **80**, 37 (1998).
12. J. Decharge *et al.*, Phys. Lett. B **451**, 275 (1999).
13. K. Dietrich, in *Proceedings of the International Workshop on Fusion Dynamics at the Extremes, Dubna, Russia, 2000* (World Sci., Singapore, 2001), p. 155.

Physics of Atomic Nuclei, Vol. 67, No. 9, 2004, pp. 1731–1736. From Yadernaya Fizika, Vol. 67, No. 9, 2004, pp. 1759–1763.

Relativistic and Nonrelativistic Calculations of the Isoscalar Monopole and Dipole States*

G. Colò[1] and N. Van Giai[2]

Received January 21, 2004

Abstract—The study of the isoscalar giant monopole resonance (ISGMR) should allow extracting a value for the nuclear incompressibility coefficient K_∞. In this contribution, we review the most recent attempts along this line. While the nonrelativistic (Skyrme, Gogny) models predict K_∞ to be around 220–235 MeV, the values obtained from the relativistic calculations are significantly larger (250–270 MeV). We argue that the most plausible reason for this discrepancy lies in the different behavior of the symmetry energy in the two classes of models. We also discuss the role of the isoscalar giant dipole resonance (ISGDR). We conclude that a number of experimental ambiguities still prevent us from deducing K_∞ from the ISGDR with a comparable accuracy as from the ISGMR. © *2004 MAIK "Nauka/Interperiodica".*

1. INTRODUCTION

The most important reason to study the isoscalar giant monopole resonance (ISGMR) stems from the fact that its energy location can provide information about the nuclear incompressibility coefficient K_∞.

The ISGMR is the isotropic compression mode of finite nuclei (it is sometimes called the "breathing mode"). The first pieces of evidence date back to the end of the 1970s (see, e.g., [1] and references therein). The ISGMR corresponds to a well-defined peak, at energy around $80A^{-1/3}$ MeV, in medium-heavy nuclei. In light nuclei the monopole strength is quite fragmented. In recent years, some very accurate data have been collected. For instance, the recent (α, α') experiments performed at Texas A&M University [2] have provided us with moments of the monopole strength function determined up to a $\pm 2\%$ accuracy.

The isoscalar giant dipole resonance (ISGDR) is a nonisotropic collective mode which should, in principle, provide an alternative way to deduce K_∞. As we will discuss below, however, the experimental results are much less clear.

The nuclear incompressibility gives a measure of the curvature of the nuclear matter energy per particle E/A as function of the density ϱ close to the empirical saturation point ϱ_0. It is defined as

$$K_\infty = 9\varrho_0^2 \frac{d^2}{d\varrho^2} \left.\frac{E}{A}\right|_{\varrho=\varrho_0}. \quad (1)$$

The properties of nuclear matter cannot be an object of direct experimental study in the laboratory. Therefore, the only way to obtain information about K_∞ is to attempt extracting it from the compressional modes of finite nuclei, like the ISGMR.

To establish the link between the energy of the ISGMR and the nuclear incompressibility, we usually rely on some basic results derived by Blaizot [3]. By calculating explicitly the second derivative of E/A in a finite system, he has shown that a plausible way to define the finite nucleus incompressibility is

$$E_{\mathrm{ISGMR}} = \sqrt{\frac{\hbar^2 K_A}{m\langle r^2\rangle}}, \quad (2)$$

where m is the nucleon mass and $\langle r^2\rangle$ is the ground-state mean-square radius.

Actually, the second derivative of E/A contains terms which can be labeled in a similar way as those of the mass formula, so that K_A can be written as

$$K_A = K_\infty + K_{\mathrm{surf}}A^{-1/3} + K_\tau\alpha^2 + K_{\mathrm{Coul}}\frac{Z^2}{A^{4/3}}, \quad (3)$$

where $\alpha = (N-Z)/A$. Attempts were made to deduce K_∞ from the experimental values of E_{ISGMR}, that is, of K_A, by making a simultaneous fit of all the unknowns on the right-hand side of (3). Different authors [4] have shown that those fits are not reliable, because of the scarcity of experimental points and

*This article was submitted by the authors in English.

[1]Dipartimento di Fisica, Università degli Studi, and INFN Sezione di Milano, Milano, Italy; e-mail: gianluca.colo@mi.infn.it

[2]Institut de Physique Nucléaire, IN2P3-CNRS, Orsay, France.

of the correlations existing among the unknown parameters. These "macroscopic approaches" to extract K_∞ have now been abandoned.

A physically more sound procedure, the so-called "microscopic approach," is based on the fact that microscopic nuclear energy functionals can provide the link between nuclear matter and the ISGMR. The nonrelativistic functionals are essentially those based on the Skyrme or Gogny effective forces. Given the effective force $V_{\rm eff}$, the energy functional $E[\varrho]$ is obtained from the expectation value of $H_{\rm eff} = T + V_{\rm eff}$ on an independent-particle wave function (i.e., a Slater determinant) whose associated density is ϱ. In the relativistic case, the starting point is an effective Lagrangian which includes the nucleons, the effective σ, ω, and ρ mesons, and the meson–nucleon coupling (as well as meson self-interactions).

In both cases, once $E[\varrho]$ is written, it is possible to restrict oneself to the special case of uniform matter and calculate analytically the value of K_∞, or to perform calculations for the ISGMR (or ISGDR) in finite nuclei. In this latter case, one calculates first the ground state of the system by solving the equation $\delta E/\delta\varrho = 0$. Then, linear response theory is applied: the system is perturbed by an external, e.g., monopole or dipole, field, and the energies of the induced small oscillations around the ground state are determined. The residual force which governs these oscillations is given by $\delta^2 E/\delta^2\varrho$. The theory is known as the self-consistent random phase approximation (RPA) and is well described in textbooks [5].

A nucleus which is often chosen for studying the monopole energy is ^{208}Pb. Experimentally, the monopole strength is concentrated in a single peak. In fact, different values of the centroid energies like $E_0 \equiv m_1/m_0$ or $E_{-1} \equiv \sqrt{m_1/m_{-1}}$[3] essentially do not differ, being, respectively, 14.17 ± 0.28 and 14.18 ± 0.11 MeV [2]. Theoretically, uncertainties related to the proper description of pairing or of effects beyond the mean field are expected to play a minor role in this nucleus.

Then, the determination of K_∞ proceeds in the following way:

(i) The calculation of $E_{\rm ISGMR}$ is performed using different parametrizations of $E[\varrho]$ (within a given class, like Skyrme or Gogny, or RMF (relativistic mean field)) which are characterized by different values of K_∞. The results for $E_{\rm ISGMR}$ are plotted as a function of K_∞.

(ii) An interpolation of the points is made. Equation (3) suggests that a relation of the type

$$E_{\rm ISGMR} = a\sqrt{K_\infty} + b \qquad (4)$$

may be expected if the other coefficients can be considered to be constant for the various functionals. This relation was first found empirically in [6]. We come back to this point in the following.

(iii) After interpolation, the experimental value of $E_{\rm ISGMR}$ is inserted in Eq. (4) and the best value of K_∞ is deduced.

In Section 2, we analyze the results of this procedure. Most of the discussion is based on [7], but we elaborate, in particular, on the differences between the Skyrme and Gogny calculations, on one hand, and the RMF calculations, on the other hand. In Section 3, we discuss the case of the ISGDR. Finally, in Section 4, we draw our conclusions.

2. DIFFERENCES BETWEEN NONRELATIVISTIC AND RELATIVISTIC DETERMINATIONS OF K_∞

The different attempts to obtain K_∞ using the "microscopic approach" that we have described are reviewed in [7]. The main outcomes of this work are as follows:

(i) The present accuracy which can be achieved by the extraction of K_∞ from the ISGMR in ^{208}Pb is of the order of ± 12 MeV.

(ii) The results from Skyrme and Gogny calculations point to values of K_∞ around 220–235 MeV. The previous value extracted from Skyrme in [8], namely, ≈ 210–220 MeV, was affected by the lack of full self-consistency in the RPA calculations. The Coulomb and spin–orbit residual interaction had been dropped, and this was shown to have an effect of about 0.5 MeV on the quantity E_{-1}. Once full self-consistency is accounted for, the discrepancy between Skyrme and Gogny predictions comes down to the level of experimental uncertainties.

(iii) The results from RMF calculations point to larger values of K_∞, of the order of 250–270 MeV [9], and the discrepancy is likely to be attributed to the different behavior of the symmetry energy.

In this paper, we discuss in some detail the last point.

The difference between Skyrme and RMF calculations for ^{208}Pb is shown in Fig. 1. In this figure, values of E_{-1} are displayed. In the case of the Skyrme model, this quantity can be accurately determined if m_1 is obtained from the usual double commutator expectation value and m_{-1} is obtained from a constrained Hartree–Fock calculation. In the case of RMF, m_1 comes from direct integration of the RPA strength function and m_{-1} comes from a constrained Hartree calculation.

[3] The moments m_k of the strength function $S(E)$ have the usual definition $m_k \equiv \int dE E^k S(E)$.

Piekarewicz was the first to suggest that the difference can originate from the different *density dependence* of the symmetry energy $S(\varrho)$ in the Skyrme and RMF models [10]. To illustrate the possible influence of this density dependence on the extraction of K_∞, in [10] some parametrizations of effective Lagrangians whose symmetry energy has different density dependences have been built. This is easy to achieve since the ρ-meson coupling constant is an adjustable parameter. By adjusting this parameter, one can at the same time soften the function $S(\varrho)$ and lower its value at the saturation point, $J = S(\varrho_0)$. It was thus found that the extracted values of K_∞ indeed differ and can even become close to Skyrme force values.

However, in [10], no systematic treatment of finite nuclei was attempted. In [11], it has been pointed out that RMF parametrizations with J lower than 36 MeV cannot describe $N \neq Z$ nuclei satisfactorily.

The results of [10] cannot be interpreted as proof of the fact that the monopole energy, and therefore the extracted value of K_∞, depends on the value of the symmetry energy at saturation J. In fact, different calculations have shown that this dependence is very weak or almost absent: $\Delta E_{\mathrm{ISGMR}}/\Delta J$ is approximately -0.06 in the RMF calculations of [11] and -0.02 in the Skyrme calculations of [12].

To understand the difference between the K_∞ values deduced from Skyrme and RMF, we propose to use Eq. (3) as a guideline. The quantity K_A is taken from experiment. Given a functional $E[\varrho]$, not only the quantity K_∞—as already mentioned—is known, but also K_τ and K_{Coul} (cf. Section 6.2 of [3]). K_{surf} cannot be calculated analytically, but extended Thomas–Fermi (ETF) calculations have shown that, both in relativistic and in nonrelativistic models, the quantity K_{surf} is essentially given by cK_∞ with $c \approx -1$ [3, 13].

Therefore, we can write, for the nonrelativistic and relativistic models, respectively,

$$K_A \sim K_\infty^{(\mathrm{nonrel})}(1 + cA^{-1/3}) + K_\tau^{(\mathrm{nonrel})}\alpha^2 + K_{\mathrm{Coul}}^{(\mathrm{nonrel})}\frac{Z^2}{A^{4/3}}, \qquad (5)$$

$$K_A \sim K_\infty^{(\mathrm{rel})}(1 + cA^{-1/3}) + K_\tau^{(\mathrm{rel})}\alpha^2 + K_{\mathrm{Coul}}^{(\mathrm{rel})}\frac{Z^2}{A^{4/3}}.$$

The assumption of the linear dependence (4) of K_A on K_∞ is a necessary condition in order to be able to extract K_∞ from the procedure described in Section 1. First, it seems likely that the third term on the right-hand side of Eq. (5) (the Coulomb contribution) does not change much from a nonrelativistic to a relativistic description. On the other hand, in the expression of K_τ {see Eq. (6.3) of [3]}, the first and second derivatives of the symmetry energy at saturation appear. K_τ is negative, and a stiffer symmetry energy leads to a smaller value of K_τ. The important conclusion is that *a smaller value of K_τ would lead to extracting a larger value of K_∞ from the experimental K_A.*

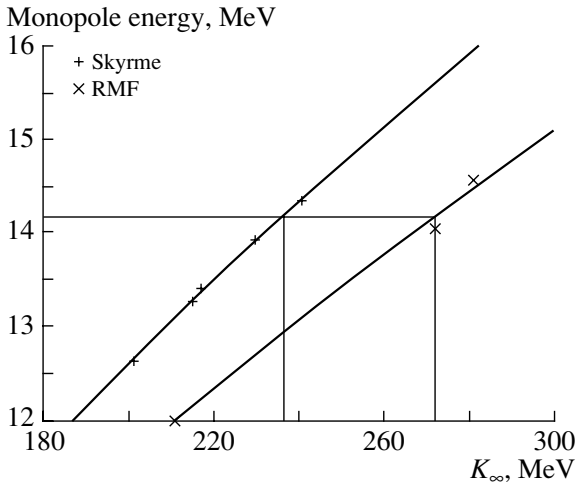

Fig. 1. Monopole energies E_{-1} in ^{208}Pb, calculated using Skyrme and RMF models and plotted as a function of K_∞. The relativistic results are taken from [9]. The lines are numerical interpolations of the type (4). The values of K_∞ deduced from the experimental E_{-1} are also displayed.

It is notable that, in a recent paper [14], a Skyrme interaction which is capable of reproducing the experimental energy of the ISGMR in ^{208}Pb, having $K_\infty = 255$ MeV, was built. Indeed, its associated value of K_τ (-499 MeV) is smaller than those of the Skyrme forces employed in [7], which lie between -305 and -349 MeV.

Unfortunately, a possible way to disentangle the role of K_∞ and K_τ is not clear at present.

More systematic tests should be undertaken to check the idea that both quantities play an important role and that the assumption (4) is not always valid.

3. THE ISGDR

While the ISGMR is, at least in medium and heavy nuclei, well concentrated in a single peak, the situation is less simple for the ISGDR. Theoretically, different calculations have clearly indicated that there is a systematic appearance, in all nuclei studied, of two separated energy regions in which the ISGDR strength is nonnegligible [15, 16]. A "high-energy" region (around $110A^{-1/3}$ MeV) and a "low-energy" region are evident in Fig. 2. A similar pattern emerges from RMF calculations. One of the main indications about the different character of the two parts of the strength comes from the fact that the centroids

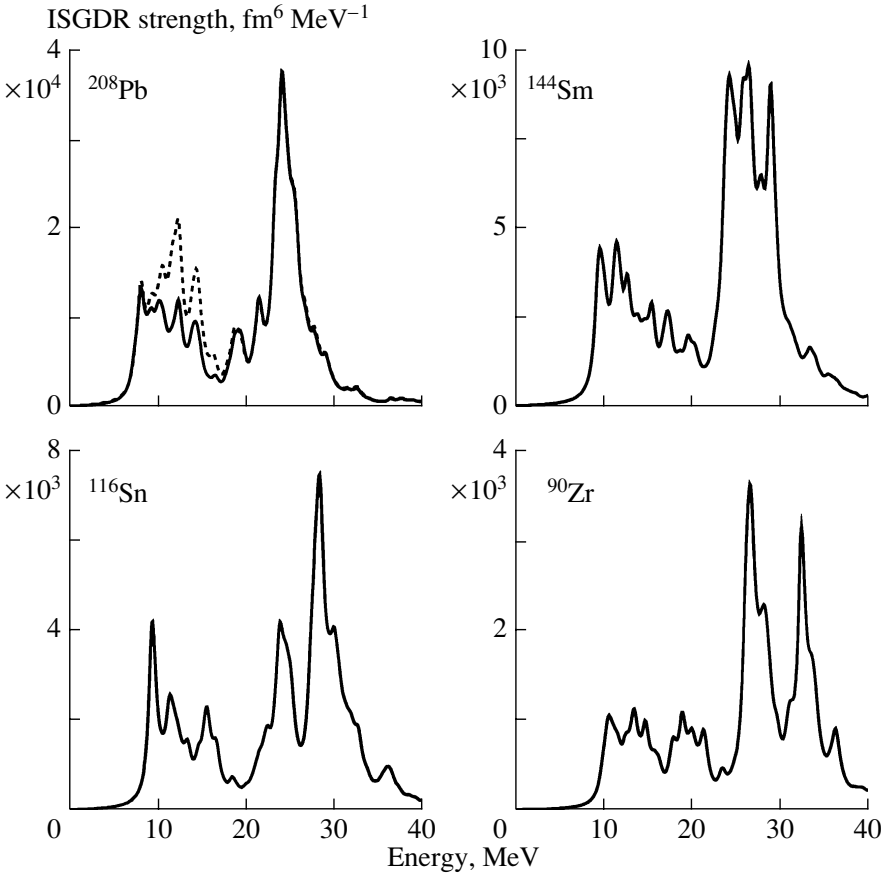

Fig. 2. ISGDR strength functions in different nuclei, calculated in RPA using the Skyrme interaction *SGII* and corrected for center-of-mass effects. In the case of ^{208}Pb the dashed line corresponds to a calculation, where the spurious center-of-mass state is not subtracted. The discrete RPA states have been smeared out by means of a Lorentzian of 1-MeV width. (Taken from [15].)

of the high-energy regions, calculated with different Skyrme forces in a given nucleus, scale with the corresponding K_∞ (which attests to their compressional nature), whereas the centroids of the low-energy regions do not. This is shown in Fig. 3. Although some specific properties of the low-energy region (amount of collectivity, details of the wave functions) depend on the model assumed for the calculations, there is a general consensus that this low-energy part should be excluded from any consideration concerning the extraction of K_∞.

On the experimental side, different (α, α') measurements have been performed over the years, but the problem of disentangling the ISGDR strength from the other multipoles (and from the IVGDR) is far from being trivial. The current status of the experimental activity on the ISGDR is reviewed in [17]. There are recent inclusive measurements from Texas A&M [18] and RCNP-Osaka [19], together with decay measurements $(\alpha, \alpha' p)$ and $(\alpha, \alpha' n)$ performed at KVI [20]. Some problems concern the high-energy tail, which is not easy to determine, especially in the singles measurement, where the continuum background is large. Moreover, there is a clear conceptual problem in the experimental analysis. While the directly measured quantity is the double-differential cross section, $d^2\sigma/d\Omega dE$, the multipole decomposition of this cross section is done by relying on distorted wave Born approximation (DWBA) calculations, where the radial form factors for the various multipole excitations are the same at all energies. This is somehow in contrast with the outcome of the theory, as we have discussed above.

The result of these ambiguities is that the experiments quoted above give results which are not fully compatible with each other for the energy of the ISGDR in ^{208}Pb: 21.7 [18] and 23 ± 0.3 MeV [19] are the results of two different (α, α') measurements, whereas 22.1 ± 0.3 and 20.9 ± 0.1 MeV are the results of the decay measurements $(\alpha, \alpha' p)$ and $(\alpha\, \alpha' n)$, respectively [20]. The natural question is what value

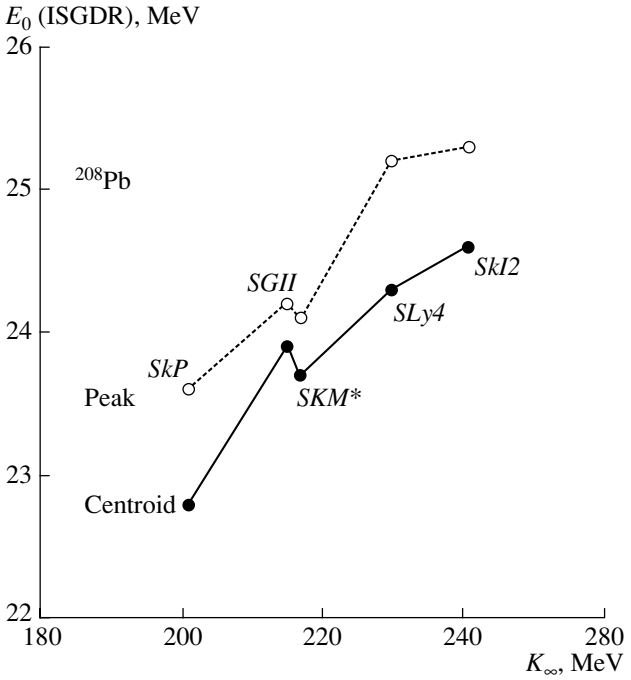

Fig. 3. ISGDR centroid energies E_0 (black circles) and peak energies (open circles) of the high-energy region in ^{208}Pb, determined by using different Skyrme interactions and plotted as a function of K_∞. The full and dashed lines are drawn as a guide to the eye.

for E_{ISGDR} should be used to extract the proper value of K_∞ from a line like that of Fig. 3 (or like that of the RMF calculations). The weighted average of the values coming from the different experiments is likely to hide possible systematic differences.

We can conclude that we still need to wait for improvements in the ISGDR studies in order to reach the same confidence that we have in K_∞ extracted from the ISGMR.

4. CONCLUSIONS

We have reviewed the present theoretical understanding of the compressional modes (ISGMR and ISGDR) in finite nuclei and of the nuclear matter incompressibility K_∞. The ISGMR experimental data are accurate enough to allow an error of only ± 12 MeV on K_∞. Nonrelativistic (Skyrme and Gogny) functionals point to a value around 220–235 MeV. The RMF functionals give a larger K_∞, namely, 250–270 MeV.

In this paper, we illustrate how the most plausible reason for this discrepancy lies in the different behavior of the symmetry energy as a function of density. The previously assumed linear relation between the finite nucleus incompressibility K_A and K_∞, should be replaced by a more general one. Using this more general relation, it can be shown that models characterized by larger values of the first and second derivatives of the symmetry energy (or by a "stiffer" curve) lead naturally to larger K_∞. New systematic calculations should test this idea.

As far as the ISGDR is concerned, more effort is needed in order to reach the same reliability of the ISGMR data. In particular, the use of microscopic, energy-dependent form factors in the experimental analysis and a better determination of the high-energy dipole strength would be highly instrumental in eliminating the still existing ambiguities.

ACKNOWLEDGMENTS

The ISGDR calculations were done in collaboration with P.-F. Bortignon and M.R. Quaglia. We are also pleased to acknowledge stimulating discussions with J.P. Blaizot, M. Centelles, H. Clark, U. Garg, I. Hamamoto, Y.-W. Lui, J. Piekarewicz, P. Ring, H. Sagawa, H. Sakaguchi, S. Shlomo, M. Uchida, D. Vretenar, and D. Youngblood.

REFERENCES

1. M. N. Harakeh and A. van der Woude, *Giant Resonances* (Clarendon Press, Oxford, 2001).
2. D. Youngblood, H. L. Clark, and Y. W. Lui, Phys. Rev. Lett. **82**, 691 (1999).
3. J. P. Blaizot, Phys. Rep. **64**, 171 (1980).
4. M. Pearson, Phys. Lett. B **271**, 12 (1991); S. Shlomo and D. Youngblood, Phys. Rev. C **47**, 529 (1993).
5. D. J. Rowe, *Nuclear Collective Motion. Models and Theories* (Methuen, London, 1970); P. Ring and P. Schuck, *The Nuclear Many-Body Problem* (Springer, New York, 1980).
6. J. P. Blaizot, J. F. Berger, J. Dechargé, and M. Girod, Nucl. Phys. A **591**, 435 (1995).
7. G. Colò and N. Van Giai, Nucl. Phys. A **731**, 15 (2004).
8. G. Colò, N. Van Giai, P.-F. Bortignon, and M. R. Quaglia, in *Proceedings of the Conference on Structure of the Nucleus at the Down of the Century, Bologna, Italy*, 2000, Ed. by G. Bonsignori *et al.* (World Sci., Singapore, 2001), p. 418; Yad. Fiz. **64**, 1119 (2001) [Phys. At. Nucl. **64**, 1044 (2001)]; N. Van Giai, P.-F. Bortignon, G. Colò, *et al.*, Nucl. Phys. A **687**, 44c (2001); see also, I. Hamamoto, H. Sagawa, and X. Z. Zhang, Phys. Rev. C **56**, 3121 (1997).
9. Z.-Y. Ma, N. Van Giai, A. Wandelt, *et al.*, Nucl. Phys. A **686**, 173 (2001); T. Nikšič, D. Vretenar, and P. Ring, Phys. Rev. C **66**, 064302 (2002).
10. J. Piekarewicz, Phys. Rev. C **66**, 034305 (2002).
11. D. Vretenar, T. Nikšič, and P. Ring, Phys. Rev. C **68**, 024310 (2003).

12. G. Colò, N. Van Giai, J. Meyer, K. Bennaceur, and P. Bonche, Phys. Rev. C (in press).
13. S. K. Patra, M. Centelles, X. Viñas, and M. Del Estal, Phys. Rev. C **65**, 044304 (2002).
14. B. K. Agrawal, S. Shlomo, and V. Kim Au, Phys. Rev. C **68**, 031304 (2003).
15. G. Colò, N. Van Giai, P.-F. Bortignon, and M. R. Quaglia, Phys. Lett. B **485**, 362 (2000).
16. D. Vretenar, A. Wandelt, and P. Ring, Phys. Lett. B **487**, 334 (2000).
17. U. Garg, Nucl. Phys. A **731**, 3 (2004).
18. Y. W. Lui *et al.*, Nucl. Phys. A **731**, 28 (2004).
19. M. Uchida *et al.*, Phys. Lett. B **557**, 12 (2003).
20. M. Hunyadi *et al.*, Nucl. Phys. A **731**, 49 (2004).

Physics of Atomic Nuclei, Vol. 67, No. 9, 2004, pp. 1737–1741. From Yadernaya Fizika, Vol. 67, No. 9, 2004, pp. 1764–1768.

Effects of Coupling between Particles and Surface Vibrations on Isoscalar Response of Nuclei*

V. I. Abrosimov[1)], O. I. Davidovskaya[1)], A. Dellafiore[2)], and F. Matera[2)]**

Received January 21, 2004

Abstract—The isoscalar quadrupole and octupole response of heavy spherical nuclei is studied in a semiclassical model that includes a coupling between the motion of nucleons and surface vibrations. By using a separable approximation for the residual interaction, an analytical expression has been obtained for the isoscalar response function of different multipolarity. A unified description of the low- and high-energy response is achieved within our semiclassical model. The inclusion of surface vibrations leads to the low-energy modes. The low-lying quadrupole mode is strongly affected by the surface tension but its frequency is still finite if, in the absence of Coulomb repulsion, the surface tension is set to zero. The frequency of the low-lying octupole mode, instead, goes to zero for vanishing surface tension, which would correspond to shape instability with respect to octupole deformation. Closed classical trajectories of triangular shape play an essential role in the damping of the low-lying octupole mode. Our octupole response displays also a novel resonance-like structure between the low-energy octupole resonance and the high-energy one (at around 13 MeV for a system with $A = 208$ nucleons) that might have a toroidal character like the low-energy isoscalar dipole resonance. © *2004 MAIK "Nauka/Interperiodica".*

1. INTRODUCTION

It is well known that a coupling between the motion of nucleons and surface vibrations plays an essential role in low-energy nuclear collective modes (see, e.g., [1–3]). However, semiclassical models of the fluid-dynamical type [4, 5] do not contain single-particle degrees of freedom, so that they cannot include effects of coupling between nucleons and surface motion. The scope of our present work is to study the effects of coupling between the motion of individual nucleons and surface oscillations within a semiclassical approach that does include the single-particle degrees of freedom explicitly. Our approach is based on the linearized Vlasov kinetic equation. Solutions of this equation for finite systems have been obtained by using different boundary conditions (fixed and moving surface [6, 7]; see also [8]). While the fixed-surface solution can give a reasonable picture of the high-energy giant multipole resonances, it does not satisfactorily describe also the low-lying states. However, a unified description can be achieved within this model if the moving-surface boundary conditions introduced in [7] are employed. Physically, this means that we are including in our model a coupling between the motion of individual nucleons and the surface vibrations.

2. ISOSCALAR RESPONSE FUNCTION

In this paper, we are interested in the quadrupole ($L = 2$) and octupole ($L = 3$) response function of the kind

$$\tilde{\mathcal{R}}_L(\omega) = \frac{1}{\beta}\int d\mathbf{r} r^L Y_{LM}(\hat{\mathbf{r}})\delta\varrho_L(\mathbf{r},\omega). \qquad (1)$$

Here we put a tilde over the moving-surface response function to distinguish it from the untilded fixed-surface one. The fluctuation $\delta\varrho_L(\mathbf{r},\omega)$ is the time Fourier transform of the density fluctuation $\delta\varrho_L(\mathbf{r},t)$ induced by an external isoscalar field $V_{\rm ext}(\mathbf{r},t) = \beta\delta(t)r^L Y_{LM}(\hat{\mathbf{r}})$. This fluctuation can be obtained by integrating over momentum the phase-space density fluctuation $\delta n_L(\mathbf{r},\mathbf{p},t)$ that is given by the solution of the linearized Vlasov equation, either with fixed-surface [6] or with moving-surface [7] boundary conditions:

$$\delta\varrho_L(\mathbf{r},t) = \int d\mathbf{p}\delta n_L(\mathbf{r},\mathbf{p},t). \qquad (2)$$

We refer to the papers [9, 10] for further details on the formalism and discuss here only the main results.

Within the fixed-surface theory and under the assumption of a simplified residual interaction of separable form,

$$v(r_1,r_2) = \kappa_L r_1^L r_2^L, \qquad (3)$$

*This article was submitted by the authors in English.

[1)]Institute for Nuclear Research, National Academy of Sciences of Ukraine, Kiev, Ukraine.

[2)]Istituto Nazionale di Fisica Nucleare and Dipartimento di Fisica, Università di Firenze, Firenze, Italy.

**e-mail: abrosim@kinr.kiev.ua

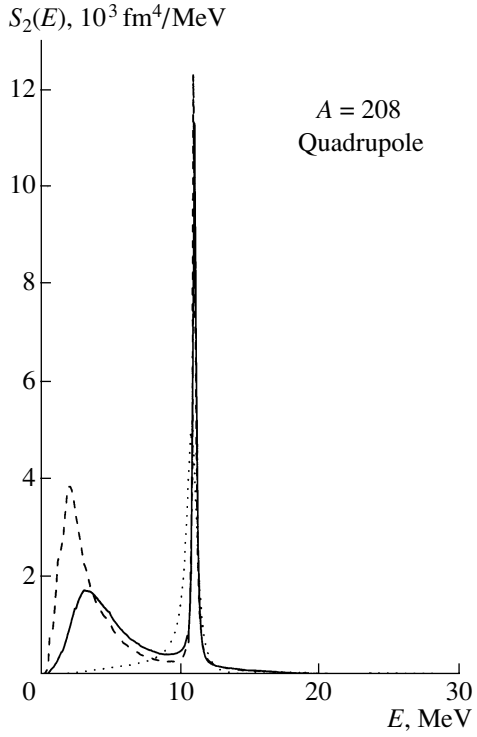

Fig. 1. The solid curve shows the quadrupole strength function evaluated by using moving-surface boundary conditions in the Vlasov equation; the dotted curve, instead, corresponds to fixed-surface boundary conditions. The dashed curve has been obtained in the moving-surface approach for vanishing surface tension.

the isoscalar response function of a spherical nucleus described as a system of A interacting nucleons contained within a cavity of radius $R = 1.2A^{1/3}$ fm is given by [11]

$$\mathcal{R}_L(s) = \frac{\mathcal{R}_L^0(s)}{1 - \kappa_L \mathcal{R}_L^0(s)}, \tag{4}$$

where, instead of the frequency ω, we have used the dimensionless quantity $s = \omega/(v_{\rm F}/R)$ ($v_{\rm F}$ is the Fermi velocity) as an independent variable. The zero-order response function $\mathcal{R}_L^0(s)$ is analogous to the single-particle response function of the quantum theory and, for a square-well type of mean field, it is given explicitly by [9] (see also [10, 12])

$$\mathcal{R}_L^0(s) = \frac{9A}{8\pi}\frac{1}{\epsilon_{\rm F}} \sum_{n=-\infty}^{+\infty} \sum_{N=-L}^{N=L} (C_{LN})^2 \tag{5}$$
$$\times \int_0^1 dx x^2 s_{nN}(x) \frac{(Q_{nN}^{(L)}(x))^2}{s + i\varepsilon - s_{nN}(x)}.$$

Here, $\epsilon_{\rm F}$ is the Fermi energy and the quantity ε is a vanishingly small parameter that determines the integration path at poles.

The functions $s_{nN}(x)$ are defined as

$$s_{nN}(x) = \frac{n\pi + N \arcsin x}{x}. \tag{6}$$

The variable x is related to the classical angular momentum λ of a nucleon. The relation is $x = \sin\alpha$, where α is the angle spanned by the radial vector when the particle moves from the inner to the outer turning point. For a square-well potential, one has $\cos\alpha = \lambda/\bar{\lambda}$, where $\bar{\lambda}$ is the maximum particle angular momentum $\bar{\lambda} = p_{\rm F}R$, $p_{\rm F}$ being the Fermi momentum.

The quantities C_{LN} in Eq. (5) are classical limits of the Clebsch–Gordan coefficients coming from the angular integration. Their explicit value is given by

$$(C_{LN})^2 = \frac{4\pi}{2L+1} \left| Y_{LN}\left(\frac{\pi}{2}, \frac{\pi}{2}\right)\right|^2. \tag{7}$$

In principle, the integer N takes values between $-L$ and L; however, only the coefficients C_{LN}, where N has the same parity as L, are nonvanishing.

The coefficients $Q_{nN}^{(L)}(x)$ appearing in the numerator of Eq. (5) have been defined in [6]; they are essentially the classical limit of the radial matrix elements of the multipole operator r^L and can be evaluated explicitly. The quadrupole coefficients $Q_{nN}^{(2)}(x)$ are given by [10]

$$Q_{nN}^{(2)}(x) = (-1)^n R^2 \frac{2}{s_{nN}^2(x)}\left(1 + N\frac{\sqrt{1-x^2}}{s_{nN}(x)}\right) \tag{8}$$

for $(n, N) \neq (0, 0)$ and

$$Q_{00}^{(2)}(x) = R^2\left(1 - \frac{2}{3}x^2\right), \tag{9}$$

and the octupole ones $Q_{nN}^{(3)}(x)$ can be found as [12]

$$Q_{nN}^{(3)}(x) = (-1)^n R^3 \frac{3}{s_{nN}^2(x)} \tag{10}$$
$$\times \left(1 + \frac{4}{3}N\frac{\sqrt{1-x^2}}{s_{nN}(x)} - \frac{2}{s_{nN}^2(x)} + 4(|N|-1)\frac{1-x^2}{s_{nN}^2(x)}\right).$$

It should be noted that the octupole modes with $N = \pm 3$ have an interesting property since the associated eigenfrequencies $s_{nN}(x)$ can vanish in the interval $0 < \alpha(x) < \pi/2$ [the equation $(n\pi + N\alpha) = 0$ has a solution for $\alpha = \pi/3$, corresponding to closed triangular orbits]. In [13], it has been pointed out that the vanishing of this eigenfrequency might give rise to a possible instability against octupole-type deformations in nuclei heavier than ^{208}Pb. Although at first sight it might seem that the coefficients (10) would

diverge when $s_{nN}(x) \to 0$, it is actually possible to check that

$$\lim_{x \to \frac{\sqrt{3}}{2}} Q^{(3)}_{\mp 1 \pm 3}(x) = -\frac{1}{4}R^3. \qquad (11)$$

The very fact that this limit is finite is important for our discussion about the role of triangular nucleon orbits.

The response function (5) involves an infinite sum over n; however, in practice it is sufficient to include only a few terms around $n = 0$ in order to fulfill the energy-weighted sum rule with good accuracy.

Within the moving-surface theory of [7], the collective response function (4) is replaced by

$$\tilde{\mathcal{R}}_L(s) = \mathcal{R}_L(s) + \mathcal{S}_L(s), \qquad (12)$$

with $\mathcal{R}_L(s)$ still given by Eq. (4), while $\mathcal{S}_L(s)$ represents the moving-surface contribution. With the simple interaction (3), the function $\mathcal{S}_L(s)$ can be evaluated explicitly as [10, 12]

$$\mathcal{S}_L(s) = -\frac{R^6}{1 - \kappa_L \mathcal{R}^0_L(s)} \frac{[\chi^0_L(s) + \kappa_L \varrho_0 R^L \mathcal{R}^0_L(s)]^2}{[C_L - \chi_L(s)][1 - \kappa_L \mathcal{R}^0_L(s)] + \kappa_L R^6 [\chi^0_L(s) + \varrho_0 R^L]^2}, \qquad (13)$$

with $C_L = \sigma R^2 (L-1)(L+2) + (C_3)_{\rm Coul}$ ($\sigma \approx 1$ MeV fm^{-2} is the surface tension parameter obtained from the mass formula, and $(C_3)_{\rm Coul}$ gives the Coulomb contribution to the restoring force), and $\varrho_0 = A/(4\pi R^3/3)$ being the equilibrium density.

The functions $\chi^0_L(s)$ and $\chi_L(s)$ are defined as in [9] and are given by

$$\chi^0_L(s) = \frac{9A}{4\pi}\frac{1}{R^3} \sum_{n=-\infty}^{+\infty} \sum_{N=-L}^{N=L} (C_{LN})^2 \qquad (14)$$
$$\times \int_0^1 dx x^2 s_{nN}(x) \frac{(-1)^n Q^{(L)}_{nN}(x)}{s + i\varepsilon - s_{nN}(x)}$$

and

$$\chi_L(s) = -\frac{9A}{2\pi} \epsilon_{\rm F}(s + i\varepsilon) \sum_{nN} (C_{LN})^2 \qquad (15)$$
$$\times \int_0^1 dx x^2 \frac{1}{s + i\varepsilon - s_{nN}(x)},$$

their structure being similar to that of the zero-order propagator (5).

Equation (13) is the main result of the present paper; its explicit derivation is lengthy but straightforward, and the main steps are outlined in Appendix A of paper [10]. Together with Eqs. (4) and (12), Eq. (13) gives a unified expression for the isoscalar response function, including both the high-energy resonance and the low-energy excitations. By comparing the two response functions (4) and (12), we can appreciate the effect of the additional surface degree of freedom and, in particular, the effect of coupling the motion of nucleons with surface vibrations.

3. EFFECTS OF SURFACE VIBRATIONS ON STRENGTH FUNCTION

We study the isoscalar strength function that is defined as ($E = \hbar\omega$)

$$S_L(E) = -\frac{1}{\pi} {\rm Im} \tilde{\mathcal{R}}_L(E). \qquad (16)$$

In Fig. 1, we display the quadrupole strength function [$L = 2$ in Eq. (16)] obtained for $A = 208$ using different approximations. The dotted curve is obtained from the collective fixed-surface response function (4). The collective fixed-surface response has one giant quadrupole peak. The strength of the interaction (3), chosen in order to reproduce the experimental value of the giant quadrupole resonance energy in ^{208}Pb, is $\kappa_2 = -1 \times 10^{-3}$ MeV fm^{-4}. This value is close to that suggested by the Bohr–Mottelson prescription ([13], p. 509),

$$\kappa_2 = -\frac{4\pi}{3}\frac{m\omega_0^2}{AR^2} \approx -0.5 \times 10^{-3} \text{ MeV fm}^{-4} \qquad (17)$$

(with $\omega_0 = 41 A^{-1/3}$ MeV).

We notice that the width of the giant quadrupole resonance is underestimated by the fixed-surface model; this is a well-known limit of all mean-field calculations that include only Landau damping. Moreover, there is no sign of a low-energy peak in the fixed-surface response function. The solid curve instead shows the moving-surface response given by Eqs. (12) and (13). Now a broad bump appears in the low-energy part of the response and a narrower peak is situated at the giant resonance energy; thus, the moving-surface solution of the Vlasov equation accounts for both quadrupole modes, although only qualitatively. Of course the details of the low-energy excitations are determined by quantum effects; nonetheless, the present semiclassical approach does

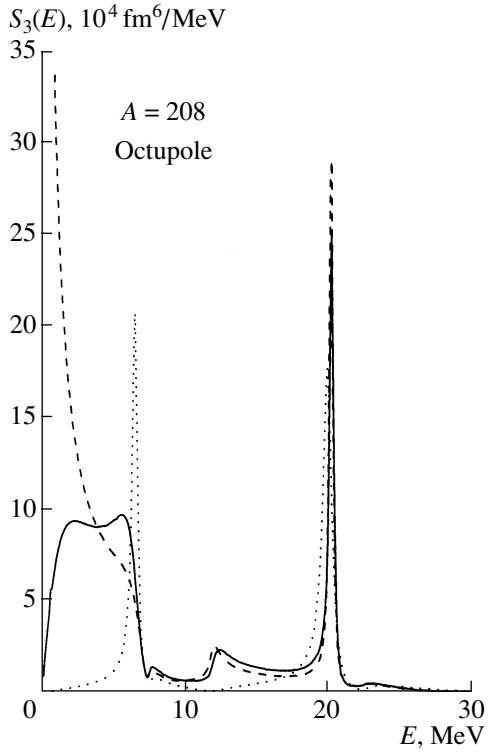

Fig. 2. The same as in Fig. 1 for the octupole strength function.

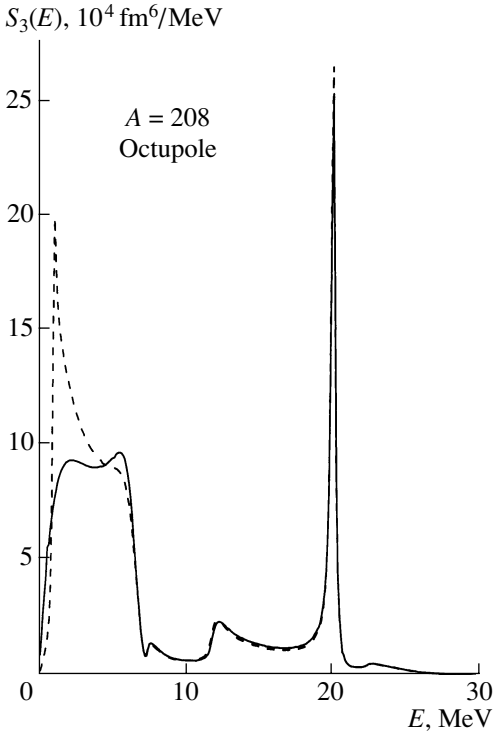

Fig. 3. Moving-surface octupole strength function with (solid curve) and without (dashed curve) contribution of closed triangular orbits.

reproduce the average behavior of this systematic feature of the quadrupole response.

It can be seen from Fig. 1 that, while the fixed-surface response (dotted curve) has only one collective pole, the moving-surface quadrupole response function (solid curve) displays a two-pole structure. In order to get more information about the nature of the low-energy peak, we have performed calculations by setting the surface tension parameter σ equal to zero. The result is shown in Fig. 1, where the dashed curve corresponds to $\sigma = 0$. As expected, the giant resonance peak is practically unaffected by the surface tension, while the low-energy peak is affected quite substantially. The surface tension increases the frequency of the low-energy peak, which, however, is present at a nonvanishing frequency also in the absence of surface tension. In the opposite limit, if we let $\sigma \to \infty$, the fixed-surface response is obtained.

In Fig. 2, we report the octupole strength function [$L = 3$ in Eq. (16)] given by the moving-surface response function (12) (solid curve) and compare it to the collective fixed-surface response given by Eq. (4) (dotted curve). As for the quadrupole response, we determine the strength parameter κ_3 phenomenologically by requiring that the peak of the high-energy octupole resonance agree with experiment. We can clearly see that the fixed-surface response given by the dotted curve has two sharp peaks around 20 and 6–7 MeV. The experimentally observed [14] concentration of isoscalar octupole strength in the two regions usually denoted by HEOR (high-energy octupole resonance) and LEOR (low-energy octupole resonance) is qualitatively reproduced; however, the considerable strength experimentally observed at lower energy (low-lying collective states) is absent from our fixed-surface response function. The most relevant change induced by the moving surface (see the solid curve in Fig. 2) is the large double hump appearing at low energy. This feature is in qualitative agreement both with experiment [14] and with the result of RPA-type calculations [15, 16]. We interpret this low-energy double hump as a superposition of surface vibrations and LEOR. The octupole moving-surface response also displays a novel resonance structure between LEOR and HEOR (at around 13 MeV for a system with $A = 208$ nucleons) (see Fig. 2).

In order to explain why we do not obtain one or more sharp 3^- states at low energy, we have to analyze our moving-surface response function in some detail. It has already been pointed out in [17] that the Landau damping of the low-energy collective modes is due only to nucleons moving along closed classical trajectories. In our theory, only nucleons moving along closed triangular trajectories can contribute to

the damping of octupole surface vibrations. In order to check that indeed the closed triangular orbits are the main source of Landau damping in the low-energy octupole response, we also study the response that is obtained when the contribution of these orbits is excluded (see [12] for details). In Fig. 3, we show the moving-surface strength function with (solid curve) and without (dashed curve) contribution of closed triangular orbits. The shape of the low-energy hump changes dramatically because of the lack of damping due to the missing triangular trajectories. A very sharp peak is now developed at low energy. We see that the closed triangular orbits, rather than generation of a shape instability in the octupole channel, are the main source of Landau damping in this response function. Of course, quantum effects can play an essential role at this level since in quantum mechanics the angular momentum is quantized and there could be no value of angular momentum corresponding to triangular trajectories.

We would also like to point out that our moving-surface response function can display a shape instability in the octupole channel, which can arise if the restoring force parameter C_3 vanishes. This could happen if the repulsive Coulomb term $(C_3)_{\mathrm{Coul}}$ exactly balances the attractive surface-tension part of the restoring force. In this case, our moving-surface response function develops a pole at the origin, as shown in Fig. 2 by the dashed curve. For odd multipolarities, the instability condition in our model is the same as for the liquid-drop model [17].

We have also performed calculations of the quadrupole and octupole response functions for other values of A corresponding to medium-heavy spherical nuclei and the results are qualitatively similar to the $A = 208$ case, so we do not report them here.

4. CONCLUSIONS

We have obtained an analytical expression for the isoscalar response function of nuclei that qualitatively describes the main systematic features of the quadrupole and octupole excitation spectrum. The found octupole response displays a novel resonance structure. It is of interest to study the nature of this resonance in more detail. Taking into account results for the isoscalar dipole response [9], we may expect that this resonance has the same origin as the low-energy isoscalar dipole resonance and that it has a toroidal character [18]. We have found that the triangular trajectories of nucleons have no consequences on the shape instability of heavy spherical nuclei against octupole-type deformations; rather, triangular orbits are essential in providing a damping of low-energy octupole excitations.

As a further remark, we would like to add that the problem of which boundary conditions to use in the linearized Vlasov equation for finite systems, rather than being a limitation of the approach, may be seen as a richness of the theory: different boundary conditions allow us to study different physical properties of the system.

REFERENCES

1. P. F. Bortignon and R. A. Broglia, Nucl. Phys. A **371**, 405 (1981).
2. G. F. Bertsch and R. A. Broglia, *Oscillations in Finite Quantum Systems* (Cambridge Univ. Press, Cambridge, 1994), Chap. 6.
3. D. Lacroix, S. Ayik, and Ph. Chomaz, Phys. Rev. C **63**, 064305 (2001).
4. G. F. Bertsch, in *Nuclear Physics with Heavy Ions and Mesons*, Ed. by R. Balian, M. Rho, and G. Ripka (North-Holland, Amsterdam, 1978), p. 178.
5. G. Holzwarth and G. Eckart, Nucl. Phys. A **325**, 1 (1979).
6. D. M. Brink, A. Dellafiore, and M. Di Toro, Nucl. Phys. A **456**, 205 (1986).
7. V. Abrosimov, M. Di Toro, and V. Strutinsky, Nucl. Phys. A **562**, 41 (1993).
8. V. I. Abrosimov, A. Dellafiore, and F. Matera, *Recent Research Developments in Physics* (Transworld Res. Network, India, 2002), Vol. 3, p. 325.
9. V. I. Abrosimov, A. Dellafiore, and F. Matera, Nucl. Phys. A **697**, 748 (2002).
10. V. I. Abrosimov, A. Dellafiore, and F. Matera, Nucl. Phys. A **717**, 44 (2003).
11. G. F. Burgio and M. Di Toro, Nucl. Phys. A **476**, 189 (1988).
12. V. I. Abrosimov, O. I. Davidovskaja, A. Dellafiore, and F. Matera, Nucl. Phys. A **727**, 220 (2003).
13. A. Bohr and B. R. Mottelson, *Nuclear Structure* (Benjamin, Reading, Mass., 1975), Vol. II, App. 6A.
14. A. Van Der Woude, Prog. Part. Nucl. Phys. **18**, 217 (1987).
15. K. F. Liu and G. E. Brown, Nucl. Phys. A **265**, 385 (1976).
16. K. F. Liu, H. Luo, Z. Ma, *et al.*, Nucl. Phys. A **534**, 1 (1991).
17. V. Abrosimov, A. Dellafiore, and F. Matera, Nucl. Phys. A **653**, 115 (1999).
18. D. Vretenar, A. Wandelt, and P. Ring, Phys. Lett. B **487**, 334 (2000).

Physics of Atomic Nuclei, Vol. 67, No. 9, 2004, pp. 1742–1749. From Yadernaya Fizika, Vol. 67, No. 9, 2004, pp. 1769–1776.

Structure of the Gamow–Teller Resonance in ^{58}Cu Studied via the Proton- and γ-Decay Measurements*

M. Fujiwara**

Research Center for Nuclear Physics, Osaka University, Osaka, Japan

Received January 21, 2004

Abstract—The Gamow–Teller (GT) states in ^{58}Cu have been studied by ^{58}Ni(^{3}He, $t+p$) and ^{58}Ni(^{3}He, $t+\gamma$) coincidence experiments at $E(^3\mathrm{He}) = 450$ MeV and $\theta = 0°$. Proton emissions from the GT states in ^{58}Cu to the hole states in ^{57}Ni have been observed with solid-state detectors in coincidence with high-energy tritons measured with a magnetic spectrometer. For the first time, γ-ray emissions from the excited states in ^{58}Cu and in ^{57}Ni, following the ^{58}Ni(^{3}He, $t+p$) reaction at intermediate energies, have also been observed in coincidence with tritons. The wave functions of the $T = 1$ and $T = 2$ GT states with the $f_{7/2}^{-1}$ neutron–hole configuration are inferred to be strongly coupled to $2p$–$2h$ configurations, making fragmented GT strengths in ^{58}Cu. © *2004 MAIK "Nauka/Interperiodica".*

1. INTRODUCTION

Structures of the excited levels in pf-shell nuclei provide good cases to test the validity of the model calculations and to extend their applicability to nuclei far from the β-stability line. For example, the Gamow–Teller (GT) transitions from the ground state of ^{58}Ni to the excited states in ^{58}Cu are excellent candidates for the study of various coupling modes of collective one-particle–one-hole ($1p$–$1h$) excitations with two-particle–two-hole ($2p$–$2h$) configurations.

In ^{58}Cu, the proton-separation energy is relatively low ($S_p = 2.873$ MeV). However, the one-neutron and two-proton separation energies are very high, as $S_n = 12.426$ MeV and $S_{2p} = 10.202$ MeV, respectively. Because of the high S_n value, the states below $E_x = 12$ MeV decay mainly by proton emission, and their widths are narrow (a few keV) due to the Coulomb barrier for proton emission. In fact, fragmented GT states have been observed in high-resolution ^{58}Ni(^{3}He, t)^{58}Cu measurements at 450 MeV [1, 2]. A single broad resonance at $E_x \sim 10$ MeV, which has originally been observed in the ^{58}Ni(p, n)^{58}Cu charge-exchange reactions [3–5], is now found to have a fine structure consisting of many fragmented GT states. This kind of fragmentation is caused by the coupling between $1p$–$1h$ and $2p$–$2h$ states via the residual interaction [6, 7]. In the target nucleus ^{58}Ni with isospin $T_0 = 1$, fragmented $M1$ states with isospin quantum numbers of $T = 1$ and $T = 2$ are reported in (e, e'), (γ, γ'), and (p, p') measurements [8–15]. Therefore, the isobaric analogs (GT states) in ^{58}Cu corresponding to these $M1$ states in ^{58}Ni should be excited in charge-exchange reactions.

Proton emission from the GT states in ^{58}Ni leads to neutron–hole states with $T = 1/2$ and $T = 3/2$ in ^{57}Ni. The hole-state analogs ($T = 3/2$) in ^{57}Ni have already been systematically studied via the ^{58}Ni(p, d)^{57}Ni reaction at 65 MeV [16, 17]. Many fragmented $7/2^-$ and $3/2^-$ hole-state analogs have been reported above $E_x = 5.135$ MeV in ^{57}Ni. Due to the isospin selection rule, proton emission from the $T = 2$ GT states in ^{58}Cu into the $T = 1/2$ states in ^{57}Ni is forbidden since decay by one nucleon only carries $\Delta T = 1/2$. Transitions from the $T = 1$ states to both $T = 1/2$ and $T = 3/2$ states in ^{57}Ni are allowed. If one observes a strong feeding of proton decay from the excited GT states in ^{58}Cu into the $T = 3/2$ states in ^{57}Ni, this provides good evidence that these states have $T = 2$ character.

However, the final-state resolution of the ^{58}Ni (^{3}He, $t+p$)^{57}Ni experiment at 450 MeV is not good enough to resolve the fine structure of the isobaric analog final states in ^{57}Ni, since the final-state resolution is dominated by the resolution of the ^{3}He^{++} beam used. Thus, an additional complementary experiment was necessitated. To establish the final states in ^{57}Ni fed by proton emission from ^{58}Cu, we have obtained ^{58}Ni(^{3}He, $t+\gamma$) coincidence data, which allows us to assign the final states in

*This article was submitted by the author in English.

** e-mail: fujiwara@rcnp.osaka-u.ac.jp

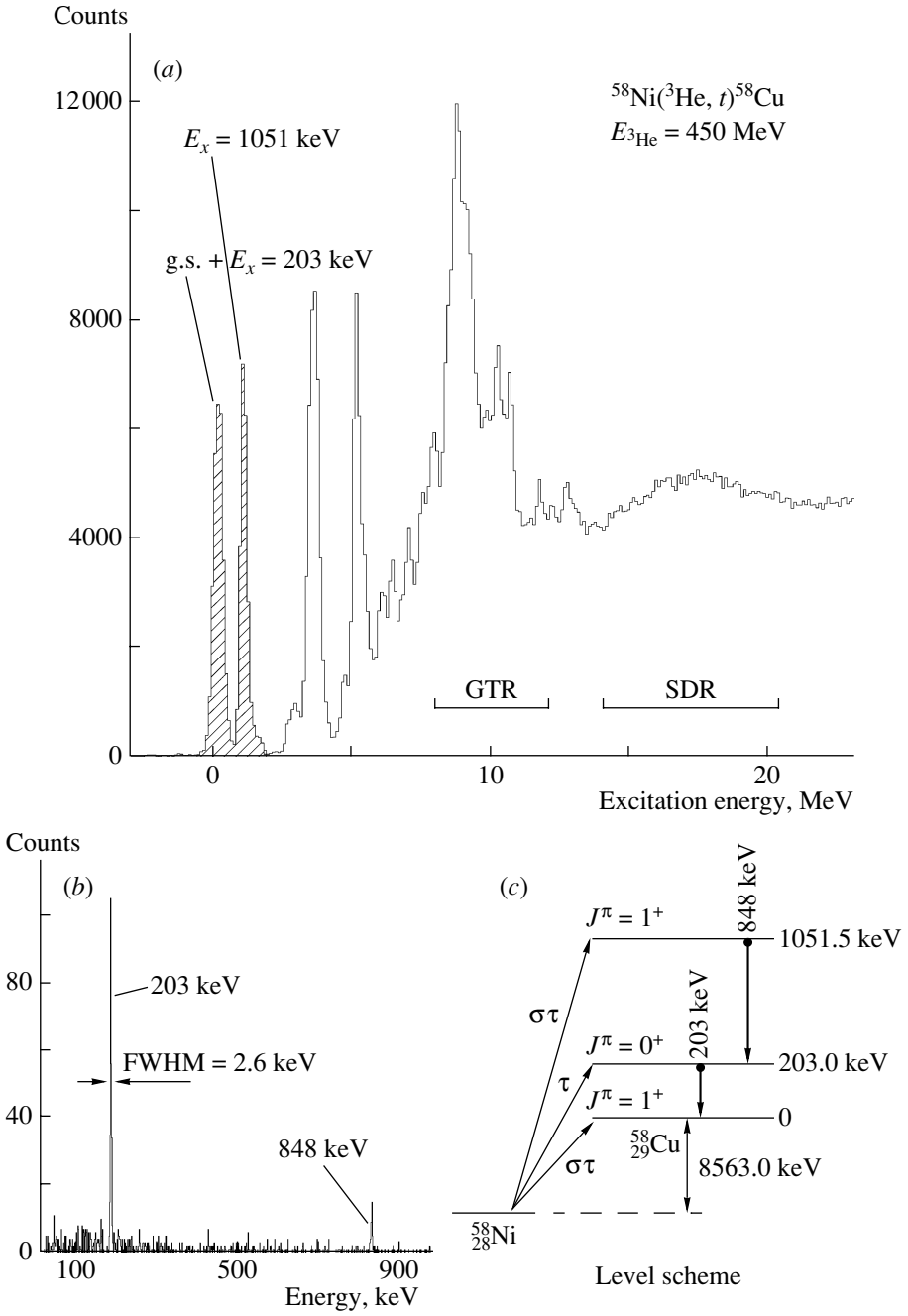

Fig. 1. (*a*) Singles spectrum of the ^{58}Ni(^{3}He, t)^{58}Cu reaction measured at 0° and a bombarding energy of 450 MeV. (*b*) Coincidence γ-ray spectrum of a Ge detector obtained by gating on the (^{3}He, t) peaks for the ground, 203-, and 1051-keV states. Two sharp γ-ray peaks at 203 and 848 keV are clearly visible. These γ rays are due to the decays from the 1051.5-keV (1^+) and 203.0-keV (0^+) states in ^{58}Cu. (*c*) Relevant levels in ^{58}Cu. Excitation modes via the (^{3}He, t) charge-exchange reaction and γ-ray decay scheme are indicated.

^{57}Ni thanks to a high-resolution γ-ray measurement with high-purity Ge (HPGe) detectors. In the present paper, we report the results obtained from ^{58}Ni(^{3}He, $t+p$) and ^{58}Ni(^{3}He, $t+\gamma$) coincidence experiments at 450 MeV to discuss the nature of the GT states in ^{58}Cu.

2. EXPERIMENT

The ^{58}Ni(^{3}He, $t+p$) and ^{58}Ni(^{3}He, $t+\gamma$) experiments were carried out at the ring cyclotron facility of the Research Center for Nuclear Physics (RCNP), Osaka University. The detailed descriptions of the experimental techniques are given in [2, 18, 19]. Thus, we present only a brief summary of the

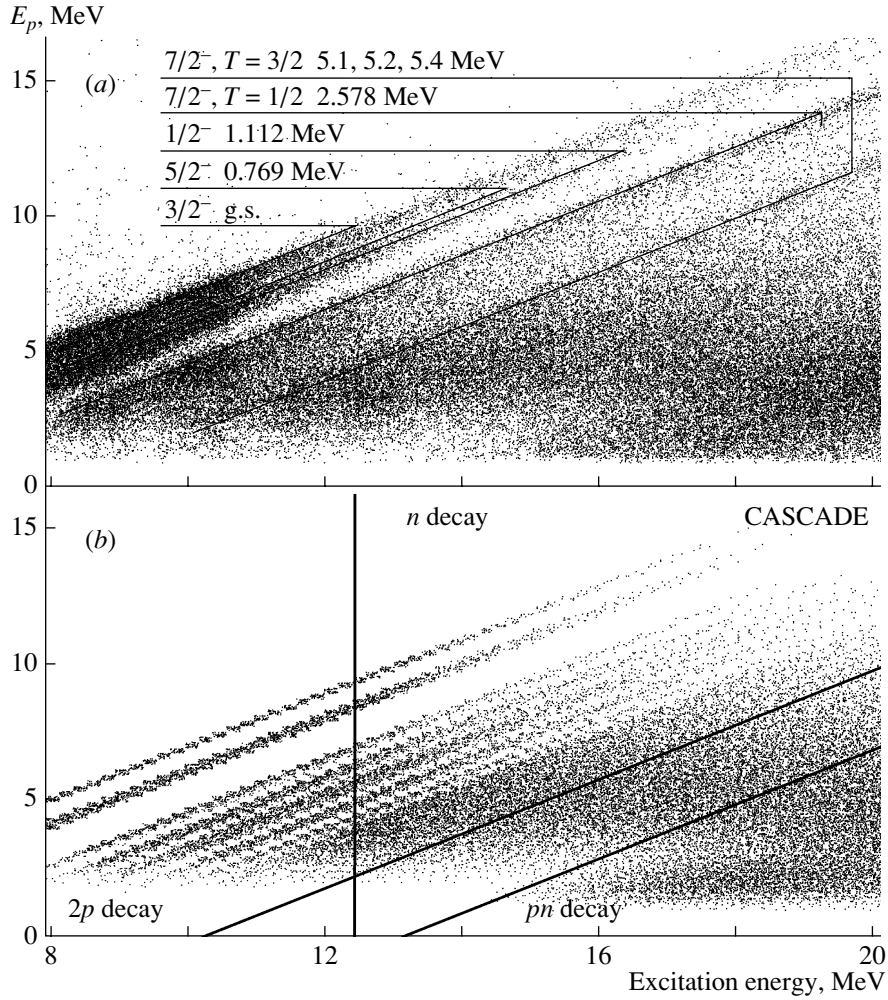

Fig. 2. (*a*) Two-dimensional scatter plot of proton–triton coincidence events induced by the ^{58}Ni(^{3}He, t) reaction at 0°. The loci indicate proton-decay events from the excited states in ^{58}Cu to the final states in ^{57}Ni. (*b*) Results of the statistical-model calculation with CASCADE [20].

present experiment, by using the obtained experimental data. Figure 1*a* shows a typical spectrum of the ^{58}Ni(^{3}He, t)^{58}Cu reaction. Several discrete states in ^{58}Cu up to about 8 MeV have been reported to be 1^+ GT states in the high-resolution (^{3}He, t) measurement using the dispersion-matching technique [2]. The bump at $E_x = 8$–12 MeV is the Gamow–Teller resonance (GTR). The differential cross section for the GTR is strongly peaked at 0°. The global shape of the present (^{3}He, t) spectrum is similar to that obtained in the ^{58}Ni(p, n)^{58}Cu reaction at 160 MeV and 0° by Rapaport *et al.* [4, 5]. The bump around $E_x = 18$ MeV is the spin-dipole resonance (SDR). The differential cross section for the SDR is peaked around 1°, which is characteristic of $\Delta L = 1$ transitions at this bombarding energy. To perform the present proton- and γ-coincidence measurements, reduction of beam halo was essential to obtain a good signal-to-noise ratio. Therefore, the achromatic transport technique of the ^{3}He beam was chosen. The energy resolution of the (^{3}He, t) experiment was 250 keV. The 1^+ ground state and the 0^+ isobaric-analog state at $E_x = 203$ keV were not resolved. Figure 1*b* demonstrates the usefulness of the coincidence measurement with γ-ray decay with high-resolution Ge detectors in coincidence to identify the relevant excited states (shown in Fig. 1*c*).

3. RESULTS AND DISCUSSION

Figure 2*a* shows a two-dimensional scatter plot of proton energy vs. E_x(^{58}Cu) for t–p coincidence events induced by the ^{58}Ni(^{3}He, t) reaction at 0°. The loci for proton decay from the excited states in ^{58}Cu to the $3/2^-$ ground state; $5/2^-$ at 0.769 MeV; $1/2^-$ at 1.112 MeV; $7/2^-$, $T = 1/2$ at 2.578 MeV; and $7/2^-$, $T = 3/2$ at 5.1, 5.2, and 5.4-MeV states

in ^{57}Ni can be identified as lines corresponding to $E_t + E_p \simeq$ const. Figure 2*b* shows the results of a statistical-model calculation performed for decay protons from the excited states in ^{58}Cu, using the Hauser–Feshbach formalism with the code CASCADE [20].

In the calculation, spin, isospin, and parity of the reported excited states in ^{58}Cu, ^{57}Ni, ^{57}Cu, ^{56}Fe, and ^{56}Ni are used as the input parameters. Individual level parameters were taken from the experimental data compiled in Nuclear Data Sheets [21–23]. Global parameters for the level-density formula were used to describe the unknown levels at high excitation energies [24–26]. We took a procedure in making the level-density inputs in the CASCADE calculations similar to those given in [27]. Formation cross sections of ^{58}Cu were normalized to the ^{58}Ni(^{3}He, t) singles spectrum measured in this experiment. The gross features of the proton-decay pattern agree with the results obtained in the statistical-model calculation. However, decay from the states at high excitation energies in ^{58}Cu to the low-lying discrete states in ^{57}Ni is enhanced in comparison with the results obtained in the statistical-model calculation. For example, the event locus corresponding to proton decay to the $7/2^-$, 2.578-MeV level in ^{57}Ni continuously extends to $E_x(^{58}\mathrm{Cu}) = 20$ MeV. This suggests that the SDR in ^{58}Cu has a wave function with the main $\pi g_{9/2}\nu f_{7/2}^{-1}$ configuration and emits a proton from the $g_{9/2}$ orbit by the direct process to the $T = 1/2$, $f_{7/2}^{-1}$ neutron–hole state in ^{57}Ni.

In Fig. 3, the final-state spectra for the excited states in ^{57}Ni generated by gating on decay protons from excited states in ^{58}Cu are compared with the results of the statistical-model calculation. The calculated relative strengths of decay protons from the $T = 0$ states and $T = 1$ states in ^{58}Cu reproduce well the final-state spectra, irrespective of their excitation energies. Since most of the decay properties are characterized by the $T = 1/2$ states in ^{57}Ni to which decay from $T = 0$ states and $T = 1$ states in ^{58}Cu is allowed, there is no significant difference between the decay patterns calculated for these $T = 0$ and $T = 1$ states as typically shown in Figs. 3*c*, 3*d*, and 3*e*.

The proton-decay branching ratio for $T = 2$ states in ^{58}Cu should be much different from other isospin states, because proton decay from $T = 2$ states to $T = 1/2$ states in ^{57}Ni is isospin forbidden. A statistical-model calculation code which allows for three different isospin components in one nucleus is not available at present. The modified and extended CASCADE code [20] allows for two isospin components starting from the ground-state isospin, e.g., in ^{58}Cu, $T = 0$ and $T = 1$. Therefore, it is not possible to treat proton decay from the $T = 2$ states in ^{58}Cu to the $T = 3/2$ states in ^{57}Ni. It is clear though that, in a one-step process, without isospin mixing, $T = 2$ states can only populate $T = 3/2$ states by proton decay. Thus, we could not compare the experimental results with the statistical-model calculation for the proton decay from the $T = 2$ states.

In Figs. 3*c*–3*e*, proton-decay events from the states at high excitation energies in ^{58}Cu into the $T = 1/2$, $7/2^-$ state at 2.578 MeV in ^{57}Ni are clearly visible. These proton decays are not predicted in the statistical-model calculation. In addition, proton decays into the $T = 3/2$, $f_{7/2}^{-1}$ state at $E_x \sim 5.2$ MeV in ^{57}Ni have been identified in Figs. 3*d* and 3*e*. This experimental observation indicates that the SDR with the wave function having mainly the $\pi g_{9/2}\nu f_{7/2}^{-1}$ configuration directly decays to the $T = 1/2$, $f_{7/2}^{-1}$ state in ^{57}Ni. However, from the present measurement, we cannot determine whether the SDR decays to the $T = 3/2$, $f_{7/2}^{-1}$ state in ^{57}Ni or the $T = 2$, GT states coexisting with the SDR in ^{58}Cu decay to the $T = 3/2$ states.

Figure 4 shows a two-dimensional scatter plot of triton–γ-coincidence events induced by the ^{58}Ni(^{3}He, t) reaction at 0°. The loci for γ decay indicate that several excited states in ^{58}Cu decay by proton emission into discrete final states in ^{57}Ni and ^{56}Co. The loci corresponding to the photopeaks due to these decay events are seen as horizontal lines in Fig. 4, i.e., in the case of γ decay subsequent to decay by nucleon emission from the giant-resonance region at $E_x = 8$–24 MeV in ^{58}Cu. On the contrary, the loci corresponding to the γ-decay events from the discrete states between 0 and 5 MeV in ^{58}Cu are recognized. Event points dispersed in Fig. 4 are due to Compton-scattered events of coincident γ rays and due to events with a small photopeak. To understand the global features of the triton–γ-coincidence data in more detail, decay patterns are examined by dividing the excitation energy in ^{58}Cu into three regions, I, II, and III.

In region I, γ-ray transitions from the discrete states in ^{58}Cu have been observed, although the proton-decay threshold ($S_p = 2.873$ MeV) opens. The photopeaks at 203, 444, and 3475 keV are clearly identified, suggesting that proton decay from the low-lying states in ^{58}Cu is largely suppressed due to the Coulomb barrier, and γ decay competes with proton decay for the states at $E_x < 5$ MeV.

The individual transition strength for the two states at 3.460 and 3.678 MeV was not deduced in

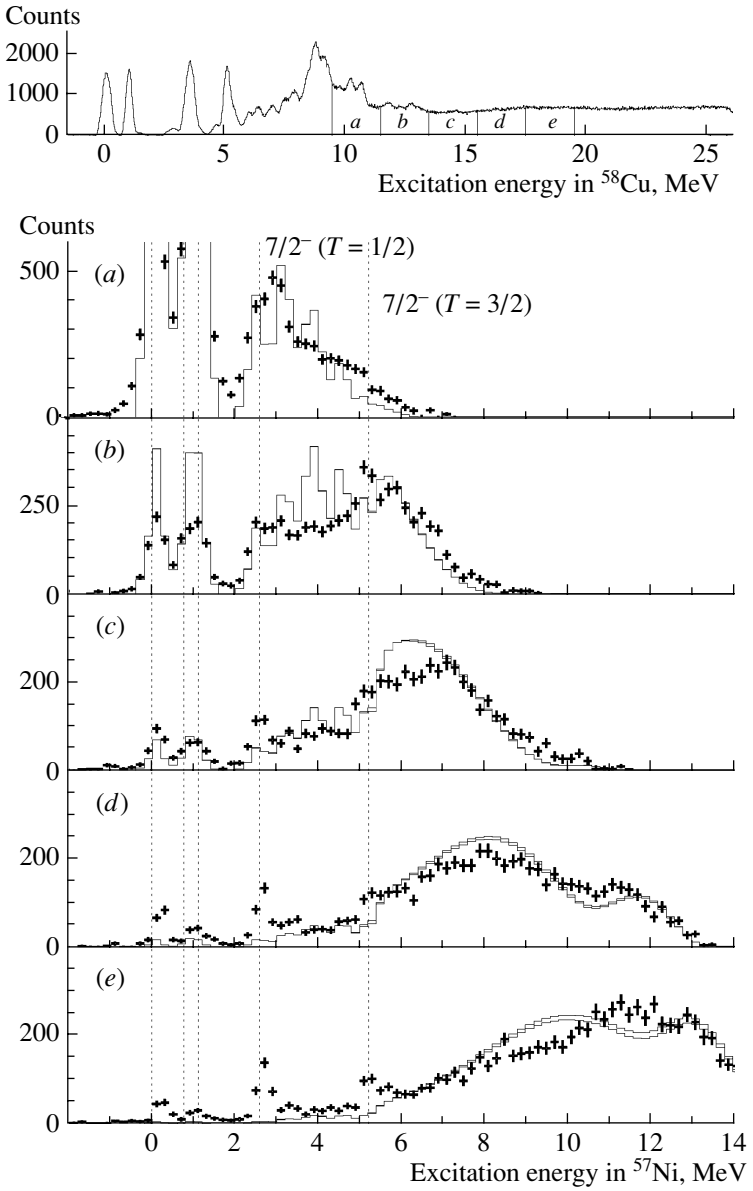

Fig. 3. Final-state spectra of the excited states in ^{57}Ni populated by proton decay from the excited states in ^{58}Cu. The spectra are obtained by projecting loci of Fig. 2*a* onto the ^{57}Ni excitation-energy axis. A singles ^{58}Ni(^{3}He, t) spectrum is shown in the upper part to indicate the gate positions (from 9.5 to 19.5 MeV, in steps of 2 MeV) for each final-state spectrum denoted by (*a*)–(*e*). The dotted lines show the excitation energies for discrete levels in ^{57}Ni ($3/2^-$ ground state; $5/2^-$ at 0.769 MeV; $1/2^-$ at 1.112 MeV; $7/2^-$, $T = 1/2$ at 2.578 MeV; and $7/2^-$, $T = 3/2$ at 5.1, 5.2, and 5.4 MeV). The experimental data are shown by the cross symbols. The results of the statistical-model calculations for proton decays from the $T = 1$ and $T = 0$ states in ^{58}Cu are shown by the solid histograms.

the analysis of the present (^{3}He, t) singles spectrum. However, the relative transition strengths of the states at 3.460 and 3.678 MeV are reported by Fujita *et al.* [2]. Therefore, the transition strengths for the states at 3.460 and 3.678 MeV were estimated by using the summed yield for a peak at ~ 3.5 MeV observed in the ^{58}Ni(^{3}He, t)^{58}Cu spectrum. The proton-decay branching ratios of the 3.460 and 3.678 MeV states thus amount to $(62 \pm 11)\%$ and $(15 \pm 17)\%$, respectively.

In region II, γ-decay transitions cannot compete with proton decay anymore. The loci in this region mainly correspond to the events due to γ decays from the excited states in ^{57}Ni. Two loci of the γ-decay events for the 769-keV ($5/2^-_1 \to 3/2^-_{\mathrm{g.s}}$) and 1112-keV ($1/2^-_1 \to 3/2^-_{\mathrm{g.s}}$) transitions in ^{57}Ni are observed.

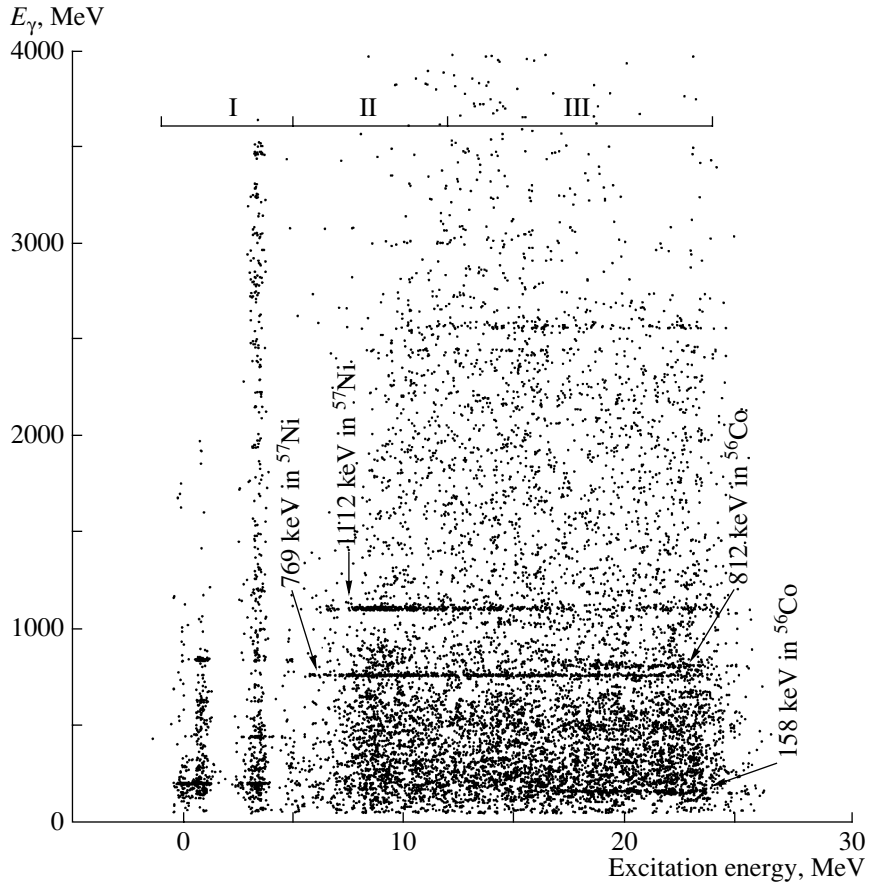

Fig. 4. Two-dimensional scatter plot of triton–γ-coincidence events for the ^{58}Ni(^{3}He, t) reaction at 0°. Accidental events have been subtracted. The various loci indicate γ-decay events from the excited states of ^{58}Cu, ^{57}Ni, and ^{56}Co. For the clarification of the regions denoted as I ($E_x = 0-5$ MeV), II ($E_x = 5-14$ MeV), and III ($E_x = 14-24$ MeV), see text.

The loci corresponding to these transitions continue to the high excitation energy of $E_x \sim 24$ MeV in ^{58}Cu. This indicates that the probability for direct proton decay is still not negligible for the states at high excitation energies in ^{58}Cu.

Comparing the results of the proton-decay measurement and the γ-decay measurement, it is possible to reveal the characteristics of the giant-resonance states in ^{58}Cu. Figure 5*a* shows the coincidence γ-ray spectrum obtained by gating on the events for the GTR region at $E_x = 8-14$ MeV in the ^{58}Ni(^{3}He, t)^{58}Cu spectrum measured at 0°. Photopeaks at 769, 1112, 2443, and 2578 keV correspond to the ground-state transitions from the excited states in ^{57}Ni. The partial level scheme of ^{57}Ni is shown in Fig. 5*b*. The direct-decay protons from the GTR in ^{58}Cu to the $3/2^-$ ground state; $5/2^-$ at 0.769 MeV; $1/2^-$ at 1.112 MeV; $7/2^-$, $T = 1/2$ at 2.578 MeV; and $7/2^-$, $T = 3/2$ at 5.1-, 5.2-, and 5.4-MeV states in ^{57}Ni have been observed in the proton-decay measurement. In agreement with these facts, the 769-keV ($5/2^- \to 3/2^-_{\mathrm{g.s}}$), 1112-keV ($1/2^- \to 3/2^-_{\mathrm{g.s}}$), and 2578-keV ($7/2^-, T = 1/2 \to 3/2^-_{\mathrm{g.s}}$) γ-decay transitions were observed.

To corroborate the proton decay from the GTR in ^{58}Cu to the 2.578-MeV ($7/2^-$, $T = 1/2$) state in ^{57}Ni, the consistency of the 2578-keV γ-decay yields with the proton-decay data is examined. We observed 21 ± 5 events for the 2578-keV peak in Fig. 5*a* in coincidence with the triton events for the GTR region at $E_x = 8-14$ MeV in the ^{58}Ni(^{3}He, t)^{58}Cu spectrum at 0°. After the corrections of the absolute efficiencies, solid angles, and dead time, we obtained 28 ± 4 for the γ-decay yields expected from the proton decay from the same 8–14-MeV GTR region to the 2.578-MeV state. This estimated number of 28 ± 4 already exceeds the observed number of 21 ± 5. Thus, the 2578-keV peak is considered to be mainly originated from the subsequent γ decay after the proton decay from the GTR in ^{58}Ni to the 2.578-MeV state in ^{57}Ni.

In the ^{58}Ni(p, d)^{57}Ni experiment by Ikegami *et al.* [16], the 5.230-MeV $7/2^-$ state is strongly excited in the $T = 3/2$ region. On the basis of the

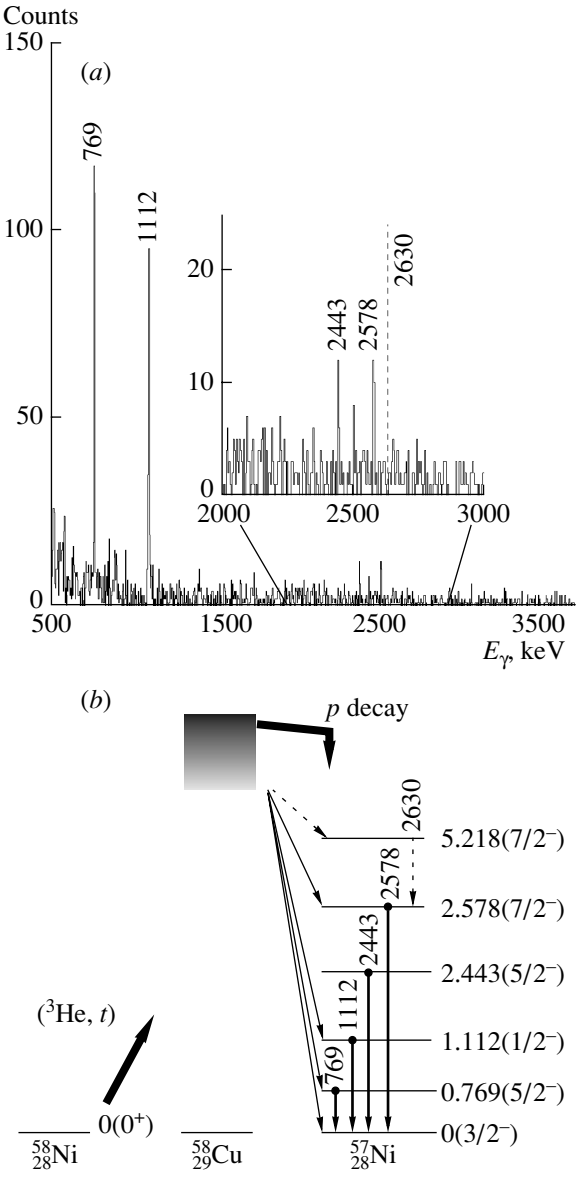

Fig. 5. (*a*) Coincidence γ-ray spectrum of a HPGe detector obtained by gating on the events for the GTR region at $E_x = 8-14$ MeV in the ^{58}Ni(^{3}He, t)^{58}Cu spectrum at 0°. Photopeaks at 769, 1112, 2443, and 2578 keV correspond to the ground-state transitions from the excited states in ^{57}Ni. The dashed line inserted in the figure indicates the position of the γ-ray energy of 2630 keV, which is the transition energy from the 5.218-MeV state to the 2.578-MeV state. (*b*) Partial level scheme of ^{57}Ni. The labels for the γ decays are given in keV. The labels for the excited states in ^{57}Ni are given in MeV. Missing proton and γ transitions are indicated by the dashed arrows.

^{58}Ni(^{3}He, $\alpha+\gamma$) experiment, Gould *et al.* reported that the 5.230-MeV, $T = 3/2$ state decays strongly to the 2.578-MeV state with a branching ratio of 50% [28]. If we assume that 100% of the proton decay from the GTR in ^{58}Cu to the 5.2-MeV region in ^{57}Ni concentrates only to the state at $E_x = 5.230$ MeV, 9.7 ± 1.0 events for the 2652-keV γ peak are expected for the spectrum in Fig. 5*a*. However, the measured counts are 7.0 ± 4.6. It is very difficult to deduce any decisive conclusion from this statistical error. Reasonable conjecture deduced from the coincidence γ-decay yields for the 2578- and 2652-keV peaks is to attribute the observed facts to that the proton decay from the GTR in ^{58}Cu to the 5.230-MeV $7/2^-$ state in ^{57}Ni is very weak.

In region III, p-decay, n-decay, and pp-decay processes compete with each other. Several γ decays from excited states in ^{57}Ni and ^{56}Co are assigned. Two loci for the 970-keV$(2_1^+) \rightarrow$ 158-keV(3_1^+) and 158-keV$(3_1^+) \rightarrow$ 0-keV$(4_{\text{g.s}}^+)$ transitions in ^{56}Co have been observed. On the other hand, γ-ray decays from the excited states in ^{57}Cu have not been identified. One possible explanation for this experimental result is that there is no γ-ray transition in ^{57}Cu since the proton-decay threshold from ^{57}Cu to ^{56}Ni is extremely low ($S_p = 0.695$ MeV).

When neutron decay occurs to excited levels in ^{57}Cu, the subsequent proton decay partially leads to excited levels in ^{56}Ni, from which it is possible to observe γ decay in the present experiment. However, we did not identify any 2701-keV γ-ray events from the transition 2701 keV $(2_1^+) \rightarrow 0$ keV $(0_{\text{g.s}}^+)$ in ^{56}Ni. Another plausible explanation is that there is no sizeable neutron decay from the excited states in region III in ^{58}Cu since the (^{3}He, t) reaction at 450 MeV selectively excites the spin-flip $T = 2$ GT states at high excitation energy, from which neutron decay carrying only $\Delta T = 1/2$ is strongly suppressed in making the final $T_0 = -1/2$ states in ^{57}Cu, and/or since the wave function of the SDR with the main $\pi g_{9/2} \nu f_{7/2}^{-1}$ configuration does not allow such decay.

4. SUMMARY

On the basis of the coincidence measurements of the (^{3}He, $t+p$) and (^{3}He, $t+\gamma$) reactions on ^{58}Ni, we have discussed the branching ratios for proton and γ decays from the GT states and the SDR in ^{58}Cu. The deduced branching ratios for proton decay from the $T = 0$ and $T = 1$ GT states are in good agreement with the results of the statistical-model calculation. The proton-decay strength from the GT states in ^{58}Cu to the $7/2^-$, $T = 3/2$ states in ^{57}Ni is not consistent with the results of the statistical-model calculation. The underestimation of the population of the $7/2^-$, $T = 3/2$ states in ^{57}Ni is qualitatively explained by the fact that the $T = 2$ GTR component, which decays only to these states by

isospin-allowed transitions, is not included explicitly in the statistical-model calculations. Therefore, a sizeable amount of the $T = 2$ GTR component, which the present statistical-model calculation code cannot deal with exactly, is inferred to exist in the bump region for the GT states above $E_x = 9.7$ MeV.

In addition, we have confirmed that the $T = 1$ and $T = 2$ GT states do not strongly decay into a neutron–hole state at 5.230 MeV in ^{57}Ni, which is strongly excited via the ^{58}Ni(p, d)^{57}Ni reaction. The absence of proton decay into the 5.230-MeV $7/2^-$ state is understood if the wave function of the GTR in ^{58}Cu does not have a dominant $1p$–$1h$ component and the proton-decay strengths do not strongly concentrate on any of three $7/2^-$ states with isospin $T = 3/2$ in ^{57}Ni [16]. These facts indicate that the wave functions of $T = 1$ and $T = 2$ GT states with the $f_{7/2}^{-1}$ neutron–hole configuration have a strong coupling to the $2p$–$2h$ configuration, supporting the $2p - 2h$ fragmentation mechanism for the GT resonances in nuclei [6, 7].

The branching ratios for proton decay from the SDR in ^{58}Cu to the low-lying discrete states in ^{57}Ni are enhanced in comparison with the results of the statistical-model calculation. The SDR in ^{58}Cu is expected to have a wave function with the $\pi g_{9/2}\nu f_{7/2}^{-1}$ configuration and strongly decays by the direct process to the $T = 1/2$, $f_{7/2}^{-1}$ neutron hole state in ^{57}Ni.

We did not observe any γ rays due to the deexcitations from the low-lying states in ^{57}Cu and in ^{56}Ni subsequent to neutron decays from the SDR in ^{58}Cu and/or proton decays from ^{57}Cu. This result is understood in terms of the isospin selection rule. In the case of $T = 2$ states at high excitation energies in ^{58}Cu, neutron decay with an isospin transfer of $\Delta T = 1/2$ is forbidden to final $T = 1/2, T_z = -1/2$ states in ^{57}Cu. However, the (^{3}He, t) reaction at 450 MeV excites both $T = 1$ and $T = 2$ states at high excitation energies. Thus, the SDR with $T = 1$ coexists with the $T = 2$ GTR there. Although the decay of $T = 1$ states to final $T = 1/2$, $T_z = -1/2$ states in ^{57}Cu is isospin allowed, the wave functions of the SDR with the main $\pi g_{9/2}\nu f_{7/2}^{-1}$ configuration seem to suppress such decay.

The present results will serve to establish a good understanding of the fragmented fine structure of the GTR in ^{58}Cu. Further theoretical work including the development of the statistical-model calculation with $T = 2$ is required to describe the fine structure of the GTR as well as the decay properties of the GTR and SDR in ^{58}Cu.

ACKNOWLEDGMENTS

I would like to thank the collaborators of the E53, E173, E160 experiments at RCNP.

This work was supported in part by the Ministry of Education, Culture, Sports, Science, and Technology of Japan.

REFERENCES

1. H. Akimune *et al.*, Nucl. Phys. A **569**, 245c (1994).
2. Y. Fujita *et al.*, Eur. Phys. J. A **13**, 411 (2002).
3. C. Gaarde, J. S. Larsen, and J. Rapaport, in *Spin Excitations in Nuclei, Telluride, 1982,* Ed. by F. Petrovich *et al.* (Plenum Publ., New York, 1984), p. 65.
4. J. Rapaport *et al.*, Phys. Lett. B **119B**, 61 (1982).
5. J. Rapaport *et al.*, Nucl. Phys. A **410**, 371 (1983).
6. A. Arima, K. Shimizu, W. Bentz, and H. Hyuga, Adv. Nucl. Phys. **18**, 1 (1987).
7. G. Bertsch, P. Bortignon, and R. A. Broglia, Rev. Mod. Phys. **55**, 287 (1983).
8. R. A. Lindgren *et al.*, Phys. Rev. C **14**, 1789 (1976).
9. R. Frey *et al.*, J. Phys. Soc. Jpn. **44**, 202 (1978).
10. K. Ackermann *et al.*, Nucl. Phys. A **372**, 1 (1981).
11. N. Anantaraman *et al.*, Phys. Rev. Lett. **46**, 1318 (1981).
12. G. M. Crawley *et al.*, Phys. Rev. C **26**, 87 (1982).
13. C. Djalali *et al.*, Nucl. Phys. A **388**, 1 (1982).
14. M. Fujiwara *et al.*, Nucl. Phys. A **410**, 137 (1983).
15. W. Mettner *et al.*, Nucl. Phys. A **473**, 160 (1987).
16. H. Ikegami *et al.*, Nucl. Phys. A **329**, 84 (1979).
17. H. M. Sen Gupta *et al.*, Phys. Rev. C **63**, 017601 (2001). Note that the excitation energies above $E_x \sim 4$ MeV presented in this work are systematically deviated from the compilation values (see [22]).
18. M. Fujiwara *et al.*, Nucl. Instrum. Methods Phys. Res. A **422**, 484 (1999).
19. H. Akimune *et al.*, Phys. Rev. C **52**, 604 (1995).
20. F. Pühlhofer, Nucl. Phys. A **280**, 267 (1977); M. N. Harakeh, Extended Version of CASCADE Code (1995, in press).
21. M. R. Bhat, Nucl. Data Sheets **80**, 789 (1997).
22. H. Junde, Nucl. Data Sheets **67**, 523 (1992).
23. M. R. Bhat, Nucl. Data Sheets **85**, 415 (1998).
24. E. Gadioli and R. Zetta, Phys. Rev. **167**, 1016 (1968).
25. W. Dilg, W. Schantl, H. Vonach, and M. Uhl, Nucl. Phys. A **217**, 269 (1973).
26. W. D. Myers, *Droplet Models of Atomic Nuclei* (Plenum, New York, 1977).
27. R. G. T. Zegers *et al.*, Phys. Rev. C **61**, 054602 (2000).
28. C. R. Gould *et al.*, Phys. Rev. **188**, 1792 (1969).

Physics of Atomic Nuclei, Vol. 67, No. 9, 2004, pp. 1750–1755. From Yadernaya Fizika, Vol. 67, No. 9, 2004, pp. 1777–1782.

The Nature of Low-Lying $K^\pi = 0^+$ Bands in Nuclei*

A. Aprahamian**

Department of Physics, University of Notre Dame, USA

Received January 21, 2004

Abstract—Low-lying $K^\pi = 0^+$ bands are one of the most fundamental excitation modes in the spectra of deformed nuclei; however, very little is known about the nature of these excitations. We report on some new lifetime measurements using the GRID technique at ILL, and high-precision (p, t) reactions to elucidate the character of low-lying $K^\pi = 0^+$ bands in deformed nuclei. We also present results from a recent calculation on the nature of 0^+ states using the projected shell model. © *2004 MAIK "Nauka/Interperiodica"*.

1. INTRODUCTION

The dynamics of various quantum mechanical systems such as molecules, atomic clusters, and nuclei are crucial to our most fundamental understanding of motion. In the low-lying energy spectra of nuclei, these dynamics can be understood in terms of rotational and vibrational degrees of freedom. Rotational degrees of freedom are well understood in nuclei, while vibrational degrees of freedom remain elusive. The existence of low-lying collective vibrational motion in nuclei is one of the most fundamental questions in nuclear structure physics today. The answer involves deciphering between the roles of single-particle effects which are relevant in the nuclear fermionic system and collective motion described in terms of phonons or linear superpositions of particle–hole excitations.

Vibrational degrees of freedom in both spherical and deformed nuclei are described by phonon excitations resulting from the oscillations around an equilibrium shape. In spherical nuclei, harmonic vibrational motion results in an excitation spectrum consisting of equally spaced degenerate multiplets. Although exact harmonic phonon excitations have never been observed, there are numerous examples of nuclei exhibiting near-harmonic or anharmonic vibrational motion. In fact, one- and two-phonon excitations have been observed in tens of nuclei, as well as isolated cases of three-phonon excitations [1, 2] and in one case up to five quadrupole phonons [2].

In the low-lying energy spectra of deformed nuclei, there are two types of quadrupole vibrations superimposed on the rotational states: β and γ. The β vibration has its angular momentum aligned along the symmetry axis, whereas the γ vibration breaks axial symmetry and has a projection of $K^\pi = 2^+$ on the symmetry axis. Extending this description to the spectra of deformed nuclei, the first excited $K^\pi = 2^+$ and $K^\pi = 0^+$ bands have traditionally been labeled as single-phonon "γ" and "β" vibrational excitations. The "γ" ($K^\pi = 2^+$) excitations show typical $B(E2{:}2^+_\gamma \to 0^+_{\mathrm{g.s}})$ transition probabilities of 1–10 Weisskopf units (W.u.) that vary smoothly across a given isotopic chain and can be theoretically understood, whereas the single $K^\pi = 0^+$ "β" types of excitations have remained a mystery in nuclear structure physics. Figure 1 contains a compilation of all the known absolute $B(E2{:}2^+_{K^\pi=0^+_2} \to 0^+_{\mathrm{g.s}})$ and $B(E2{:}2^+_{K^\pi=0^+_2} \to 4^+_{\mathrm{g.s}})$ transition probabilities in

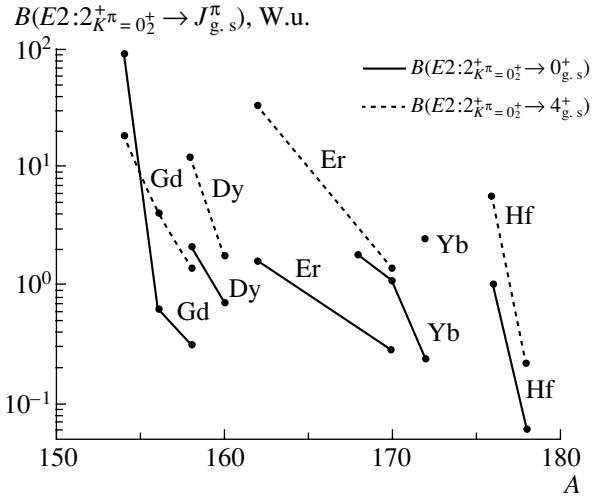

Fig. 1. A compilation of $B(E2{:}2^+_{K^\pi=0^+_2} \to J^\pi_{\mathrm{g.s}})$ values in W.u. extracted from all the known lifetimes of first excited $K^\pi = 0^+$ bands in deformed nuclei as a function of A.

*This article was submitted by the author in English.

**e-mail: aapraham@mozart.helios.nd.edu

W.u. depopulating the 2^+ state of the first excited $K^\pi = 0^+$ bands. In contrast to the $K^\pi = 2^+$ γ bands, there are enormous variations in collectivity for the $B(E2{:}2^+_{K^\pi=0^+_2} \to 0^+)$ values. For example, in the ^{154,156,158}Gd nuclei, this $B(E2)$ value varies from 90 to 0.31 W.u. This large variation in $B(E2)$ values across the region is an indication of the complexity and varying nature of the first excited $K^\pi = 0^+$ bands. While there have been many suggestions regarding the nature of these low-lying excitations, $K^\pi = 0^+$ bands in deformed nuclei remain enigmatic and the focus of intense discussions as well as a flurry of activity from both theoretical and experimental aspects. In this paper, we present some of our recent results highlighting various aspects of $K^\pi = 0^+$ excitations based on lifetime measurements, γ-ray spectroscopy, and reaction studies. In the ^{178}Hf nucleus, we show an example of a $K^\pi = 0^+$ band which is a collective excitation built on the first excited $K^\pi = 0^+$ band. In the ^{158}Gd nucleus, we show results from a (p, t) reaction pointing to the existence of 13 0^+ states below 3.1 MeV, and in the ^{156}Gd nucleus, we show an excited $K^\pi = 0^+$ band with all the characteristics of a two-phonon $\gamma\gamma$ vibrational band. Finally, we present results of a recent calculation [3] performed within the framework of the projected shell model, aimed at understanding the nature of these $K^\pi = 0^+$ bands in deformed nuclei.

2. COLLECTIVE EXCITATIONS: ^{178}Hf

The ^{178}Hf nucleus is one of the most extensively studied nuclei besides ^{168}Er. It has been studied by a variety of reactions using high-precision methods for the measurements of γ rays and conversion electrons [4]. The resulting level scheme has five known $K^\pi = 0^+$ bands, including the ground-state band, below an excitation energy of 2 MeV. Figure 2 shows all the known $K^\pi = 0^+$ bands. We have measured the lifetimes of the levels at 1276.7, 1450.4, 1496.5, and 1818.3 keV.

We have measured [5] the lifetimes of these levels using the GRID technique [6]. GRID allows lifetime measurements of levels populated in thermal neutron capture reactions from the Doppler broadening of a transition affected by the recoil of a previously emitted γ ray. The recoil velocities are very small (typically 10^{-4} to 10^{-6} of c) with resulting Doppler shifts on the order of a few eV and very short slowing-down times in the target.

The most important result of this study concerns the $K^\pi = 0^+_5$ band in ^{178}Hf at an excitation energy of 1772.2 keV. The 0^+, 2^+, and 4^+ members of this band were known from very early work. All three states show large $E0$ transitions to the ground state, supporting the $K^\pi = 0^+$ assignment of the band. The decay of the 4^+ member of this $K^\pi = 0^+_5$ band is predominantly to the $4^+_{K^\pi=0^+_2}$, $4^+_{K^\pi=0^+_3}$, and the $2^+_{K^\pi=0^+_4}$ levels, favoring the decay to the $K^\pi = 0^+_{2,3}$ bands by a factor of six in relative $B(E2)$ values. The extracted $B(E2{:}2^+_{K^\pi=0^+_5} \to 4^+_{\mathrm{g.s}})$ is ≤ 2 W.u., while the transitions to the first excited $K^\pi = 0^+_2$ band at 1199.4 keV are highly collective. The most important results emerge from the $B(E2)$ values of the 618.9- and 541.6-keV transitions to the 0^+ and 2^+ of the first excited $K^\pi = 0^+_2$ band at 1199.4 and 1276.7 keV, respectively. The multipolarity of the 618.9-keV transition is $E2$, while the 541.6-keV transition is $M1 + (50 \pm 11)\%$ $E2$ [4]. The deduced $B(E2{:}2^+_{K^\pi=0^+_5} \to 0^+_{K^\pi=0^+_2})$ has a range of $1.3 \to 5.7$ W.u., while the $B(E2{:}2^+_{K^\pi=0^+_5} \to 2^+_{K^\pi=0^+_2})$ range is $6.3 \to 27$ W.u. for the $E2$ component of the transition. The observed high level of collectivity for the $E2$ component of the 541.59-keV transition is of particular importance since it is a $J \to J$ transition and therefore it is not affected by mixing matrix elements between $K^\pi = 0^+$ bands.

A five-band mixing calculation was carried out including four $K^\pi = 0^+$ bands (ground-state band and the three excited $K^\pi = 0^+$ bands for which lifetimes are measured) along with the $K^\pi = 2^+$ band. The matrix elements to the ground-state band were extracted from the lifetime measurements and the bands were allowed to mix in order to see whether it would be possible to produce collective transitions between the $K^\pi = 0^+_5$ and the first excited $K^\pi = 0^+_2$ band. The only possibility of creating collective transitions between these two bands was via mixing of the $K^\pi = 0^+_5$ and the $K^\pi = 2^+$ bands. Even then, when the mixing matrix element was a factor of 10 larger than the other mixing matrix elements between all the other bands, it was impossible to reproduce both of the observed collective transitions. Therefore, we conclude that no mixing matrix element between the $K^\pi = 2^+$ and the $K^\pi = 0^+$ bands can result in the two observed collective transitions simultaneously.

This measurement [5] revealed for the first time the existence of two excited $K^\pi = 0^+$ bands connected by strongly collective transitions. The $B(E2)$ values from the second and third excited $K^\pi = 0^+$ bands to the ground-state band would perhaps raise a question regarding the identification of either band as the collective one-phonon β vibrational excitation. However, the observed preference of decay from the 2^+ and 4^+ members of the $K^\pi = 0^+_5$ band at 1772.2-keV band is

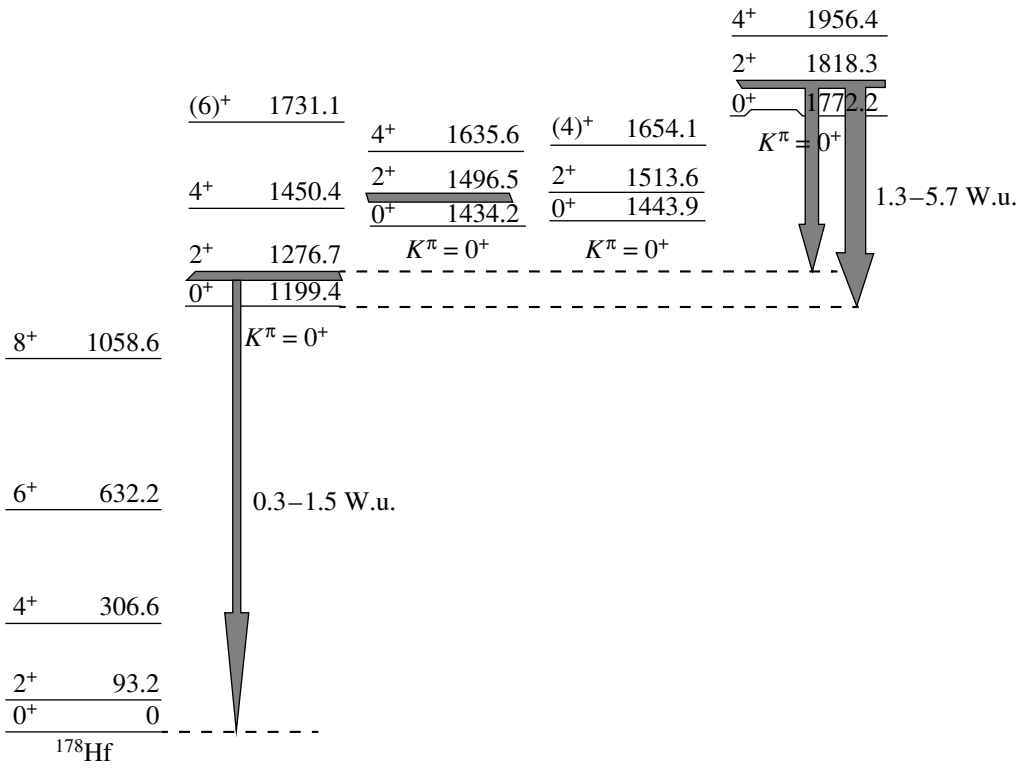

Fig. 2. The known $K^\pi = 0^+$ bands in the nucleus ^{178}Hf. The thicker lines indicate the measured level energies (in keV).

to the band at 1199.4 keV. This is compatible with the expected behavior of a collective-vibrational excitation built on the 1199.4-keV band. The outstanding question is the collectivity of the first excited $K^\pi = 0^+$ band. Our new measurements are in excellent agreement with Coulomb excitation results for all three states. Our results indicate some significant degree of collectivity for the first excited $K^\pi = 0^+$ band. The most important result is the indication for the first time of the existence of a collective $K^\pi = 0^+$ excitation built on an excited $K^\pi = 0^+$ band in any nucleus. If the collectivity of the first excited $K^\pi = 0^+$ band can be more forcefully established, then this work would also point to the first observation of a two-phonon $\beta\beta$ vibration. Finally, five-band mixing calculations clearly show that it is impossible to reproduce the collective transitions between the two excited bands by $\Delta K = 2$ or 0 mixing matrix elements. Two-phonon vibrational excitations are expected to occur at twice the excitation energy of the one-phonon vibration. The harmonic value for the ratio of $B(E2{:}2^+_{\beta\beta} \to 0^+_\beta)$ and $B(E2{:}2^+_\beta \to 0^+_{\rm g.s})$ is 2.0. In ^{178}Hf, the excitation energy ratio of the two bands is 1.5 and the range for the $B(E2)$ ratio is approximately $1 \to 17$, consistent with the expected harmonic value. The two-phonon $\gamma\gamma$ vibrational excitation in ^{232}Th was similarly anharmonic in energy with an energy ratio of 1.8 and a $B(E2{:}4^+_{\gamma\gamma} \to 2^+_\gamma)/B(E2{:}2^+_\gamma \to 0^+_{\rm g.s})$ ratio of 3.1 ± 0.4 [7], in agreement with the expected harmonic value of 2.78.

In summary, the lifetimes of five levels in three excited $K^\pi = 0^+$ bands have been measured in the ^{178}Hf nucleus using the GRID technique. The $K^\pi = 0^+_2$ band is less collective but on the same order of magnitude as some of the single-phonon γ vibrational bands in this region of deformed nuclei. An excited $K^\pi = 0^+_5$ band at 1772.2 keV shows a preference of decay with transitions of collective strength to the $K^\pi = 0^+_2$ band at 1199.4 keV. The collective transitions between the two bands cannot be reproduced by band mixing. The consequence is the characterization of the $K^\pi = 0^+_5$ band as a collective excitation built on the first excited $K^\pi = 0^+_2$ band at 1199.4 keV.

3. NEW 0^+ STATES IN ^{158}Gd

The motivation to study 0^+ states in ^{158}Gd is based on the intense current interest in this topic. In order to carry out a meaningful discussion or a comprehensive theoretical effort to understand the nature of these $K^\pi = 0^+$ bands, it is first necessary to establish a more complete set of $K^\pi = 0^+$ excitations in deformed nuclei. We carried out [8] a new high-precision ^{160}Gd$(p, t)^{158}$Gd measurement. The ^{158}Gd

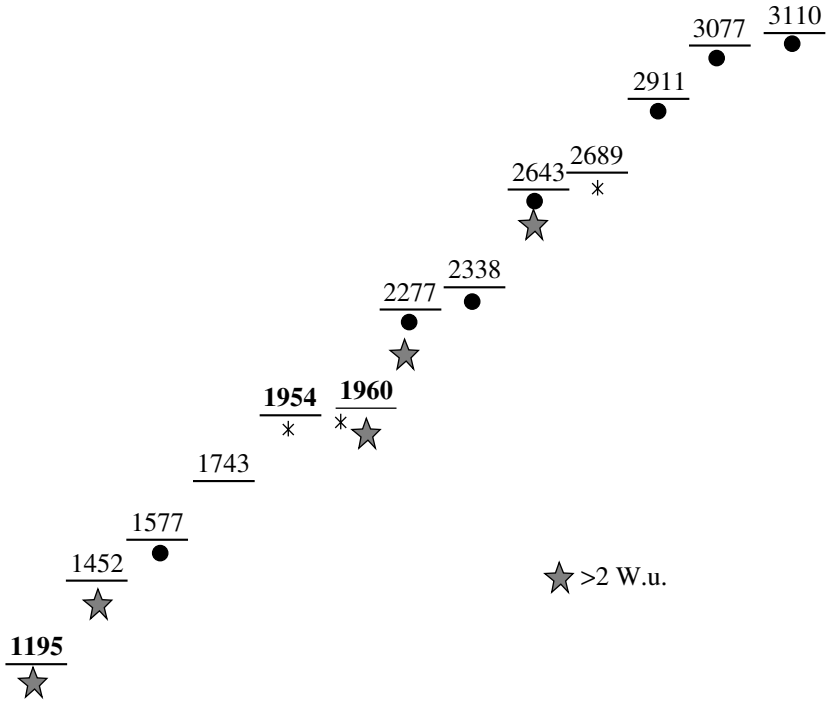

Fig. 3. Results of the new (p, t) measurement indicating the excitation energies (in keV) of all the observed 0^+ states in ^{158}Gd.

nucleus prior to this work had three positively and four tentatively identified excited $K^\pi = 0^+$ states below 3 MeV. We report on the existence of thirteen excited $K^\pi = 0^+$ bands in one nucleus below an excitation energy of approximately 3.1 MeV. This number is by far the largest ever seen in any nucleus and provides a unique laboratory for developing and testing new models on the nature of $K^\pi = 0^+$ excitations in nuclei. Figure 3 shows the thirteen observed excited 0^+ states.

The measurement was carried out at the high-precision Q3D spectrometer of the University of Munich MP tandem accelerator laboratory using a 27-MeV proton beam on a 122-μg/cm^2 target of isotopically enriched ^{160}Gd (98.10%) with a 14-μg/cm^2 carbon backing. A 1.8-m-long focal plane detector provided the particle identification of the ejectiles of mass 1–4 in the Q3D spectrometer [9] with an unprecedented energy resolution of approximately 4–6 keV for the energy range of interest from 1 to 3 MeV. This resolution is a spectacular achievement for transfer reactions. We were able to identify thirteen excited $K^\pi = 0^+$ bands below 3.1 MeV in excitation energy in the spectrum of ^{158}Gd. Three of these 0^+ states were previously identified. Four of the thirteen had previous tentative assignments. We confirm three of these four to be 0^+ states. In addition, there were seven new 0^+ assignments. The new 0^+ assignments are further strengthened by the placement of γ rays that were clearly identified as belonging to the ^{158}Gd nucleus with no previous level assignments. Such an abundance of 0^+ states has not previously been seen in nuclei until the very present. In a well-deformed nucleus, such as ^{158}Gd, it is not yet possible to decipher the nature of all the observed 0^+ states. With the present measurement, ^{158}Gd provides an unprecedented opportunity for the investigation of the nature of $K^\pi = 0^+$ bands. The observation of thirteen excited $K^\pi = 0^+$ excitations in one nucleus below an excitation energy of 3.1 MeV will be the strongest challenge yet to our understanding of these excitations. There are already two theoretical studies [3, 10] using completely different approaches. The first one [10] shows calculations with the geometric collective model and the interacting boson approximation to account for the many 0^+ states that have been observed in this nucleus. The conclusion of this study was that most of the 0^+ states are collective in nature, including the possibility of double-octupole character, and very few are quasiparticle in character. The second study is one done by Sun *et al.* [3] in the framework of the projected shell model, aiming at understanding the nature of these states in ^{158}Gd. This model contains projected two- and four-quasiparticle states as building blocks in the basis, and it is able to reproduce reasonably well the energies for all the observed 0^+ states. Upon comparing the theoretical and experimental 0^+ states (up to 3.2 MeV in energy) in order of excitation energy, the predicted 0^+ states are found to be in the right energy range. What we

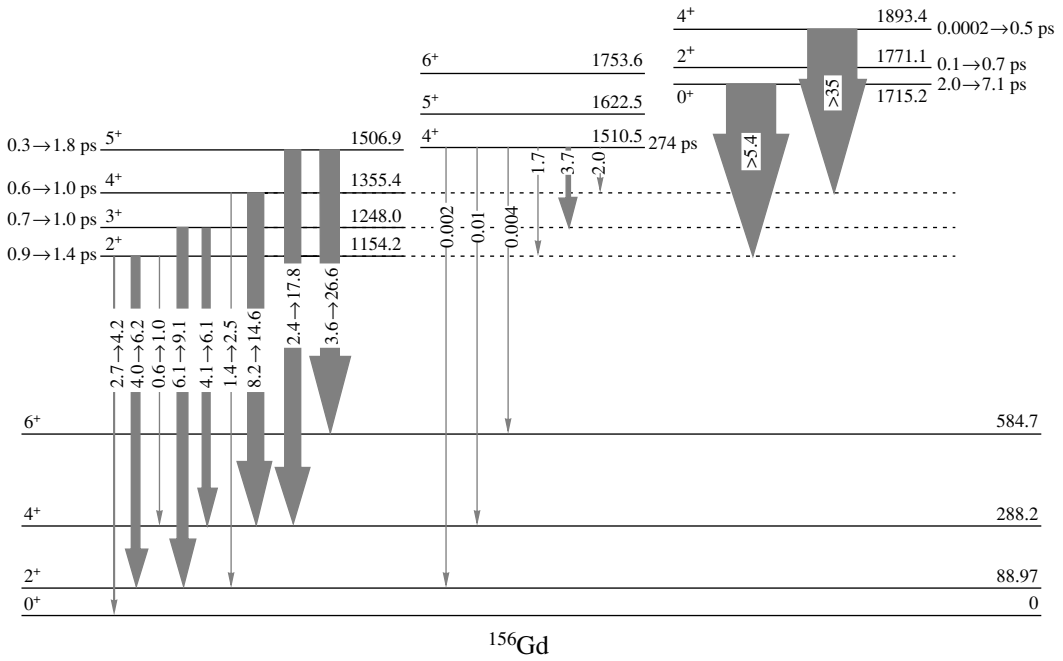

Fig. 4. A partial level scheme for ^{156}Gd (in keV). The ranges of measured lifetimes are shown, as well as the evaluated $B(E2)$ value ranges or limits.

found impressive is the number of 0^+ states predicted by the calculation. The PSM produces a sufficient number of 0^+ states to be compared with data. The obtained $B(E2)$ values, however, tend to suggest that these 0^+ states might be mostly quasiparticle in character with some limited admixtures of collective vibrations.

4. $K^\pi = 0^+$ $\gamma\gamma$ VIBRATION: ^{156}Gd

The lifetimes of twelve levels from four different excitation bands were measured in ^{156}Gd using the GRID technique. Nine of these measurements are new and the other three agree very well with previously measured values. Transitions from the $K^\pi = 0_2^+$ band at 1049 keV to the ground-state band show it to be collective, and this is strong evidence that this band is indeed the collective phonon β vibrational band. $B(E2)$ calculations for transitions from the $K^\pi = 2^+$ band to the ground-state band supports the assignment of this band as the γ band. The $K^\pi = 0_4^+$ band at 1715 keV is shown to be strongly connected to the $K^\pi = 2^+$ γ band, which is evidence of this being a $K^\pi = 0^+$ multiphonon $\gamma\gamma$ vibrational band or at the very least a 0^+ band with sizeable admixture of two-phonon $\gamma\gamma$. There is only one other nucleus [11] (^{166}Er), where a $K^\pi = 0^+$ $\gamma\gamma$ excitation has been observed at 2.47 times the excitation energy of the γ band. This is the first evidence for a $K^\pi = 0^+$ $\gamma\gamma$ band at 1.4 times the excitation energy of the γ band. Figure 4 shows a partial level scheme with the associated $B(E2)$ range of values or limits indicated on the arrows.

5. WHAT IS THE NATURE OF $K^\pi = 0^+$ BANDS IN DEFORMED NUCLEI?

All three nuclei discussed in this paper exhibit a different aspect of $K^\pi = 0^+$ bands in deformed nuclei. These new measurements have greatly enhanced our understanding of $K^\pi = 0^+$ bands even though a clear explanation is far from reach. There are, however, two interesting observations to make regarding the observed level of collectivity associated with the lowest excited $K^\pi = 0^+$ bands in these nuclei. In the $^{154-158}$Gd isotopes, the first excited $K^\pi = 0^+$ band is typically below the first excited $K^\pi = 2^+$ band in excitation energy. The largest energy separation is for the ^{154}Gd nucleus, which also exhibits the largest $E2$ collectivity for this band in depopulating to the ground-state band. The ^{166,168}Er isotopes exhibit an energy spectrum, where the first excited $K^\pi = 0^+$ band is well above the $K^\pi = 2^+$ γ band. In these cases, the transitions from the excited $K^\pi = 0^+$ band to the ground-state band are weakly collective, yet they show a high level of collectivity to the first excited $K^\pi = 2^+$ γ band several hundred keV below in excitation energy. It seems that the relative position of the first excited $K^\pi = 0^+$ and the $K^\pi = 2^+$ γ band plays a key role. In addition, at the beginning of the onset

of deformation, the $2n$ and $2p$ pairing gaps are well above the excitation energies of the first excited $K^\pi = 0^+$ bands. An example is the pairing gap estimated from five nearby masses for ^{154}Gd ($2p = 2.2$ MeV; $2n = 2.5$ MeV) in comparison with the energy of the first excited $K^\pi = 0^+$ bandhead at 680 keV. This in comparison with ^{168}Er, where the pairing gaps are at 1.8 and 1.5 MeV, respectively, and the first excited $K^\pi = 0^+$ band is at 1.2 MeV in the spectrum.

In conclusion, new advances in technology, sensitivities in measurements, ultrahigh precision in transfer reactions, and lifetime measurements have tremendously improved our knowledge base regarding the character of excited $K^\pi = 0^+$ bands in deformed nuclei. The results are puzzling at best, but the new information now provides the possibility of developing and testing new models on the nature of $K^\pi = 0^+$ bands.

ACKNOWLEDGMENTS

The present work is the result of many close collaborations with our group at Notre Dame, the ILL in France, and the TU in Munich. The work includes part of the dissertations of author's students R.C. de Haan, Plamen Boutachkov, and Xiang Wu.

We gratefully acknowledge the support of this work from the National Science Foundation, contract no. 01-40324.

REFERENCES

1. A. Aprahamian *et al.*, Phys. Rev. Lett. **59**, 535 (1987).
2. R. F. Casten *et al.*, Phys. Lett. B **297**, 19 (1992).
3. Yang Sun *et al.*, Phys. Rev. C **68**, 061301 (2003).
4. A. M. I. Haque *et al.*, Nucl. Phys. A **455**, 231 (1986).
5. A. Aprahamian *et al.*, Phys. Rev. C **65**, 031301 (2002).
6. H. Börner and J. Jolie, J. Phys. G **19**, 217 (1993).
7. W. Korten *et al.*, Phys. Lett. B **317**, 19 (1993).
8. S. R. Lesher *et al.*, Phys. Rev. C **66**, 051305(R) (2002).
9. E. Zanotti *et al.*, Nucl. Instrum. Methods Phys. Res. A **310**, 706 (1991).
10. V. Zamfir *et al.*, Phys. Rev. C **66**, 057303 (2002).
11. P. E. Garrett *et al.*, Phys. Rev. Lett. **78**, 4545 (1997).

Physics of Atomic Nuclei, Vol. 67, No. 9, 2004, pp. 1756–1759. From Yadernaya Fizika, Vol. 67, No. 9, 2004, pp. 1783–1786.

Low-Lying States and Separabelized Skyrme Interactions*

A. P. Severyukhin[1)], V. V. Voronov[1)], Ch. Stoyanov[2)], and N. Van Giai[3)]**

Received January 21, 2004

Abstract—A finite-rank separable approximation for the quasiparticle RPA calculations with Skyrme interactions that was proposed in our previous work is extended to take into account the coupling between one- and two-phonon terms in the wave functions of excited states. It is shown that the phonon–phonon coupling effect can be very important to reproduce experimental data. © *2004 MAIK "Nauka/Interperiodica".*

1. INTRODUCTION

The random phase approximation (RPA) [1–4] with the self-consistent mean field derived by making use of the Gogny interaction [5] or the Skyrme-type interactions [6, 7] is nowadays one of the standard tools of performing nuclear structure calculations. Many properties of the nuclear collective states can be described successfully within these models [7–15], but due to the anharmonicity of vibrations, in many cases one needs to take into account coupling between one-phonon and more complex states [2, 4].

It is well known that, using simple separable forces, one can perform calculations of nuclear characteristics in very large configuration spaces, since there is no need to diagonalize matrices whose dimensions grow with the size of configuration space. That is why a finite-rank approximation for the particle–hole (p–h) interaction resulting from Skyrme-type forces was suggested in our previous work [16]. Thus, the self-consistent mean field can be calculated in the standard way with the original Skyrme interaction, whereas the RPA solutions would be obtained with the finite-rank approximation to the p–h matrix elements. Other schemes to construct a separable approximation for Skyrme forces were considered in [17, 18].

Recently, we extended the finite-rank approximation for p–h interactions of Skyrme type to take into account the pairing [19] and phonon–phonon coupling effects [20]. To illustrate the phonon–phonon coupling effect, we present the results of our calculations for the quadrupole and octupole states in ^{124}Sn.

2. BASIC FORMULAS AND DETAILS OF CALCULATIONS

We start with the effective Skyrme interaction [6] and use the notation of [21] containing explicit density dependence and all spin-exchange terms. The single-particle spectrum is calculated within the HF method. The continuous part of the single-particle spectrum is discretized by diagonalizing the HF Hamiltonian on the harmonic-oscillator basis [22]. The p–h residual interaction $\tilde{V}_{\rm res}$ corresponding to the Skyrme force and including both direct and exchange terms can be obtained as the second derivative of the energy density functional with respect to the density [23]. Following our previous papers [16, 19], we simplify $\tilde{V}_{\rm res}$ by approximating it by its Landau–Migdal form [7]. For Skyrme interactions, all Landau parameters F_l, G_l, F_l', G_l' with $l > 1$ are zero. Here, we keep only the $l = 0$ terms in $V_{\rm res}$, and in the coordinate representation, one can write the interaction in the following form:

$$V_{\rm res}(\mathbf{r}_1, \mathbf{r}_2) = N_0^{-1}[F_0(r_1) + G_0(r_1)\boldsymbol{\sigma}_1 \cdot \boldsymbol{\sigma}_2 \quad (1)$$
$$+ (F_0'(r_1) + G_0'(r_1)\boldsymbol{\sigma}_1 \cdot \boldsymbol{\sigma}_2)\boldsymbol{\tau}_1 \cdot \boldsymbol{\tau}_2]\delta(\mathbf{r}_1 - \mathbf{r}_2),$$

where $\boldsymbol{\sigma}_i$ and $\boldsymbol{\tau}_i$ are the spin and isospin operators, and $N_0 = 2k_{\rm F}m^*/(\pi^2\hbar^2)$ with $k_{\rm F}$ and m^* standing for the Fermi momentum and nucleon effective mass. The expressions for F_0, G_0, F_0', G_0' in terms of the Skyrme force parameters can be found in [21]. Because of the density dependence of the interaction, the Landau parameters of Eq. (1) are functions of the coordinate $\mathbf{r}$.

The p–h residual interaction can be represented as a sum of N separable terms [16]. In what follows,

*This article was submitted by the authors in English.

[1)]Bogolyubov Laboratory of Theoretical Physics, Joint Institute for Nuclear Research, Dubna, Moscow oblast, 141980 Russia.

[2)]Institute for Nuclear Research and Nuclear Energy, Bulgarian Academy of Sciences, Sofia, Bulgaria.

[3)]Institut de Physique Nucléaire, Université Paris Sud, Orsay, France.

**e-mail: sever@thsun1.jinr.ru

we use the second quantized representation and $V_{\rm res}$ can be written as

$$\hat{V}_{\rm res} = \frac{1}{2}\sum_{1234} V_{1234} : a_1^+ a_2^+ a_4 a_3 :, \qquad (2)$$

where a_1^+ (a_1) is the particle creation (annihilation) operator and "1" denotes the quantum numbers $(n_1 l_1 j_1 m_1)$.

A matrix element of two-body interaction V_{1234} contains the radial integrals including the Landau parameters. For example, the contribution of the term F_0 includes the radial integral

$$I(j_1 j_2 j_3 j_4) \qquad (3)$$
$$= N_0^{-1}\int_0^\infty F_0(r) u_{j_1}(r) u_{j_2}(r) u_{j_3}(r) u_{j_4}(r)\frac{dr}{r^2},$$

where $u_j(r)$ is the radial part of the HF single-particle wave function. As is shown in [16, 19], the radial integrals can be calculated accurately by choosing a large enough cutoff radius R and using the N-point integration Gauss formula with abscissas r_k and weights w_k:

$$I(j_1 j_2 j_3 j_4) \simeq N_0^{-1}\frac{R}{2} \qquad (4)$$
$$\times \sum_{k=1}^{N}\frac{w_k F_0(r_k)}{r_k^2} u_{j_1}(r_k) u_{j_2}(r_k) u_{j_3}(r_k) u_{j_4}(r_k).$$

So we employ the Hamiltonian including an average nuclear HF field, pairing interactions, and the isoscalar and isovector p–h residual forces in the finite-rank separable form [19]. This Hamiltonian has the same form as the QPM Hamiltonian with N separable terms [4, 24], but in contrast to the QPM, all parameters of this Hamiltonian are expressed through parameters of the Skyrme forces.

In what follows, we work in the quasiparticle representation defined by the canonical Bogolyubov transformation:

$$a_{jm}^+ = u_j \alpha_{jm}^+ + (-1)^{j-m} v_j \alpha_{j-m}. \qquad (5)$$

Single-particle states are specified by the quantum numbers (jm). The quasiparticle energies, the chemical potentials, the energy gap, and the coefficients u_j,v_j of the Bogolyubov transformations (5) are determined from the BCS equations.

We introduce the phonon creation operators

$$Q_{\lambda\mu i}^+ = \frac{1}{2}\sum_{jj'}[X_{jj'}^{\lambda i} A^+(jj';\lambda\mu) \qquad (6)$$
$$- (-1)^{\lambda-\mu} Y_{jj'}^{\lambda i} A(jj';\lambda\ -\mu)],$$

where

$$A^+(jj';\lambda\mu) = \sum_{mm'}\langle jmj'm'|\lambda\mu\rangle \alpha_{jm}^+ \alpha_{j'm'}^+. \qquad (7)$$

The index λ denotes a total angular momentum and μ is its z projection in the laboratory system. One assumes that the QRPA ground state is the phonon vacuum $|0\rangle$, i.e., $Q_{\lambda\mu i}|0\rangle = 0$. We define the excited states in this approximation by $Q_{\lambda\mu i}^+|0\rangle$.

Making use of the linearized equation-of-motion approach [1], one can derive the standard QRPA equations [3, 4]:

$$\begin{pmatrix} \mathcal{A} & \mathcal{B} \\ -\mathcal{B} & -\mathcal{A} \end{pmatrix}\begin{pmatrix} X \\ Y \end{pmatrix} = w\begin{pmatrix} X \\ Y \end{pmatrix}. \qquad (8)$$

Exact expressions for $\mathcal{A}$ and $\mathcal{B}$ are given in [19]. Solutions of this set of linear equations yield the eigenenergies and the amplitudes X, Y of the excited states. The dimension of the matrices $\mathcal{A}, \mathcal{B}$ is a space size of two-quasiparticle configurations. Expressions for $\mathcal{A}, \mathcal{B}$ and X, Y are given in [19].

Using the finite-rank approximation, one needs to invert a matrix having a dimension $4N \times 4N$ independently of the configuration-space size. One can find a prescription how to solve the system (8) within our approach in [16, 19]. The QRPA equations in the QPM [4, 24] have the same form as the equations derived within our approach [16, 19], but the single-particle spectrum and parameters of the p–h residual interaction are calculated by making use of the Skyrme forces.

In this work, we use the parametrizations *SLy4* [25] of the Skyrme force. It is well known [4, 11, 12] that the constant-gap approximation leads to overestimation of occupation probabilities for subshells that are far from the Fermi level, and it is necessary to introduce a cutoff in the single-particle space. Above this cutoff, subshells do not participate in the pairing effect. In our calculations, we choose the BCS subspace to include all subshells lying below 5 MeV.

Energies and $B(E\lambda)$ values for up-transitions to the first 2^+, 3^- states in ^{124}Sn

	2_1^+		3_1^-	
	Energy, MeV	$B(E2)$, e^2 fm^4	Energy, MeV	$B(E3)$, e^2 fm^6
Exp.	1.13	1660 ± 40	2.60	$73\,000 \pm 10\,000$
QRPA	1.92	1800	3.64	210 000
2PH	1.03	1500	3.25	200 000

The pairing constants are fixed to reproduce the odd–even mass difference of the neighboring nuclei. In order to perform RPA calculations, the single-particle continuum is discretized [22] by diagonalizing the HF Hamiltonian on the basis of twelve harmonic-oscillator shells and cutting off the single-particle spectra at the energy of 160 MeV. This is sufficient to exhaust practically the whole value of the energy-weighted sum rule. Our investigations [19] enable us to conclude that $N = 45$ is sufficient for multipolarities $\lambda \leq 3$ in nuclei with $A \leq 208$. Our calculations show that, for the normal parity states, one can, as a rule, neglect the spin–multipole interactions and this reduces by a factor 2 the total matrix dimension. For example, for the octupole excitations in ^{206}Pb [19], we need to invert a matrix having a dimension $2N = 90$ instead of diagonalizing a 1376×1376 matrix, as it would be without the finite-rank approximation. Thus, for heavy nuclei, our approach gives a large gain in comparison with exact diagonalization. To take into account the mixing of the configurations in the simplest case, one can write the wave functions of excited states as

$$\Psi_\nu(\lambda\mu) = \left\{ \sum_i R_i(\lambda\nu) Q^+_{\lambda\mu i} + \sum_{\lambda_1 i_1, \lambda_2 i_2} P^{\lambda_2 i_2}_{\lambda_1 i_1}(\lambda\nu) \left[Q^+_{\lambda_1\mu_1 i_1} Q^+_{\lambda_2\mu_2 i_2} \right]_{\lambda\mu} \right\} |0\rangle \quad (9)$$

with the normalization condition

$$\langle \Psi_\nu(JM) | \Psi_\nu(JM) \rangle = \sum_i R_i^2(J\nu) + 2 \sum_{\lambda_1 i_1, \lambda_2 i_2} (P^{\lambda_1 i_1}_{\lambda_2 i_2}(J\nu))^2 = 1. \quad (10)$$

The matrix element coupling one- and two-phonon configurations reads

$$\left\langle Q_{Ji} \middle| H \middle| \left[Q^+_{\lambda_1 i_1} Q^+_{\lambda_2 i_2} \right]_J \right\rangle = U^{\lambda_1 i_1}_{\lambda_2 i_2}(Ji), \quad (11)$$

where $U^{\lambda_1 i_1}_{\lambda_2 i_2}(Ji)$ is some combination of the geometrical factors and the QRPA phonon amplitudes [4, 26].

The energies of states $\Psi_\nu(\lambda\mu)$ are solutions of the following equation [4]:

$$F(E_\nu) \equiv \det \left| (\omega_{\lambda i} - E_\nu)\delta_{ii'} - \frac{1}{2} \sum_{\lambda_1 i_1, \lambda_2 i_2} \frac{U^{\lambda_1 i_1}_{\lambda_2 i_2}(\lambda i) U^{\lambda_1 i_1}_{\lambda_2 i_2}(\lambda i')}{\omega_{\lambda_1 i_1} + \omega_{\lambda_2 i_2} - E_\nu} \right| = 0. \quad (12)$$

The rank of the determinant equals the number of one-phonon configurations included in the first term of the wave function $\Psi_\nu(\lambda\mu)$.

It is worthwhile to point out that, after solving the RPA problem with a separable interaction, taking into account the coupling with two-phonon configurations demands diagonalizing a matrix having a size that does not exceed 40 even for the giant-resonance calculations in heavy nuclei, whereas one would need to diagonalize a matrix with a dimension of the order of a few thousand at least for a nonseparable case.

3. RESULTS OF CALCULATIONS

As an example, we consider the 2^+_1-, 3^-_1-state energies and transition probabilities $B(E\lambda)$ in ^{124}Sn. The experimental data [27, 28] and the results of our calculations within the QRPA and upon taking into account the two-phonon terms (2PH) are shown in the table. In our calculations, the two-phonon terms of the wave function (9) include phonons with multipolarities $\lambda = 2, 3, 4, 5$. One can see that there is some overestimation of the energies and transition probabilities for the QRPA calculations. The inclusion of two-phonon configurations results in reduction of the energies and transition probabilities for the 2^+_1, 3^-_1 states in ^{124}Sn. Generally, there is a reasonable agreement between theory and experiment, but calculations overestimate the octupole energy and $B(E3)$ value.

4. CONCLUSION

A finite-rank separable approximation for the QRPA calculations with Skyrme interactions, which was proposed in our previous work, is extended to take into account the coupling between one- and two-phonon terms in the wave functions of excited states.

It is shown that the suggested approach enables one to reduce remarkably the dimensions of the matrices that must be inverted to perform structure calculations in very large configuration spaces.

As an illustration of the method, we have calculated the energies and transition probabilities of the 2^+_1 and 3^-_1 states in ^{124}Sn. It is found that there is reasonable agreement with experimental data and

inclusion of two-phonon terms is very important. A systematic study of the influence of the two-phonon terms on properties of the low-lying states in the neutron-rich Sn isotopes is in progress now.

ACKNOWLEDGMENTS

A.P.S. and V.V.V. thank the hospitality of IPN-Orsay, where part of this work was done. This work is partly supported by INTAS Fellowship Grant for Young Scientists (Fellowship Reference no. YSF 2002-70), by IN2P3–JINR agreement, and by the Bulgarian Science Foundation (contract no. Ph-801).

REFERENCES

1. D. J. Rowe, *Nuclear Collective Motion, Models and Theory* (Barnes and Noble, 1970).
2. A. Bohr and B. Mottelson, *Nuclear Structure* (Benjamin, New York, 1975), Vol. 2.
3. P. Ring and P. Schuck, *The Nuclear Many-Body Problem* (Springer, Berlin, 1980).
4. V. G. Soloviev, *Theory of Atomic Nuclei: Quasiparticles and Phonons* (Inst. of Phys., Bristol, England, 1992).
5. D. Gogny, in *Nuclear Self-Consistent Fields*, Ed. by G. Ripka and M. Porneuf (North-Holland, Amsterdam, 1975).
6. D. Vautherin and D. M. Brink, Phys. Rev. C **5**, 626 (1972).
7. A. B. Migdal, *The Theory of Finite Fermi Systems and Atomic Nuclei Properties* (Nauka, Moscow, 1983) [in Russian].
8. H. Flocard and P. Quentin, Annu. Rev. Nucl. Part. Sci. **28**, 523 (1978).
9. J. Dobaczewski, W. Nazarewicz, T. R. Werner, *et al.*, Phys. Rev. C **53**, 2809 (1996).
10. G. Colò, N. Van Giai, P.-F. Bortignon, and R. A. Broglia, Phys. Rev. C **50**, 1496 (1994).
11. E. Khan and Nguyen Van Giai, Phys. Lett. B **472**, 253 (2000).
12. G. Colò and P.-F. Bortignon, Nucl. Phys. A **696**, 427 (2001).
13. S. A. Fayans *et al.*, Nucl. Phys. A **676**, 49 (2000).
14. E. E. Saperstein, S. A. Fayans, and V. A. Khodel, Sov. J. Part. Nucl. **9**, 221 (1978).
15. G. Giambrone *et al.*, Nucl. Phys. A **726**, 3 (2003).
16. Nguyen Van Giai, Ch. Stoyanov, and V. V. Voronov, Phys. Rev. C **57**, 1204 (1998).
17. T. Suzuki and H. Sagawa, Prog. Theor. Phys. **65**, 565 (1981).
18. V. O. Nesterenko, J. Kvasil, and P.-G. Reinhard, Phys. Rev. C **66**, 044307 (2002).
19. A. P. Severyukhin, Ch. Stoyanov, V. V. Voronov, and Nguyen Van Giai, Phys. Rev. C **66**, 034304 (2002).
20. A. P. Severyukhin, V. V. Voronov, Ch. Stoyanov, and Nguyen Van Giai, Nucl. Phys. A **722**, 123c (2003).
21. Nguyen Van Giai and H. Sagawa, Phys. Lett. B **106B**, 379 (1981).
22. J. P. Blaziot and D. Gogny, Nucl. Phys. A **284**, 429 (1977).
23. G. F. Bertsch and S. F. Tsai, Phys. Rep. **18C**, 126 (1975).
24. V. G. Soloviev, Yad. Fiz. **50**, 40 (1989) [Sov. J. Nucl. Phys. **50**, 25 (1989)].
25. E. Chabanat, P. Bonche, P. Haensel, *et al.*, Nucl. Phys. A **635**, 231 (1998).
26. V. V. Voronov and V. G. Soloviev, Sov. J. Part. Nucl. **14**, 583 (1983).
27. S. Raman, C. W. Nestor, Jr., and P. Tikkanen, At. Data Nucl. Data Tables **78**, 1 (2001).
28. T. Kibedi and R. H. Spear, At. Data Nucl. Data Tables **80**, 35 (2002).

Physics of Atomic Nuclei, Vol. 67, No. 9, 2004, pp. 1760–1765. From Yadernaya Fizika, Vol. 67, No. 9, 2004, pp. 1787–1792.

Complex Shape Effects in Nuclear Rotational Spectra*

N. Minkov[1),2)], S. B. Drenska[1)], P. Yotov[1)], and W. Scheid[2)***]**

Received January 21, 2004

Abstract—We study the evolution of collectivity in the structure of nuclear rotational bands based on complex quadrupole–octupole shapes. We apply an extended version of a quadrupole–octupole rotation model capable of reproducing both the low-lying states of alternating parity bands interpreted on the basis of octupole vibrations and the higher spin states considered as members of a single octupole rotational band. In such a way, the complicated odd–even staggering effects observed in light actinide nuclei are described successfully. The implemented model analysis suggests a unified mechanism in which the octupole band structure is formed as the result of the transition from an octupole vibration (soft) mode to a rotation of a shape with a stable quadrupole–octupole deformation. © *2004 MAIK "Nauka/Interperiodica".*

1. INTRODUCTION

Recently, a model formalism applicable to rotational motion of nuclei with octupole deformations has been proposed [1]. It provides a useful theoretical tool in the study of rotational motion in nuclear systems with complex quadrupole–octupole shapes. This quadrupole–octupole rotation model (QORM) is based on the point-symmetry group theory which allows one to construct a rotational Hamiltonian for octupole deformations superposed on the top of a quadrupole shape. It suggests specific properties of collective motion characterized by "wobbling"-type modes. On this basis, QORM provides an explanation and successful description [2, 3] of the fine staggering effects [4] observed in nuclear octupole bands.

In the present work, we extend the model formalism by including the lowest states of the spectrum in which the octupole shape properties are not well pronounced. This development reproduces the angular-momentum region, where the separate sequences of negative- and positive-parity levels merge into a single octupole rotational band. Our purpose is to obtain a consistent QORM description of all angular-momentum regions in the spectrum as well as to study the evolution of collectivity in the formation of octupole structure in nuclear rotational bands.

2. THE QUADRUPOLE–OCTUPOLE ROTATION MODEL

The basic ingredient of QORM is the collective octupole Hamiltonian [1]

$$\hat{H}_{\rm oct} = \hat{H}_{A_2} + \sum_{r=1}^{2}\sum_{i=1}^{3}\hat{H}_{F_r(i)} \qquad (1)$$

constructed by the irreducible representations A_2, $F_1(i)$, and $F_2(i)$ $(i = 1, 2, 3)$ of the octahedron (O) point-symmetry group, where

$$\hat{H}_{A_2} = a_2\frac{1}{4}[(\hat{I}_x\hat{I}_y + \hat{I}_y\hat{I}_x)\hat{I}_z + \hat{I}_z(\hat{I}_x\hat{I}_y + \hat{I}_y\hat{I}_x)], \qquad (2)$$

$$\hat{H}_{F_1(1)} = \frac{1}{2}f_{11}(5\hat{I}_z^3 - 3\hat{I}_z\hat{I}^2), \qquad (3)$$

$$\hat{H}_{F_2(1)} = \frac{1}{2}f_{21}[\hat{I}_z(\hat{I}_x^2 - \hat{I}_y^2) + (\hat{I}_x^2 - \hat{I}_y^2)\hat{I}_z],$$

$$\hat{H}_{F_1(2)} = \frac{1}{2}f_{12}(5\hat{I}_x^3 - 3\hat{I}_x\hat{I}^2),$$

$$\hat{H}_{F_2(2)} = f_{22}(\hat{I}_x\hat{I}^2 - \hat{I}_x^3 - \hat{I}_x\hat{I}_z^2 - \hat{I}_z^2\hat{I}_x),$$

$$\hat{H}_{F_1(3)} = \frac{1}{2}f_{13}(5\hat{I}_y^3 - 3\hat{I}_y\hat{I}^2),$$

$$\hat{H}_{F_2(3)} = f_{23}(\hat{I}_y\hat{I}_z^2 + \hat{I}_z^2\hat{I}_y + \hat{I}_y^3 - \hat{I}_y\hat{I}^2).$$

The different terms in the above Hamiltonian (cubic combinations of angular-momentum operators in the body fixed frame) generate rotational degrees of freedom for the system in correspondence to various octupole shapes with a magnitude determined by the model parameters a_2 and f_{ri} $(r = 1, 2; i = 1, 2, 3)$.

The octupole degrees of freedom are superposed on the top of the leading quadrupole degrees of free-

*This article was submitted by the authors in English.

[1)]Institute for Nuclear Research and Nuclear Energy, Bulgarian Academy of Sciences, Sofia, Bulgaria.

[2)]Institut für theoretische Physik der Justus-Liebig-Universität, Giessen, Germany.

**e-mail: nminkov@inrne.bas.bg

***e-mail: Werner.Scheid@theo.physik.uni-giessen.de

dom of the system. So we take the quadrupole rotation Hamiltonian

$$\hat{H}_{\rm quad} = A\hat{I}^2 + A'\hat{I}_z^2 + C'(\hat{I}_x^2 - \hat{I}_y^2), \qquad (4)$$

which provides the general energy scale for rotational motion of the nucleus. In addition, we assume the presence of a high-order quadrupole–octupole interaction, restricting ourselves to its diagonal term in the total angular-momentum space,

$$\hat{H}_{\rm qoc} = f_{\rm qoc}\frac{1}{I^2}(15\hat{I}_z^5 - 14\hat{I}_z^3\hat{I}^2 + 3\hat{I}_z\hat{I}^4). \qquad (5)$$

Equations (2)–(5) represent the Hamiltonian of the collective QORM [1]. The total model Hamiltonian includes an additional low-energy term carrying information about the vibrational degrees of freedom. Its origin and explicit involvement in the formalism will be discussed in the next section.

In this general framework, the yrast rotational spectrum of the system is obtained by minimizing the energy in the diagonal Hamiltonian terms with respect to the third intrinsic projection K of the collective angular momentum I in the states $|I, K\rangle$ and diagonalizing the total Hamiltonian. The so determined energy spectrum is built on different intrinsic K configurations which provide a $\Delta I = 1$ staggering behavior of rotational energy. The changing values of the quantum number K are related to a wobbling-type collective motion resulting from the complicated shape characteristics of the system.

3. LOW-ENERGY EXTENSION OF QORM

The above-presented collective rotation Hamiltonian is constructed under the assumption of well-determined shape characteristics of the nucleus. However, the analysis of experimental data shows that the stable octupole deformations appear at some higher angular-momentum region of the spectrum. For an example (which is also the case of our interest) in the alternating parity bands of light rare-earth nuclei, this is the region of angular momenta $I \sim 7$–8 [5]. Below this region, the negative-parity states are shifted up with respect to the positive-parity states, so they do not form a single rotational band. The reason is that the system undergoes a tunneling between two reflection asymmetric (octupole) shape orientations (up and down) separated by a slightly pronounced potential barrier. As a result, a strong parity-splitting effect is observed. This situation can be described approximately as a vibration of the system with respect to some octupole deformation variable β in a symmetric double-well potential. The variable β can represent the parameter of the axial octupole deformation or some appropriate combination of the all seven collective coordinates characterizing the octupole shape. For higher angular momenta $I >$ 7–8, the potential barrier becomes higher and the tunneling effect sharply decreases. Then the vibration mode is reduced and the octupole shape properties of the system are stabilized. The rotation mode becomes favorable and a well-formed single octupole band can be observed.

The above-mentioned higher angular-momentum region ($I > 7$–8) is the original area of application for the QORM rotational Hamiltonian (2)–(5). In order to consider the lowest part of the spectrum $I < 7$–8, we need to take into account the strong parity effect due to the octupole vibration mode. This can be done through the solution of the Schrödinger equation for the following octupole vibration Hamiltonian:

$$H_{\rm vib} = -\frac{\hbar^2}{2B_3}\frac{d^2}{d\beta^2} + U(\beta), \qquad (6)$$

where the quantity B_3 is an effective octupole mass parameter and determines the energy scale for the octupole motion.

The potential for the collective motion in the coordinate β can be taken in the form [6]

$$U(\beta) = \frac{1}{2}C\beta^2 + D(e^{-\beta^2/a^2} - 1). \qquad (7)$$

The structure of the spectrum generated in the potential (7) depends on the relative magnitude of the constants C and D. First of all, when the condition $D/C > a^2/2$ is fulfilled, the potential has a double-well shape. The increase in the ratio D/C leads to an increase in the barrier separating the deformation minima and vice versa. It is known [6] that, when D is relatively small (low potential barrier), the levels in the potential are spaced similarly to the oscillator spectrum with alternatively changing parity. The respective collective spectrum of the system will exhibit a strong parity shift between odd and even angular-momentum level sequences. For sufficiently large D (high potential barrier), the space between the neighboring positive- and negative-parity levels is smaller, with the respective parity-shift effect also being smaller. In the limiting case of an infinitely high barrier, the potential is divided into two separate oscillators with the neighboring positive- and negative-parity states appearing with the same energy, so that parity doublets are formed. Then the collective states built on such a potential will not feel any parity-splitting effect, which is a condition for the appearance of a nonperturbed rotational spectrum.

The evolution of the octupole dynamics as a function of the collective angular momentum of the system I can be taken into account by considering the angular-momentum dependence of the potential $U(\beta) = U(\beta, I)$. Here, we assume that the energy-barrier term depends on I as $D = D(I) = d_0 +$

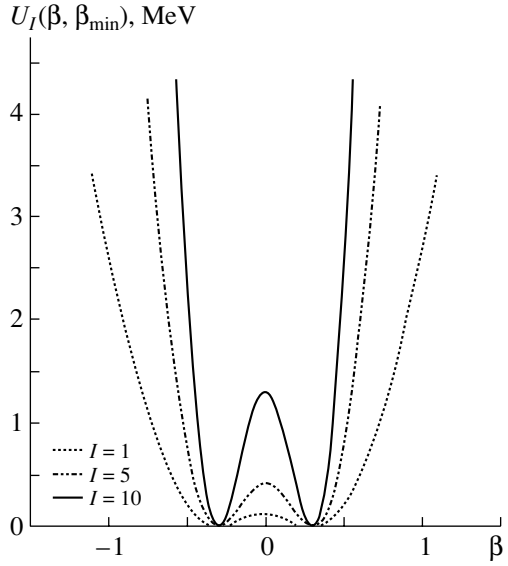

Fig. 1. The octupole deformation potential (10) for three different values of the angular momentum $I = 1, 5, 10$. The parameters values used in Eq. (10) are given in Figs. 3*a*, 3*b*.

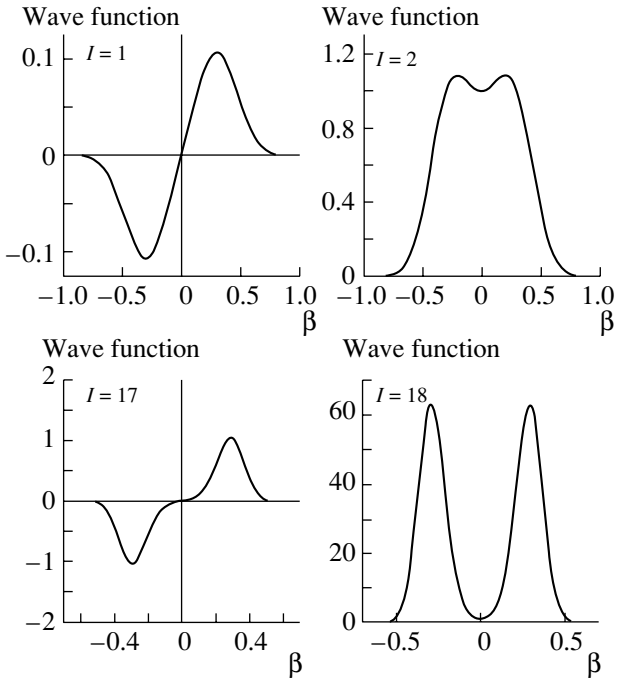

Fig. 2. Negative- and positive-parity eigenfunctions (not normalized) for the Hamiltonian (6) with the potential (10) and for several collective angular momenta. The parameters values used in Eq. (10) are given in Figs. 3*a*, 3*b*.

$dI(I+1)$. The function $D(I)$ has the meaning of a centrifugal term added to the harmonic part $\frac{1}{2}C\beta^2$. The Gaussian factor $e^{-\beta^2/a^2} - 1$ determines the magnitude of the centrifugal interaction as a function of the deformation coordinate β. Further, we consider that the potential $U(\beta, I)$ has a minimum at some fixed value of $\beta = \beta_{\min}$. The extremum condition $\frac{\partial}{\partial\beta}U(\beta, I)\Big|_{\beta_{\min}} = 0$ leads to the relation

$$C = (2/a^2)D(I)e^{-\beta^2_{\min}/a^2}. \tag{8}$$

Thus, the vibration parameter C also depends on the angular momentum with the condition $D(I)/C > a^2/2$ being automatically fulfilled. The above result suggests a nonadiabatic rotational–vibrational character of the collective motion. The substitution of Eq. (8) into (7) leads to the following form of the octupole potential:

$$U'_I(\beta, \beta_{\min}) \tag{9}$$
$$= [d_0 + dI(I+1)]e^{-\beta^2_{\min}/a^2}[\beta^2/a^2 + e^{-(\beta^2-\beta^2_{\min})/a^2} - e^{\beta^2_{\min}/a^2}].$$

After fixing the origin of the energy scale in the minimum value $U'_I(\beta_{\min}, \beta_{\min})$, we finally obtain

$$U_I(\beta, \beta_{\min}) \tag{10}$$
$$= [d_0 + dI(I+1)]e^{-\beta^2_{\min}/a^2}[(\beta^2 - \beta^2_{\min})/a^2 + e^{-(\beta^2-\beta^2_{\min})/a^2} - 1].$$

The evolution of the shape of the potential (10) as a function of the angular momentum is demonstrated in Fig. 1, while the respective evolution of the wave functions in the Schrödinger equation for the Hamiltonian (6) is illustrated in Fig. 2.

We have developed a numerical code which generates a collective energy spectrum based on the solutions of the Schrödinger equation for the potential (10). Thus, we produced a schematic energy sequence characterizing the contribution of the octupole vibration mode to the low-lying part of the alternating parity band. This is shown in Fig. 3*a*. We see that it reproduces the correct order of the neighboring positive- and negative-parity states in the angular-momentum region $I < 7–8$. Above this region, the schematic levels are ordered normally and increase almost linearly with I.

Further, we examined the above schematic spectrum by means of the fourth (discrete) derivative of the energy difference $\Delta E(I) = E(I+1) - E(I)$,

$$\mathrm{Stg}(I) = 6\Delta E(I) - 4\Delta E(I-1) \tag{11}$$
$$- 4\Delta E(I+1) + \Delta E(I+2) + \Delta E(I-2).$$

As can be seen in Fig. 3*b*, this quantity shows a well-developed staggering pattern with a rapidly decreasing magnitude of oscillations. This is consistent with the staggering behavior observed in the low-energy

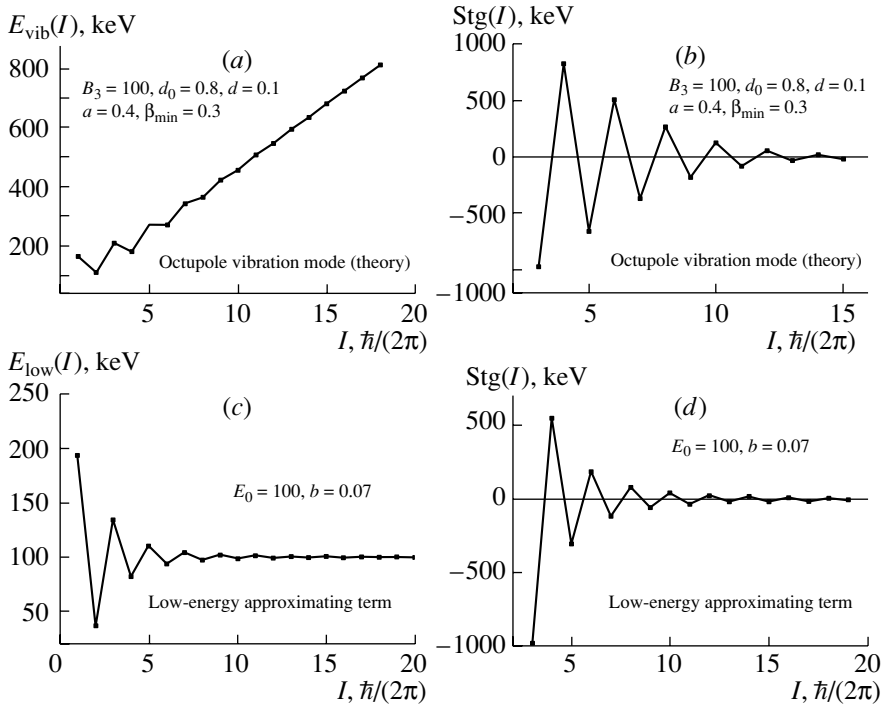

Fig. 3. Schematic energies and staggering patterns obtained by the potential (10) (*a* and *b*) and by the phenomenological term (12) (*c* and *d*). The parameters B_3, d_0, and d are given in MeV, and E_0 is in keV, while the other parameters are dimensionless.

part of alternating parity bands of light actinide nuclei [4]. However, we have to remark immediately that, while the solutions of the Schrödinger equation (6) suggest a complete disappearance of the staggering at some point, the experimental data show a more complicated "beat" pattern with the presence of further staggering regions at higher angular momenta.

Thus, the above consideration suggests that the entire structure of the alternating parity (octupole) bands, including all angular-momentum regions, can be reproduced through a unified model formalism based on both the QORM Hamiltonian (2)–(5) and the Schrödinger equation for the octupole vibration Hamiltonian (6) with the potential (10). As a first step in this direction, in the present work, we introduce a phenomenological term carrying certain characteristics of the above-considered vibrational model. We choose it so that it reproduces the strong parity-splitting effect in the low-spin region together with the abnormal ordering of the odd and even levels, as well as its reduction at the higher spin levels. We take this term in the form

$$\hat{H}_{low} = E_0[1 - \hat{P}/(1 + bI^3)], \qquad (12)$$

where $\hat{P}$ is the parity operator with the eigenvalue $(-1)^I$. Equation (12) effectively takes into account the parity effect caused by the vibration mode. The parameter b in the denominator of (12) determines the rapidity of decrease in the parity splitting with the increase in the angular momentum. In the framework of QORM, it is restricted, so that the effect of $\hat{H}_{low}$ in the staggering pattern vanishes near the region where the octupole band is formed. Note that Eq. (12) suggests a stabilization of the intrinsic (vibration) energy to some constant value E_0, while the schematic energies obtained through the potential (10) increase with the angular momentum. This is illustrated in Figs. 3*c* and 3*d*, where the contribution of (12) to the energy levels and the staggering pattern of the spectrum is shown. The study of the angular-momentum dependence of the vibration mode will be the subject of further work.

The analysis implemented in this section suggests the presence of a *critical angular-momentum region* for the formation of the octupole band structure which could be interpreted as the region of a transition from the quadrupole plus soft octupole to a stable quadrupole–octupole shape structure of the system. The proposed extended application of QORM matches two separate dynamical manifestations of collectivity represented both by the term (12) and by the rotational terms (2)–(5).

4. NUMERICAL RESULTS

We have applied the above-extended QORM formalism to the alternating parity bands in the light actinide nuclei ^{224,226}Ra and ^{224,226}Th. After adjusting

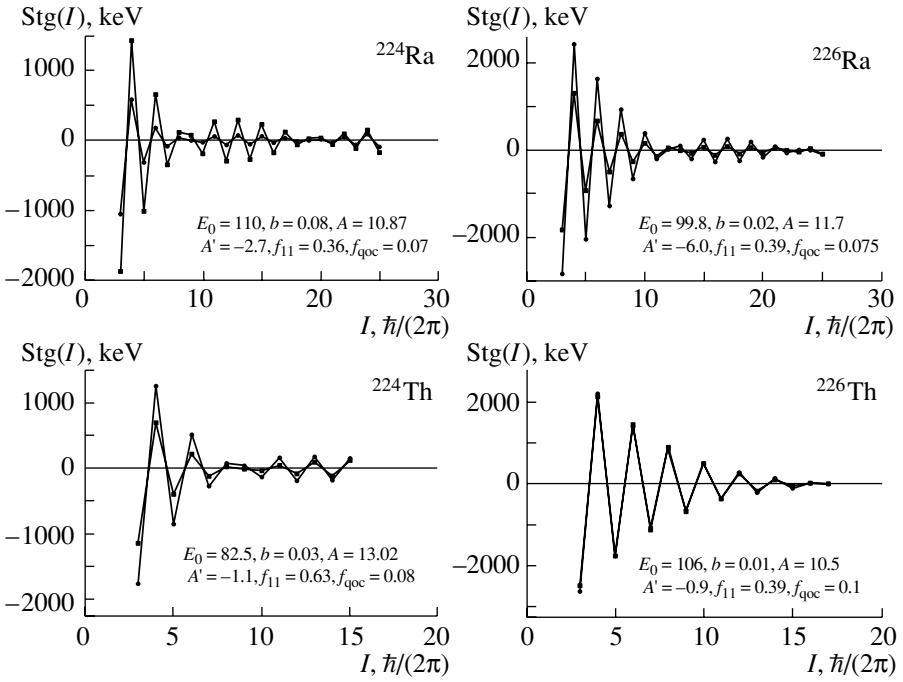

Fig. 4. $\Delta I = 1$ staggering patterns for the octupole bands in ^{224,226}Ra and ^{224,226}Th: experiment (●) (data from [5]) and theory (■) (the parameter values are given in keV).

model parameters with respect to the experimental data, we successfully described the energy levels in all angular-momentum regions in these bands, including the lowest levels. As a result, the respective $\Delta I = 1$ staggering patterns have also been reproduced successfully. This is demonstrated in Fig. 4, where the theoretical and experimental staggering patterns of the considered nuclei are compared. The parameters of the model fits are displayed in the figures.

An important feature of our model description is the correct reproduction of the nodes (points with near zero staggering amplitude) separating the different beat regions in the staggering patterns. In this way, the theoretical patterns clearly indicate the angular-momentum region, where the two separate sequences of negative- and positive-parity levels merge into a single octupole rotational band. The model description clearly identifies it as a critical region in which the octupole band is formed. This is provided by the fast decrease in the oscillations of the low-energy term (12). In fact, the observed change in collectivity appears consistently with the appearance of the first node in the corresponding beat staggering pattern. For example, in the case of $^{224-226}$Ra, this happens in the region near $I \sim 10$, while in ^{226}Th the critical region is shifted to $I \sim 15$ (see Fig. 4).

It is important to remark that the presence of the octupole-forming region is typical for the considered light actinide nuclei and identifies them as the best examples of octupole-deformed nuclear systems. The wider systematics of actinide and rare-earth nuclei shows that this type of collective properties is gradually reduced towards the midshell regions [7]. In the latter cases, only the lowest part of the staggering pattern is developed, where the amplitude slightly decreases with the angular momentum without reaching any node, so the octupole-band-forming region is not observed.

Finally, we remark that the successful reproduction of the second and the third beat regions in the staggering patterns of ^{224,226}Ra and ^{224}Th (demonstrated in Fig. 4) provides a relevant model interpretation of the fine octupole band structure at high angular momenta. Thus, the applied model formalism successfully describes not only the energy-level structure but also the angular-momentum properties of the system and the related staggering effects, which are extremely sensitive characteristics of the collective nuclear dynamics.

5. CONCLUSION

In conclusion, we demonstrated that an extended QORM formalism can be applied to reproduce the entire structure of alternating parity bands in light actinide nuclei, including the angular-momentum regions below and above the critical region of the forming octupole band. The implemented model analysis clearly outlines the transition between different collective modes of nuclear motion, vibration, and rotation, based on the quadrupole and octupole degrees of

freedom and their interaction. It suggests a dynamical mechanism in which the two separate sequences of negative- and positive-parity levels merge into a single octupole rotational band. We suggest that such a mechanism can govern more general collective properties in nuclei with complex shapes.

ACKNOWLEDGMENTS

This work is supported by DFG.

One of us (N.M.) is grateful to DAAD for support during the beginning of this study.

REFERENCES

1. N. Minkov, S. Drenska, P. Raychev, *et al.*, Phys. Rev. C **63**, 044305 (2001).
2. N. Minkov and S. Drenska, Prog. Theor. Phys. Suppl. **146**, 597 (2002).
3. N. Minkov, S. Drenska, and P. Yotov, in *Proceedings of the 21st International Workshop on Nuclear Theory, Rila, Bulgaria, 2002*, Ed. by V. Nikolaev (Heron, Soña, 2002), p. 290.
4. D. Bonatsos *et al.*, Phys. Rev. C **62**, 024301 (2000).
5. J. F. C. Cocks *et al.*, Phys. Rev. Lett. **78**, 2920 (1997); A. Artna-Cohen, Nucl. Data Sheets **80**, 227 (1997); Y. A. Akovali, Nucl. Data Sheets **77**, 433 (1996).
6. G. A. Leander *et al.*, Nucl. Phys. A **388**, 452 (1982).
7. D. Bonatsos *et al.*, in *Algebraic Methods in Nuclear Theory,* Ed. by A. Antonov (Heron, Sofia, 2002), p. 89.